DIELECTRIC PROPERTIES OF TITANATE NANOTUBES PREPARED BY HYDROTHERMAL ROUTE

Pristanuch Kasian

A Thesis Submitted in Partial Fulfillment of the Requirements for the

Degree of Doctor of Philosophy in Physics

Suranaree University of Technology

Academic Year 2015

สมบัติไดอิเล็กตริกของท่อไททาเนตเตรียมโดยวิธีไฮโดรเทอร์มอล

นางสาวปริศฑนุช เกษียร

วิทยานิพนธ์นี้เป็นส่วนหนึ่งของการศึกษาตามหลักสูตรปริญญาวิทยาศาสตรดุษฎีบัณฑิต
สาขาวิชาฟิสิกส์
มหาวิทยาลัยเทคโนโลยีสุรนารี
ปีการศึกษา 2558

DIELECTRIC PROPERTIES OF TITANATE NANOTUBES PREPARED BY HYDROTHERMAL ROUTE

Suranaree University of Technology has approved this thesis submitted in partial fulfillment of the requirements for the Degree of Doctor of Philosophy.

Thesis Examining Committee

(Asst. Prof. Dr. Worawat Meevasana)
Chairperson

(Prof. Dr. Santi Maensiri)
Member (Thesis Advisor)

(Assoc. Prof. Dr. Rattikorn Yimnirun)
Member

(Dr. Saroj Rujirawat)
Member

(Asst. Prof. Dr. Prasit Thongbai)
Member

(Prof. Dr. Sukit Limpijumnong)
Vice Rector for Academic Affairs
and Innovation

(Prof. Dr. Santi Maensiri)
Dean of Institute of Science

ปริศฑนุช เกษียร : สมบัติไดอิเล็กตริกของท่อไททาเนตเตรียมโดยวิธีไฮโดรเทอร์มอล (DIELECTRIC PROPERTIES OF TITANATE NANOTUBES PREPARED BY HYDROTHERMAL ROUTE) อาจารย์ที่ปรึกษา : ศาสตราจารย์ ดร.สันติ แม้นศิริ, 212 หน้า.

ในงานวิจัยนี้ได้ทำการสังเคราะห์ท่อไททาเนต ($Na_xH_{2-x}Ti_3O_7.nH_2O$; TNTs) และ Fe/Co-doped TNTs (i.e., $A(B_xTi_{3-x}O_7)$ ($A = Na_{0.96}H_{1.04}\cdot 3.42H_2O$, B = Fe หรือ Co ที่ซึ่ง x = 0 0.05 0.1 0.2 0.3 และ 0.4) ด้วยวิธีไฮโดรเทอร์มอล โดยใช้ไททาเนียมไดออกไซด์และสารละลายโซเดียมไฮดรอกไซด์ความข้นข้น 10 โมล ทำปฏิกิริยาที่อุณหภูมิ 130 องศาเซลเซียส เป็นเวลา 24 ชั่วโมง จากนั้นนำสารที่เตรียมได้ไปทำการศึกษาลักษณะเฉพาะโดยใช้เทคนิค XRD SEM TEM HRTEM EDX TGA FTIR UV-Vis และVSM ศึกษาสถานะประจุของ Ti Fe และ Co โดยใช้เทคนิค XPS และ XANES จากผลการศึกษาโครงสร้างของตัวอย่างทั้งหมดที่เตรียมได้พบว่า มีเฟส tritanate ($A_2Ti_3O_7$, A = Na or H) และไม่พบการเกิดเฟสปลอมปนของสารประกอบอื่น การศึกษาโครงสร้างทางจุลภาคพบว่ามีโครงสร้างแบบท่อ มีขนาดเส้นผ่านศูนย์กลางประมาณ 7-15 นาโนเมตร และความยาวระดับไมครอน มีโครงสร้างผนังหลายชั้นประมาณ 3 ถึง 4 ชั้น และมีระยะห่างระหว่างชั้นประมาณ 0.782-0.788 นาโนเมตร ผลจากการศึกษา TGA และ FTIR พบว่ามีปริมาณน้ำจำนวนมากอยู่ภายในโครงสร้างของท่อนาโน ผลจากศึกษาสถานะประจุของ Fe Co และ Ti พบว่ามีประจุ Fe^{2+} Fe^{3+} Co^{2+} และ Ti^{4+} และพบการเกิดช่องว่างของออกซิเจนในโครงสร้าง จากการศึกษาเทคนิค UV-Vis พบว่าตัวอย่างที่เตรียมได้แสดงพฤติกรรม redshift โดยมีสาเหตุมาจากการเจือของ Fe หรือ Co เมื่อศึกษาสมบัติทางแม่เหล็กของตัวอย่างที่เตรียมได้พบว่า ที่อุณหภูมิห้องท่อนาโนไททาเนตแสดงพฤติกรรมแม่เหล็กแบบไดอา ในทางกลับกันการเจือของ Fe หรือ Co แสดงพฤติกรรมแม่เหล็กแบบเฟอร์โรและพารา ผลของความเป็นแม่เหล็กแบบเฟอร์โร มีสาเหตุมาจากช่องว่างของออกซิเจน ซึ่งเป็นตัวกลางของการเกิดอัตรกิริยาการแลกเปลี่ยน ในขณะที่พฤติกรรมแม่เหล็กแบบพารามีสาเหตุมาจากประจุอิสระของโลหะที่เจือ

การศึกษาสมบัติทางไดอิเล็กตริกและสมบัติทางไฟฟ้าที่ความถี่และอุณหภูมิต่างๆ พบว่าวัสดุท่อนาโนไททาเนต วัสดุเจือ Fe หรือ Co มีค่าคงที่ไดอิเล็กตริกที่สูง โดยมีค่าประมาณ 10^4 ถึง 10^5 กระบวนการผ่อนคลายทางไดอิเล็กตริกสามารถอธิบายได้โดยการประยุกต์แบบจำลองการผ่อนคลายทางไดอิเล็กตริก Cole-Cole ร่วมกับพจน์ของการนำไฟฟ้ากระแสตรง สำหรับการเจือ Fe ค่าคงที่ไดอิเล็กตริกมีค่าเพิ่มขึ้น แต่การเจือด้วย Co จะทำให้ค่าคงที่ไดอิเล็กตริกลดลง แต่ที่น่าสนใจ

คือค่าการสูญเสียทางไดอิเล็กตริกมีค่าลดลงอย่างมีนัยสำคัญในขณะที่ค่าคงที่ไดอิเล็กตริกยังคงมีค่าสูง พฤติกรรมการตอบสนองทางไดอิเล็กตริกสามารถอธิบายด้วยการโพราไรเซชันที่ชั้นฉนวนภายในที่เกิดขึ้นในวัสดุที่มีโครงสร้างจุลภาคไม่สม่ำเสมอ

สาขาวิชาฟิสิกส์ ลายมือชื่อนักศึกษา________________________

ปีการศึกษา 2558 ลายมือชื่ออาจารย์ที่ปรึกษา___________________

ลายมือชื่ออาจารย์ที่ปรึกษาร่วม________________

ลายมือชื่ออาจารย์ที่ปรึกษาร่วม________________

PRISTANUCH KASIAN : DIELECTRIC PROPERTIES OF
TITANATE NANOTUBES PREPARED BY HYDROTHERMAL
ROUTE. THESIS ADVISOR : PROF. SANTI MAENSIRI, Ph.D.
212 PP.

TITANATE NANOTUBES/DIELECTRIC PROPERTIES/HYDROTHERMAL METHOD/ NANOTUBES

In this work, the titanate nanotubes ($Na_xH_{2-x}Ti_3O_7.nH_2O$; TNTs) and Fe/Co-doped TNTs (i.e., $A(B_xTi_{3-x}O_7)$ ($A = Na_{0.96}H_{1.04}\cdot 3.42H_2O$, B = Fe or Co, where x = 0, 0.05, 0.1, 0.2, 0.3 and 0.4) were synthesized by hydrothermal method. These samples were prepared using TiO_2 in 10M NaOH at temperatures of 130 °C for 24 h. The prepared samples were characterized by X-ray diffraction (XRD), scanning electron microscopy (SEM), transmission electron microscopy (TEM), high-resolution transmission electron microscopy (HRTEM), energy-dispersive X-ray spectroscopy (EDX), thermal gravimetric analysis (TGA), fourier transform infrared (FTIR), UV-Vis spectroscope (UV-Vis) and vibrating sample magnetometer (VSM). The valence states of Ti, Fe and Co ions were determined by using X-ray photoelectron spectroscopy (XPS) and X-ray absorption near edge structure (XANES). The XRD result indicated that all sample had trititanate ($A_2Ti_3O_7$, A = Na or H) phase without any impurity phases. The diameter and length of the nanotubes were found to be ~7-15 nm and micrometer scales, respectively. The wall involves multilayer about 3-4 layers with distances between layers of ~ 0.782-0.788 nm. The TGA and FTIR results indicated that the large amount of water molecules for TNTs was within the nanotubes. The valence states of Fe, Co and Ti ions were in the Fe^{2+}, Fe^{3+} and Co^{2+} and Ti^{4+} state, as observed evidence of oxygen vacancy (V_O) in structure. UV-Vis spectra showed a redshift to the band gap energy due to Fe or Co substitution. Room temperature magnetization results indicated that TNTs are diamagnetic, whereas Fe/Co-doped TNTs are ferromagnetic and paramagnetic. The Room temperature Ferromagnetic observed in Fe/Co-doped TNTs originates due to the V_O, supporting the V_O mediated ferromagnetic exchange mechanism. Our samples the observed paramagnetic signal is because of the free ions of TM without magnetic impurities. The dielectric and electrical properties are investigated as functions of frequency, temperature, dc bias voltage and current voltage. For the dielectric properties, all the TNTs and Fe/Co-doped exhibited high dielectric constant (ε') values of about 10^4-10^6. The dielectric relaxation in the samples can be ascribed by Cole-Cole relaxation equation combining with the dc conduction term. For Fe/Co-doped TNTs, the ε' increases with increasing concentration of Fe doping ions, whereas, the ε' decreases with increasing concentration of Co doping ions. This suggests that the Fe or Co doping influences the TNTs substitution and second phase. Interestingly, the loss tangent ($\tan\delta$) of Fe/Co-doped TNTs significantly decreased; while the dielectric constant remained high. The dielectric response behavior could be attributed to interfacial polarization mechanism, resulting from the inhomogeneous structure.

School of Physics	Student's Signature____________________
Academic Year 2015	Advisor's Signature____________________
	Co-advisor's Signature__________________
	Co-advisor's Signature__________________

ACKNOWLEDGEMENTS

There are many people, to whom I would like to express my sincere word of acknowledgments:

I would like to express my deepest and sincere gratitude to my supervisor, Prof. Dr. Santi Maensiri for their effective scientific supervision, instructive guidance, generous personal encouragement, and supporting. Working under the tutelage of great materials scientists like them gave me the opportunity to learn about different techniques and processes in material research including state of the art nanoparticles preparation and characterization, which helped in vastly improving my understanding in fields of Applied Physics and Materials Science. Not only his scientific expertise, but also his optimism and trust were a great help and motivation throughout my work.

I would like to thank my co-advisor, Dr. Teerapon Yamwong, Assoc. Prof. Dr. Rattikorn Yimnirun and Dr. Saroj Rujirawat for serving on my PhD. In addition, they took effort in reading and providing me with valuable comments.

I would like to thank my thesis examination committee members, Asst. Prof. Dr. Pasit Thongbai, and Asst. Prof. Dr. Worawat Meevasana for serving on my PhD. In addition, they took effort in reading and providing me with valuable comments.

I would like to thank the School of Physics Institute of Science Suranaree University of Technology, Suranaree University of Technology, Advanced Materials Physics (AMP) Laboratory, Khon Kaen University, Chiang Mai University, and National Metal and Materials Technology Center (MTEC) for providing many research facilities, The Synchrotron Light Research Institute (Public Organization),

Nakhon Ratchasima, Thailand for XANES facilities. I am grateful to Science Achievement Scholarship Programme of Thailand (SAST) from Thai Government for financial support.

Specials thanks to Dr. Teerapon Yamwong and Mr. Bundit Putasaeng for electrical measurement and data analysis and Capt. Chaiyawan Masakul for him love and encouragement.

It is impossible to list all of my fellow graduate students, who were a great support during my Ph.D. study, for all the great times we had together.

Finally, I would like to thank my parents: my father, Mongkol Kasian; my mother, Chayanan Kaonapathana and my sister, Princhaket Kasian and Prankhanit Kasian, my grandmother, Bualee Timajai and my grandfather, Jumrus Timajai their love for always standing by me, to bring me up and give the good life.

Pristanuch Kasian

CONTENTS

Page

CHAPTER

CONTENTS (Continued)

CONTENTS (Continued)

CONTENTS (Continued)

Page

CONTENTS (Continued)

LIST OF TABLES

LIST OF TABLES (Continued)

LIST OF TABLES (Continued)

LIST OF FIGURES

Figure **Page**

LIST OF FIGURES (Continued)

LIST OF FIGURES (Continued)

Figure **Page**

LIST OF FIGURES (Continued)

Figure **Page**

LIST OF FIGURES (Continued)

LIST OF FIGURES (Continued)

LIST OF FIGURES (Continued)

Figure **Page**

LIST OF FIGURES (Continued)

Figure **Page**

LIST OF FIGURES (Continued)

Figure **Page**

LIST OF FIGURES (Continued)

Figure **Page**

LIST OF FIGURES (Continued)

LIST OF ABBREVIATIONS

$\overline{E}$	Electric filed
ε_0	The permittivity of free space (8.854×10^{-12} Fm^{-1})
ε_{permit}	The permittivity of dielectric materials
ε'	The dielectric constant
μ_0	The vaccum permeability
c_0	The speed of light in vaccum
C_0	The capacitance of the free space capacitor
C	The capacitance
$\overline{\mu}$	The electric dipole moment
$\pm Q$	The electric charges
$\overline{P}$	The polarization
N	The number of the displaced molecules per unit volume
σ'_b	The bound charge density
I_c	The charging current
V	The sinusoidal voltage ($V = V_0 \exp(j\omega t)$)
G	The conductance
I_{tatal}	The total current
I_l	The loss current

LIST OF ABBREVIATIONS (Continued)

δ	The loss angle
ε^*	The complex dielectric constant
ε'	The real part of ε^* (the dielectric constant)
ε''	The imaginary part of ε^* (the dielectric loss)
ω	The angular frequency
$\tan\delta$	The loss tangent or the dissipation factor
$\overline{D}$	The total electric displacement field
$\varepsilon^*{}_{permit}$	The complex permittivity of a dielectric material
χ	The electric susceptibility
N_i	The number of dipoles of type i per unit volume
$\overline{\mu}_i$	The average dipole moment
α	The polarizability
α_{SC}	The space charge polarizability
P_{tatal}	The total polarization
P_e	The electronic polarization
P_a	The atomic polarization
P_{or}	The orientational polarization
P_∞	The high-frequency polarization
ε'_∞	The dielectric constant at a high frequency range

LIST OF ABBREVIATIONS (Continued)

ε'_s	The the low-frequency dielectric constant or the relaxed static dielectric constant
τ	The relaxation time
k_B	The Boltzmann constant (1.38×10^{-23} J/K)
T	The absolute temperature (K)
b	The distance separating the potential well
α	The Cole-Cole constant parameter ($0<\alpha\leq1$)
J_{total}	The total current density
J	The conduction current or current density
σ_{dc}	The dc electrical conductivity
σ_{ac}	The ac electrical conductivity
Y^*	The complex admittance
E_a	The activation energy for relaxation
$E_{a\sigma dc}$	The activation energy of conductivity
$f_{p(\varepsilon'')}$	The frequencies at the peak of ε''
$f_{p(\delta)}$	The frequencies at the peak of $\tan\delta$
Z^*	The complex impedance
Z'	The real part of the complex impedance
Z''	The imaginary part of the complex impedance
(R_g, R_{gb})	The resistances of grains and grain boundary, respectively

LIST OF ABBREVIATIONS (Continued)

(C_g, C_{gb})	The capacitances of grains and grain boundary, respectively
$\sigma_{palaron}$	The polaron conductivity
K	The equilibrium constant
X	The reactance
G	The conductance
B	The susceptance
D	The dissipation factor
R	The resistance
C_p	The capacitance of the parallel plate capacitor
F	The structure factor
f	The atomic scattering factor
α	The absorption coefficient
h	The Planck constant the energy band gap energy
ν	The wavenumber
E_g	The energy band gap energy
λ	The wave length of X-ray
θ	The Bragg angle of X-ray diffractions
β	The FWHM (full width at haft maximum)

CHAPTER I

INTRODUCTION

1.1 Principle and reason

In recent years, one-dimensional nanostructures such as nanowires, nanorods, nanoparticles, nanosheets and nanotubes have been intensively studied because of the promising applications of these materials in various fields of technology. Since the discovery of carbon nanotubes in 1991 (Iijima, 1991), low-dimensional nanostructures, especially nanotubes, have been of great interest for their potential applications. The elongated structure and increased surface area of nanotubes are of interest for promising applications such as photovoltaics, photocatalysis. Titanium dioxide (TiO_2) particularly its anatase phases polymorph, is of interest for its photocatalytic activity occurring from its inherent (wide bandgap) semiconducting property. Furthermore, they are capable of ion-exchange (Zhao *et al.*, 2007; Bavykin *et al.*, 2006; Sun and Li, 2003), ion mobility due to their inherently layered structure.

Titanate nanotubes (TNTs) have been recently developed for many applications such as photocatalysis (Zhang *et al.*, 2004), support/carriers (Hodos *et al.*, 2004), ion-exchange (Sun and Li, 2003), adsorption (Umek *et al.*, 2005), photochemistry and electrochemistry (Zhu *et al.*, 2006; Hu *et al.*, 2006). Recently, a number of modifications can be used to enhance the attributes of titanium nanotubes which are feasible for extensive applications. Over the years many efforts have made to understand the mechanism of nanostructure formation and to thoroughly study the properties of the nanostructures (Dmistry *et al.*, 2010). The number of publications in these materials increases every year.

Almost previous works on TNTs focus on the improvement methods of nanostructure formation in order to the better control morphology (Niu *et al.*, 2008; Sreekantan and Wei, 2010; Liu *et al.*, 2010; Mozia *et al.*, 2010; Tsai and Teng, 2008), including mechanistic studies, the exploration the physical and chemical properties, with a focus on potential application. However, study of TNTs bulks on the dielectric and electrical properties as functions of frequency and temperature have rarely been researched, and this needs to be explored for future applications of TNTs as electronic devices.

Recently, high-permittivity dielectric materials with a static dielectric constant (ε_0') value above 10^3 including of ferroelectric oxide and relaxor oxide such as $BaTiO_3$ (Schileo *et al.*, 2013) and $PbMg_{1/3}Nb_{2/3}O_3$ have been studies intensively (Yimnirun *et al.*, 2005). High dielectric constant has been also discovered in perovskite oxide ($CaCu_3Ti_4O_{12}$), which shows a dielectric constant at 1 kHz of about 10^5 that is relatively constant from room temperature to 300 °C (Subramanian *et al.*, 2000; Smith *et al.*, 2009). Consequently, the dielectric materials with high dielectric constants and thermally stability are needed for future electronic applications. Recently, Hu et al. (2010) reported the giant dielectric and polarization behavior of TNTs (i.e., $Na_xH_{2-x}Ti_3O_7.nH_2O$). The dielectric constant (ε') of TNTs bulks was found to be about 10^4 at room temperature and low frequency with temperature independent in the range of 25-260 °C. The giant dielectric properties of TNTs bulks were proposed to be attributed to grain conductivity, which is the effect based on the Maxwell-Wagner polarization (interfacial polarization) mechanism. With applying an electric field across the TNTs bulks, the heavy charge carrier accumulations can induce the interfacial polarization at interfaces between $T_3O_7^{2}$- skeleton layers and H_2O molecule layer confined inside TNTs, playing the predominant role in accumulation of charged species.

The giant dielectric and electrical properties of TiO_2-based nanotubes such as $Na_xH_{2-x}Ti_3O_7.nH_2O$ have been reported (Hu *et al.*, 2010; Hu *et al.*, 2009). However, the explanation of the dielectric behavior of TiO_2-based nanotubes bulk systems is still unclear and uncompleted. Therefore, it is important to seek a low-loss dielectric giant system of TiO_2-based nanotubes with clear exploration of its origin of giant dielectric. Furthermore, the effect of Co and Fe doping on the dielectric and electrical properties of TNTs as functions of frequency, temperature, dc bias and current voltage should be also carried out.

In this research, the titanate nanotubes ($Na_xH_{2-x}Ti_3O_7.nH_2O$, TNTs) and Fe/Co doped TNTs are prepared by hydrothermal route. The prepared TNTs samples are characterized by thermogravimetric/differential thermal analysis (TG-DTA), transmission electron microscopy (TEM), X-ray diffraction (XRD), fourier transform infrared spectroscopy (FT-IR), Raman spectroscopy, X-ray photoelectron spectroscopy (XPS), X-ray absorption spectroscopy (XAS), UV-vis spectrophotometer (UV-vis) and Vibrating sample magnetometer (VSM). The dielectric properties of the prepared TNTs are investigated as a function of frequency, temperature, and dc bias under 0-10 V. The non-linear properties and effects of transition metals doping (i.e., Co, Fe) at Ti site on the electrical properties of titanate nanotubes are also investigated. The origin of the giant dielectric behavior of the TNTs and Co/Fe doped TNTs are explored.

1.2 Objectives of the dissertation

1.2.1 To synthesize titanate nanotubes (TNTs) and Fe/Co-doped TNTs by the hydrothermal route.

1.2.2 To characterize the microstructure and phase composition of the synthesized titanate nanotubes.

1.2.3 To study the dielectric and electrical properties of the synthesized titanate nanotubes as functions of frequency, temperature, dc bias and current voltage.

1.2.4 To study the effect of Co and Fe doping on the dielectric and electrical properties of the prepared TNTs as functions of frequency, temperature, dc bias and current voltage.

1.2.5 To explain the origin of the giant dielectric behavior of the prepared TNTs and Co/Fe-doped TNTs.

1.3 Limitation of the study

1.3.1 Synthesis of titanate nanotubes ($Na_xH_{2-x}Ti_3O_7.nH_2O$) and Fe/Co-doped titanate nantubes.

1.3.2 Study of microstructure and phase composition of the synthesized titanate nanotubes by using the XRD, TEM and EDS techniques.

1.3.3 Study of absorption or reflectance of the synthesized titanate nanotubes by using UV-Vis and FT-IR techniques.

1.3.4 Study of chemical state or electronic state of the synthesized titanate nanotubes by using XPS and XANES.

1.3.5 Study of magnetic properties of the synthesized titanate nanotubes by using VSM technique.

1.3.6 Study the dielectric and electrical properties of the synthesized titanate nantubes as functions of frequency, temperature, dc bias, and current voltage.

1.4 Location of research

1.4.1 Advanced Materials Physics Laboratory (AMP), School of Physics, Institute of Science, Suranaree University of Technology (SUT), Nakhon Ratchasima, 30000 Thailand.

1.4.2 The Center for Scientific and Technological Equipment (SUT), Suranaree University of Technology (SUT), Nakhon Ratchasima, 30000 Thailand.

1.4.3 National Metal and Materials Technology Center (MTEC), Thailand Science Park, 114 Paholyothin Rd., Klong 1, Klong Luang, Pathumthani, 12120 Thailand.

1.4.4 Department of Physics, Faculty of Science, Khon Kaen University, Khon Kaen, 40002 Thailand.

1.4.5 Department of Chemistry, Faculty of Science, Khon Kaen University, Khon Kaen, 40002 Thailand.

1.4.6 Faculty of Science, Chiang Mai University, Amphur Muang, Chiang Mai, 50200 Thailand.

1.4.7 Synchrotron Light Research Institute (SLRI), 111 Surapat 3, Suranaree University of Technology, University Aveneu, Muang District, Nakorn Ratchasima, Thailand, 30000.

1.5 Anticipated outcomes

1.5.1 Knowhow of synthesis of titanate nanotubes with excellent good dielectric properties.

1.5.2 The most possible mechanism of dielectric response in the titanate nanotubes.

1.5.3 International publications (ISI).

1.6 Dissertation structure

This dissertation is divided into five chapters. The introduction of the project is given in Chapter I. Review of literature which is relevant to this research, including background of titanate nanotubes, theoretical background for dielectric properties and electrical response in materials are presented in Chapter II. Chapter III presents the preparation, characterization of all the samples. And then, the results obtained in this research and discussions of the results are given in Chapter IV. Finally, conclusions and suggestions are described and future works are proposed in Chapter V.

CHAPTER II

LITERATURE REVIEW

This chapter presents a review of the background of titanate nanotubes (TNTs), basic theories which are used to describe the electrical, dielectric properties and models for effective dielectric permittivity of undoped TNTs and Fe/Co-doped TNTs. Moreover, general structure of TNTs, preparation for synthesis of undoped TNTs and Fe/Co-doped TNTs, optical, electrical and magnetic properties of TNTs are reviewed.

2.1 Electrical properties and polarization of materials

2.1.1 Dielectric properties of materials (Hench and West, 1990)

Dielectric responses result from the short range motion of charge carriers under the influence of an applied electric field. The motion of charges leads to the storage of electric energy and the capacitance of the dielectric. Capacitance is following by

$$C = \frac{Q}{V} \tag{2.1}$$

The capacitance of a vacuum capacitor is determined by the geometry. It can be shown from elementary electrostatics that the charge density on the plate, Q is proportional to the area, *A* in square meters and the electric intensity applied

$$E = \frac{V}{d},$$

where *d* is the distance between the plate. The capacitance of the vacuum capacitor is

$$C_0 = \frac{\varepsilon_0 A}{d}. \tag{2.2}$$

Where ε_0 is the permittivity or dielectric constant of a vacuum (ε_0 = 8.854×10^{-12} C^2/m^2 or F/m), *A* is a sample area and *d* is the sample thickness. If a ceramic materials of dielectric constant, ε, is inserted between the capacitor plates,

$$C = C_0 \frac{\varepsilon}{\varepsilon_0} = C_0 \varepsilon', \tag{2.3}$$

where ε' is the relative permittivity or relative dielectric constant. From Eqs. (2.2) and (2.3), we can write for a dielectric constant. This is the material property determining the capacitance of a circuit element and is of principal concern to the ceramist.

A dielectric material reacts to an electric field differently from a free space because it contains charge carrier that can displace and charge displacement within the dielectric can neutralize a part to applied field. From Eqs. (2.1) and (2.3), we can write for a capacitor containing a dielectric

$$V = \frac{Q/\varepsilon'}{C_0} \tag{2.4}$$

That, is only a factor of the total charge, the free charge, Q/ε', set up and electric field and voltage toward the outside; the bound charge, is neutralized by polarization of the dielectric. The schematic of the dielectric polarization is represented in Figure 2.1.

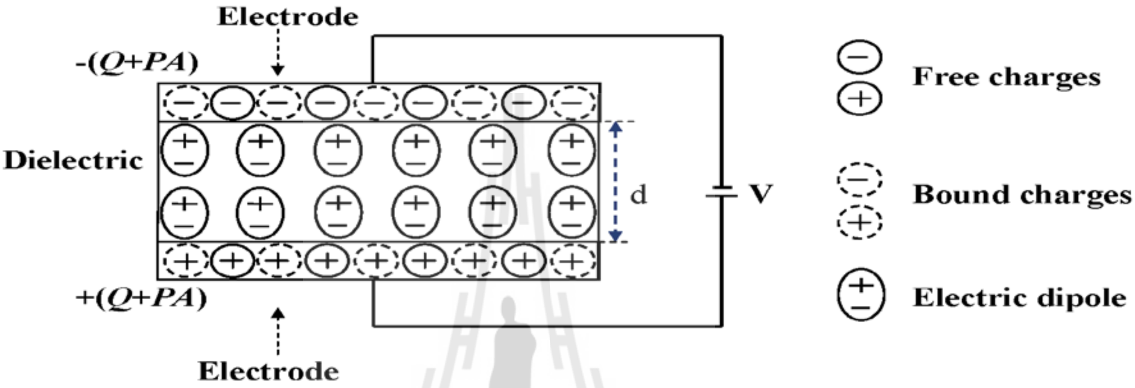

Figure 2.1 Schematic representation of dielectric polarization (Adapted from Hence and West (1990).

2.1.2 Polarization of materials

The electrical polarization is the relative tendency of a charge distribution, like the electron cloud of an atom or molecule, to be distorted from its normal shape by an external electric field, which is applied typically by inserting the molecule in a charged parallel-plate capacitor, but many also be caused by the presence of a nearby ion or dipole. There are various possible mechanisms for polarization in a dielectric material. These include electronic polarization and space charge polarization. The detail of each mechanism is given as follows.

2.1.2.1 Electronic polarization

It is the displacement of the valence electron could of the ion within a material with respect to the positive nucleus. This polarization mechanism can occur at very high frequencies in the ultraviolet optical rage, 10^{15} Hz. This mechanism related to the optical properties of material, i.e., the index of refraction.

2.1.2.2 Atomic polarization

The atomic polarization can occur at high frequencies up to the rage of about 10^{12}-10^{13} Hz. When the external electric field is applied, the separation between the ions further increases. Hence, the net dipole moment of the materials also increases.

2.1.2.3 Orientation polarization

Orientation polarization occurs only in polar dielectric material, which process permanent electric dipole. The electric field causes the reorientation of the dipole toward the direction of the field. This can usually be responsible for the dielectric constant values of 10^3 or more in the frequency range of 10^2-10^6 Hz.

2.1.2.4 Space charge polarization

It is called “Interfacial polarization or Maxwall Wagner Polarization”, the polarization occurs is material in with only the few charge carrier are capable of moving through small distances. When the external electric field is applied, these charge carriers move. During the motion, they get trapped or pile up against lattice defects. These localized charges induce their image charge on the surface of the dielectric material. This led to the development of net dipole moment across the material. This polarization can occur in the frequency range from 10^0- 10^3 Hz. The typical dependence of the polarizability on frequency over a wide range is shown in Figure 2.2

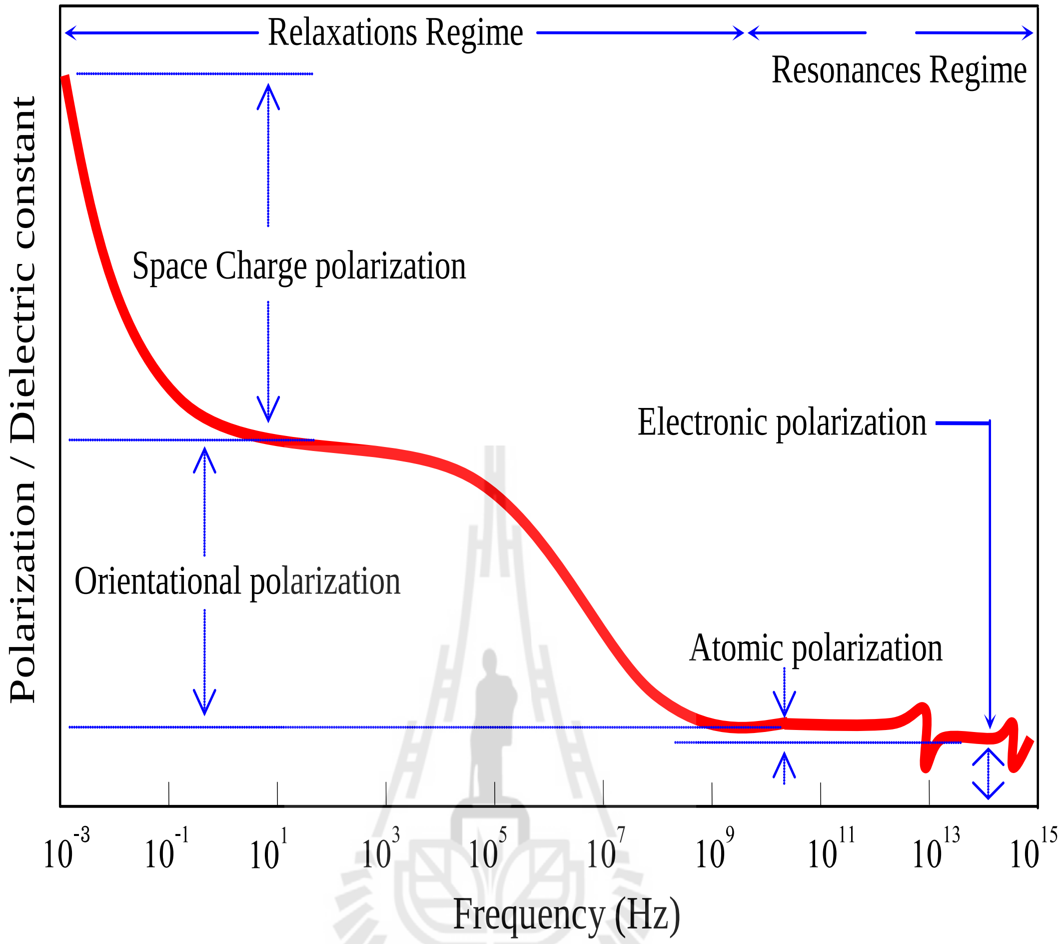

Figure 2.2 Frequency dependence of the polarization mechanism in dielectrics (Adapted from Hence and West (1990)).

2.1.3 The dielectric behaviors in alternating fields (von Hippel, 1954)

In order to measure the permittivity of a sample, the alternation voltage given by the real part of $V = V_0 e^{i\omega t}$ (where V_0 is the amplitude, ω is the angular frequency and t is the time) is applied across the bulk sample. The measurement current is the real part of complex current, I^*, given

$$I^* = \frac{dQ}{dt} = C^* \frac{dV}{dt} = \varepsilon^* C_0 \frac{dV}{dt} = i\omega\varepsilon^* C_0 V \qquad (2.5)$$

where $Q = CV$, C^* is the complex capacitance of the sample and C_0 is the vacuum capacitance between the two electrodes (the distance between to electrod is equal to the thickness of the sample, h^s)

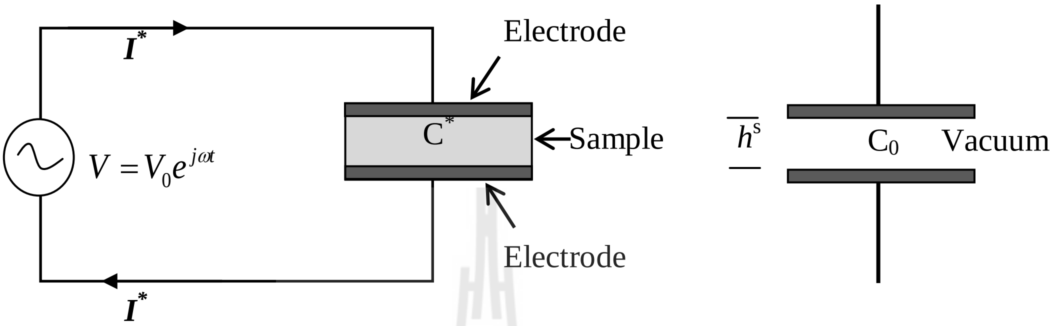

Figure 2.3 A circuit diagram of dielectric measurement (Adapted from von Hippel (1954)).

In addition, a complex dielectric constant (ε^*) should also be used to described the dielectric properties of materials:

$$\varepsilon^* = \varepsilon' - i\varepsilon'' \tag{2.6}$$

where $i = \sqrt{-1}$, ε' is the real part of the relative dielectric constant with expresses the maximum stored electrical energy and ε'' is the imaginary part of the relative dielectric loss of the dielectric material. Both ε' and ε'' are experimentally measurable quantities which may be used to characterize the dielectric dispersion over the range of frequency and temperatures.

The dielectric loss tangent or dissipation factor and is expressed as:

$$\tan\delta = \frac{\varepsilon''}{\varepsilon'} \tag{2.7}$$

where δ is the loss angular and $90-\delta$ is the phase angle between current and voltage.

Substituting Eq. (2.6) into Eq. (2.5), I^* can be written as

$$I^* = \omega C_0(\varepsilon'' + i\varepsilon')V \tag{2.8}$$

The dielectric sample can be considered as an equivalent parallel circuit as shown in Figure 2.4. The admittance, Y^*, (reciprocal of the impedance) of the circuit can be expressed as:

$$Y^* = \frac{1}{R_p} + i\omega C_p \tag{2.9}$$

where R_p and C_p are the parallel resistance and capacitance of the of sample dielectric respectively. The current I^*, passing through the circuit can be represented as:

$$I^* = VY^* = (\frac{1}{R_p} + i\omega C_p)V = I_R + iI_C \tag{2.10}$$

where I_R and I_C are the real and imaginary part of the current, respectively.

Substituting Eqs. (2.8) and (2.10) yields:

$$(\omega C_0\varepsilon'' + i\omega C_0\varepsilon')V = (\frac{1}{R_p} + i\omega C_p)V = I_R + iI_C \qquad (2.11)$$

From Eq. (2.15) ε' and ε'' can be calculated as follows:

$$\varepsilon' = \frac{1}{\omega C_0 V} = \frac{C_p}{C_o} \qquad (2.12)$$

and then,

$$\varepsilon'' = \frac{I_R}{\omega C_0 V} = \frac{1}{\omega C_o R_p} \qquad (2.13)$$

and

$$\tan\delta = \frac{\varepsilon''}{\varepsilon'} = \frac{I_R}{I_C} \qquad (2.14)$$

Eq. (2.13) can be rewritten as:

$$\varepsilon'' = \frac{1}{\omega C_o R_p} = \frac{G_p}{\omega C_0} \qquad (2.15)$$

where $G_p = \frac{1}{R_p}$ is the AC conductance, which in general is a combination of genuine conductivity (i.e. the motion of charges) and the conductance due to any time dependent polarization processes (i.e. the motion of dipoles). If the electrode plates have area A and separation, h^s (sample thickness), G_p and C_0 can be presented as:

$$G_p = \frac{\sigma A}{h^s} \tag{2.16}$$

and

$$C_0 = \frac{\varepsilon_0 A}{h^s} \tag{2.17}$$

hence,

$$\varepsilon'' = \frac{\sigma}{\varepsilon_0 \omega} \tag{2.18}$$

where σ is the conductivity, In general, σ will include both the time dependent polarization effect and genuine σ_{dc} arising from free charges, and is assumed to be frequency independent at these low frequencies. R_p and C_p are the parallel resistance and capacitance of the polymer dielectric, respectively.

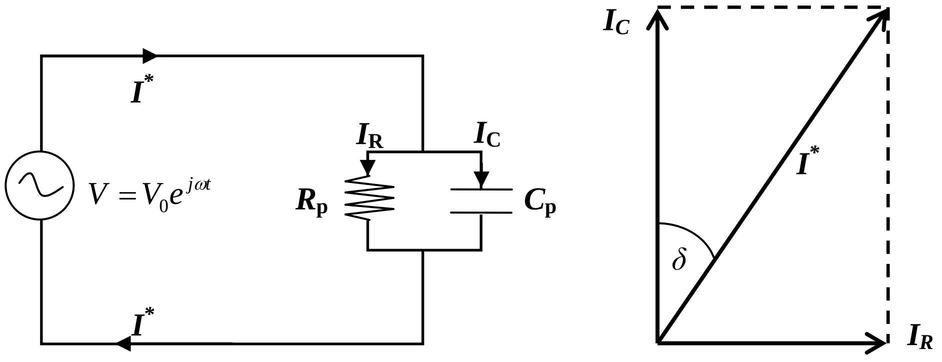

(a) **(b)**

Figure 2.4 (a) The equivalent parallel circuit of a dielectric sample (a) and corresponding phasor diagram (b) (Adapted from von Hippel (1954)).

2.1.4 Relationship between complex dielectric constant and polarization

In the dielectric materials, the presence of an electric field causes the bound charges in the materials to slightly separate, including a local electric dipole moment as demonstrated in Figure 2.1. The total electric displacement ($\vec{D}$), as the sum of the electric field ($\vec{E}$) and dipole charge ($\vec{P}$) is given as:

$$\vec{D} = \varepsilon_0\vec{E} + \vec{P} = \varepsilon\vec{E} = \varepsilon^*{}_{permit}\vec{E}, \tag{2.19}$$

where ε^* is the complex permittivity of the dielectric material. The displacement field is the sum of polarization field within the dielectric material and the product of an electric field between the plates without the dielectric between them and ε_0. The polarization can be defined as

$$\vec{P} = \vec{E}(\varepsilon^{*}{}_{permit} - \varepsilon_0), \tag{2.20}$$

Since

$$\varepsilon^{*} = \frac{\varepsilon^{*}{}_{permit}}{\varepsilon_0} \tag{2.21}$$

Note that ε^{*} is the complex dielectric constant. The polarization can be rearranged as

$$\vec{P} = \vec{E}(\varepsilon_0\varepsilon^{*} - \varepsilon_0) = (\varepsilon^{*} - 1)\varepsilon_0\vec{E} \tag{2.22}$$

and then

$$\varepsilon^{*} - 1 = \frac{\vec{P}}{\varepsilon_0\vec{E}} \tag{2.23}$$

Because of $\vec{P}$ and $\vec{E}$ are in the same direction, equation (2.23) can be presented in scalar form,

$$\varepsilon^{*} - 1 = \frac{P}{\varepsilon_0 E} \tag{2.24}$$

or

$$\varepsilon^* = 1 + \frac{P}{\varepsilon_0 E} \tag{2.25}$$

and defining

$$\frac{P}{\varepsilon_0 E} = \chi \tag{2.26}$$

where χ is the electric susceptibility

$$\varepsilon^* = 1 + \chi \tag{2.27}$$

Eqs. (2.25) and (2.27) give a correlation desired between the dielectric constant and the total polarization in the material.

The polarization $(\vec{P})$ is the surface charge density of the bound charge, equal to the dipole moment per unit volume of material

$$\vec{P} = N\vec{\mu} \tag{2.28}$$

where N is a number of dipole per unit volume and $\vec{\mu}$ is the average dipole moment, which is proportional to the local electric field. The electric dipole moment correspond to two electric charges of opposite polarity, $\pm Q$, separated by the distance, $\vec{d}$:

$$\vec{\mu} = Q\vec{d} \tag{2.29}$$

The average dipole moment to the local electric field can be defined as the *polarizability* (α),

$$\alpha = \frac{\overline{\mu}_i}{E'} \tag{2.30}$$

Thus, the total polarization can be written as

$$P = N_i \alpha_i E' \tag{2.31}$$

In the case of insulating dielectric solids, polarization of the surrounding medium substantially have enough to affect the magnitude of the local field. The local field contribution was firstly derived by Mosotti via the integration of the normal component of the polarized vector over the surface of a spherical cavity in the material (Kao, 2004). The obtained result is

$$E' = E_a + \frac{P}{3\varepsilon_0} \tag{2.32}$$

Since $N_i \alpha_i = P / E'$ from Eq. (2.31) then

$$N_i \alpha_i = \frac{P}{E_a + P / 3\varepsilon_0} \tag{2.33}$$

By substituting Eqs. (2.20) and (2.21) into Eq. (2.32), we obtain

$$\frac{\varepsilon^*-1}{\varepsilon^*+2}=\frac{1}{3\varepsilon_0}N_i\alpha_i \tag{2.34}$$

Eq. (2.34) is the classical Clausius-Mossotti equation, which describes the relationship between the complex dielectric constant of a materials and the number polarizable species N_i as well as the polarizability of the species α_i.

According to Figure 2.2, there are four major classes of polarization species in the ceramics and glasses; consequently,

$$\frac{\varepsilon^*-1}{\varepsilon^*+2}=\frac{1}{3\varepsilon_0}[N_e\alpha_e+N_a\alpha_a+N_{or}\alpha_{or}+N_{sc}\alpha_{sc}] \tag{2.35}$$

where $\alpha_e, \alpha_a, \alpha_{or}$, and α_{sc} are electronic, atomic, orientational, and space charge polarizabilities, respectively.

2.1.5 Time-dependent electric Polarization (Koa, 2004)

In general, the time required for electronic and atomic polarization and depolarization is very short (<10^{-12}sec), as shown Figure 2.5. This deformational polarization process is also referred to as the resonance process because it involves vibrating modes. Resonance of a vibrating system occurs when an excitation field oscillates at a frequency close to the natural frequency of the system. The time required for orientational, hopping, or space charge polarization and depolarization is quite long and varies in a wide range, depending on the dielectric systems; such polarization processes are sometimes referred to as relaxation processes because they involve a relaxation time. A relaxation phenomenon occurs when restoring action tends to bring the excited system back to its original equilibrium state. For simplicity, hopping and space charge polarization are therefore, ignored.

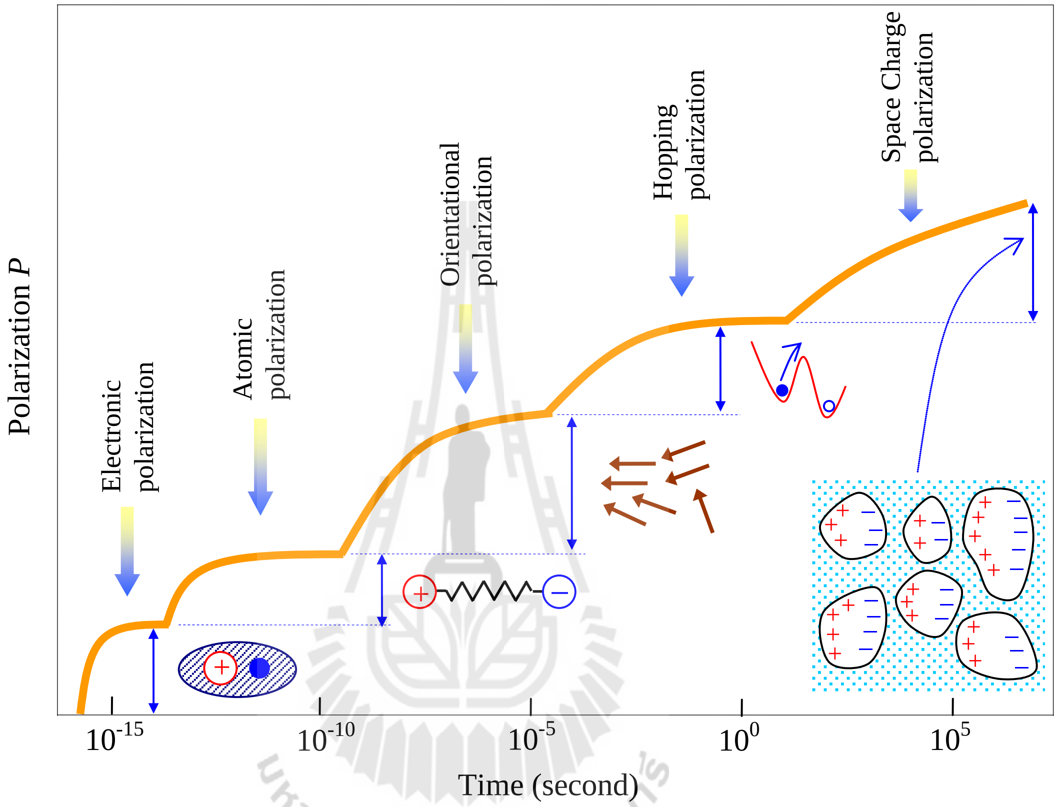

Figure 2.5 The variation of different types of polarization with time under the step-function electric field (Adapted from Kao (2004).

The total polarization of dielectrics can be expressed as

$$P_{tatal} = P_e + P_a + P_{or} \tag{2.36}$$

The total polarization of dielectrics can be expressed as

$$P_{tatal} = P_e + P_a + P_{or} \tag{2.36}$$

Since the response time for electronic and atomic polarization is so short, which and can be assumed to be practically constant for all frequencies from 0 - 10^{12} Hz. Consequently, these two polarizations can be included as the high-frequency polarization (P_∞):

$$P_\infty = P_e + P_a \tag{2.37}$$

From Eq. (2.25), P_∞ can be approximated as

$$\varepsilon'_\infty \approx 1 + \frac{P_\infty}{\varepsilon_0 E} \tag{2.38}$$

ε'_∞ is the dielectric constant at a high frequency range or the unrelaxed high-frequency dielectric constant, and then,

$$P_\infty = (\varepsilon'_\infty - 1)\varepsilon_0 E \tag{2.39}$$

These two types of polarization can be considered to follow instantaneously the excitation field E without time lag, in other words, P_∞ and E can be considered to be in phase. Similarly, the low-frequency dielectric constant or the relaxed static dielectric constant (ε_s') can be expressed as

$$\varepsilon_s' = 1 + \frac{P_{tatal}}{\varepsilon_0 E} = 1 + \frac{P_{or} + P_\infty}{\varepsilon_0 E} \tag{2.40}$$

By substituting Eq. (2.39) into (2.40) and simplifying, the orientational polarization can be written in terms of ε_∞' and ε_s' as

$$P_\infty = (\varepsilon_s' - \varepsilon_\infty') + \varepsilon_0 E \tag{2.41}$$

From Eq. (2.39) and (3.41), P_{total} can be written as

$$P_{tatal} = P_\infty + P_{or} = (\varepsilon_\infty' - 1)\varepsilon_0 E + (\varepsilon_s' - \varepsilon_\infty')\varepsilon_0 E \tag{2.42}$$

Supposing that the orientational polarization takes time to respond to the applied excitation field *F*, and that at the removal of the excitation field making $E = 0$ at $t = 0$, the polarization will decay at a rate proportional to its change from its equilibrium state (as shown in Figure 2.6). The polarization will decay at a rate,

$$\frac{dP_{or}(t')}{dt'} = \frac{P_{or}(t')}{\tau} \tag{2.43}$$

where τ is the macroscopic relaxation time. Using the boundary condition that at $t =$ 0, $P_{or} = (\varepsilon_s' - \varepsilon_\infty')\varepsilon_0 E$; consequently, the solution of Eq. (3.43) is

$$P_{or}(t') = [(\varepsilon'_s - \varepsilon'_\infty)\varepsilon_0 E]\exp(t/\tau) \tag{2.44}$$

Similarly, if a step-function excitation field E is applied to the dielectric system at t = 0, then $P_{or}(t) = 0$ at t = 0, $P_{or}(t)$ and increases with time. The orientational polarization will increase at a rate,

$$P_{or}(t) = (\varepsilon'_s - \varepsilon'_\infty)\varepsilon_0 E[1 - \exp(-t/\tau)] \tag{2.45}$$

In this case, $dP_{or}(t)/dt$ gives the polarization rate. The approximate time required for polarization is shown in Figure 2.6.

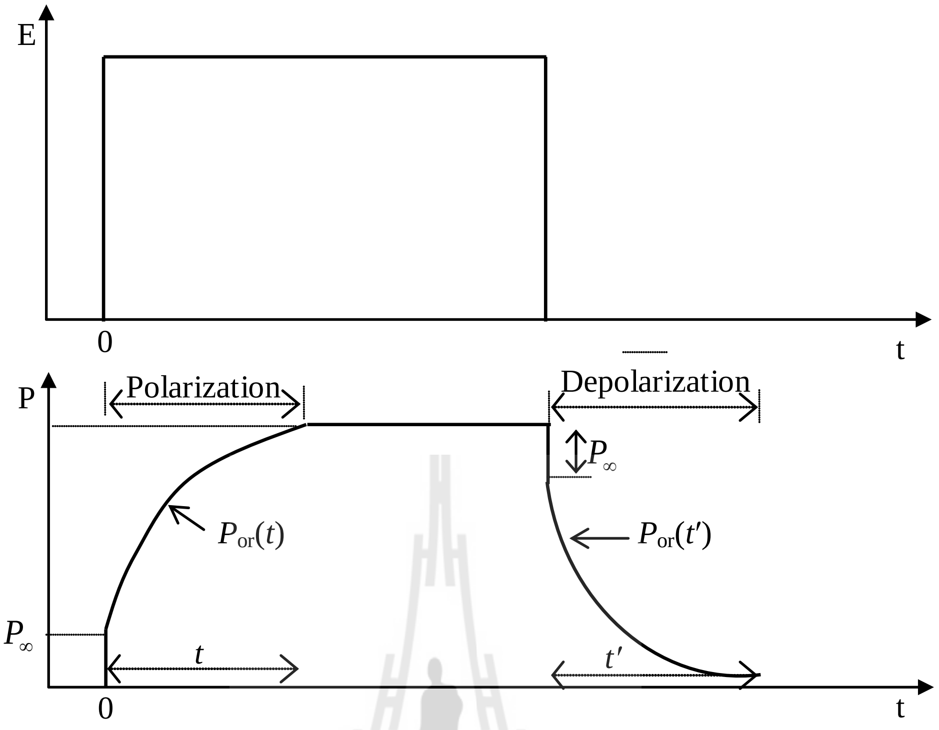

Figure 2.6 The variation of different types of polarization with time under a step-function electric field.

As demonstrated in Figure 2.7, supposing that during the time interval between u and $u + du$, an excitation field $E(u)$ is applied to the dielectric system. At $E = 0$ for $t < u$ and $t > u + du$; consequently, $P_{or}(t)$ will take time to respond and will change for $t > u$. Then $P_{or}(t)$ reaches the value of $P_{or}(u + du)$ at $u = t + du$; the polarization will decay gradually. During the polarization period $u \le t \le u + du$, the change of the polarization can be written as (Kao, 2004).

$$P_{or}(t-u) = (\varepsilon_s' - \varepsilon_\infty')\varepsilon_0 \left\{1 - \exp - \left(\frac{t-u}{\tau}\right)\right\} E(u) \qquad (2.46)$$

The term of $1-\exp\{-(t-u/\tau)\}$ can be referred to a response function. From Eq. (2.42), The total P_{tatal} consists of two parts: P_{∞}, which can follow the excitation field immediately, and $P_{or}(t)$, which is governed by Eq. (2.46). The increment of total polarization, dP_{tatal} is

$$dP_{total}(t-u) = dP_{\infty}(t-u) + dP_{or}(t-u) \tag{2.47}$$

By considering Eqs. (2.39) and (2.46), Eq. (2.47) can be written as

$$dP_{total}(t-u) = (\varepsilon'_{\infty}-1)\varepsilon_0 dE(u) + (\varepsilon'_s - \varepsilon'_{\infty})\varepsilon_0 \left\{1-\exp-\left(\frac{t-u}{\tau}\right)\right\} dE(u) \tag{2.48}$$

According to the superposition principle, the total polarization at time *t* is a superposition of all increments dP; therefore, dP_{tatal} can be obtained as

$$P_{total} = (\varepsilon'_{\infty}-1)\varepsilon_0 E(t) + (\varepsilon'_s - \varepsilon'_{\infty})\varepsilon_0 \int_0^1 \left\{1-\exp-\left(\frac{t-u}{\tau}\right)\right\} dE(u) \tag{2.49}$$

Integrating by part, Eq. (2.49) can be obtained as

$$P_{total} = (\varepsilon'_{\infty}-1)\varepsilon_0 E(t) + (\varepsilon'_s - \varepsilon'_{\infty})\varepsilon_0 \int_0^1 \frac{E(u)}{\tau} \exp\left(-\frac{t-u}{\tau}\right) d(u) \tag{2.50}$$

where the term of $\exp[-(t-u)/\tau]$ is the decay function that tends to approach zero at $t \to \infty$. If E is the step-function electric field with E = 0 at t = 0 and E = E at t = 0^+, then Eq. (2.50) is expressed as

$$P_{total} = (\varepsilon'_\infty - 1)\varepsilon_0 E + (\varepsilon'_s - \varepsilon'_\infty)\varepsilon_0 E\left[1 - \exp(-t/\tau)\right] \tag{2.51}$$

The first term on the right hand side of Eq. (2.51) is a time dependent electric polarization function, whereas the second term is a function that dependent on time. The variation of total polarization (P_{tatal}) with time (t) is revealed in Figure 2.6.

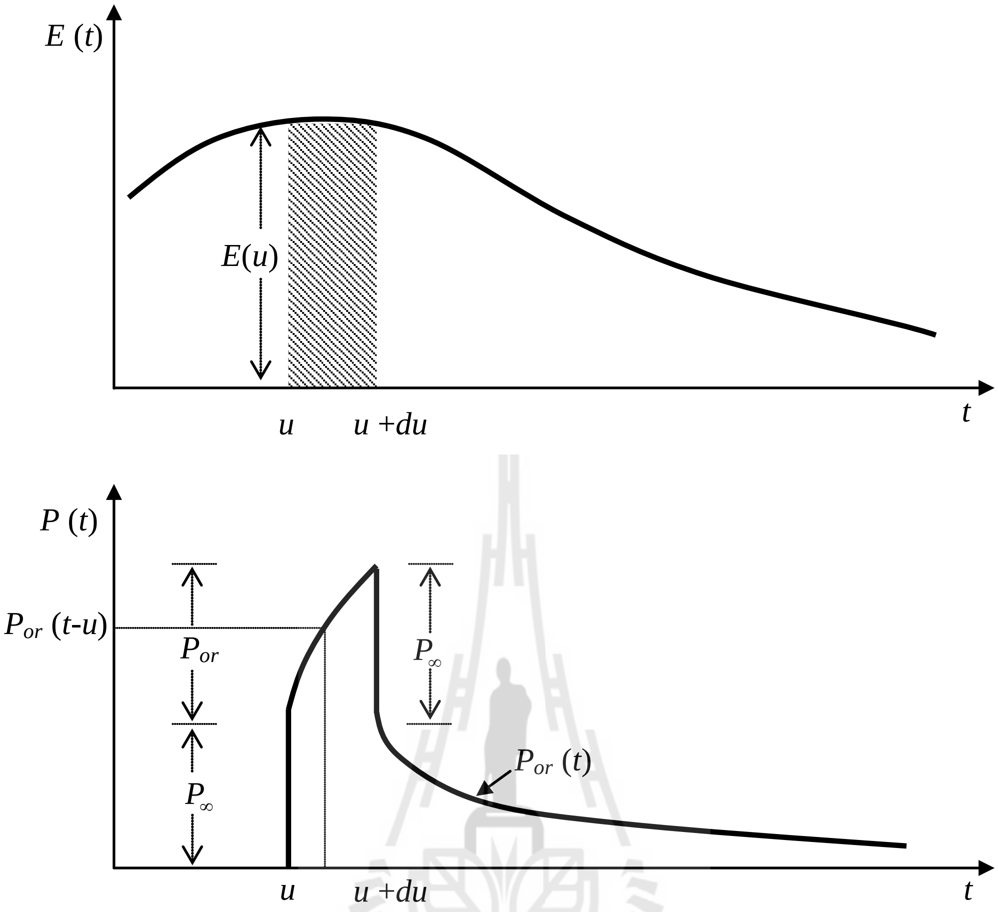

Figure 2.7 The response of $P(t)$ to a delta function electric field $E(u)$ of strength $E(u)$ within the time period of $u \leq t \leq u + du$ (Adapted from Kao (2004)).

2.1.6 Debye relaxation model

The Debye relaxation model is based on a single relaxation time; all the dipoles in a system have a same relaxation time. An alternative and more concise way of expressing Debye equations is

$$\varepsilon^{*} = \varepsilon' - j\varepsilon''\varepsilon'_{\infty} + \frac{\varepsilon'_{s} - \varepsilon'_{\infty}}{1 + j\omega\tau} \tag{2.52}$$

The dielectric constant (ε') and dielectric loss (ε'') can be separated as

$$\varepsilon' = \varepsilon'_{\infty} + \frac{\varepsilon'_{s} - \varepsilon'_{\infty}}{1 + (\omega\tau)^{2}} \tag{2.53}$$

$$\varepsilon'' = \varepsilon'_{\infty} + \frac{\varepsilon'_{s} - \varepsilon'_{\infty}}{1 + (\omega\tau)^{2}}\,\omega\tau \tag{2.54}$$

and

$$\tan\delta = \frac{\varepsilon''}{\varepsilon'} = \frac{(\varepsilon'_{s} - \varepsilon'_{\infty})\omega\tau}{\varepsilon'_{s} + \varepsilon'_{\infty}(\omega\tau)^{2}} \tag{2.55}$$

According to Eqs. (2.54) and (2.55), the angular frequencies of the applied electric field at which ε'' and $\tan\delta$ are maximal can be obtained by setting $d\varepsilon''/d\omega = 0$ and $d(\tan\delta)/d\omega = 0$. For example, it can be shown that

$$\frac{d\varepsilon''}{d\omega}=\frac{d[\Delta\varepsilon'\omega\tau/(1+\omega^2\tau^2)]}{d\omega}=\frac{\Delta\varepsilon'(\tau+\omega^2\tau^3)-2\Delta\varepsilon'\omega^2\tau^3}{(1+\omega^2\tau^2)^2}\omega\tau \tag{2.56}$$

where $\Delta\varepsilon'=\varepsilon'_s-\varepsilon'_\infty$. Therefore, $d\varepsilon''/d\omega$ will be zero when

$$\Delta\varepsilon'(\tau+\omega^2\tau^3)=2\Delta\varepsilon'\omega^2\tau^3 \tag{2.57}$$

From Eq. (2.57), the frequency at which ε'' is maximal will occur at $\omega=\omega_{p(\varepsilon'')}$

$$\omega_{p(\varepsilon'')}=\frac{1}{\tau} \tag{2.58}$$

Similarly, it can be proved that the frequency at which $\tan\delta$ is maximal will occur at $\omega=\omega_{p(\delta)}$,

$$\omega_{p(\delta)}=\frac{\sqrt{\varepsilon'_s/\varepsilon'_\infty}}{\tau} \tag{2.59}$$

At the frequency of $\omega=\omega_{p(\varepsilon'')}$ and $\omega_{p(\varepsilon'')}=1$ the dielectric parameters of the dielectric are given by

$$\varepsilon'=\frac{(\varepsilon'_s+\varepsilon'_\infty)}{2} \tag{2.60}$$

$$\varepsilon'' = \frac{\left(\varepsilon'_s - \varepsilon'_\infty\right)}{2} \tag{2.61}$$

$$\tan\delta = \frac{\varepsilon'_s - \varepsilon'_\infty}{\varepsilon'_s + \varepsilon'_\infty} \tag{2.62}$$

At the frequency of $\omega = \omega_{p(\delta)}$, $\tan\delta$ is given by

$$\tan\delta = \frac{\varepsilon'_s - \varepsilon'_\infty}{\varepsilon'_s + \varepsilon'_\infty} \tag{2.63}$$

The frequency dependent of the dielectric parameters is illustrated in Figure 2.8. The dielectric spectra are obtained by assuming ε'_s = 600, ε'_∞ = 100, and τ = 10^{-5} s and taking into Eqs. (2.53), (2.54), and (2.55). The results reveal that the angular frequency of the applied electric field (ω), at which ε'' is maximal, is 10^5 Hz corresponding to Eq. (2.58). At this frequency, the values of the ε' and ε'' are 350 and 250, respectively. In general, ε'_s is always larger than ε'_∞ and ($\sqrt{\varepsilon'_s\varepsilon'_\infty}$ >1) consequently, the frequency at the peak of $\tan\delta$ should be higher than that of ε'' by

$$\Delta\omega = \omega_{p(\delta)} - \omega_{p(\varepsilon'')} = \frac{1}{\tau}\left(\sqrt{\frac{\varepsilon'_s}{\varepsilon'_\infty}} - 1\right) \tag{2.64}$$

As shown in Figure 2.8, $\Delta\omega$ is about 1.45×10^5 Hz; hence, $\omega_{p(\delta)} = 2.45\times10^5$ Hz.

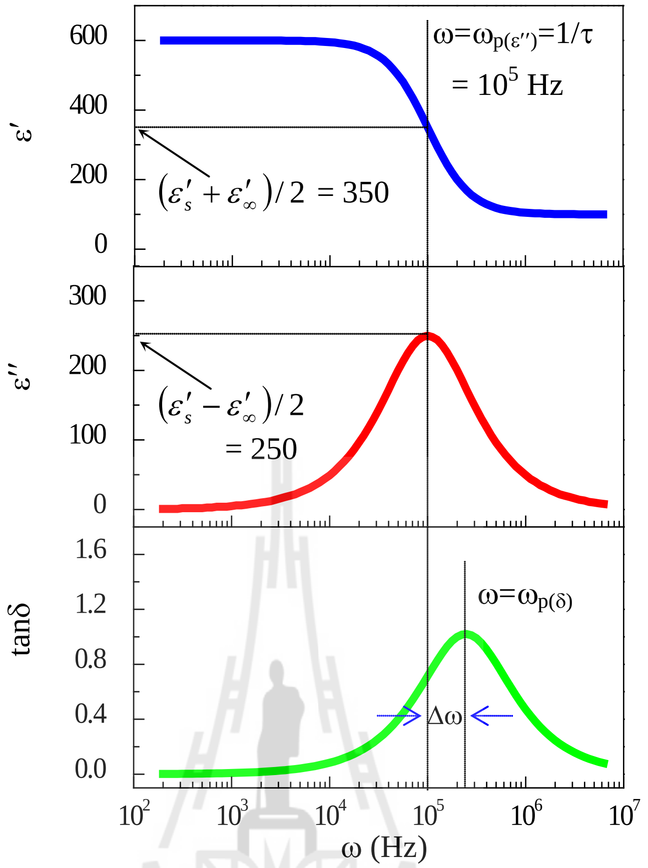

Figure 2.8 Frequency dependent of dielectric properties of dielectric materials (plotted using Eqs. (2.53)-(2.55)).

2.1.7 Cole-Cole and other relaxation model

Polar dielectrics that have more than one relaxation time do not satisfy Debye equations. In these materials, a distribution of relaxation times is important to interpret the experimental results. KS Cole, RH Cole (1941) have adapted the Debye relaxation model to obtain the suitable model for ascribe the relaxation behavior of real dielectric materials. Cole-Cole relaxation model, the empirical relation, is

$$\varepsilon^* = \varepsilon'_\infty + \frac{\varepsilon'_s - \varepsilon'_\infty}{1+(j\omega\tau)^\alpha} \tag{2.65}$$

where α is constant parameter with 0 < α ≤ 1. When $\alpha = 1$, the Cole-Cole relaxation model is transformed to Debye relaxation model. If α < 1, it implies that the relaxation has a distribution of relaxation times, leading to the broader peak shape than a Debye peak, as shown in Figure 2.9. The slop of step decrease in dielectric constant and the peak height of dielectric loss decrease with decreasing the α value. Moreover, several models have proposed to modify the Cole-Cole relaxation model; some of the models are listed below for comparison purpose:

Debye relaxation model, $$\varepsilon^* = \varepsilon'_\infty + \frac{\varepsilon'_s - \varepsilon'_\infty}{1+ j\omega\tau}$$

Cole-Cole relaxation model, $$\varepsilon^* = \varepsilon'_\infty + \frac{\varepsilon'_s - \varepsilon'_\infty}{1+(j\omega\tau)^\alpha}$$

Divison-Cole relaxation model, $$\varepsilon^* = \varepsilon'_\infty + \frac{\varepsilon'_s - \varepsilon'_\infty}{(1+ j\omega\tau)^\beta} \tag{2.66}$$

Havriliak-Negami relaxation model, $$\varepsilon^* = \varepsilon'_\infty + \frac{\varepsilon'_s - \varepsilon'_\infty}{\left[(1+ j\omega\tau)^\alpha\right]^\beta} \tag{2.67}$$

All of this model on the value of α and β chosen within the ranges of 0 < α ≤ 1 and 0 < β ≤ 1. However, the modification does not lead to better understanding of the physics behind the distribution of relaxation times. The modification of the original Cole-Cole model empirically may take the equation better fix experimental data.

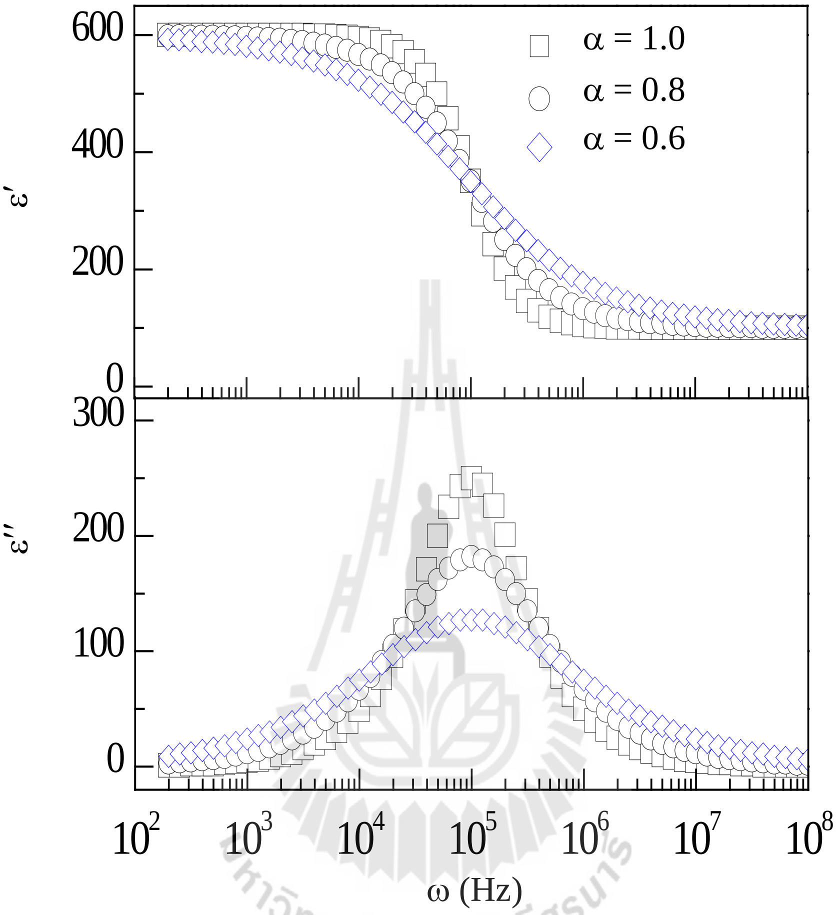

Figure 2.9 Frequency dependence of dielectric properties of dielectric materials with different distributions of relaxation times obtained from Debye and Cole-Cole relaxation models (plotted using Eq. (2.65))

2.1.8 The effect of dc conductivity on dielectric properties

When an alternating electric field is applied across a parallel-plate capacitor with the plate area of one unit and a separation by dielectric layer, the total current density is given by

$$J_{total} = J + \frac{dD}{dt} = J + \varepsilon^{*}_{permit}\frac{dE}{dt} \tag{2.68}$$

where J is the conduction current or current density. ε^{*}_{permit} allows for dielectric losses due to the friction accompanying polarization and orientation of electric dipoles.

In some dielectric materials, the dc conductivity σ_{dc} not negligibly small, σ_{dc} will contribute to the dielectric loss of the dielectric materials. The total complex dielectric constant can be demonstrated as

$$\varepsilon^{*} = \varepsilon' - j\left(\varepsilon'' + \frac{\sigma_{dc}}{\omega\varepsilon_0}\right) \tag{2.69}$$

Taking the dc conductivity into account, the Debye relaxation model as Eq. (2.53) is became to

$$\varepsilon^{*} = \varepsilon'_{\infty} + \frac{\varepsilon'_s - \varepsilon'_{\infty}}{1 + j\omega\tau} - j\frac{\sigma_{dc}}{\omega\varepsilon_0} \tag{2.70}$$

The dielectric loss ε'' is expressed as

$$\varepsilon'' = \frac{\varepsilon'_s - \varepsilon'_{\infty}}{1 + (\omega\tau)^2}\omega\tau + \frac{\sigma_{dc}}{\omega\varepsilon_0} \tag{2.71}$$

$$\tan\delta = \frac{(\varepsilon_s' - \varepsilon_\infty')\omega^2\varepsilon_0\tau + (1+\omega^2\tau^2)\sigma_{dc}}{\omega\varepsilon_0(\varepsilon_s' + \varepsilon_s'\omega^2\tau^2)} \tag{2.72}$$

When $\omega\tau \approx 1$, Eqs. (2.71) and (2.72) reduce to

$$\varepsilon'' = \frac{\sigma_{dc}}{\omega\varepsilon_0} \tag{2.73}$$

$$\tan\delta = \frac{\sigma_{dc}}{\omega\varepsilon_0\varepsilon_s'} \tag{2.74}$$

When $\omega\tau \approx 1$, Eqs. (2.71) and (2.72) reduce to

$$\varepsilon'' = \frac{\varepsilon_s' - \varepsilon_\infty'}{2} + \frac{\tau\sigma_{dc}}{\varepsilon_0} \tag{2.75}$$

$$\tan\delta = \frac{(\varepsilon_s' - \varepsilon_\infty')\varepsilon_0 + 2\tau\sigma_{dc}}{\varepsilon_0(\varepsilon_s' + \varepsilon_s')} \tag{2.76}$$

The frequency dependent of the dielectric loss ε'' including the effect of dc conductivity is revealed in Figure 2.10. It is clear that the both of conductivity and relaxation process have a remarkable influence on the dielectric properties of materials.

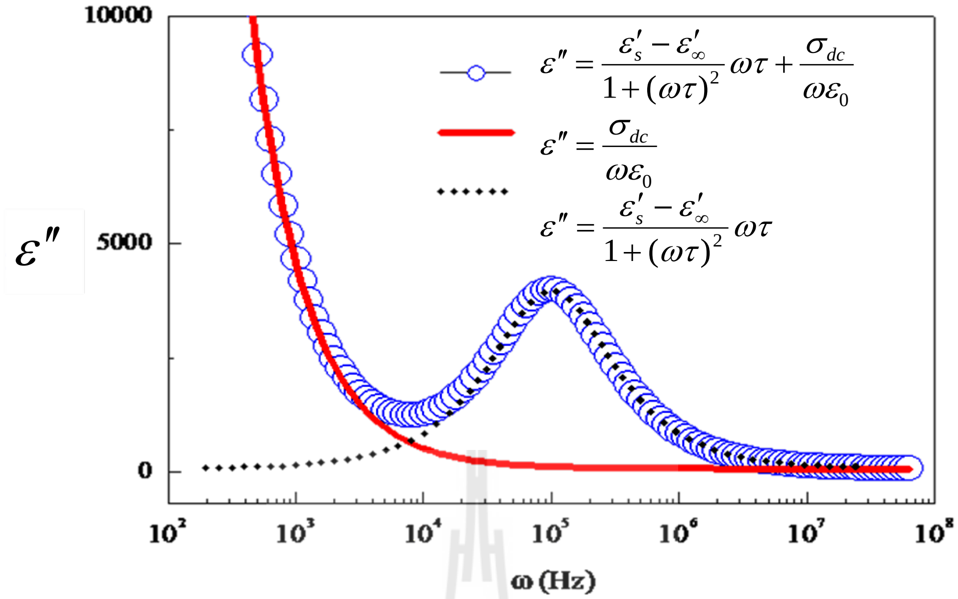

Figure 2.10 Frequency dependent of dielectric loss ε'' represented by Debye relaxation model, including the effect of dc conductivity. This Figure shows the evolution of the relaxation process and dc conductivity contributing to the dielectric loss.

2.1.9 Theory of impedance spectroscopy

Impedance spectroscopy (IS) is a powerful tool of characterizing many of the electrical properties of materials and their interfaces with electronically conducting electrodes. It may be used to investigate the dynamics of bound or mobile charge in the bulk or interfacial regions of any kind of solid or liquid material: ionic, semiconducting, mixed electronic–ionic, and even insulators (dielectrics) (Barsoukov and Macdonald, 2005). The complex impedance Z^* of a polycrystalline materials can be defined by Ohm's Law:

$$Z^* = \frac{V^*}{I^*} \tag{2.77}$$

where V^* and I^* are the applied voltage and measuring current, respectively. On the other hand, Z^* can be obtained from the complex dielectric constant ε^* :

$$Z^* = \frac{1}{j\omega C_0 \varepsilon^*} \tag{2.78}$$

where $\varepsilon^* = \varepsilon' - j\varepsilon''$, $\omega = 2\pi f$ and $C_0 = \varepsilon_0 A/d$ where A is the electrode area and d is the sample thickness. Generally, impedance data on materials can be analyzed using an equivalent circuit compose of resistor (R) and capacitor (C) element in parallel, each separated out the grain and the grain boundary (GB) effects (Xue *et al.*, 2009; Thongbai *et al.*, 2012). It can be represented by the equivalent circuit shown in Figure 2.11

The complex impedance can be expressed as follows (Lin *et al.*, 2008):

$$Z^* = Z' - jZ'' = \frac{1}{R_g^{-1} + j\omega C_g} + \frac{1}{R_{gb}^{-1} + j\omega C_{gb}}\,, \tag{2.79}$$

With excluding the real part Z' and imaginary part Z'' of Z^*, it can be shown that

$$Z' = \frac{R_g}{1 + (\omega R_g C_g)^2} + \frac{R_{gb}}{1 + (\omega R_{gb} C_{gb})^2}\,, \tag{2.80}$$

$$Z'' = R_g\left[\frac{\omega R_g C_g}{1+(\omega R_g C_g)^2}\right] + R_{gb}\left[\frac{\omega R_{gb} C_{gb}}{1+(\omega R_{gb} C_{gb})^2}\right], \qquad (2.81)$$

where R_g R_{gb} C_g and C_{gb} correspond to the resistance and capacitance of the grain and grain boundary, respectively.

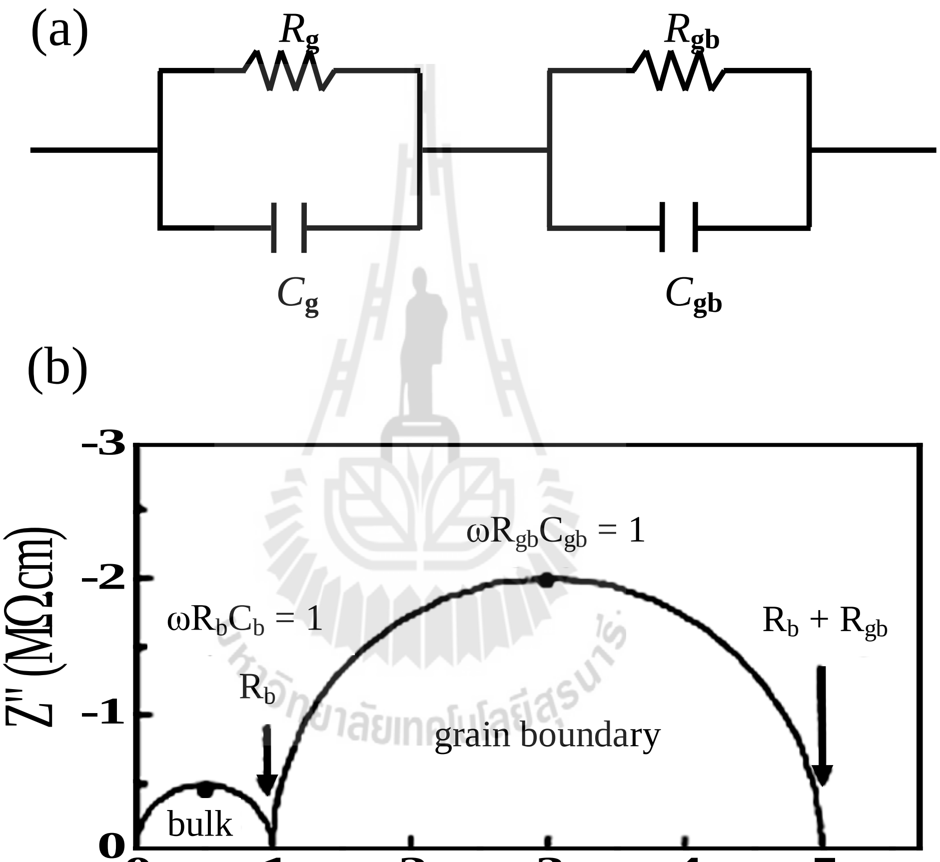

Figure 2.11 (a) The equivalent circuit used to model the electrical properties of ceramics and the parameters R_g, R_{gb}, C_g and C_{gb} correspond to the resistance and capacitance of the grain and grain boundary, (b) simulated Z^* (Li *et al.*, 2005)

2.2 Structure and formation mechanism of titanate nanotubes (TNTs)

2.2.1 Structure of titanate nanotubes (TNTs)

Titanates are generally monoclinic, orthorhombic, cubic or tetragonal in crystal structure, dependent upon their structure formula and atomic configuration. In the interest, only the alkali metal titanate structure will be explained further. Based on XRD, SAED and HRTEM result, Chen *et al*. (2002) proposed that the crystal structure of titanate nanotubes corresponded to the layered trititanic acid ($H_2Ti_3O_7$) having a monoclinic crystal structure (as shown in Table 2.1) Figure 2.12 shows a schematic of the crystal structure of monoclinic trititanic acid in a TiO_6 edge-sharing octahedron. The lattice parameters for each chemical structure are shown in Table 2.1

Chen *et al*. (2002) suggested two possible formation mechanisms of $H_2Ti_3O_7$. They proposed trititanate $(Ti_3O_7)^{2-}$ sheets may grow within the intermediate phase, caused by the reaction between NaOH and TiO_2. The nanosheets grow with an increasing tendency of curling, leading to the formation of nanotubes. Also, $Na_2Ti_3O_7$-like nanocrystal was assumed to form in this disorder-phase, and single trititanate layer subsequently peeled off from the nanocrystal and curved naturally likewood shavings into nanotube. This phenomenon was inferred from the excessive intercalation of Na^+ between the spaces of crystals. Their other studies reinforced the afore stated mechanism, where the hydrogen-deficiency on the surface of $(Ti_3O_7)^{2-}$ plates can provide the driving force (surface tension) for the peeling-off of $(Ti_3O_7)^{2-}$ plates and therefore resulting in the layers bent to form tube morphology. They proposed the optimum dimension of TNTs has also been surveyed in terms of energy views. The number of layers within TNTs was subject to Coulomb energy, which was induced by the negatively charged $(Ti_3O_7)^{2-}$ layers. Coupling energy, resulting from the contributions of unequal distribution between two sides of $(Ti_3O_7)^{2-}$ layers and the usual elastic strain energy of bent crystalline plate, optimize the radius of TNTs at 4.3 nm. They explained the tubes may be constructed by wrapping a (1 0 0) plane along AA′, as indicated in Figure 1(b). Figure 1(c) illustrates the construction of a nanotube by the displacement of A′ with a space of 0.78 nm, and the structure and cross-sectional view of TNTs are shown in Figure 2.2(a) and (d), respectively.

In addition, Wu *et al*. (2006) have proposed that the formation mechanism of nanotubes by rolling of the (100) plane monolayers of $H_2Ti_3O_7$ around the axis [001]. In both cases, the walls of the nanotubes composed of several layers, the interlayer spacing of 0.78 nm. The structure of each layer corresponds to the structure of the (100) plane of monoclinic titanate, with is a set of closely packed TiO_6, edge-sharing octahedral.

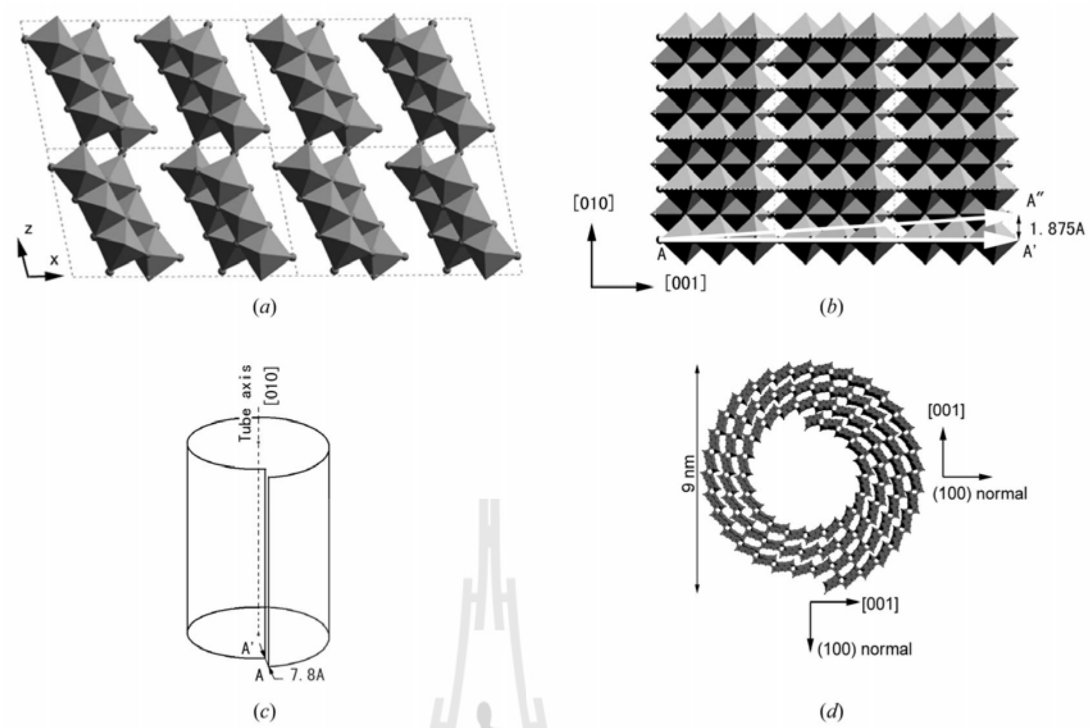

Figure 2.12 Structure models of (a) 2×2 unit cells of $H_2Ti_3O_7$ on the [010] projection and (b) layer of $H_2Ti_3O_7$ on the (100) plane from with the nanotube is constructed. AA′ and AA″ indicate the chiral vectors. Schematic diagrams show (c) the introduction of displacement vector AA′ when wapping up a sheet to form a scroll-type and (d) the structure of trititanate nanotubes. The crystal orientations indicate are the orientations according to the $H_2Ti_3O_7$ layer (Ou and Lo, 2007; Zhang *et al.*, 2003).

Table 2.1 Crystallographic phase of titanate nanotubes (TNTs) and their corresponding lattice parameters.

Crystallographic phase	Symmetry	Lattice parameter (nm)				References
		a	b	c	β	
Anatase TiO_2	Tetragonal	3.79	3.79	2.38	-	Kasuga *et al*. (1999) Du *et al*. (2001)
$Na_2Ti_3O_7$, $Na_xH_{2-x}Ti_3O_7$	Monoclinic	1.926	0.378	0.300	101.45°	Djenadic *et al.* (2007) Morgado Jr *et al.* (2006) Morgado Jr *et al.* (2007)
$H_2Ti_3O_4(HO)_2$, $Na_2Ti_2O_4(HO)_2$	Orthorhombic	1.808	0.379	0.299	-	Zhang *et al.* (2004) Zhang *et al.* (2007)
$H_xTi_{2x/4}\square_{x/4}O_4(H_2O)$	Orthorhombic	0.378	1.874	0.298	-	Ma *et al.* (2003)
$H_2Ti_4O_9$ (H_2O)	Monoclinic	1.877	0.375	1.162	104.6°	Nakahira *et al.* (2004)

2.2.2 Synthesis of titanate nanotubes (TNTs)

Many methods have been developed for the synthesis of TNTs such as assisted-template method (Hoyer, 1996; Jung *et al.*, 2002; Lee *et al.*, 2005) , sol–gel process (Wang *et al.*, 2012), electrochemical anodic oxidation (Zhao *et al.*, 2007) and hydrothermal treatment (Yoshida *et al.*, 2005; Morgado Jr *et al.*, 2006; Kasuga *et al.*, 1998; Ou and Lo, 2007; Tsai and Teng, 2006). Electrochemical acidic oxidation and hydrothermal treatment succeeded in fabricating TNTs. Each fabrication method can have unique advantage and functional features and comparisons among these three approaches have been complied in Table 2.2. These methods, other than the hydrothermal process, are either not suitable for large scale production or not able to yield very low dimensional, well separated, crystallized nanotubes. The demonstrated architecture of TiO_2-based nanotubes constructed via the hydrothermal treatment is capable of good crystalline formation and establishment of a pure-phase structure in one step in a tightly closed vessel.

In the 1998, Kasuga *et al*. (1998) first discovered alkaline hydrothermal route for the synthesis of the titanate nanotubes structure. This synthesis procedure involves the treatment of a TiO_2 powder with concentrated alkaline solutions (10 M NaOH) at 110 °C for 20 h, the morphology of nanotube with a diameter of about 8 nm and a length of about 100 nm and specific surface area of about 400 $m^2 \cdot g^{-1}$. Nanotubes can be successfully synthesized from different crystalline titania polymorphs through alkaline hydrothermal treatment (Nakahira *et al.*, 2004; Thorne *et al.*, 2005; Ou and Lo, 2007; Morgado Jr *et al.*, 2006). Nanotubes are produced when mild to moderate hydrothermal condition are employed. These condition include hydrothermal temperature between 90 and 160 °C (Chen *et al.*, 2002; Sun and Li, 2003; Seo *et al.*, 2008; Hu *et al.*, 2010) with alkaline concentrations in excess of 10 M (Chen *et al.*, 2002; Thorne *et al.*, 2005; Seo *et al.*, 2008; Hu *et al.*, 2009). These good conditions involve hydrothermal temperature at 130 °C (Chen *et al.*, 2002; Hu *et al.*, 2009; Hu *et al.*, 2010) and alkaline concentrations of 10 M (Chen *et al.*, 2002; Thorne *et al.*, 2005; Seo *et al.*, 2008; Hu *et al.*, 2009; Hu *et al.*, 2010).

In addition, nanostructure doping is achievable through either pre- or post treatment processes, producing either intercalated or surface-doped nanostructure. Alkaline earth metal or transition metal ions are often intercalated into nanostructure through ion-exchange processes, whilst transition metal and non-metal ions can be doped onto the nanostructure surface or into the lattice structure. The synthesis nanotubes are soaked in the basic solution containing transition metal ions including Co^{2+}, Fe^{2+}, Ni^{2+}, Cu^{2+} and Ag^{2+} (Umek *et al.*, 2008; Su *et al.*, 2011; Yuan *et al.*, 2013).

Moreover, the magnetic and optical properties of nanotubes were considered by Sun and Li (2003). There was compared physical chemistry between the sample washing with water only and washing with acid, studies morphologies under thermal treatment. Result of EDXA and determination of the thermal and hydrothermal stability elucidated a kind of titanate nanotubes might be molecule of $Na_xH_{2-x}Ti_3O_7$ (x = 0.75). Furthermore, they were prepared ion exchange reactions in aqueous ammonia solution with Cd^{2+}, Zn^{2+}, Co^{2+}, Ni^{2+}, Cu^{2+} and Ag+ with titanate nanotubes, and proposed that transition metal ions might be replaced sodium ions in nanotubes. However, TEM image presenting the tubular structure was retained without the agglomeration of particles or clusters that are formed the outer wall of titanate nanotubes substituted with Cd^{2+}, Zn^{2+}, Co^{2+}, Ni^{2+}, Cu^{2+}. Form UV/Vis spectra can determine band gap of titanate nanotubes about 3.1 eV, while Co^{2+}, Ni^{2+} and Cu^{2+} substituted nanotubes might be excited by visible light due to transition metal ions leading to broad absorption in the visible light.

High-purity nanotubes and nanobelts could be controllably obtained in hydrothermal treatments of anatase TiO_2 in concentrated NaOH solution depending on treating temperature and duration. Ma group represented XANES spectra of nanotubes the pre-edge peak indicated to forbidden transitions from the core 1s level to unoccupied 3d states of a Ti^{4+} due to the degree of the distortion of TiO_6 octahedron (Ma *et al.*, 2005). The core level 2p XPS spectra for as synthesized, ion-exchanged and annealed titanate (at 600 °C).

Titanate nanotubes were achieved by hydrothermal method with 10M NaOH solution at various reaction temperatures ranging from 70 to 150 °C over 48 h. They reported the spectra of Ti 2p for as-synthesize titanate investigated by a binding energy of 458.3 eV ($2p_{3/2}$) and 464.0 eV ($2p_{1/2}$) with separation energy of 5.7 eV (Seo *et al.*, 2008).

The electrical property of titanate nanotubes has recently attracted much attention. However, only a few studies have reported. In the report of Thorne group (Thorne *et al.*, 2005), which observed electrical properties of titanate nanotubes prepared by hydrothermal method. They proposed the impedance complex plane consisting of two semicircular arcs indicating that there at least two electrical responses in titanate nanotubes, which refers to the external effect. The conductivity large semicircle at low frequency effected to resistance of the electrode. The conductivity at high-frequency electrical response refers to the internal resistance due to grain and grain boundary. The conductivity (σ) is calculated about 5.5×10^{-6} S cm^{-1} at 30 °C, there is increasing with increasing temperature. Above 130 °C, the conductivity drops with calculated activation energy (E_a) about 0.57 eV.

Similar work reported by Hu group (Hu *et al.*, 2009), the $Na_{0.96}H_{1.04}Ti_3O_7\cdot3.42H_2O$ (Na-TNT) nanotubes were prepared by hydrothermal method at 130 °C for 24 h, which converted into the $Na_{0.036}H_{1.964}Ti_3O_7\cdot3.52H_2O$ (H-TNT) nanotubes by acidic rinsing (0.1 M HNO_3) for 2 weeks. They observed in terms of the defect chemistry, hydration, and the triple conductive species and presented these electrons may contribute to the grain conductivity (σ_g). The grain conductivity of TNT increases from 1.7×10^{-5} S/cm at room temperature to reach a maximum of 5.1×10^{-4} S/cm at 90 °C and then decreases with increasing temperatures. As a result, indicate the number of conductive protons decreases due to the removal of water from the nanotubes effect the heating process. Conduction in TNT may be cause structural distortion of the protonated octahedron and enhance coupling interaction between the layers; during Na^+ ions with weak bonding to TiO_6 octahedron are more mobile and conductive under external fields.

Titanium oxy-nitride has been fabricated for the first time from anhydrous sol-gel method and used as anode for water electrolysis in acid medium (Wang *et al.*, 2012). The titanium oxy- nitride is conchoidal fracture particles and the surface is smooth. The particle size is about 10 - 30 μm. The material is sensitive to the calcination temperature. The properties of the samples changed with the temperature of calcinations. Moreover, there are other techniques of synthesis and morphology of TiO_2-based nanostructures reported in the literature are summarized in Table 2.3.

Table 2.2 Comparisons of current methods in TNTs fabrication.

Fabrication method	Advantages	Disadvantages	TNTs features
Template–assisted method Hoyer *et al.* (1996) Jung *et al.* (2002) Lee *et al.* (2005)	(1) The scale of nanotube can be moderately controlled by applied template	(1) Complicated fabrication process (2) Tube morphology may be destroyed during fabrication process	Ordered arrays (powder form)
Electrochemical anodic oxidation method Zhao *et al.* (2007)	(1) More desirable for practical applications (2) Ordered alignment with high aspect ratio (3) Feasible for extensive applications	(1) Mass production is limited (2) Rapid formation kinetics is subjected (3) Highly expense of fabrication apparatus	Oriented arrays (thin film) to the utilization of HF
Hydrothermal treatment Kasuga *et al*. (1998) Chen *et al*. (2002) Sun and Li (2003) Seo *et al*. (2008) Hu *et al*. (2009)	(1) Easy route to obtain nanotube morphology (2) A number of modifications can be used to enhance the attributes of titanium nanotubes (3) Feasible for extensive applications	(1) Long reaction duration is needed (2) Highly concentrated NaOH must be added (3) Difficult in achieving uniform size	Random alignment (powder form)

Table 2.3 Lists of reports for synthesis of TNTs by hydrothermal method.

Materials	Alkaline	Condition		Morphology		Structure	References
	NaOH	Temp. (°C)	Time (h)	Diameter (nm)	Lengths (nm)		
TiO_2	5-10M	110	20	8	100	TiO_2 anatase	Kasuga *et al.* (1998)
TiO_2	10M	130	72	9	several	$H_2Ti_3O_7$	Chen *et al.* (2002)
TiO_2	10M	100-180	<48	8-20	several	$H_2Ti_3O_7$	Sun and Li (2003)
TiO_2	5-10M	110-190	12	100-300	several	$H_2Ti_3O_7$	Ma *et al.* (2005)
TiO_2	10M	150	72	10	several	$H_2Ti_3O_7$	Thorne *et al.* (2005)
TiO_2	10M	150	48	10-20	several	$H_2Ti_3O_7$	Seo *et al.* (2008)
TiO_2	10M	130	24	8-10	several	$H_2Ti_3O_7$	Hu *et al.* (2009)

2.3 Giant dielectric properties

In recent years, giant dielectric materials have been playing a significant role in microelectronic devices such as capacitors and memory devices (Subramanian *et al.*, 2000; Ramirez *et al.*, 2000; Sinclair *et al.*, 2002). This because such devices often require materials with high dielectric constants (ε') and low loss tangents ($\tan\delta$). Normally, high permittivity dielectric materials with a static dielectric constant value above 10^3 consist of ferroelectric oxide and relaxor oxide such as $BaTiO_3$ and $PbMg_{1/3}Nd_{2/3}O$ (Cross, 1987; Viehland *et al*., 1991; West *et al*., 2004).

In addition, J Wu *et al*. (2002) have reported a giant dielectric response in, a non-perovskite and non-ferroelectric materials, Li and Ti co-doped NiO ($Li_xTi_yNi_{1-x-y}O$(LTNO)) ceramics. The dielectric constant values of LTNO ceramics found to be about 10^3-10^5 with nearly temperature independent in the range of 200-450K, as shown Figure 2.13. This figure presented the temperature dependence of the dielectric constant (ε') and the loss tangent ($\tan\delta$) of LTNO ceramic prepared by a simple sol-gel method at different frequencies. The increasing the frequency up to 10^5 Hz, the rapid decrease in the dielectric constant was considered at the low temperature range, corresponding to the existence of the loss tangent peak. Both of the rapid decrease in the dielectric constant and the related relaxation peak of the loss tangent shifted to higher temperature range with increasing the frequency. This indicates to the thermally activity mechanism of this dielectric relaxation process. The dielectric relaxation behavior of the LTNO ceramic was ascribed based on the fact the electric dipoles will freeze though the relaxation process at low temperature, and there exists decay in polarization with respect to and applied electric field.

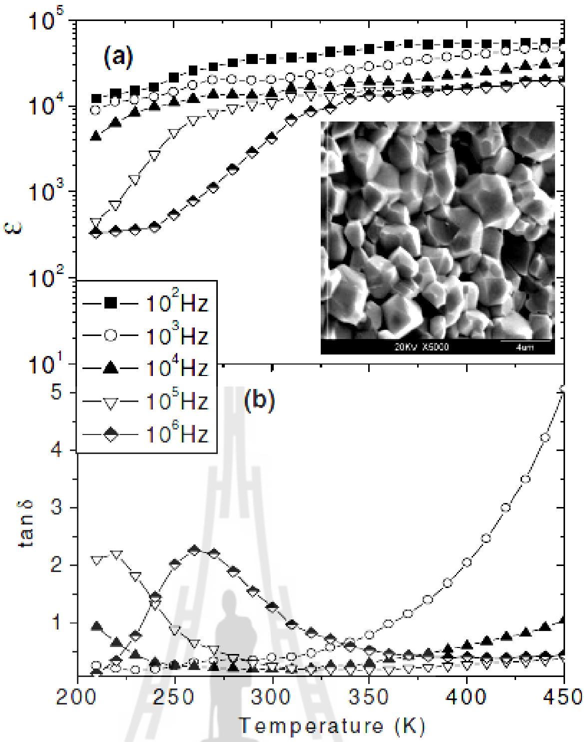

Figure 2.13 The temperature dependence of (a) the dielectric constant ε' and (b) the loss tangent $\tan\delta$ for the LTNO at various frequencies between 100 Hz and 1 MHz. The inset shows a typical SEM of the samples (Wu *et al.*, 2002).

Moreover, giant dielectric materials reported in recent years, $CaCu_3Ti_4O_{12}$ (CCTO) has gained considerable interest both scientifically and technologically. Its giant dielectric constant exhibits values in the range of 10^3–10^5 at room temperature (Thongbai *et al.*, 2012; Jumpatam *et al.*, 2012; Subramanian *et al.*, 2000), depending on ceramic microstructures and processing conditions. It is now widely accepted that the origin of the giant dielectric response in the CCTO ceramics is attributed to the Maxwell–Wagner polarization effect. This polarization can be introduced at several places. These include internal interfaces inside the ceramics such as grain boundaries (GBs), domain boundaries (DBs), and at the external interfaces such as sample–electrode interface.The dielectric relaxation behavior of CCTO ceramics was ascribed based on nanoscale barrier layer capacitance effect (Jumpatam *et al.*, 2012). The dielectric relaxation behavior and the value of dielectric of CCTO as clearly seen in Figure 2.13

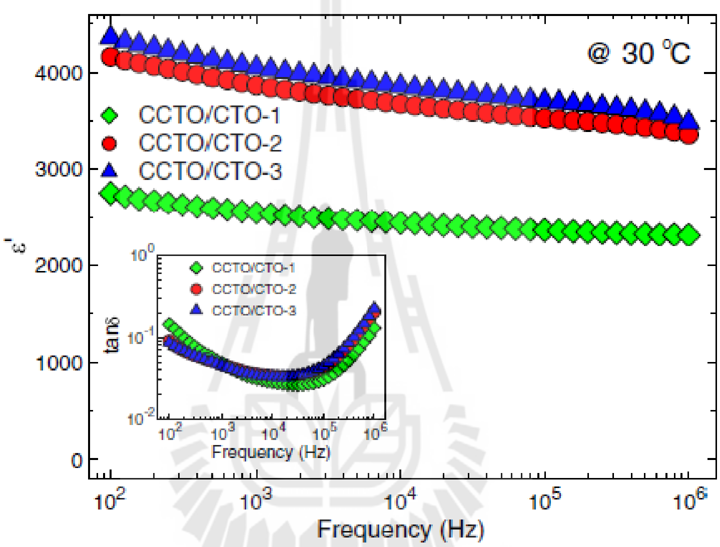

Figure 2.14 Frequency dependence of ε' for CCTO/CTO ceramics. Inset shows frequency dependence of tanδ at 30 °C (Jumpatam *et al.*, 2012).

2.4 Dielectric properties of TNTs

Hu *et al*. (2009), they considered in terms of the defect chemistry, hydration, and the triple conductive species and presented these electrons may contribute to the grain conductivity (σ_g). Figure 2.14 shows the impedance data of TNTs measured at room temperature. A semicircle with nonzero intercept in the high frequency and a spike in the low frequency were observed. The impedance data in Figure 2.14 is modeled using an equivalent circuit that consists of two parallel *RQ* elements connected in series of $(R_gQ_g)(R_{gb}Q_{gb})$, as illustrated in the inset of Figure 2.14, where R_g and R_{gb} represent the grain and grain boundary resistances, respectively. The grain conductivity of TNT increases from 1.7×10^{-5} S/cm at room temperature to reach a maximum of 5.1×10^{-4} S/cm at 90 °C and then decreases with increasing temperatures. As a result, indicate the number of conductive protons decreases due to the removal of water from the nanotubes effect the heating process.

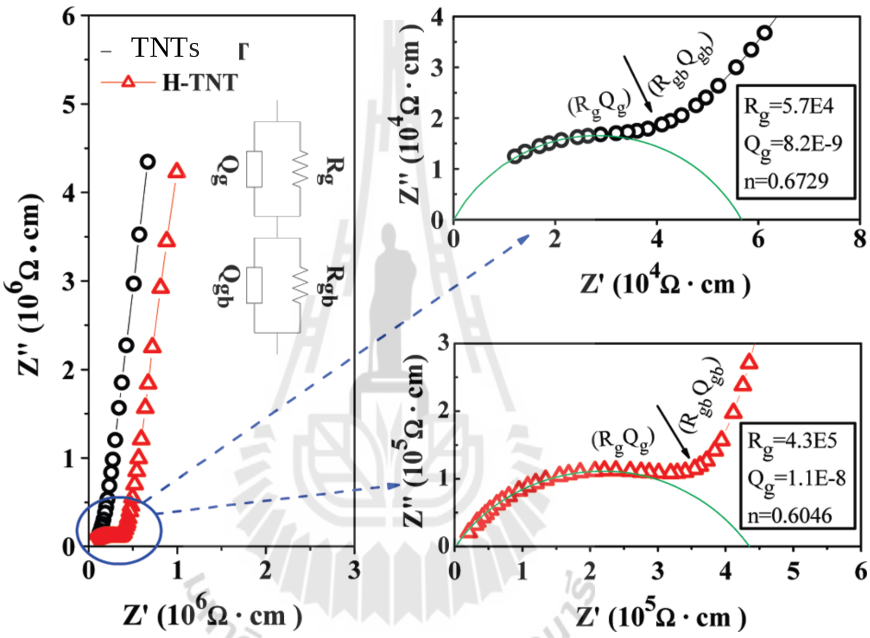

Figure 2.15 RT impedance spectra of TNTs and H-TNT. The inset shows the equivalent circuit that was used for data fit, which *R* and *Q* represent resistors and constant phase elements (Hu *et al.*, 2009).

In addition, Hu *et al.* (2010) reported a giant dielectric and polarization behavior observed in TNTs. The TNTs structure exhibited high dielectric constant (ε′) about 10^4 at room temperature and low frequency. The ε′ increased at low frequencies, with increasing temperature the relaxation peaks shift toward higher frequencies as shown in Figure 2.14.

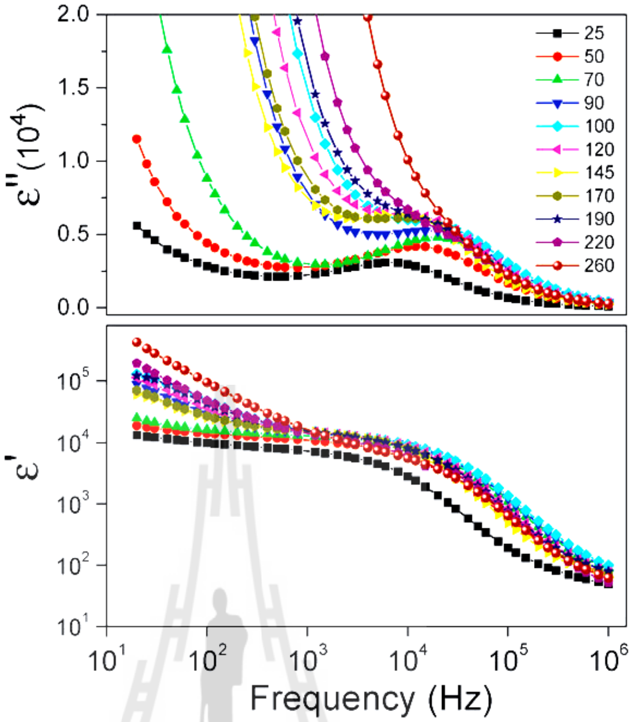

Figure 2.16 Frequency dependences of the dielectric constants ε' and ε'' at various temperatures for (a) TNTs (Hu *et al.*, 2010).

This report elucidated from the dielectric relaxation behavior of TNTs. It is closely related to the Maxwell-Wagner polarization or the interfacial polarization. The relaxation time at very low frequency of TNTs caused from along the tube of water molecules intercalated in the scrolled titanate nanotubes, due to localized and short-ranged transport of charged species, the interface between $Ti_3O_7^{2-}$ skeleton layers, i.e., H_2O molecule layer confined inside TNTs, playing the predominant role in accumulation of charged species. The relaxation under high frequencies relatively associated with the axial conductivity due to the cross-sectional linger for charge species accumulations of charges inside TNTs.

CHAPTER III

EXPERIMENTAL PROCEDURE

This chapter describes the experimental method of the research, which investigates the TNTs and Fe/Co-doped TNTs dielectric properties of TNTs and Fe/Co-doped TNTs. The powders were synthesized by hydrothermal method. The synthesized TNTs were characterized by X-ray diffraction (XRD), transmission electron microscopy (TEM), high-resolution transmission electron microscopy (HRTEM), Energy-dispersive X-ray spectroscopy (EDS), Vibrating sample magnetometer (VSM), Fourier transform infrared (FTIR), UV-Vis scanning spectroscope (UV-Vis), X-ray photoelectron spectroscopy (XPS) and X-ray Absorption Near Edge Structure (XANES). The details about the dielectric and electrical measurements are also included in the chapter.

3.1 Powder and bulk sample preparation

In this study, the titanate nanotubes ($Na_xH_{2-x}Ti_3O_7.nH_2O$; TNTs) and Fe/Co-doped TNTs were synthesized by hydrothermal method. The materials used in this research are shown in Table 3.1.

Table 3.1 List of raw materials used for titanate nanotubes preparation, quoting their source and purity.

Material	Manufacture	Purity
Titanium dioxide (TiO_2)	Riedel-dehean USP	99-100%
Sodium hydroxide (NaOH)	MERCK kGaA	99%
Iron (III) nitrate enneahydrate ($Fe(No_3)_2.9H_2O$)	Kento chemical	99.9%
Co (II) nitrate hexahydrate ($Co(No_3)_2.6H_2O$)	Kento chemical	99.95%

3.1.1 Synthesis of titanate nanotubes (TNTs)

Titanate nanotubes (TNTs) were prepared from TiO_2 powder and 10 M NaOH solution. First, 2g of TiO_2 (99-100% Riedel-dehean USP) was dispersed in solution of 10M NaOH (99% MERCK kGaA) (160 ml) under magnetic stirring at room temperature for 24 h to form a white suspension. Second, this suspension was placed into a Teflon-lined autoclave temperature at 130 °C for 24 h. Then the autoclave was cooled to room temperature naturally. Finally, the obtained sample was dissolved into deionized water several times and oven dried at 70 °C.

Throughout this thesis, the powder sample was characterized for crystal phase identification by the X-ray diffraction (XRD) using a CuKα radiation with λ=0.154060 nm (D2, Bruker, Germany) and recorded within a 5°-80° angle range of 2θ; the scan step was 0.02°/s. The morphology and size of TNTs were observed by transmission electronic microscopy (TEM) (FEI, Tecnai G^2 F20, FE-TEM, Netherlands). The structure of all sample are evaluated by fourier transform infrared (FTIR) and raman spectroscopy. Room temperature absorption spectra were recorded using a UV-Vis-NIR scanning spectroscope (UV-3101PC, Shimadzu). The X-ray Absorption Near-Edge Structure (XANES) spectroscopy measurement were performed on the prepared samples to start the valence state of Fe, Co and Ti ions in TNTs and Fe-, Co-doped TNTs structure. X-ray photoelectron spectroscopy (XPS: AXIS LUTRA^{DLD}, Kratos analytical, Manchester, U.K.) was used to determine the percentage of oxygen-deficient region and valence state of Ti, O, Na, Fe and Co in the TNTs matrix. The magnetic properties of all samples were examined at room temperature (293 K) using a vibrating sample magnetometer (VSM) (VSM 7403, Lake Shore, USA). For the dielectric measurement, the bulk samples were electroded by silver pain on both sides of the disk-shaped samples. The dielectric and electrical responses of the samples were measured using Agilent 4294A Precision LCR Meter analyzer over wide range frequency (10^2-10^6 Hz) and temperature (-50 to 180 °C) at oscillation voltage of 0.5 V. Each measuring was kept constant with an accuracy of ±1 °C. Current–voltage measurements were made using a high voltage measurement unit (Keithley Model 247). The dielectric properties of TNTs bulks were investigated as a function of dc bias under 0-10 V. The breakdown electric field (E_b) was obtained at a current density (J) of 1 mA.cm^{-2}. Numerical values for the nonlinear coefficient (α) were obtained by a linear regression of log(J) versus log(E) plot within the range of validity of the I = KV^{α} equation. A schematic illustration of TNTs and bulks preparation by hydrothermal method, characterization and measuring technique is shown in the Figure 3.1. More details of each characterization technique are given in section 3.2.

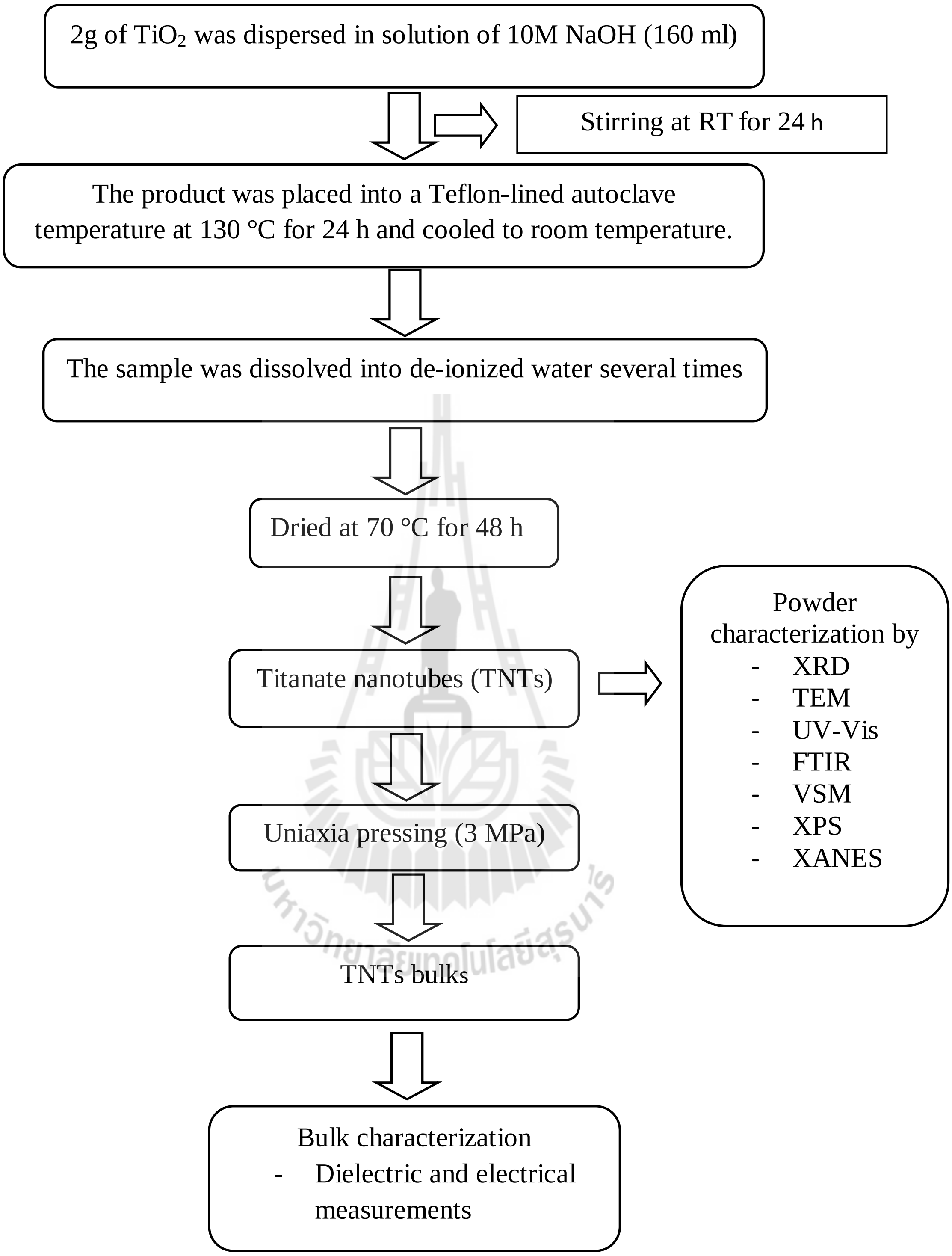

Figure 3.1 Diagram showing preparation and characterization of TNTs ($Na_{0.039}H_{1.964}Ti_3O_7\cdot nH_2O$) powder and bulk, synthesized by hydrothermal method.

3.1.2 Synthesis of Fe/Co-doped TNTs

The starting powders are calculated according to the *stoichiometric* composition A_2 $(Ti_{3-x}Fe_x)O_7$/ A_2 $(Ti_{3-x}Co_x)O_7 \cdot nH_2O$ (A_2=$Na_{0.036}$ $H_{1.964}$) with x = 0, 0.05, 0.1, 0.2, 0.3, and 0.4, respectively. First, 2g of TiO_2 (99-100% Riedel-dehean USP) and $Fe(No_3)_2.9H_2O$ (99.9% Kento) or $Co(No_3)_2.6H_2O$ (99.95% Kento) were dispersed in solution of 10M NaOH (160 ml) under magnetic stirring at room temperature for 24 h and followed by ultrasonic for 2 h. This product was placed into a Teflon-lined autoclave temperature at 130 °C for 24 h. Then the autoclave was cooled to room temperature naturally. Finally, the obtained sample was dissolved into de-ionized water and oven dried at 70 °C. A schematic illustration of the preparation of Fe/Co-doped TNTs powders and bulks, characterization and measuring technique is shown in the Figure 3.2.

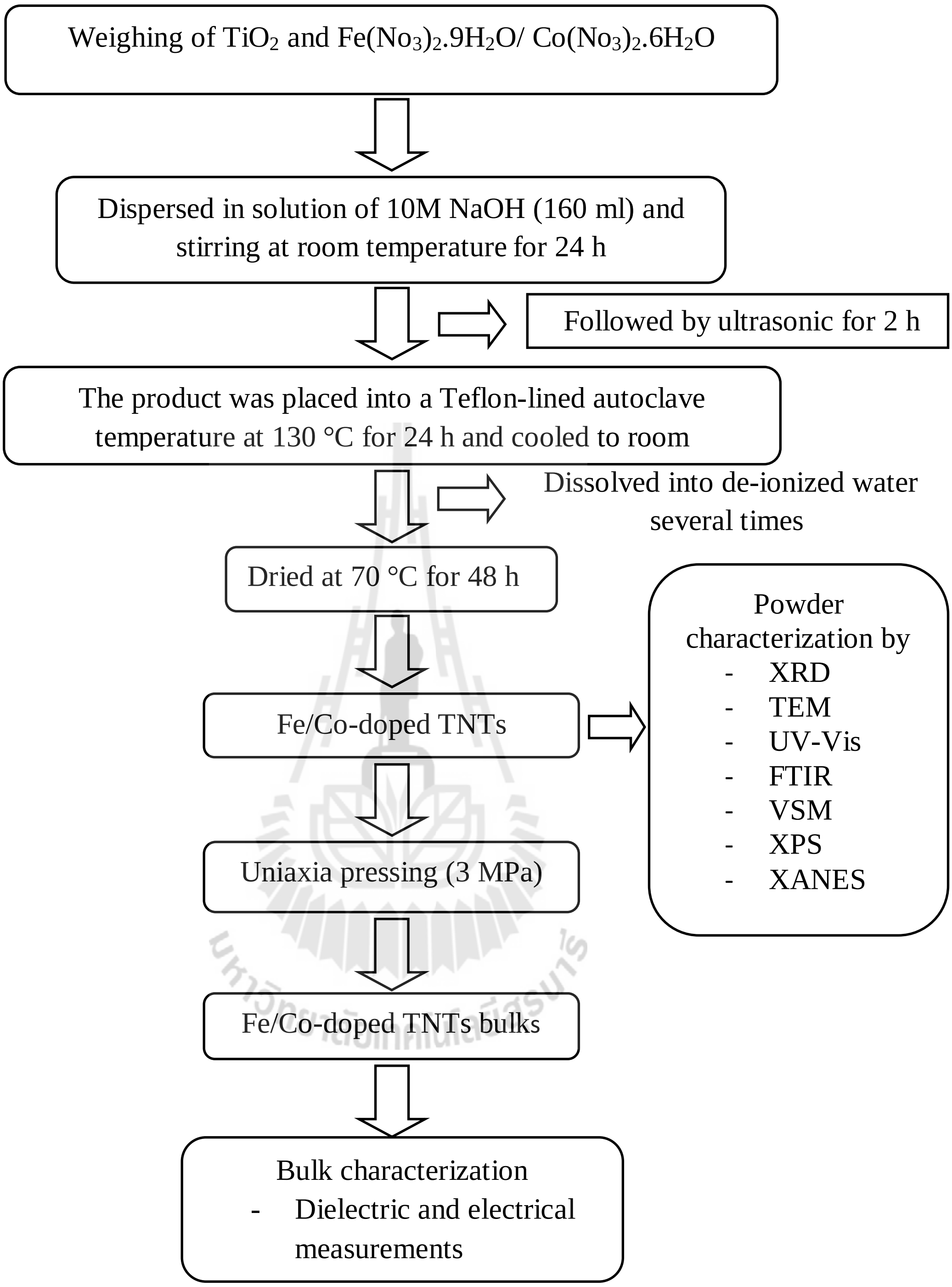

Figure 3.2 Diagram showing preparation and characterization of Fe/Co-doped TNTs powder and bulk, $A_2\ (Ti_{3-x}Fe_x)O_7$/ $A_2\ (Ti_{3-x}Co_x)O_7$ in which x varies as 0, 0.1, 0.2, 0.3 and 0.4, synthesized by hydrothermal method.

Table 3.2 The amount of commercial TiO_2 and $Fe(No_3)_2.9H_2O$/ $Co(No_3)_2.6H_2O$ used to prepare Fe/Co-doped TNTs powder with different chemical compositions.

$Na_{0.039}H_{1.964}(Ti_{3-x}Fe_x)O_7 \cdot nH_2O$

Doping Level	TiO_2 (g)	$Fe(No_3)_2.9H_2O$ (g)	NaOH 10M (ml)	Chemical compositions
x = 0.05	1.9667	0.1683	160	$Ti_{2.95}Fe_{0.05}$ A
x = 0.1	1.9333	0.3367	160	$Ti_{2.9}Fe_{0.1}$ A
x = 0.2	1.8667	0.6733	160	$Ti_{2.8}Fe_{0.2}$ A
x = 0.3	1.8000	1.0100	160	$Ti_{2.7}Fe_{0.3}$ A
x = 0.4	1.7333	1.3467	160	$Ti_{2.6}Fe_{0.4}$ A

$Na_{0.039}H_{1.964}(Ti_{3-x}Co_x)O_7 \cdot nH_2O$

Doping Level	TiO_2 (g)	$Co(No_3)_2.6H_2O$ (g)	NaOH 10M (ml)	Chemical compositions
x = 0.05	1.9667	0.1213	160	$Ti_{2.95}Co_{0.05}$A
x = 0.1	1.9333	0.2425	160	$Ti_{2.9}Co_{0.1}$ A
x = 0.2	1.8667	0.4851	160	$Ti_{2.8}Co_{0.2}$ A
x = 0.3	1.8000	0.7276	160	$Ti_{2.7}Co_{0.3}$ A
x = 0.4	1.7333	0.9701	160	$Ti_{2.6}Co_{0.4}$ A

Denote: A = $Na_{0.039}H_{1.964}O_7 \cdot nH_2O$

3.2 Powder and bulk sample characterization

The microstructure and phase composition of the TNTs and Fe/Co-doped TNTs powders, in this research were characterized by XRD, TEM and EDS techniques. Absorption or reflectance of the TNTs and Fe/Co-doped TNTs investigated by UV-Vis and FT-IR techniques. The valence state or electronic state of all samples were characterized by using XPS and XANES. Magnetic properties are evaluated by VSM. The details of each measuring technique are described in the following sections.

3.2.1 X-ray diffraction (XRD)

The prepared TNTs and Fe/Co-doped TNTs were characterized for crystal phase identification crystallite size by using the X-ray diffraction (XRD) using a CuKα radiation with λ=0.154060 nm (Bruker D2, Germany). In the X-ray diffraction (XRD), a collimated beam of X-rays is incident on a specimen and is diffracted by the crystalline phases in the specimen according to Bragg's law

$$2d\sin\theta = n\lambda \tag{3.1}$$

where d is the spacing between atomic planes in the crystal phase, n is an integer, λ is the wavelength of the X-ray radiation, and θ is the angle of incident beam made with the crystal plane. Bragg's Law can be simply obtained by calculating the path differences between the two beams in Figure 3.3. The path difference depends on incident angle (θ) and spacing between the parallel crystal planes. In the order to keep these beams in phase, their path difference ($SQ+QT=2d\sin\theta$) has to equal one or multiple X-ray wavelengths ($n\lambda$).

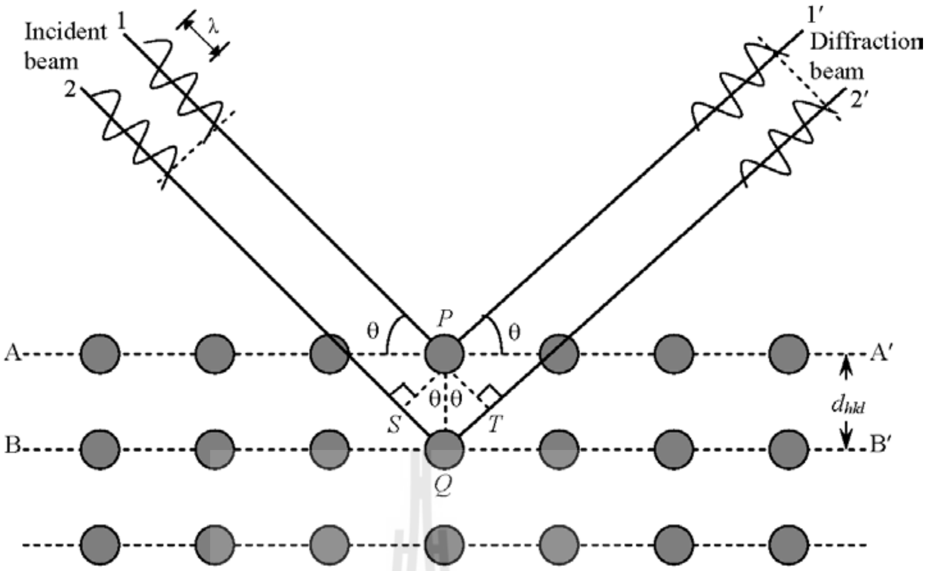

Figure 3.3 Bragg diffraction by crystal planes. The path difference between beams 1 and 2 is $SQ + QT = 2PQ\sin\theta$ (Leng, 2008).

The intensity of the diffracted X-ray is measured as a function of the diffraction angle 2θ and orientation of a specimen. In this thesis, the XRD pattern were recorded within a 5°-80° angle range of 2θ; the scan step was 0.02°/s. The crystalline phase identification was carried out by comparison with the Jiont Committee on Powder Diffraction Standards (JCPDS) diffraction files. The Rietveld refinement of X-ray diffraction pattern for TNTs at room temperature was performed using X′Pert Plus program to determine the average crystallite size in this thesis.

The estimated crystalline size of the samples were calculated from X-ray line broadening of the diffraction peak at 2θ: 5°- 55° by using Scherrer’s equation as given by

$$D = \frac{K\lambda}{\beta\cos\theta} \tag{3.2}$$

where K is a constant depending on the XRD equipment and has been determined to vary between 0.89-1.39, but is usually taken as close to unity. For this study, K=0.90, λ is the wavelength of the X-ray radiation, and θ is the diffraction angle, and β is the full-width at haft maximum of XRD peak.

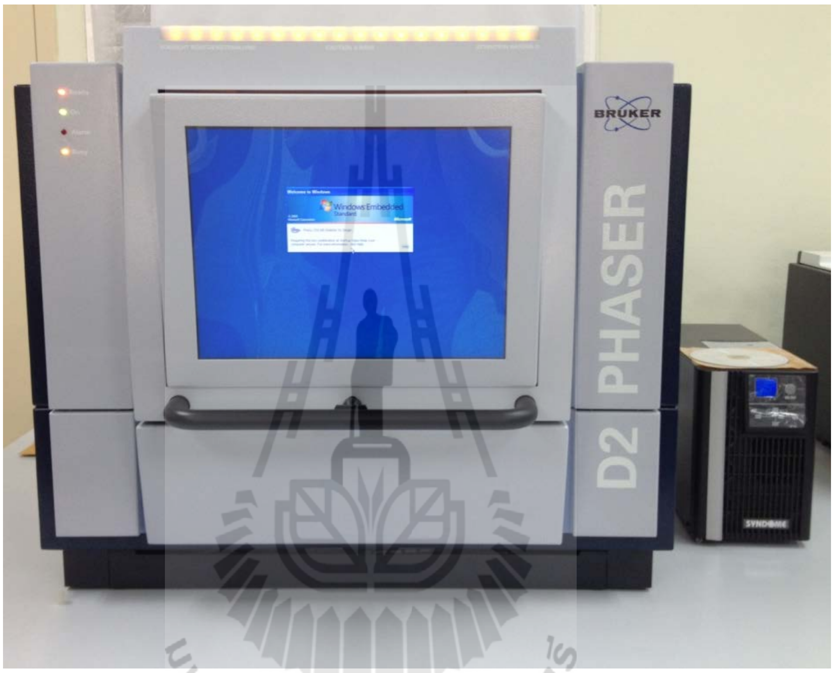

Figure 3.4 X-ray diffractometer (XRD; Bruker D2, Germany, SUT).

3.2.2 Scanning electron microscopy (SEM)

The scanning electron microscopy is a type of electron microscopy that images the sample surface by scanning it with a high-energy beam of electrons. The SEM image of the sample can be obtained by interaction between the electrons and the atoms in the sample producing signals that can be detected and that contain information about the sample's surface morphology, grain shape, porous and composition distributions. The SEM operates under a vacuum, and electrons produced by a field emission source are accelerated in a field gradient. The beam passes through electromagnetic lenses, focusing onto the specimen. As a result of this bombardment different types of electrons are emitted from the specimen. This signal electrons emitted from the specimen are collected by a detector and amplified. A detector catches the secondary electrons and an image of the sample surface is constructed by comparing the intensity of these secondary electrons to the scanning primary electron beam. Finally the image is displayed on a screen (as shown in Figure 3.5).

In this work, the morphologies of samples were obtained using scanning electron microscope LEO 1450VP (LEO, U.K.).

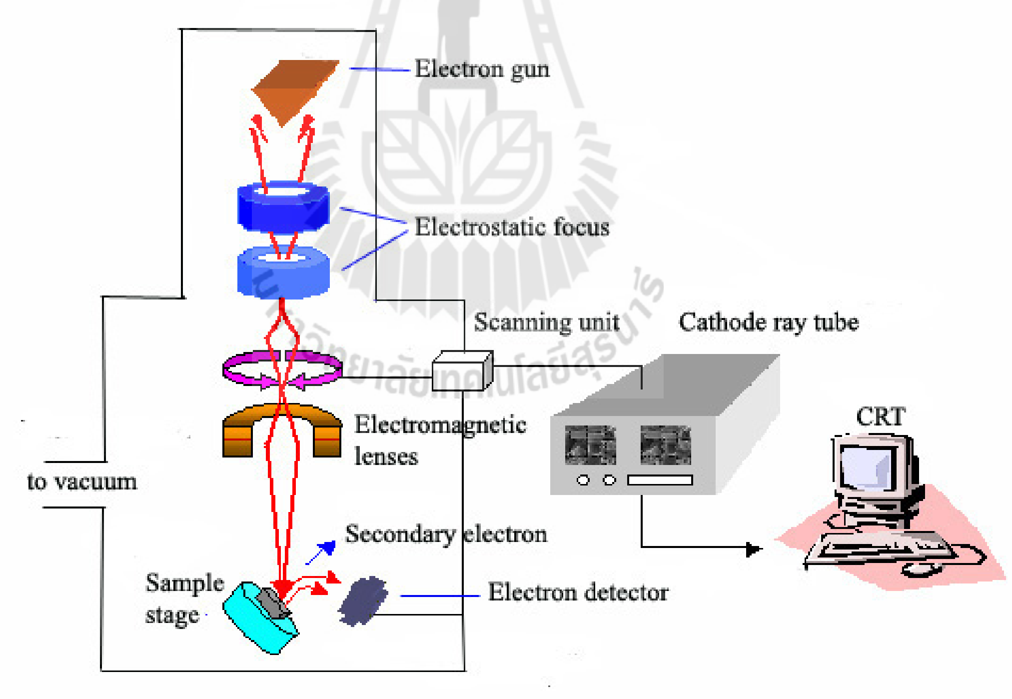

Figure 3.5 Diagram of the FE-SEM (New Mexico Tech., n.d).

Figure 3.6 Scanning Electron Microscope LEO 1450VP at Khon Kaen University.

.

3.2.3 Transmission electron microscopy (TEM)

Transmission electron microscopy (TEM) is an electron microscopy technique used to examine the powder structure, phase composition or properties in submicroscopic detail. In this technique, a beam of electrons is transmitted through an ultra-thin specimen, interacting with the specimen as it passes through. An image is formed from the interaction of the electrons transmitted through the specimen; the image is magnified and focused onto an imaging device, such as a fluorescent screen, on a layer of photographic film, or to be detected by a sensor such as a CCD camera.

A diffraction pattern is formed on the back focal plane of the objective lens when and electron beam passes through a crystalline specimen in a TEM. In the diffraction mode, a pattern of selected area diffraction (SAD) can be further enlarged on the screen or recorded by a camera. The diffraction angle in the TEM is very small (commonly $\theta < 1°$), because the reflecting lattice planes are nearly parallel to the primary beam. Using the approximation sine $\theta \approx \theta$ for a small angle, we can rewrite Bragg's Law as the following.

$$\lambda = 2d\theta \tag{3.3}$$

$$\lambda L = Rd \tag{3.4}$$

where L is the camera length of a TEM, the distance between the crystal and photographic plate of camera. L is an equivalent camera length for calculating the spacing of the lattice plane. λL is called as the camera constant of the TEM. Eq. (3.4) is the basic equation for electron diffraction in a TEM. We can calculate the spacing of crystallographic planes by measuring R (the distance from the central spot of the transmitted beam to diffraction spot) in photographic film using Eq. (3.4) L can be changed in a TEM.

In this work, the TNTs-based samples were dispersed in ethanol and sonicated for 15 min. A few drops of suspension were placed onto a carbon coated copper gride. TEM also provided selected area electron diffraction (SAED) patterns of the samples, which were used to compliment XRD results.

3.2.4 Energy dispersive X-ray spectroscopy (EDS)

Energy dispersive X-ray spectroscopy (EDS) is an analytical technique used for the elemental analysis or chemical characterization of a sample. It relies on an interaction of some source of X-ray excitation and a sample. Its characterization capabilities are due in large part to the fundamental principle that each element has a unique atomic structure allowing unique set of peaks on its X-ray spectrum. The number and energy of the X-rays emitted from a specimen can be measured by an energy-dispersive spectrometer. As the energy of the X-rays is characteristic of the difference in energy between the two shells, and of the atomic structure of the element from which they were emitted, this allows the elemental composition of the specimen to be measured.

In this research, the composition of all samples was characterized by TEM-based EDS. As a result, the chemical compositions in the sample can be determined.

3.2.5 Thermal gravimetric analysis (TGA)

Thermogravimetric analysis or thermal gravimetric analysis (TGA) is a method of thermal analysis in which changes in physical and chemical properties of materials are measured as a function of increasing temperature. TGA is generally used to determine selected characteristics of materials that exhibit either mass loss or gain due to decomposition, oxidation, or loss of volatiles (such as moisture).

Thermal analysis of the undoped TNTs was investigated by thermogravimetric analysis (TGA) using a SDT 2960 simultaneous DSC-TGA which was performed at a heating rate of 10 °C/min from room temperature to 800 °C in N_2 atmosphere at a flux of 120 ml/min.

3.2.6 Fourier transform infrared spectroscopy (FTIR)

Fourier transform infrared spectroscopy (FTIR) is the most widely used vibrational spectroscopic technique. FTIR is an infrared spectroscopy in which the Fourier transform method is used to obtain an infrared spectrum in the whole range of wavenumbers simultaneously. It differs from the dispersive method, which entails creating a spectrum by collecting signals at each wavenumber separately.

The key component in the FTIR system is the Michelson interferometer, as schematically illustrated in Figure 3.7. The infrared radiation from a source enters the Michelson interferometer. The interferometer is composed of one beam-splitter and two mirrors. The beam-splitter transmits of the infrared (IR) beam from the source and reflects the other haft. The two split beams strike a fixed mirror and moving mirror, respectively. After reflecting from the mirrors, the two split beams combine at the beam splitter again in order the irradiation the sample before the beam are received by the detector.

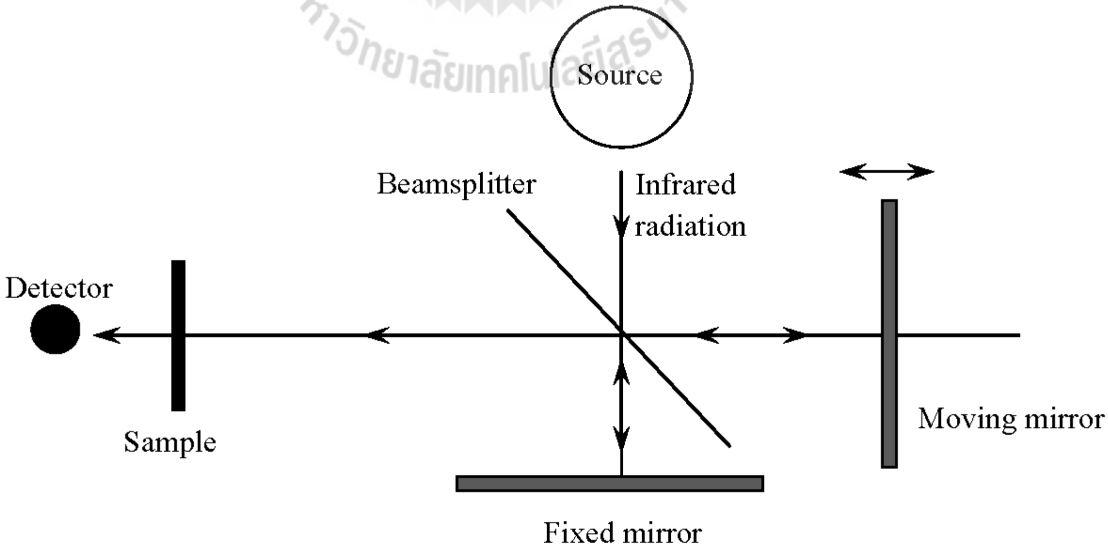

Figure 3.7 Optical diagram of a Michelson interferometer in FTIR (Leng, 2008).

In this work, the transmittance examination technique refers to the method of obtaining an infrared spectrum by passing an IR beam through a sample. Fourier transform infrared (FTIR) spectra of the prepared TNTs-based samples were measured using a Bruker Vertex 70 spectrophotometer. The prepared TNTs-based samples were mixed KBr with grinding together to obtain powder particles with size less than 2 μm. Then, the powder mixture were collected into a mould and pressed with a pressure of 1 MPa. The product was placed onto a holder sample. FTIR spectra were recorded in the 4,000-400 cm^{-1} range.

3.2.7 UV-Vis scanning spectroscopy (UV-Vis)

UV-Vis or UV/Vis refers to absorption spectroscopy or reflectance spectroscopy in the ultraviolet-visible spectral region. This means it uses light in the visible and adjacent (near-UV and near-infrared [NIR]) ranges. The absorption or reflectance in the visible range directly affects the perceived color of the chemicals involved. This technique is complementary to fluorescence spectroscopy, in that fluorescence deals with transitions from the excited state to the ground state, while absorption measures transitions from the ground state to the excited state.

In this work, the sample was investigated by absorption spectra technique. The optical behavior of the TNTs-based samples is quite similar to that of mesostructured titanium dioxide. The absorption coefficient, α' of the samples can be calculate from transmittance, T':

$$\alpha' = -2.303\frac{\log(T')}{L} \tag{3.5}$$

where L is the film thickness (or the length of the nanotubes). The absorption coefficient depends on the energy of the incident light ($h_{P\nu}$) as follows:

$$\alpha' = A' \frac{(h_{P\nu} - E_G)^n}{h_{P\nu}} \tag{3.6}$$

where E_G is the semiconductor band gap, A' is the proportionality coefficient, n is a number (which is equal to 1/2, 2, 3/2 or 3 for allowed direct, allowed indirect, forbidden direct or forbidden indirect). TiO_2 nanotubes have allowed indirect optical transition and the Tauc plot in $(\alpha h_{P\nu})^{0.5}$ *vs. hv* coordinates allow us to estimate the optical band gap by dropping a line from the maximum slope of the curve to the x-axis. Room temperature absorption spectra were recorded using a UV-Vis-NIR scanning spectroscopy (UV-3101PC, Shimadzu).

3.2.8 X-ray photoelectron spectroscopy (XPS)

X-ray photoelectron spectroscopy (XPS), also known as electron spectroscopy for chemical analysis (ESCA), is a widely used technique for the structural study of solid surfaces allowing determination of the elementar composition of a material (there are also XPS instruments capable of analyzing both liquids and solids). The theoretical foundation of XPS is based on the equation proposed by Einstein to explain the photoelectric effect:

$$h\nu = E_b - E_{kin} \tag{3.7}$$

where $h\nu$ is the quantum energy, E_b the binding energy of the electron in matter (i.e. energy required to remove an electron) and E_{kin} the kinetic energy of the ejected electron. XPS can be described as a technique for the measurement of the kinetic energy of the inner or valence electron ejected by an incident X-ray photon of known energy ($h\nu$). Knowing these values it is possible to calculate the binding energy (E_b), which is characteristic of the chemical bonds in a compound. Electron binding energies are also affected by the chemical environment of the ion, making XPS useful to identify not only the ion, but also its oxidation state. As shown in Figure 3.8, when considering the kinetic energy of an ejected electron the combined spectrometer/sample work function (ϕ_{sp}) should be taken into account. This working function is an instrument dependent factor (normally derived as part of a calibration procedure) and defines the minimum amount of energy needed to move an electron from the Fermi energy level (at which E_{kin} =0) into vacuum. Therefore, Eq. (3.7) can be rewritten as Eq. 3.8, which defines the kinetic energy measured by the analyser:

$$E_{kin} = h\nu - E_b - \phi_{sp} \tag{3.8}$$

The escape depth of ejected electrons is < 5-10 nm and XPS can be considered as a surface analysis technique, although depth profiling analysis (measure of the elemental composition as a function of depth) of a material is also feasible by ion beam etching, or by tilting the specimen (angle resolved XPS).

In order to prepare TNTs-based samples for the XPS measurements, a powder of sample was collected into a mould and pressed with a pressure of 0.5 MPa to give pellets with diameter of 0.6 mm and thickness of about 0.1-0.3 mm. In this work, the X-ray photoelectron spectroscopy (XPS: AXIS LUTRA^{DLD}, Kratos analytical, Manchester, U. K.) was also performed to determine the percentage of oxygen deficient regions and valence state of Fe, Co, Ti, and Na in the TNTs-based samples. All binding energies have been corrected for the charging effect with reference to the C 1s line at 284.6 eV.

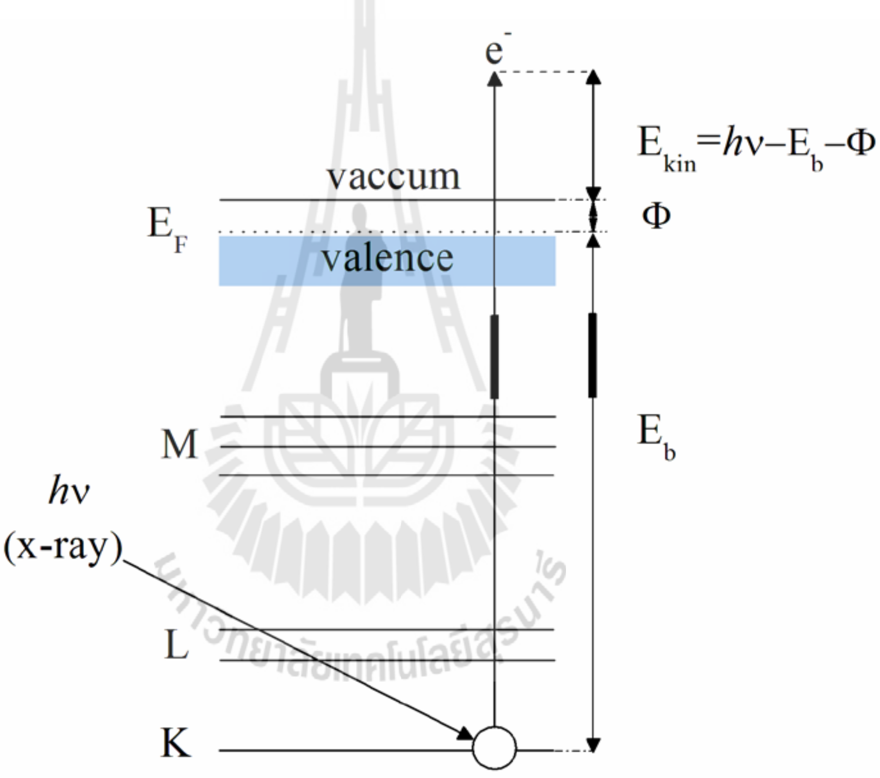

Figure 3.8 The kinetic energy of the core electron ejected following interaction with an X-ray beam depends on the energy of the X-ray beam, the binding energy of the electron and the work function of the specimen/spectrometer employed (Adapted from Leng (2008)).

3.2.9 X-ray absorption near-edge spectroscopy (XANES)

X-ray Absorption Spectroscopy (XAS) is the measurement of transitions from core electronic state of the metal to the excited electronic states and the continuum. It is broken into 2 regimes consist of X-ray absorption near-edge spectroscopy (XANES) and extended X-ray absorption fine-structure (EXAFS), which contain related but slightly different information about an element's local coordination and chemical state. An x-ray is absorbed by an atom when the energy of the X-ray is transferred to a core-level electron (K, L, or M shell) which is ejected from the atom. The atom is left in an excited state with an empty electronic level (a core hole). Any excess energy from the X-ray is given to the ejected photo-electron (Figure 3.9(a)). XAS measures the energy dependence of the X-ray absorption coefficient $\mu(E)$ at and above the absorption edge of a selected element. $\mu(E)$ can be measured two ways. First way is Transmission mode (see Eq. (3.9)). The absorption is measured directly by measuring what is transmitted through the sample. Second way is Fluorescence mode (see Eq. (3.10)). The re-filling the deep core hole is detected. Typically the fluorescent X-ray is measured (Figure 3.9(b)).

$$\mu(E)t = -\ln(I / I_0) \tag{3.9}$$

$$\mu(E)\alpha I_f / I_0 \tag{3.10}$$

where I_0 is the X-ray intensity hitting, I is the intensity transmitted, $\mu(E)$ is absorption coefficient, and t is a material of thickness. The Ti *K*-edge and Fe and Co *K* edge were determined using XANES in transmission mode at the BL5 Station at Siam Photon

Laboratory (Synchrotron Light Research Institute (Public Organization), SLRI) in Nakhon Ratchasima, Thailand.

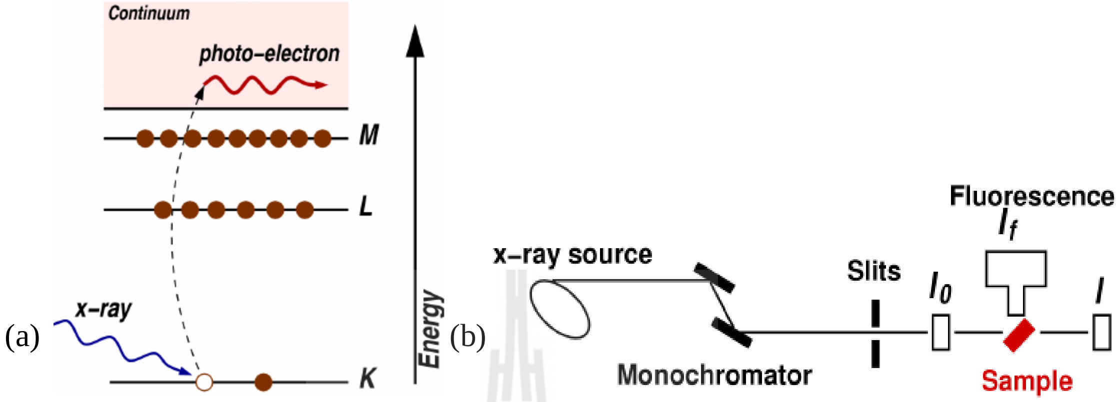

Figure 3.9 (a) Schematic diagram of the XAS (b) Schematic measured of the XANES (Newville, 2008).

3.2.10 Vibrating sample magnetometer (VSM)

A vibrating sample magnetrometer is an instrument used for measuring the magnetic behavior of magnetic materials. The VSM technique gives the magnetization (*M*) value at different magnetic field (*H*) providing a *M-H* hysteresis curve. The VSM works on Faraday's law of induction. A VSM operates by first placing the sample to be the studied in a constant magnetic field. If the sample is magnetic, this constant magnetic field will magnetize the sample by aligning the magnetic domains, or the individual magnetic spins, with the field. The stronger the constant field, the larger the magnetization will be. The magnetic dipole moment of the sample will create a magnetic field around the sample, sometimes called the magnetic stray field. As the sample is moved up and down, this magnetic stray field is changing as a function of time and can be sensed by a set of pick-up coils according to Faraday’ s law of induction. This current will be proportional to the magnetization of the sample.

In order to prepare TNTs-based samples for the VSM measurements, a powder of sample was weighed and transferred into a small sample holder. In this study, a vibrating sample megnetrometer (VSM 7403, Lake Shore, USA) was used to measure the magnetic properties of the TNTs-based samples at room temperature by varying the magnetizing field of ±10 kOe.

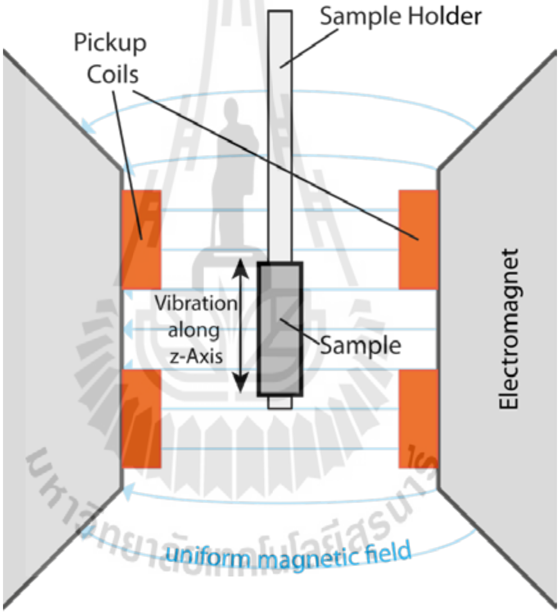

Figure 3.10 Schematic diagram of the vibrating sample magnetrometer (VSM) (https://en.wikipedia.org/wiki/Vibrating_ sample_magnetometer).

3.3 Electrical properties measurement

3.3.1 Dielectric properties measurement

The TNTs-based samples were collected into a mould and pressed with a pressure of 3 MPa to give pellets with diameter of 10 mm and thickness of about 1-

1.3 mm. For the dielectric and related electrical measurements, the both sides of the pellets were coated with silver pain-based conductive electrodes and then dried at 70 °C for 5 min. The dielectric and electrical response of the samples were measured using Agilent 4294A Precision impedance analyzer over a wide range of frequency (10^2-10^6 Hz) and temperature (-50 to 180 °C) at oscillation voltage of 0.5 V. Each measuring was kept constant with an accuracy of ±1 °C.

In addition, the dielectric properties of undoped TNTs and TM-doped TNTs samples were investigated as a function of dc bias under 0, 2.5, 5, 7.5 and 10 V at over a wide range of frequency (10^2-10^6 Hz) and room temperature.

The flowchart diagram showing the measurement procedure of bulk samples was illustrated in Figure 3.12. From the measurements, the value of C_p and tanδ at various frequency and temperature were obtained. The dielectric constant (ε') and dielectric loss (ε'') of the samples were calculated from the relations:

$$\varepsilon' = \frac{C_p d}{\varepsilon_0 A}, \tag{3.11}$$

$$\tan\delta = \frac{\varepsilon'}{\varepsilon''}, \tag{3.12}$$

where C_p is the measured capacitance (Farad, F), ε_0 is the permittivity of free space (8.854×10^{-12} F/m), A is the electrode area (m^2), and d is the thickness of the sample (m). The general term of the dielectric can be denoted by a complex dielectric constant

$$\varepsilon^* = \varepsilon' - j\varepsilon'' \tag{3.13}$$

In this thesis, the impedance spectroscopy has been used for probing the relaxation processes during the charge transport within the electronic ceramics. The impedance, Z^*, is given by:

$$Z^* = \frac{1}{i\omega C_0 \varepsilon^*} \tag{3.12}$$

where ω is the angular frequency $\omega = 2\pi f$ and $C_0 = \varepsilon_0 A/d$ is the empty cell capacitance.

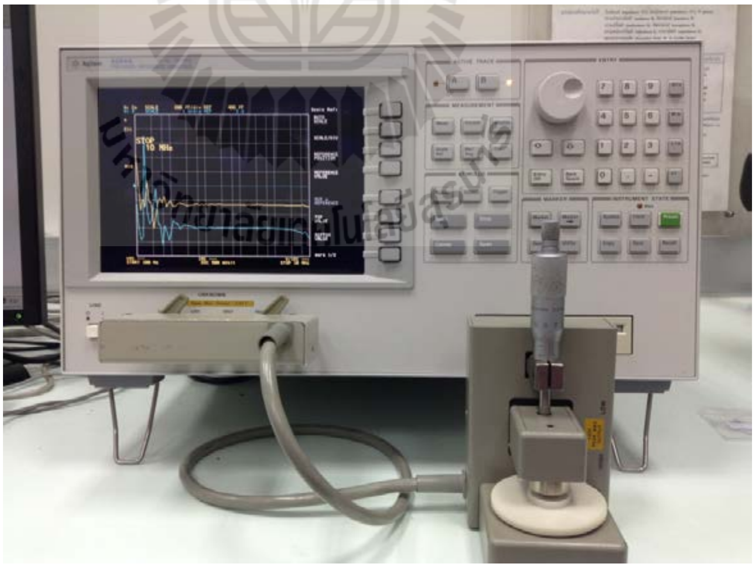

Figure 3.11 Agilent 4294A Precision impedance analyzer at National Metal and Materials Technology Center (MTEC).

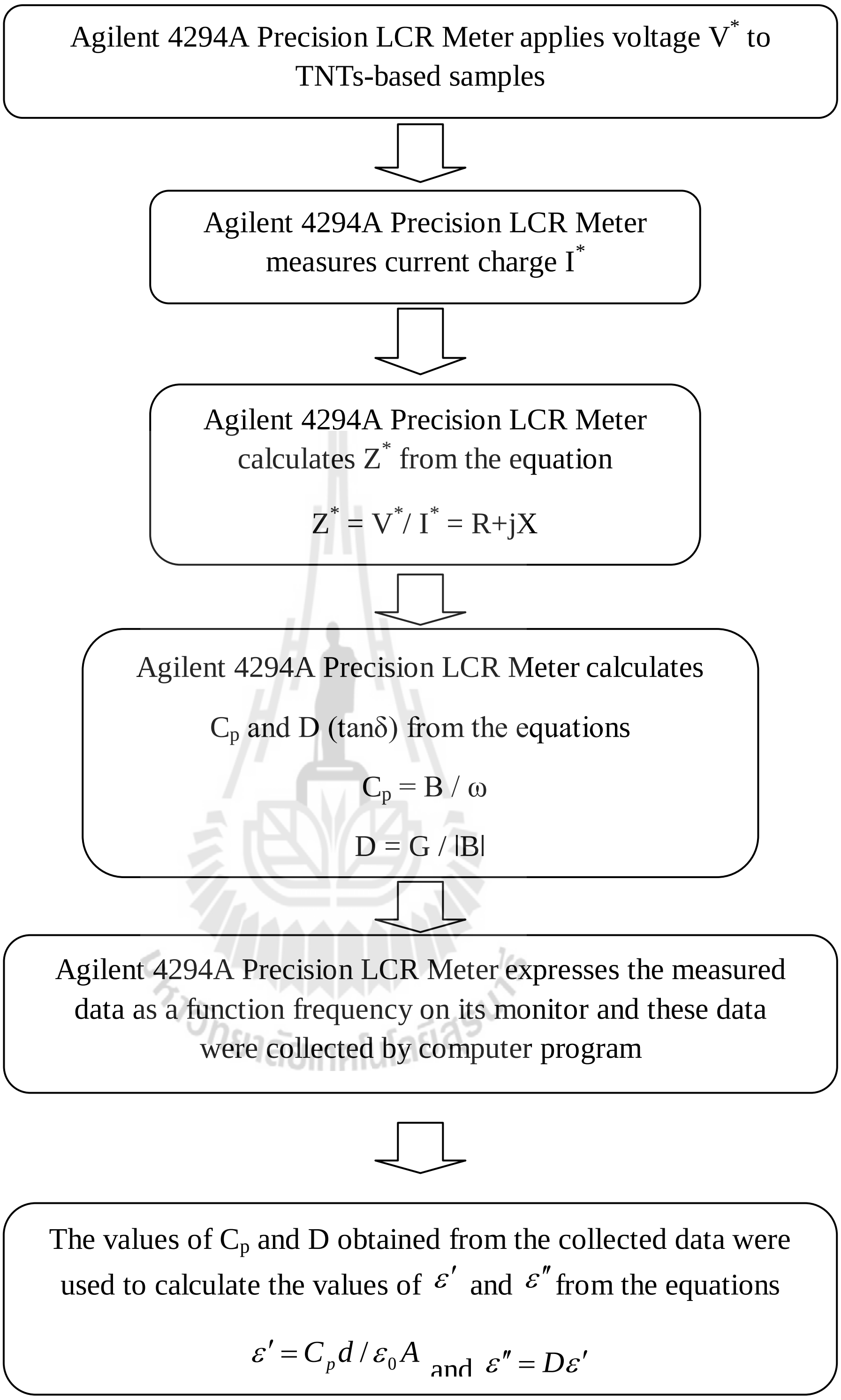

Figure 3.12 Schematic diagram of measuring dielectric parameters of the bulk TNTs-based samples using Agilent 4294A Precision impedance analyzer (MTEC).

3.3.2 Non-linear properties measurment

The current voltage (*I-V* or *J-E*) characteristic were measured atvarious temperatures by using a high voltage measurement unit (Keithley Model 247). The two most important parameters related to the non-Ohmic properties, i.e., nonlinear coefficient (α) and breakdown field (E_b), of the bulk TNTs sample can be calculated from these curves. The breakdown electric field (E_b) was obtained at J = 1 mA cm^{-2}. The non linear coefficient (α) values were calculated over the range of J = 1-10 mA cm^{-2}. The non linear coefficient (α) values were calculated from the following formula (Xue *et al.*, 2015; Thongbai *et al.*, 2012):

$$\alpha = \frac{\log(J_2 / J_1)}{\log(E_2 / E_1)} \tag{3.13}$$

where E_1 and E_2 are the voltage at current values of J_1 = 1 mA and J_2 = 1 mA, respectively.

The electric conduction in the pre-breakdown region is dominated by thermionic emission of Schottky type. The emission is related to electric field and temperature. Therefore, the electric current density (J) and electric field (E) will follow the relationship (Xue *et al.*, 2015)

$$\ln J = \frac{\beta E^{1/2}}{k_B} + \left[\ln AT^2 - \frac{\Phi_B}{k_B T} \right] \tag{3.14}$$

In Eq. (3.14) is then expressed as:

$$\ln J_0 = \ln AT^2 - \frac{\Phi_B}{k_B T} \tag{3.15}$$

where Φ_B is the Schottky potential-energy barrier height, A is the Richardson’s constant, k_B is the Boltzmann constant, T is the temperature (K), and β is a constant related to the potential barrier width. Values of $\ln J_0$ at various temperature were calculated from the plots of $\ln J$ versus $E^{1/2}$ by linearly fitting data at $E = 0$. J_0 is the extrapolated value to $E = 0$.

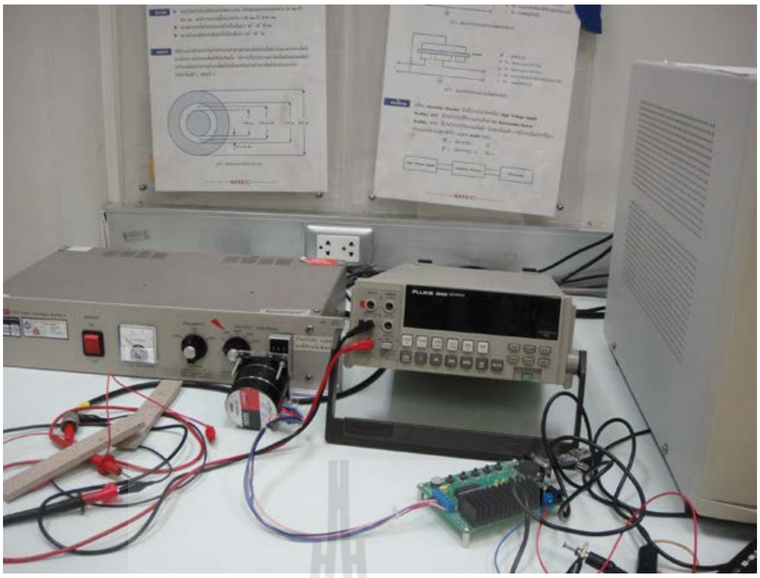

Figure 3.13 High voltage measurement unit (Keithley Model 247) at National Metal and Materials Technology Center (MTEC).

CHAPTER IV

RESULTS AND DISCUSSION

This chapter presents the experimental results and discussion for TNTs and Fe/Co doped-TNTs samples which consist of two parts. The first part is the characterization of the hydrothermal prepared TNTs and TM-doped TNTs using XRD, TEM, HRTEM, FTIR, UV-Vis, VSM, XPS and XANES. The second part describes the dielectric and electrical properties of the bulk samples. To understand the physical nature of the observed dielectric and electrical results in the TNTs samples, several dielectric and electrical models are used to explain the dielectric relaxation behavior. In addition, the effect of TM-doping on the dielectric and electrical properties of TNTs have been also investigated. Finally, the origin of the dielectric behavior of the TNTs and TM-doped TNTs sample are discussed.

4.1 The phase formation of the TNTs and Fe/Co-doped TNTs

The structure and phase composition of the samples were investigated by XRD measurements. Figure 4.1 shows the XRD patterns of the undoped TNTs and Fe/Co-doped TNTs prepared by hydrothermal at 130 °C for 24 h. The diffraction peaks of all sample corresponding (001), (110), (310), (203), $(11\bar{3})$ and (114) of the standard data (JCPDS: 4705-61; trititanate ($A_2Ti_3O_7$, A= Na or H) (Hu *et al.*, 2009). No possible impurity phases such as TiO_2, FeO, Fe_2O_3, Fe_3O_4, Co, CoO or Co_3O_4 were detected in the XRD patterns of Fe/Co-doped TNTs.

The average crystallite size (*D*) of all the samples was determined by the Debye-Scherrer equation (Inturi *et al.*, 2014; Noipa *et al.*, 2014)

$$D = \frac{0.9\lambda}{\beta \cos\theta} \tag{4.1}$$

where λ is the wave length of X-ray (0.154 nm), θ is the Bragg angle of X-ray diffractions, β is the FWHM (full width at haft maximum) for the corresponding peak. The average crystallite sizes were calculated from (001), (110), (130) and (114) planes as shown in Table 4.1. For Fe-doped TNTs, as the dopant concentration was increased, the peak intensity decreased. This is possibly due to replacement of the smaller Ti^{4+} ions (0.68 Å) by Fe^{3+} ions (0.64 Å) or Fe^{2+} ions (0.82 Å) or Co^{2+} ions (0.82 Å) or Co^{2+} ions (0.61 Å) into the TNTs lattice (Yuan *et al.*, 2013). It is known that Fe^{3+} (0.64 Å) and Ti^{4+} (0.68 Å) have almost similar ionic radius. Therefore, it was possible that Fe^{3+} could diffuse through 0.77 Å channels along the c-axis to substitute Ti^{4+} in the TNTs lattice (Pang and Abdullah, 2012). Consequently, crystal lattice deformation occurred which resulted in a decrease in the crystallite size as suggested by the broadening peak and decreasing peak intensity.

Table 4.1 Summary of crystallite size of undoped and Fe/Co-doped TNTs prepared by hydrothermal method at 130 °C for 24 h.

Doping level	Crystallite size (nm)	
	Fe doping	Co doping
x=0	19.93±0.927	19.93±0.927
x=0.05	17.13±0.404	18.68±0.467
x=0.1	15.40±0.504	23.25±0.124
x=0.2	19.30±0.135	19.94±0.595
x=0.3	14.33±0.092	25.20±0.790
x=0.4	13.35±0.034	13.30±0.420

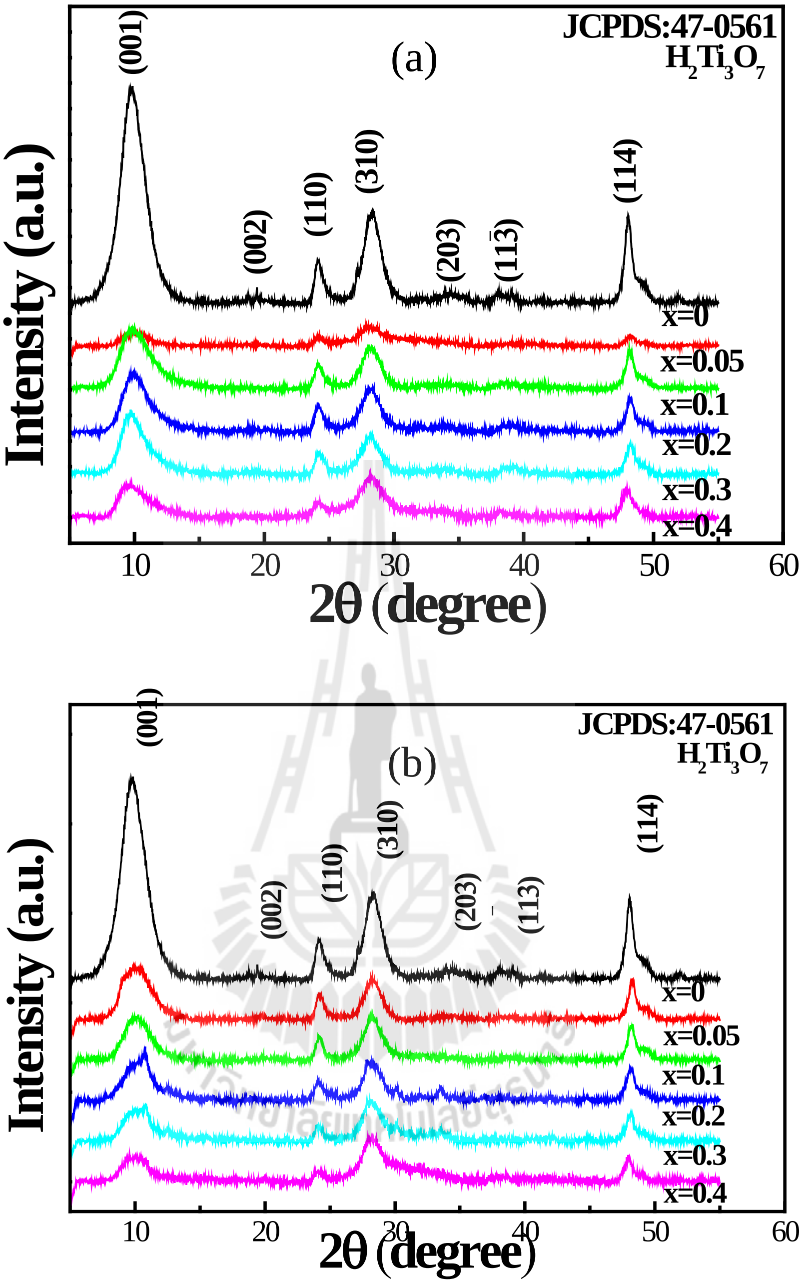

Figure 4.1 XRD patterns of $Na_{0.96}H_{1.04}Ti_3O_7 \cdot nH_2O$ and A_2 $(Ti_{3-x}Co_x)$/ A_2 $(Ti_{3-x}Co_x)$ $O_7 \cdot nH_2O$ ($A_2=Na_{0.036}$ $H_{1.964}$) powders with different concentration of (a) Fe-doped TNTs and (b) Co-doped TNTs prepared at 130 °C for 24 h.

4.2 The morphologies formations of undoped TNTs and Fe/Co-doped TNTs

The morphology and microstructure of undoped TNTs and Fe/Co-doped TNTs are investigated by transmission electron microscopy (TEM), High resolution TEM (HRTEM), selected area electron diffraction (SAED) and energy dispersive X-ray spectroscopy (EDX). Figures 4.2(a) - 4.12(a) shows the TEM bright file images of the prepared samples. It was revealed that all the samples compose of uniform nanotubes long cylinders having a hollow cavity positioned at their centre and lying along their length. The diameters of the nanotubes are of about 7-15 nm with lengths of several hundreds of nanometer or micrometer in scales. The wall involves multilayer about 3-4 layers. HRTEM micrographs present the distances between layers ~ 0.782-0.788 nm. In addition some nanotubes have solid nanowires inside the tubes; the diameter of these nanowires is approximately 0.37 nm. The unequal wall number on different sides of undoped TNTs and TM-doped TNTs concluded that they were formed through scrolling up the single layer sheet. These are good agreement with the standard data (JCPDS: 4705-61). The SAED patterns in Figures 4.2(c)-4.12(c) show spotty ring patterns, revealing their $H_2Ti_3O_7$ structure. These are consistent with those of (110), (003), (202) and (114) planes of XRD results. Moreover the chemical compositions of all the samples were characterized by an energy dispersive X-ray (EDX) spectroscopy. It was observed that the undoped TNTs sample consisted of Na, O and Ti as shown in Figure 4.2(d), for TM-doped TNTs samples consisted of Na, O, Ti, Co (Co-doped TNTs) and Fe (Fe-doped TNTs)(see in Figures 4.3(d)-4.12(d)). This result is good according with the FTIR results.

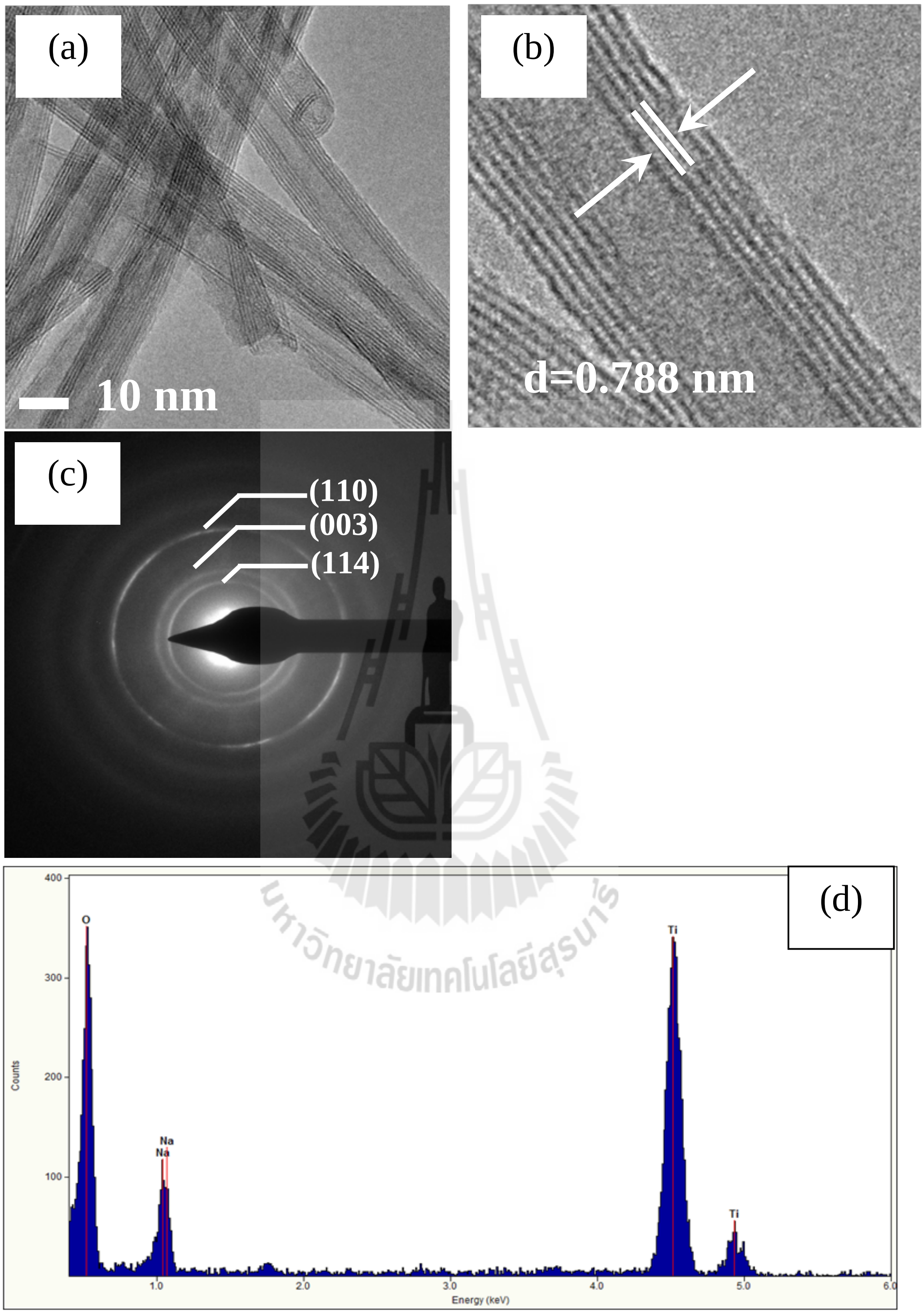

Figure 4.2 TEM images of undoped powder (a) bright-field images (b) lattice fringes from HRTEM (c) SAED patterns and (d) EDS spectrum of TNTs sample.

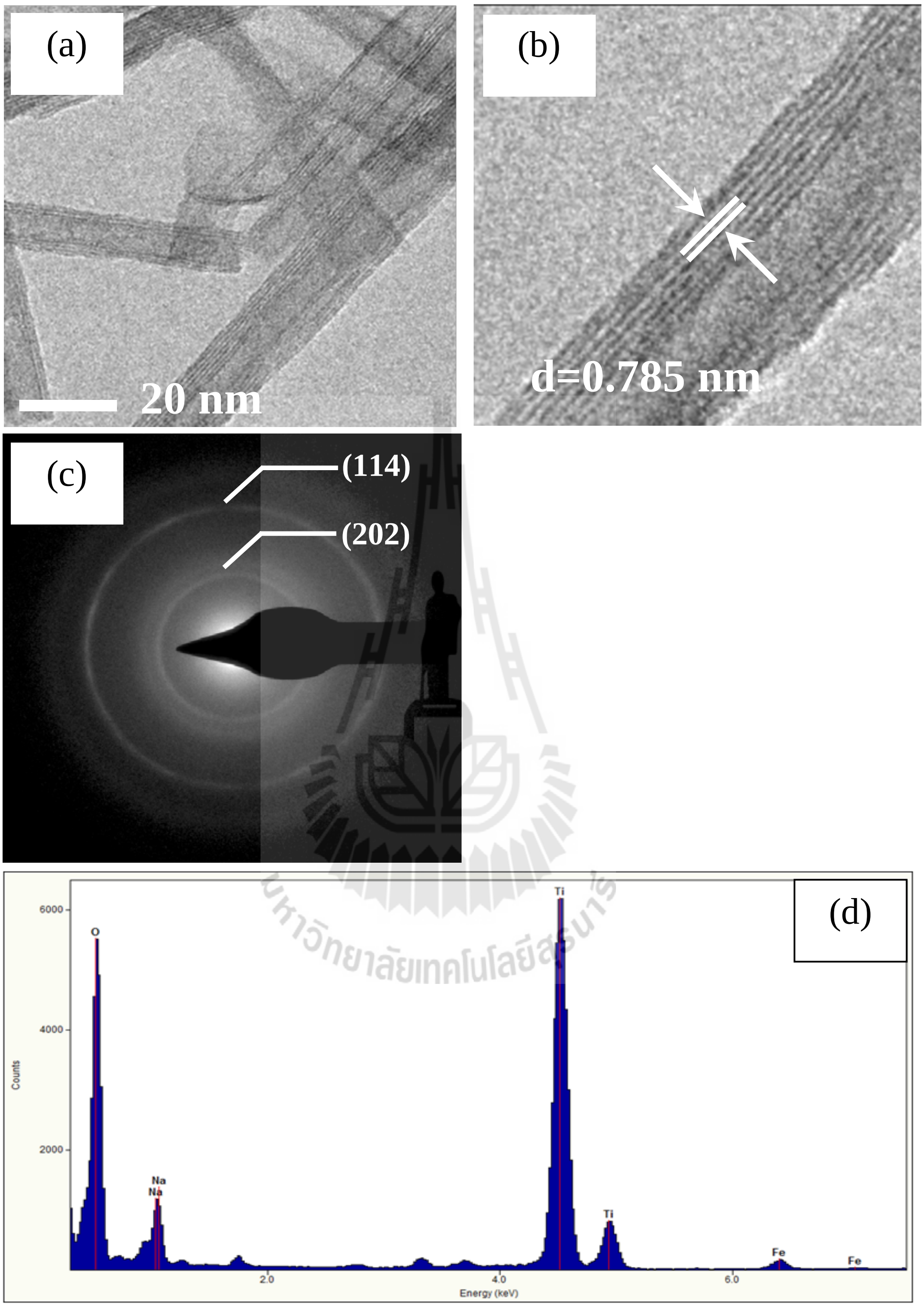

Figure 4.3 TEM images of Fe-doped TNTs (x=0.05) powder (a) bright-field images (b) lattice fringes from HRTEM (c) SAED patterns and (d) EDS spectrum of Fe-doped TNTs (x=0.05) sample.

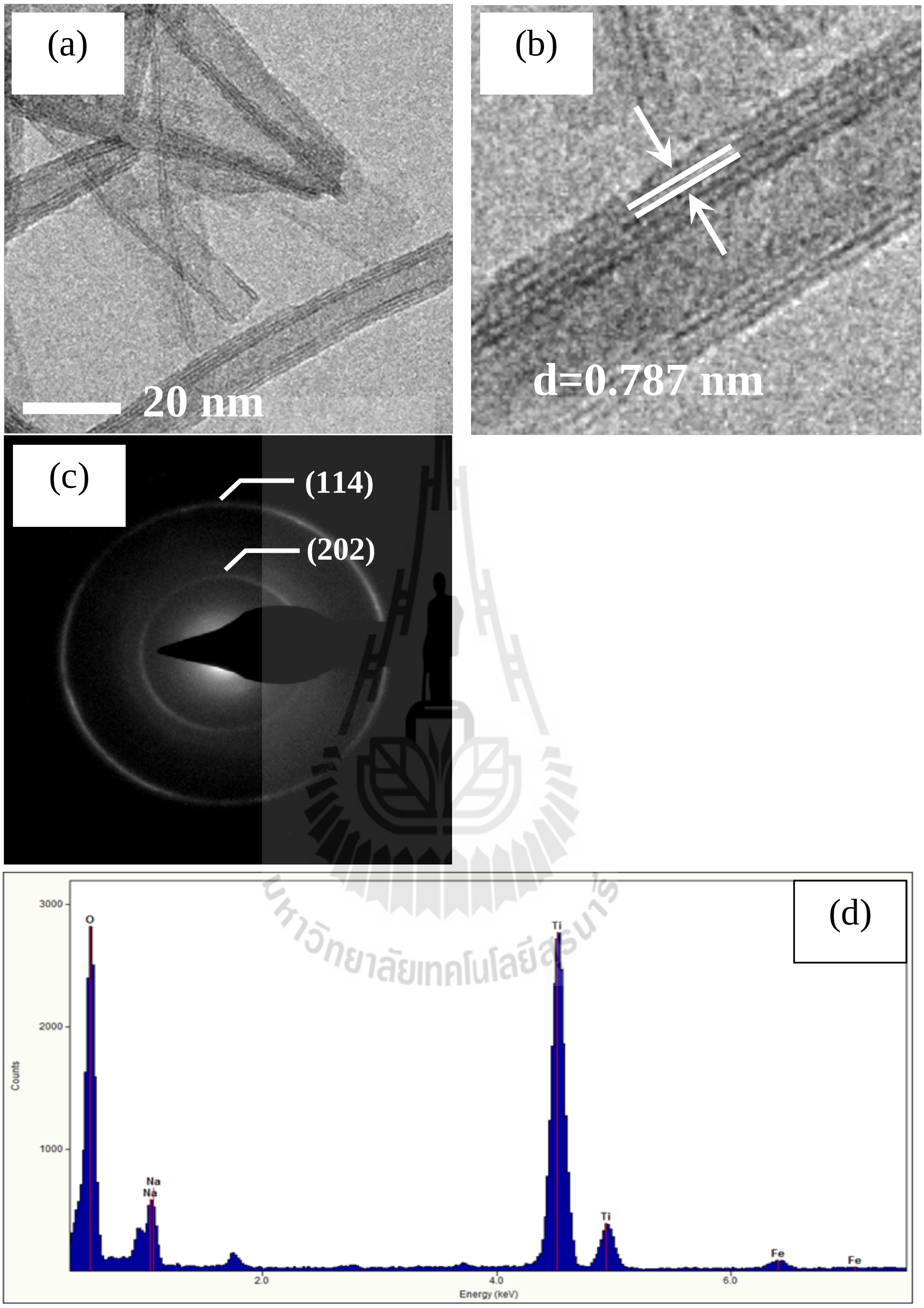

Figure 4.4 TEM images of Fe-doped TNTs (x=0.1) powder (a) bright-field images (b) lattice fringes from HRTEM (c) SAED patterns and (d) EDS spectrum of Fe-doped TNTs (x=0.1) sample.

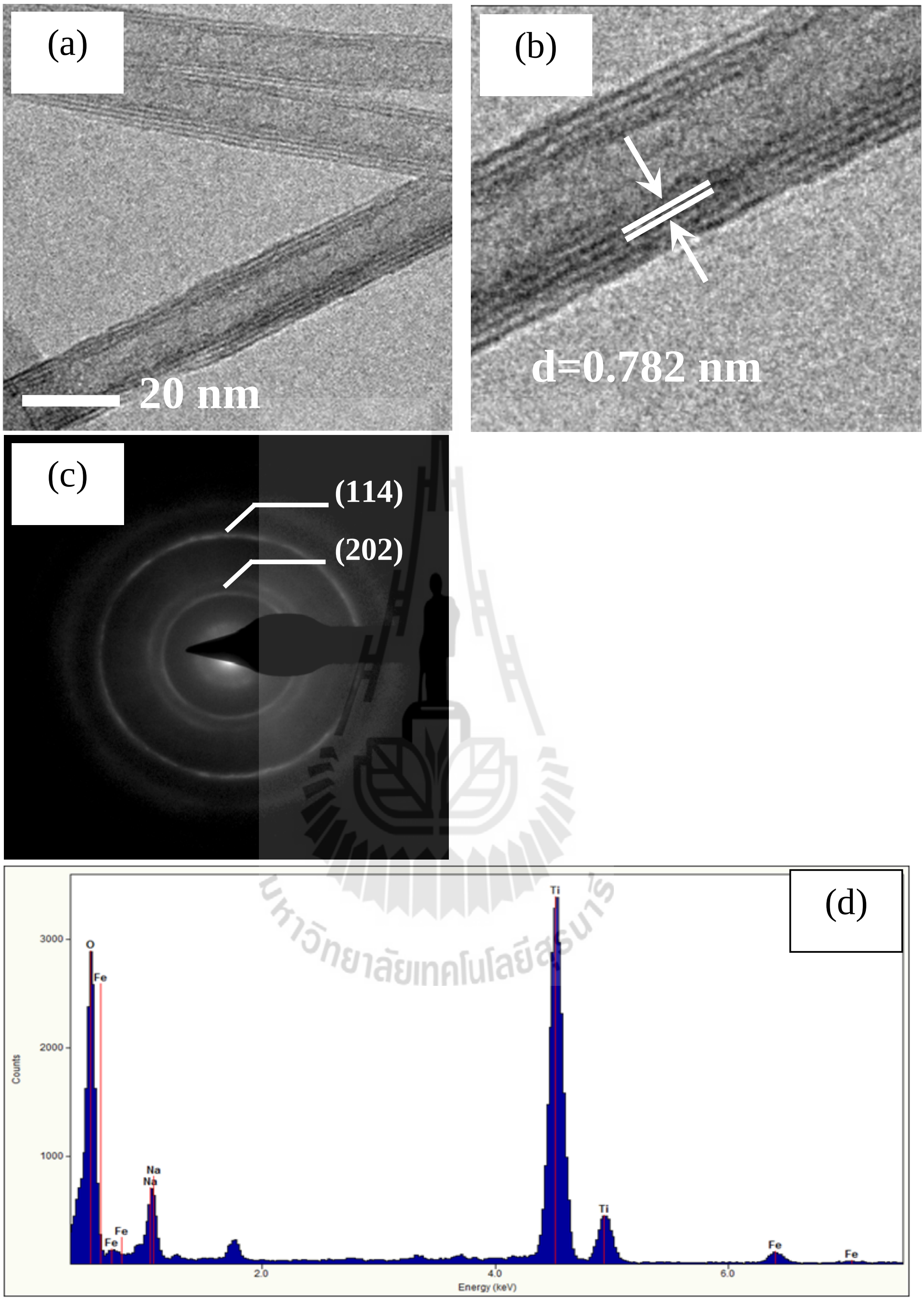

Figure 4.5 TEM images of Fe-doped TNTs (x=0.2) powder (a) bright-field images (b) lattice fringes from HRTEM (c) SAED patterns and (d) EDS spectrum of Fe-doped TNTs (x=0.2) sample.

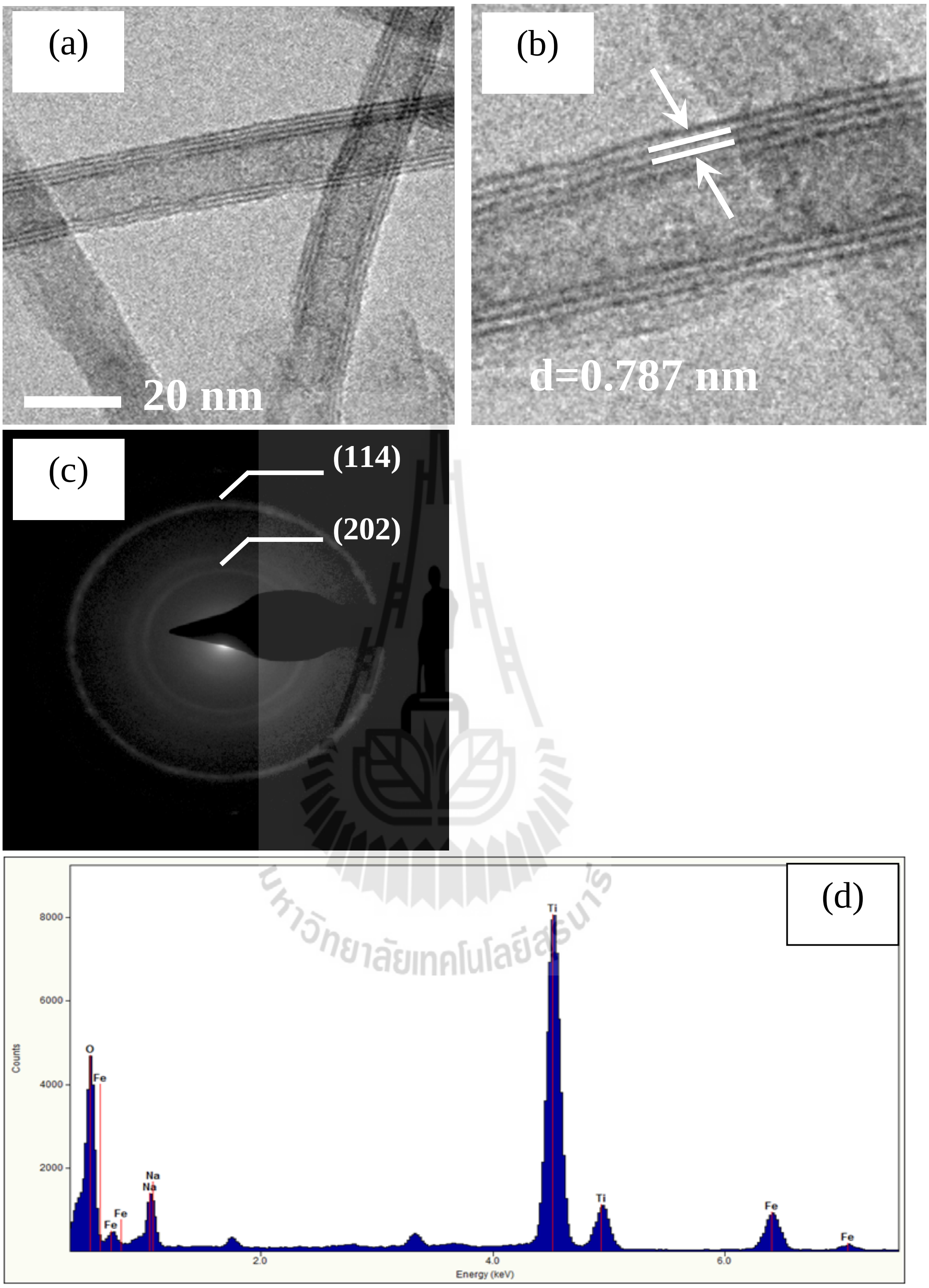

Figure 4.6 TEM images of Fe-doped TNTs (x=0.3) powder (a) bright-field images (b) lattice fringes from HRTEM (c) SAED patterns and (d) EDS spectrum of Fe-doped TNTs (x=0.3) sample.

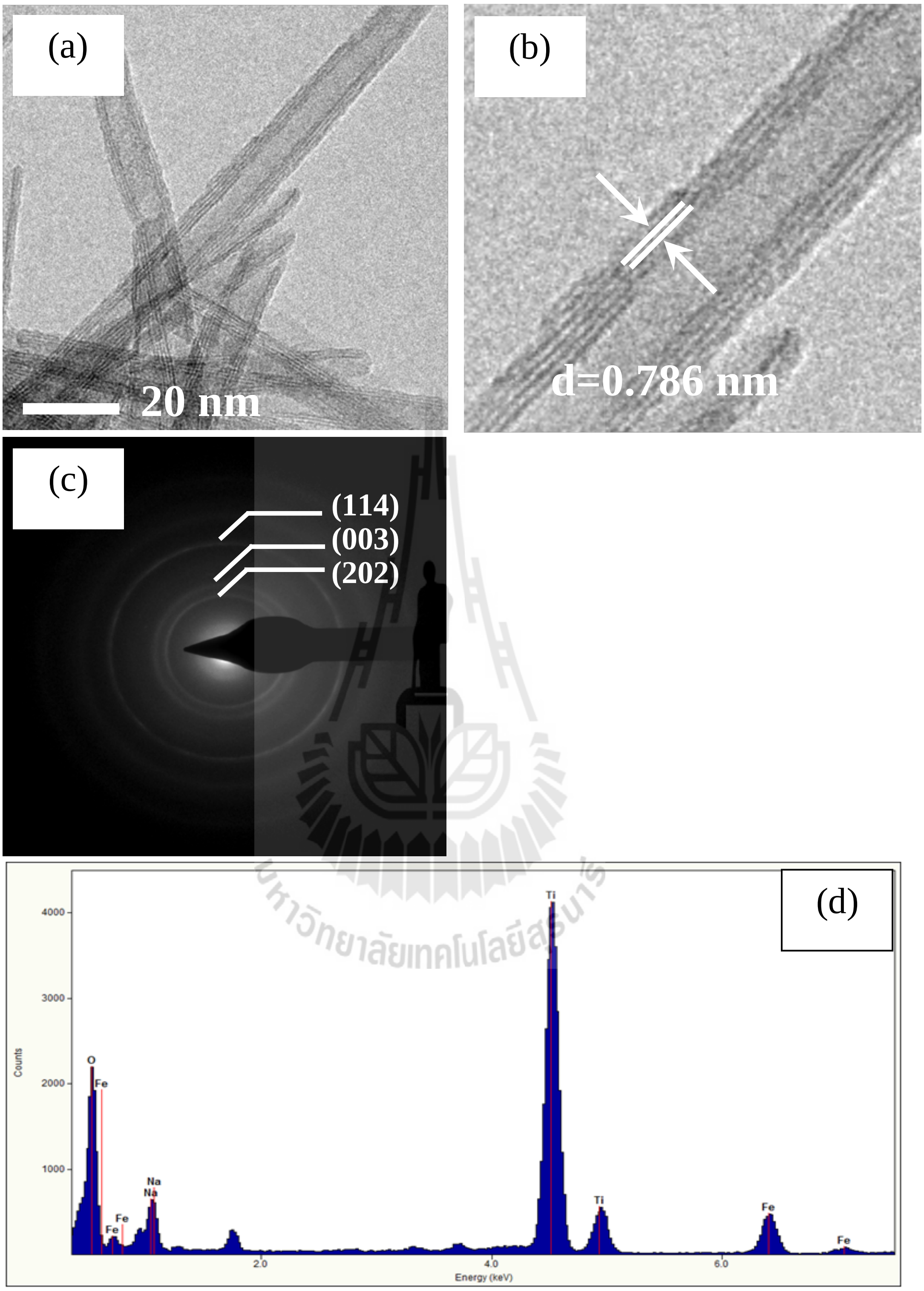

Figure 4.7 TEM images of Fe-doped TNTs (x=0.4) powder (a) bright-field images (b) lattice fringes from HRTEM (c) SAED patterns and (d) EDS spectrum of Fe-doped TNTs (x=0.4) sample.

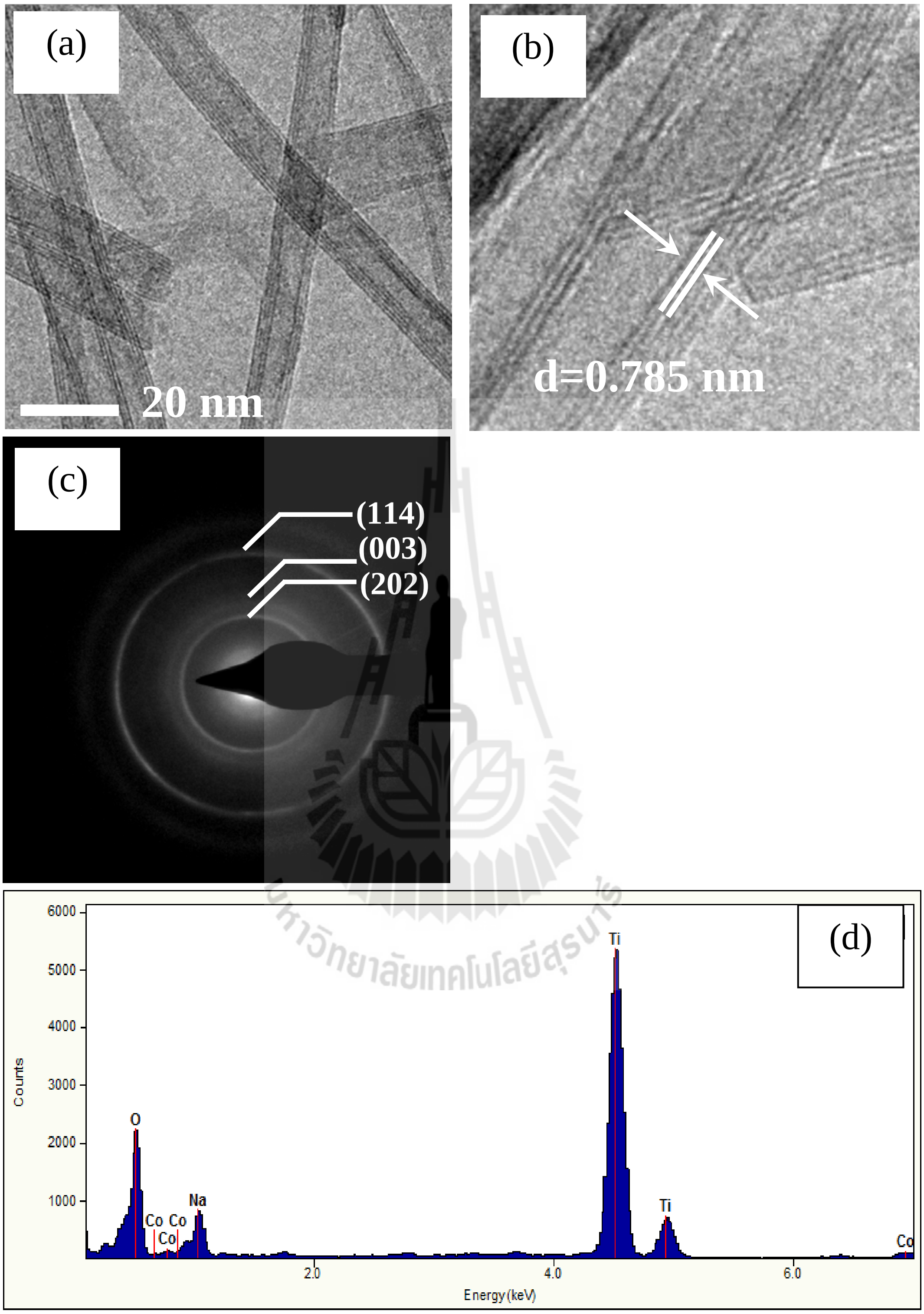

Figure 4.8 TEM images of Co-doped TNTs (x=0.05) powder (a) bright-field images (b) lattice fringes from HRTEM (c) SAED patterns and (d) EDS spectrum of Co-doped TNTs (x=0.05) sample.

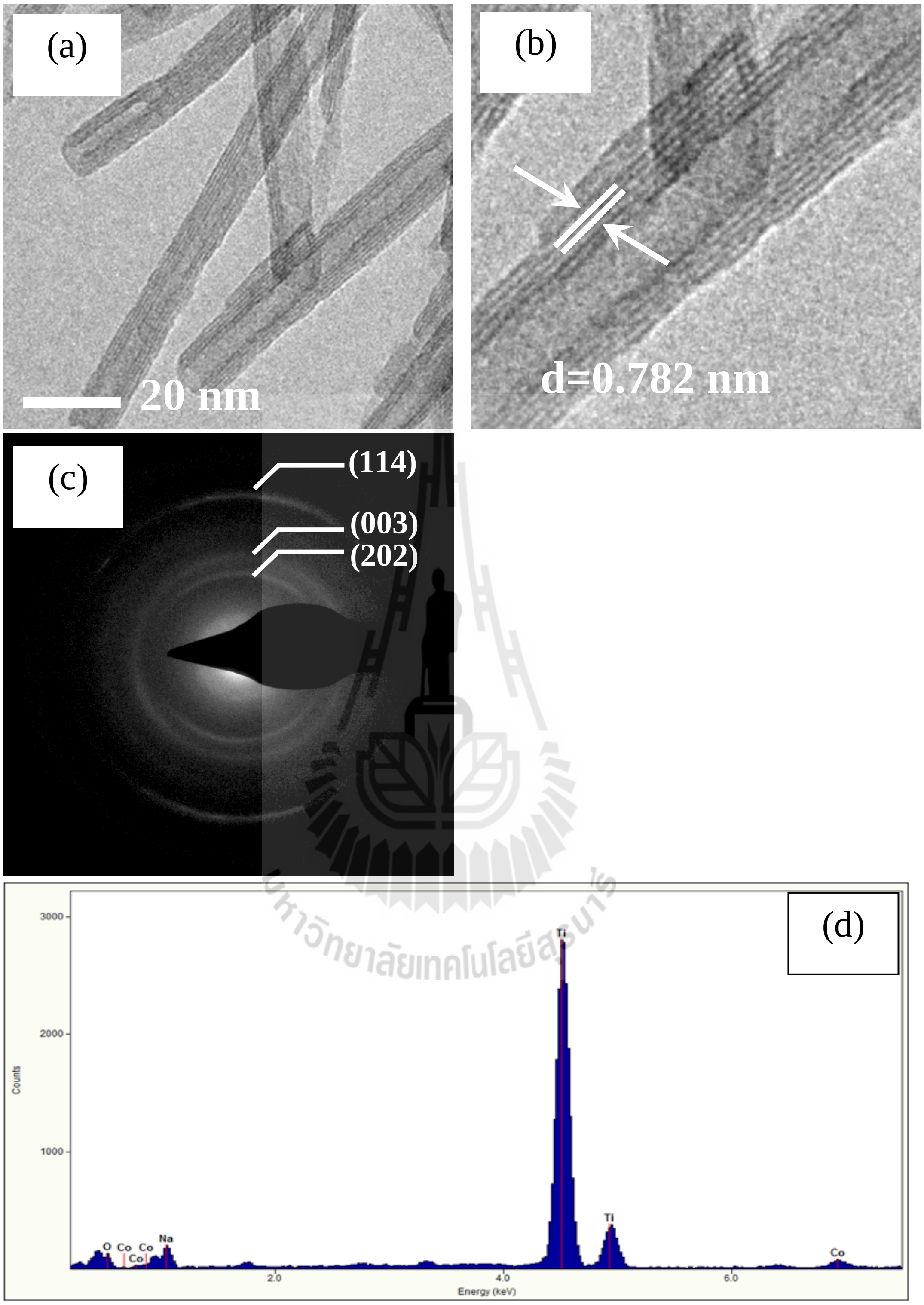

Figure 4.9 TEM images of Co-doped TNTs (x=0.1) powder (a) bright-field images (b) lattice fringes from HRTEM (c) SAED patterns and (d) EDS spectrum of Co-doped TNTs (x=0.1) sample.

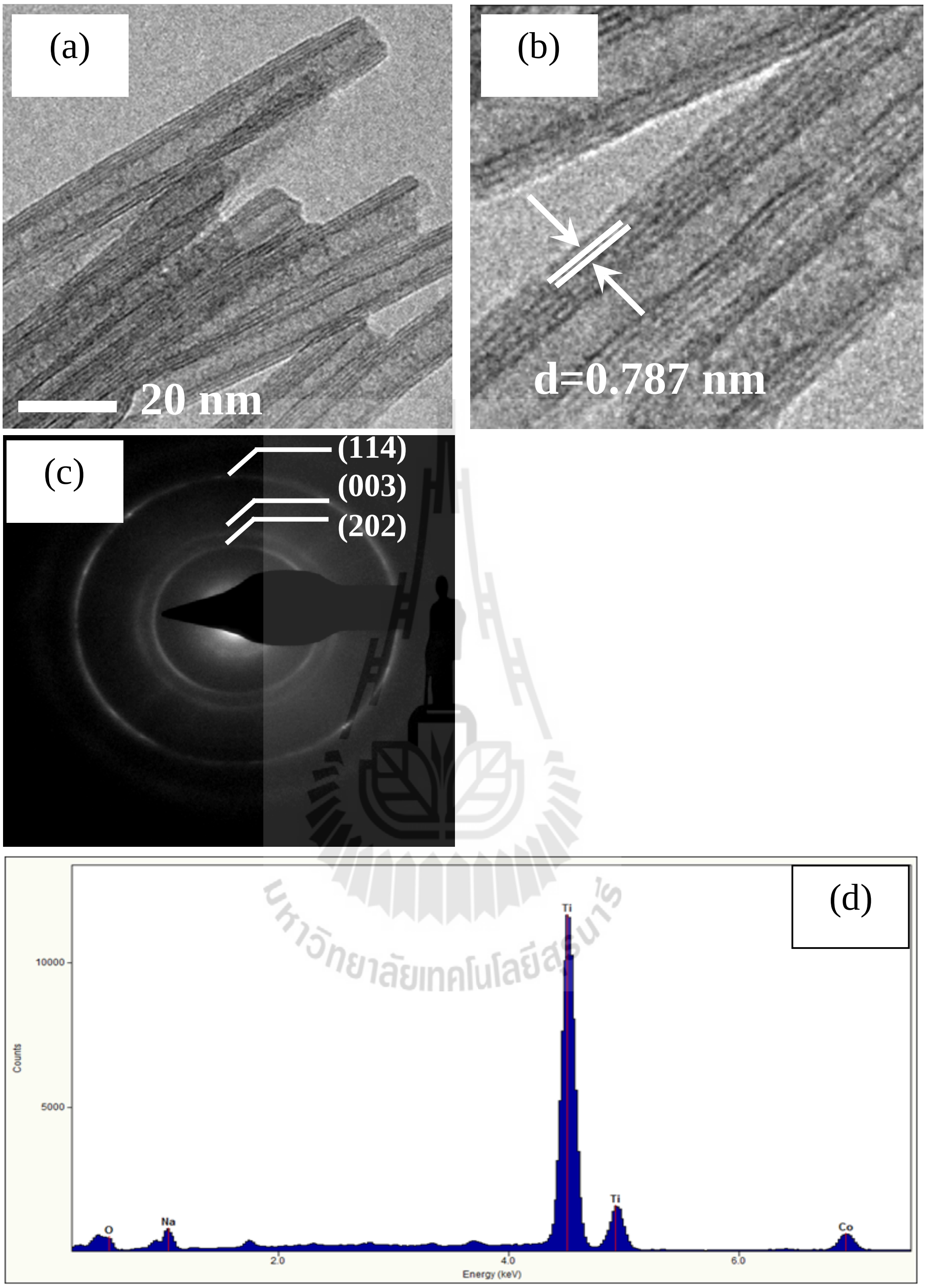

Figure 4.10 TEM images of Co-doped TNTs (x=0.2) powder (a) bright-field images (b) lattice fringes from HRTEM (c) SAED patterns and (d) EDS spectrum of Co-doped TNTs (x=0.2) sample.

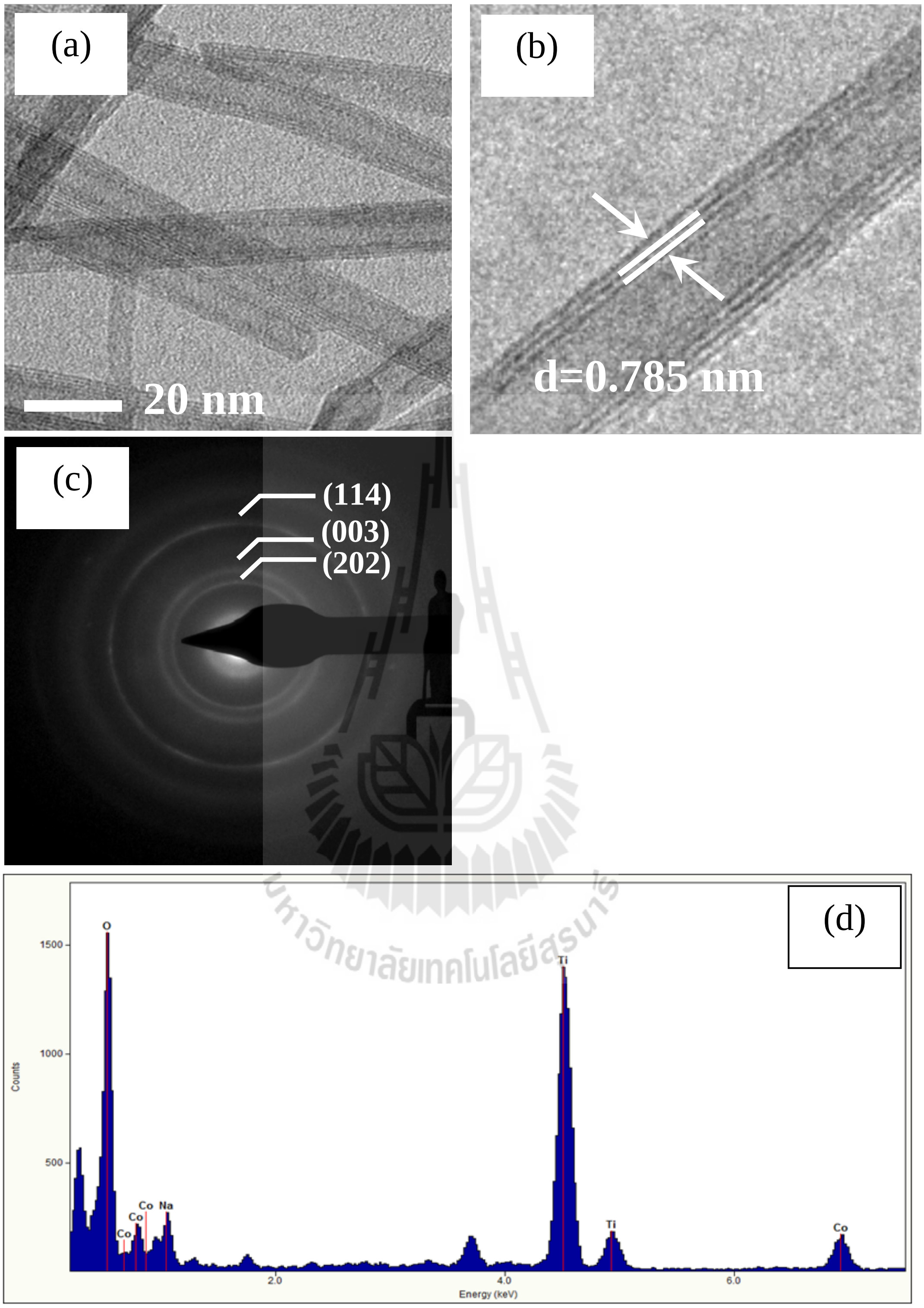

Figure 4.11 TEM images of Co-doped TNTs (x=0.3) powder (a) bright-field images (b) lattice fringes from HRTEM (c) SAED patterns and (d) EDS spectrum of Co-doped TNTs (x=0.3) sample.

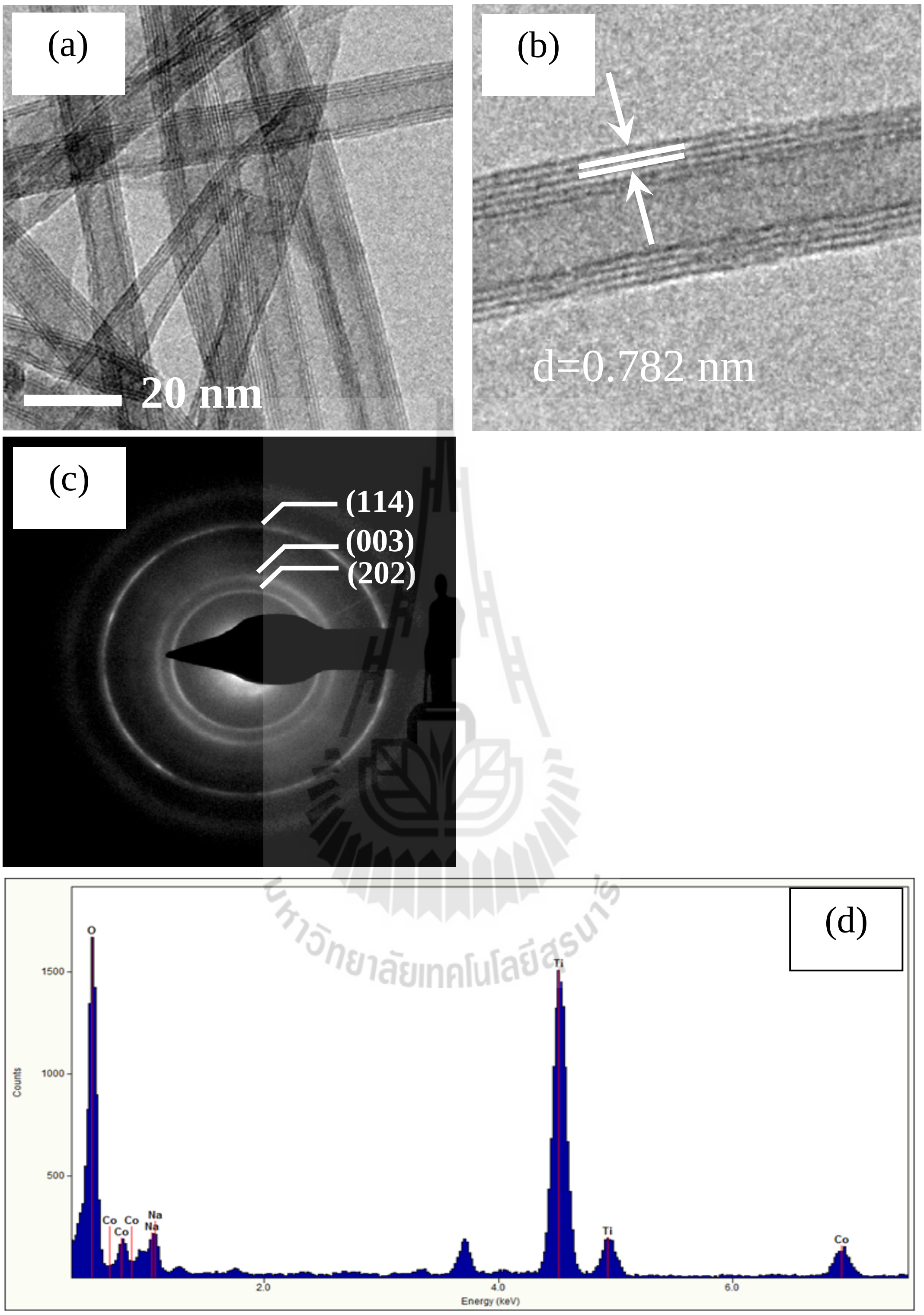

Figure 4.12 TEM images of Co-doped TNTs (x=0.4) powder (a) bright-field images (b) lattice fringes from HRTEM (c) SAED patterns and (d) EDS spectrum of Co-doped TNTs (x=0.4) sample.

Table 4.2 Summary of diameter size and the *d* spacing of undoped TNTs and Fe/ Co-doped TNTs prepared by hydrothermal method at 130 °C for 24 h.

Doping Level	Diameter size (nm)		*d* distances between layers (nm)	
	Fe doping	Co doping	Fe doping	Co doping
x=0	10.0±1.283	10.0±1.283	0.788	0.788
x=0.05	9.3±0.770	10.6±1.411	0.785	0.785
x=0.1	9.7±0.989	9.3±0.809	0.787	0.782
x=0.2	9.0±0.722	11.1±1.148	0.782	0.787
x=0.3	9.0±0.634	10.9±0.645	0.787	0.785
x=0.4	10.1±0.714	10.4±0.937	0.786	0.782

4.3 Thermal decomposition analysis of undoped TNTs

Thermal behavior of undoped TNTs sample was obtained by TG-DTA analysis. As indicated in Figure 4.13, when the temperature increased to 800 °C, undoped TNTs presented a total mass loss of 10.7 %, which the endothermic peak around 93 °C. This result is related to the losses of moisture and water within the TNTs. These weight loss and exothermic process that occur in the temperature range of 25 to 450 °C, are usually associated with the removal water. These observations confirm that the large amount of water molecules for undoped TNTs within the nanotubes. Therefore, majority of water molecules may form water nanotubes intercalated in the scrolled titanate nanotubes (Hu *et al.*, 2010).

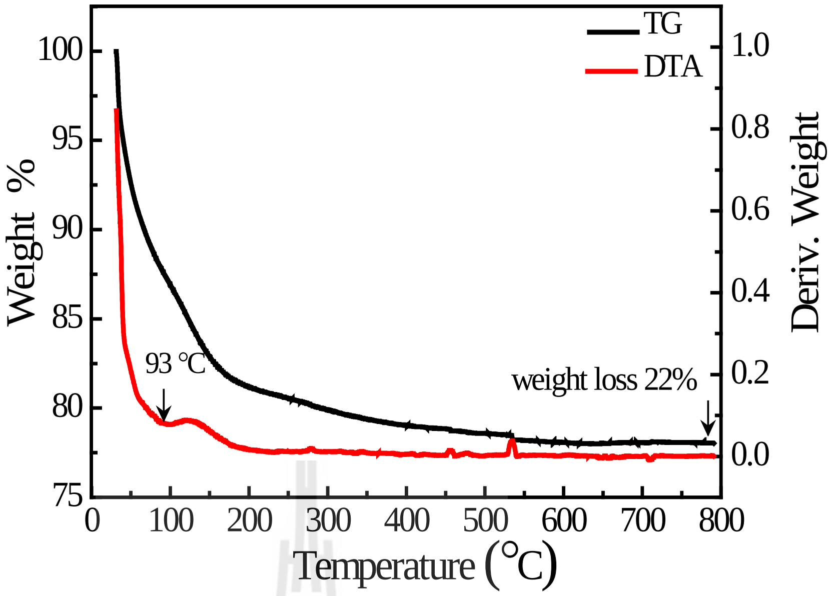

Figure 4.13 TG-DTA data of undoped TNTs prepared by hydrothermal method at 130 °C for 24 h.

4.4 The chemical state or electronic state of undoped TNTs and Fe/Co-doped TNTs

The chemical state or electronic state of the sample by using X-ray photoelectron spectroscopy (XPS). Figure 4.14(a) shows a typical XPS spectrum of TNTs prepared at 130 °C for 24 h. The spectrum shows the region of the Ti 2p signals. The peak at a binding energy of 458.29 eV and 464 eV can be attributed to the Ti^{4+} $2p_{3/2}$ state and Ti^{4+} $2p_{1/2}$, respectively. The nature of oxygen states in TNTs as shown in Figure 4.14(b). The spectra O 1*s* signals can be observed four peaks at 529.84, 531.33, 532.87 and 534.98 eV.

After the hydrothermal reactions, chemical compositions of undoped and Fe/Co-doped TNTs were calculated using the data from XPS analysis and listed in the

Tables 4.3 and 4.4. The data in Tables 4.3 and 4.4 indicates that all the samples are composed of Ti, Na, O, Co and Fe demonstrating an increase in actual Fe or Co concentration with the increase of nominal Fe or Co doping in TNTs. All binding energies have been corrected for the charging effect with reference to the C 1*s* line at 285 eV. The spectra show the region of Ti 2*p* signals [see in Figures 4.15(a) and 4.18(a)], the peak of Ti $2p_{3/2}$, Na 1*s* and O 1*s* appeared at 458.28-458.83 eV is oxidation state of Ti^{4+}, 1071.21-1071.72 eV, 529.84-530.39 eV (as shown in the Tables 4.3 and 4.4), respectively. The Ti 2*p*, Na 1*s* and O 1*s* binding energy of Fe-doped TNTs shift to higher energies. The spectra O 1*s* for x = 0.05 in Figures 4.16(d) and 4.19(d) can be consistently fitted by three nearly Gussian curve centers at about 530.14, 531.67 and 532.80 eV. The low binding energy centered at 530.14 eV is corresponding to Ti-O group on the structure of Fe/Co-doped TNTs. The medium binding energy located at 531.67 eV is attributed to O^{2-} ions in the oxygen deficient regions with in matrix of Fe/Co-doped TNTs. These results suggested that there are some oxygen vacancies in the nanotubes. The high binding energy located at 532.80 eV is attributed to -OH group. It is particularly interesting that the O 1*s* spectra of Fe-doped TNT have a small binding energy shift compared with that of undoped TNT. The results can be explained to an increase in the ionic state of the oxygen bond causing the binding energies of all electronic state of oxygen to shift.

The XPS spectra for irons species intercalated in to TNTs layer are shown in Figure 6. This peak shows that Fe existed in the Fe^{3+} and Fe^{2+}. For low Fe doping at x = 0.05 and 0.1 were expect responsible for the weak signals. The spectra Fe $2p_{3/2}$ of Fe-doped TNT in Figures 4.17(c)-(d) can be consistently fitted by three nearly Gussian curve centers at about 710.97-711.27 eV (Fe^{3+}), 708.67-709.27 eV (Fe^{2+}).

The shift in binding energy possible to that in Fe_2O_3 (710.8 eV) or FeO (709.4 eV) (Ram *et al.*, 2007) indicates the successful incorporation of Fe^{3+} or Fe^{2+} in the TNT lattice to form Ti–O–Fe bonds (Yuan *et al.*, 2013; Hung *et al.*, 2008). These the results indicate that Fe-doped TNTs samples are associated with of the mixture of Fe ions state (Fe^{3+} and Fe^{2+}).

The XPS spectra of Co 2*p* regions presented in Figure 4.20 show that all samples have four peaks: $2p_{3/2}$, $2p_{1/2}$ doublet. The obtained binding energies for Co $2p_{3/2}$(781.9 eV) and $2p_{1/2}$ (797.4 eV) are similar those reported for Co^{2+} ions in Co-O bonding with an energy difference between Co $2p_{3/2}$ and Co of $2p_{1/2}$ of 15.5 ± 0.1 eV (Shah *et al.*, 2009). The binding energies for Co $2p_{3/2}$ and Co of $2p_{1/2}$ are observed at 781.9 and 797 eV (x = 0.3). This indicates that the cobalt in Co-doped TNTs is present in Co^{2+} or Co^{3+} oxidation state. The XPS analysis thus implies that cobalt in the sample is in oxidized state and not in the form of cobalt metal. This was further confirmed by the absence of any detectable ferromagnetic signal in the sample.

Table 4.3 Summary of The binding energy and a atomic percentages of Fe 2p, energy shift and atomic percentages of Ti 2p, Na 1s and O 1s calculated by XPS spectra of undoped TNTs and Fe-doped TNTs.

Samples	Binding energy of Fe $2p_{3/2}$ (eV)		Atomic percentages of Fe	Energy shift ΔE (eV)	Atomic percentages		
	Fe^{3+}	Fe^{2+}			O 1s	Ti 2p	Na 1s
x = 0	-	-	-	-	50.98	14.22	17.44
x = 0.05	-	-	0.36	-	52.43	18.73	10.14
x = 0.1	-	-	0.66	-	53.13	19.00	10.36
x = 0.2	711.16	708.94	2.53	2.2	52.76	18.97	12.15
x = 0.3	711.27	709.27	2.61	2.0	53.38	18.76	11.88
x = 0.4	710.97	708.67	2.49	2.3	50.20	16.18	13.93

Table 4.4 Summary of The binding energy and a atomic percentages of Co 2p, energy shift and atomic percentages of Ti 2p, Na 1s and O 1s calculated by XPS spectra of undoped TNTs and Co-doped TNTs.

Samples	Binding energy of Co $2p_{3/2}$ (eV)		Atomic percentages of Co	Energy shift ΔE (eV)	Atomic percentages		
	Co^{3+}	Co^{2+}			O 1s	Ti 2p	Na 1s
x = 0	-	-	-	-	50.98	14.22	17.44
x = 0.05	-	-	-	-	55.64	18.10	13.89
x = 0.1	780.6	782.3	0.93	1.7	52.86	20.17	15.30
x = 0.2	780.5	782.2	2.01	1.7	51.77	17.36	16.91
x = 0.3	780.3	781.9	2.48	1.6	51.51	17.86	16.75
x = 0.4	780.2	782.0	3.00	1.8	52.14	16.44	17.03

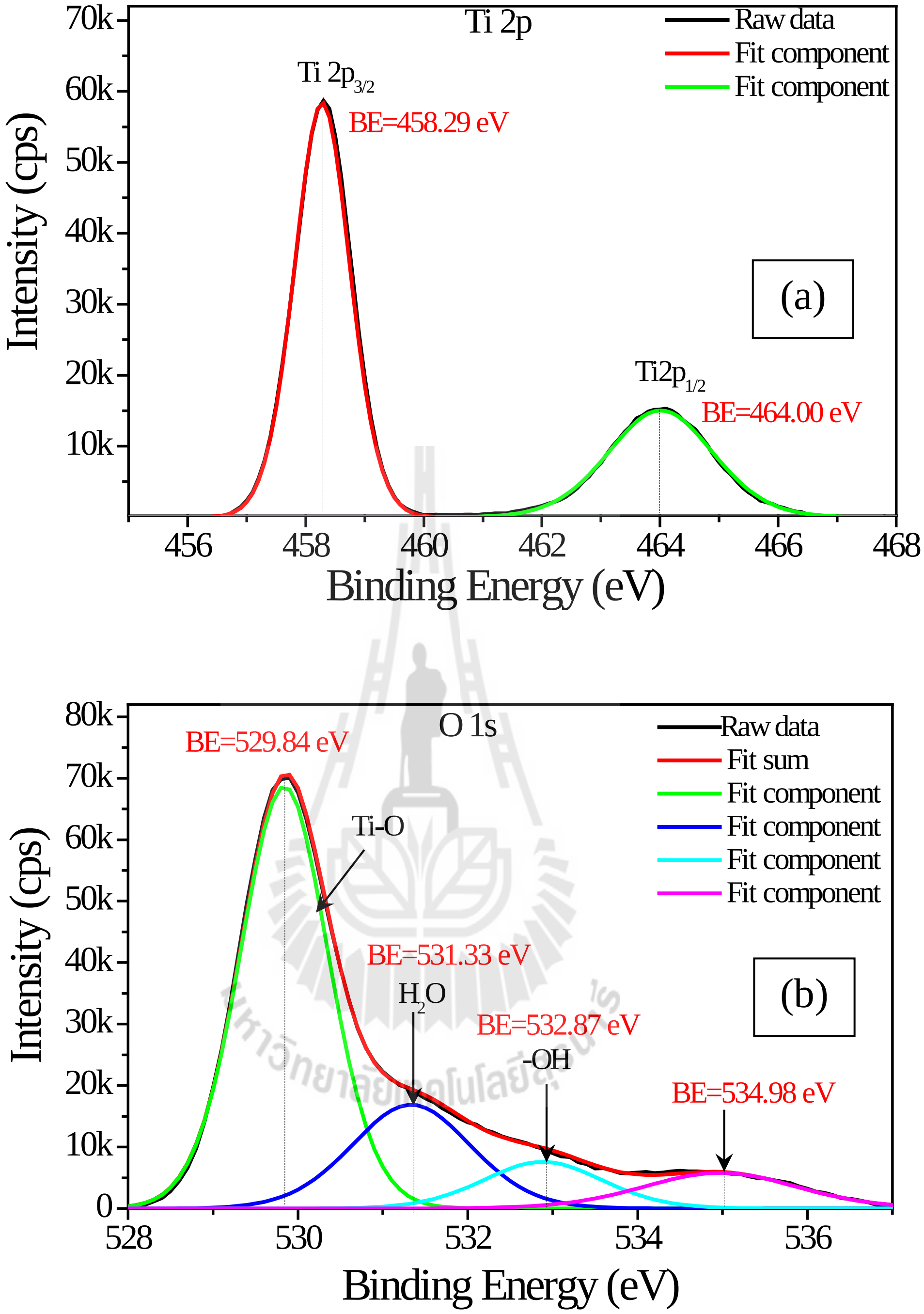

Figure 4.14 XPS integral spectra of TNTs sample (a) Ti 2*p* and (b) O 1*s*.

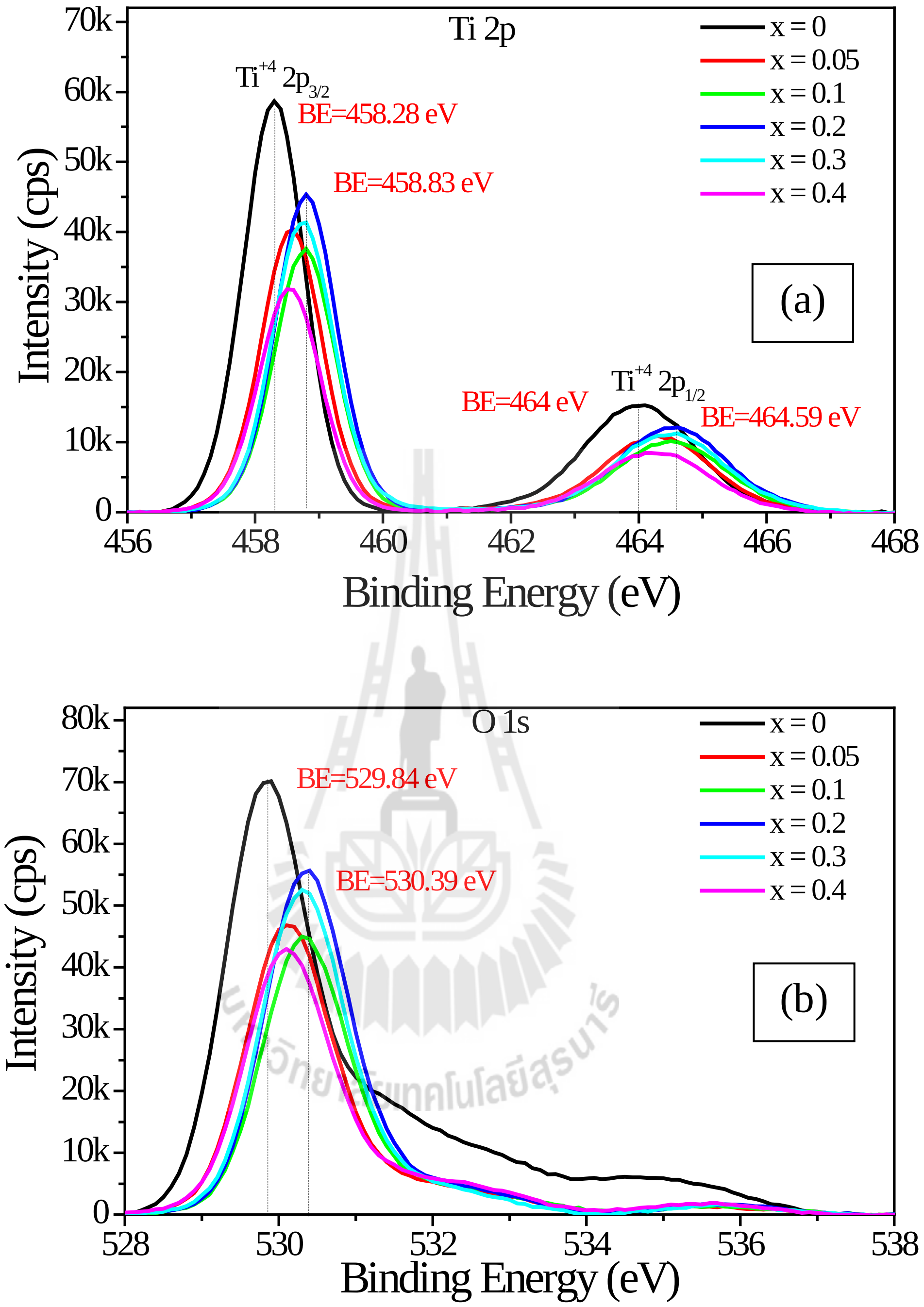

Figure 4.15 XPS integral spectra of undoped TNTs and Fe-doped TNTs samples (a) Ti 2*p*, (b) Na 1*s*.

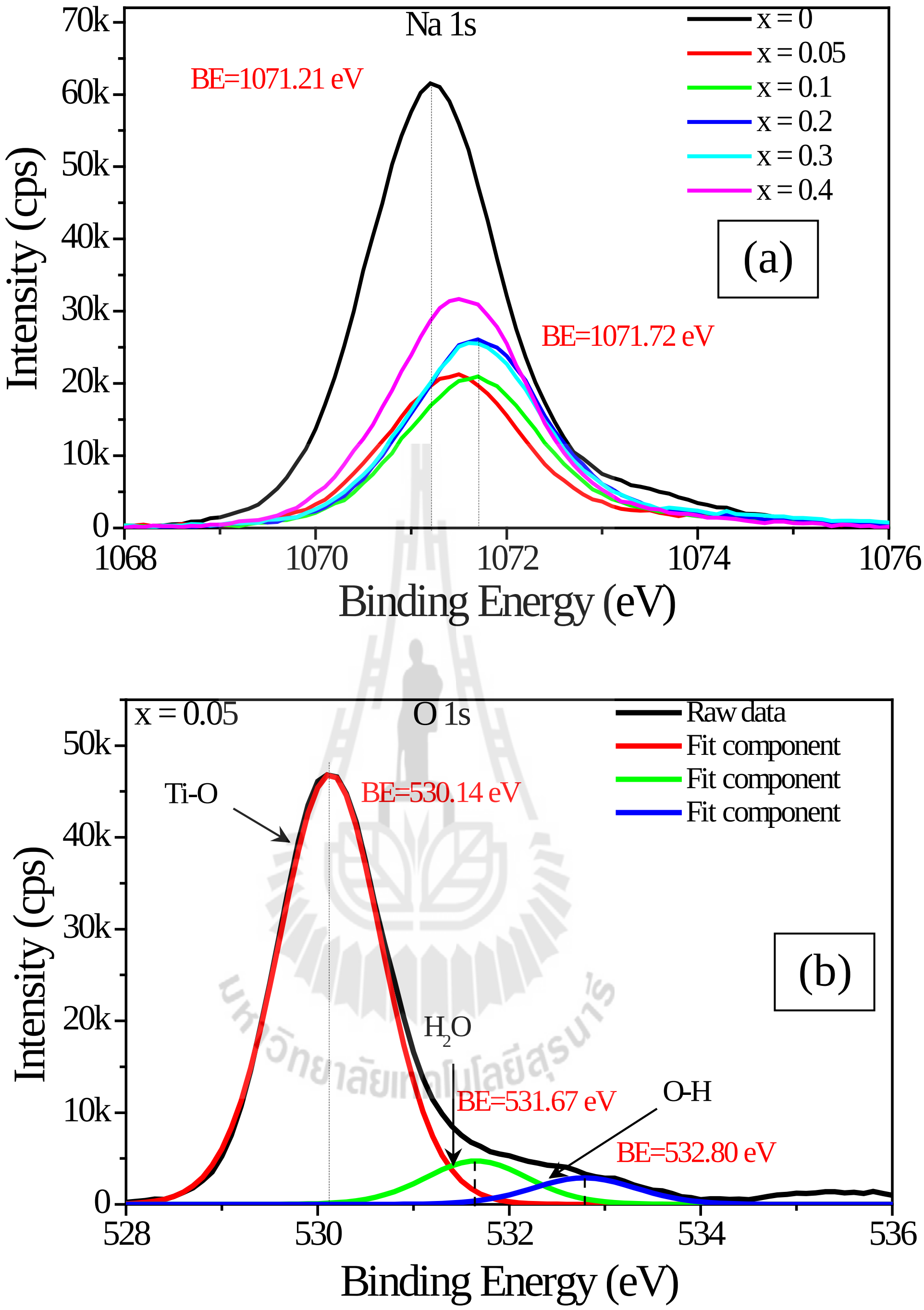

Figure 4.16 XPS integral spectra of undoped TNTs and Fe-doped TNTs samples (a) O 1*s* and (b) O 1*s* of Fe-doped TNTs at x = 0.05 sample.

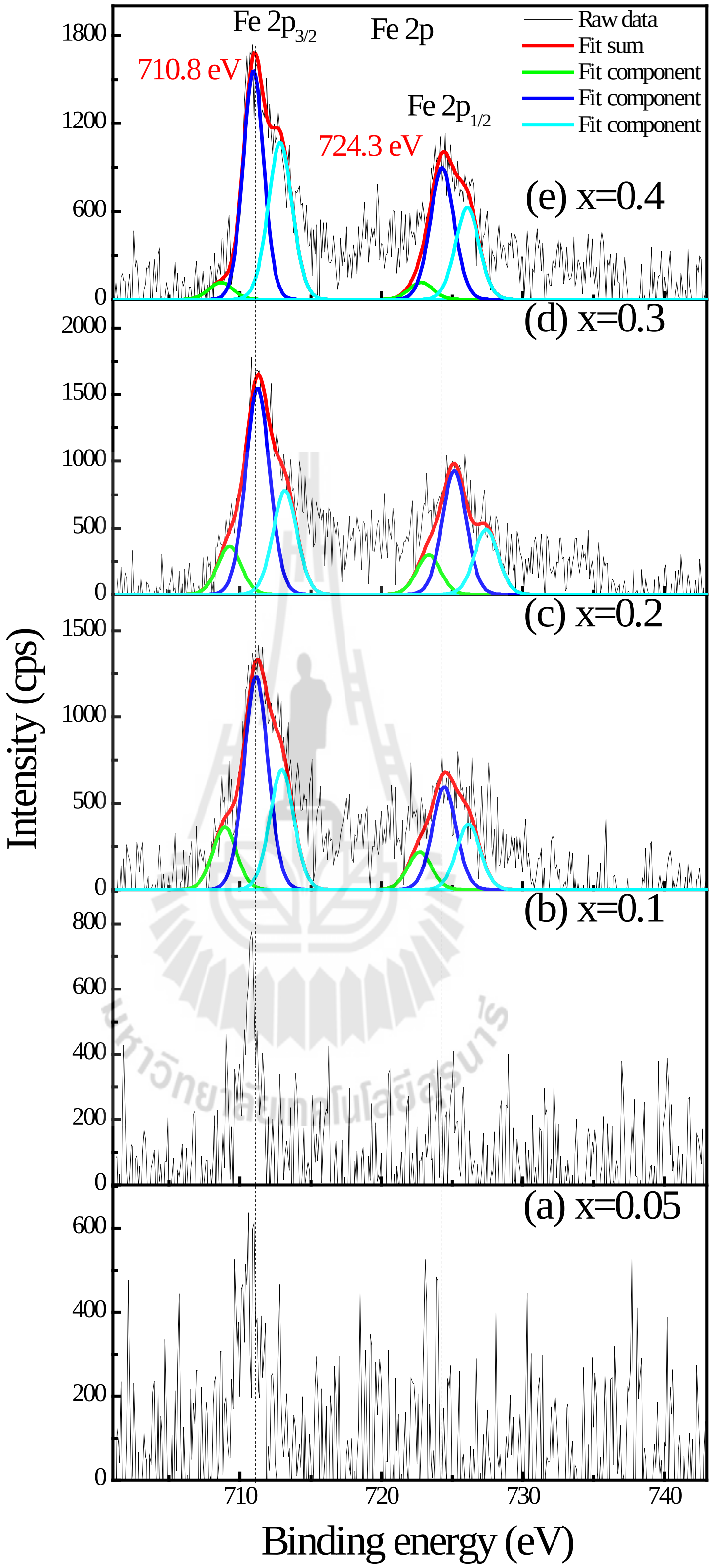

Figure 4.17 Fe 2*p* X-ray photoelectron spectra (XPS) of Fe-doped TNTs samples (a) x = 0.05, (b) x = 0.1, (c) x = 0.2, (d) x = 0.3 and (e) x = 0.4 samples

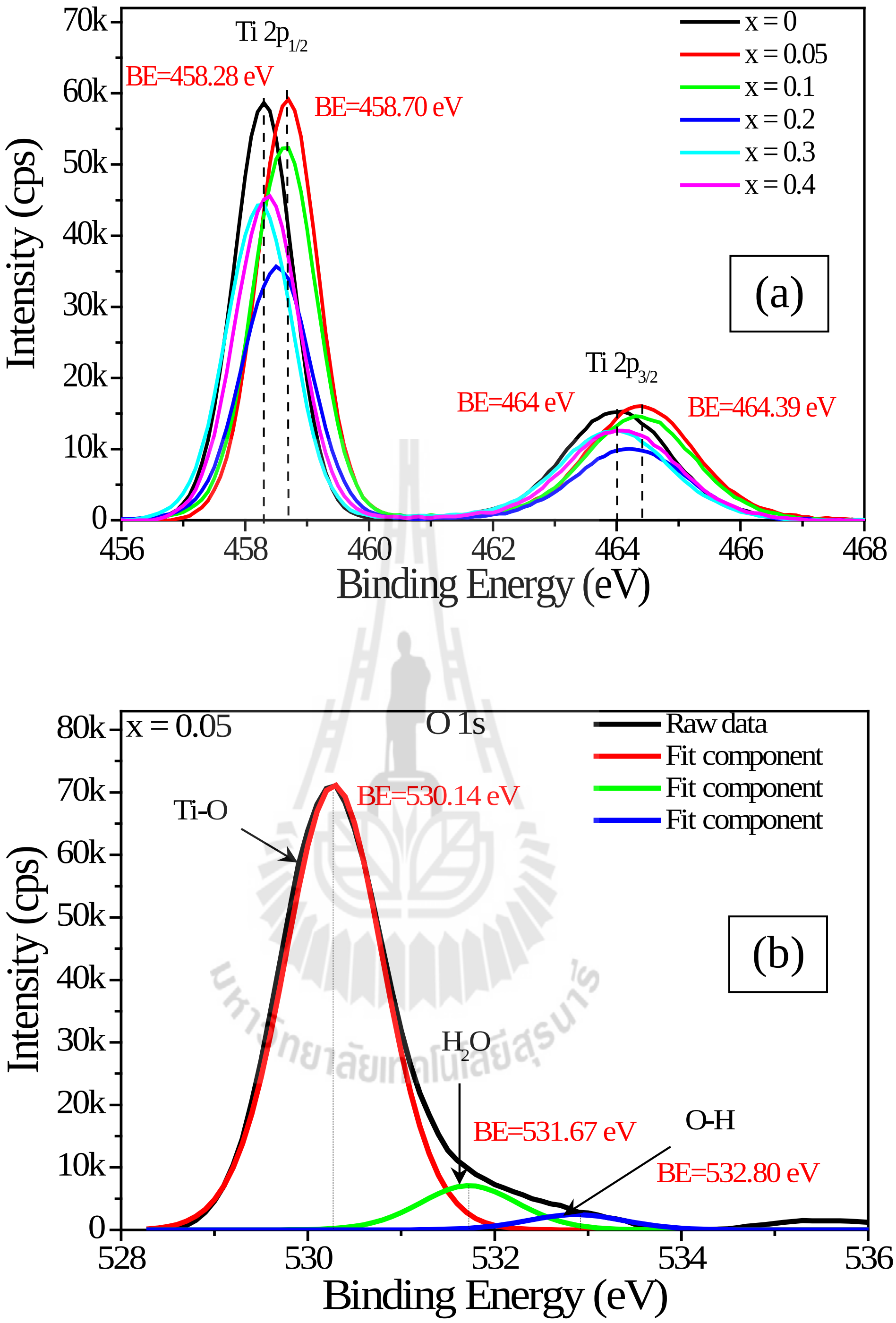

Figure 4.18 XPS integral spectra of undoped TNTs and Co-doped TNTs samples (a) Ti 2*p* and (d) O 1*s* of Co-doped TNTs sample.

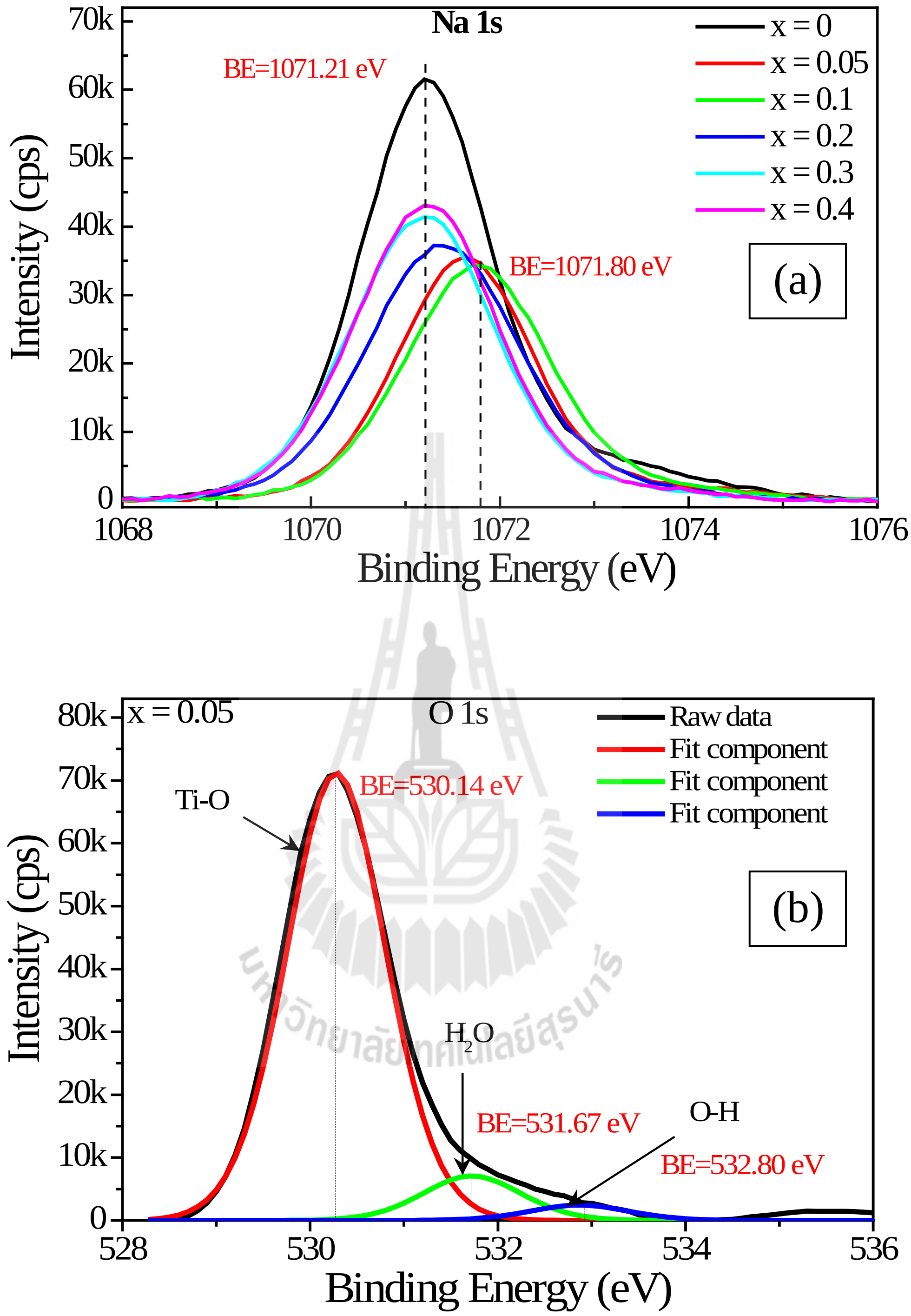

Figure 4.19 XPS integral spectra of undoped TNTs and Co-doped TNTs samples (a) Na 1*s* and (b) O 1*s* of Co-doped TNTs at x = 0.05 sample.

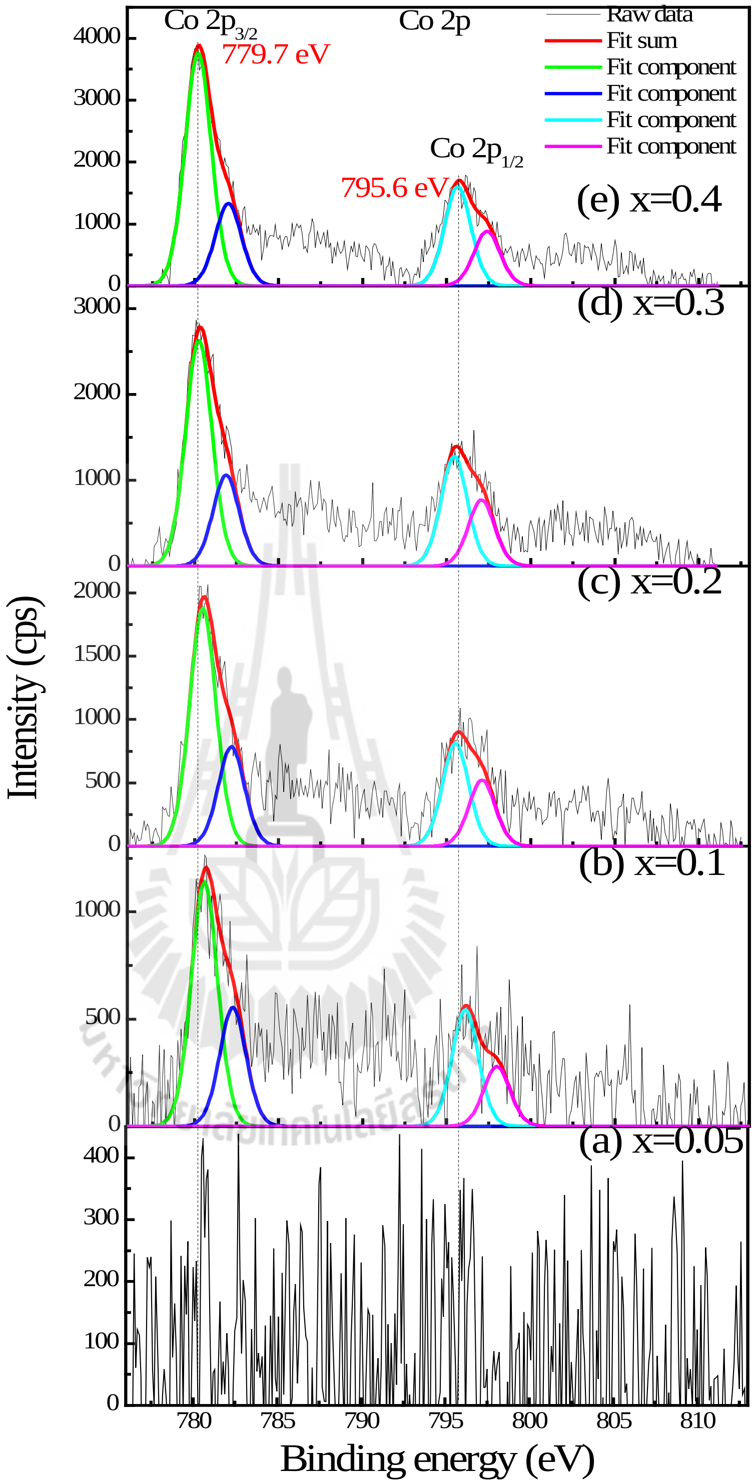

Figure 4.20 Co 2*p* X-ray photoelectron spectra (XPS) of Co-doped TNTs samples (a) x = 0.05, (b) x = 0.1, (c) x = 0.2, (d) x = 0.3 and (e) x = 0.4 samples.

4.5 Oxidation state of undoped TNTs and Fe/Co-doped TNTs studied by XANES

X- ray Absorption Near-Edge structure (XANES) spectra of TM-doped TNTs samples at the Ti (4966 eV), Fe (7112 eV) and Co (7709 eV) *K*-egde were measured at room temperature to study the valence states of the Ti, Fe and Co ions in the structure of undoped TNTs and TM-doped TNTs samples. The normalized absorption Ti *K*-egde, Fe *K*-egde and Co *K*-egde of XANES spectra for undoped TNTs and TM-doped TNTs samples compared with those of reference materials for Ti, Fe and Co are presented in Figures 4.21-4.22. In order to determine the Ti oxidation state of all the samples, standard powder of TiO was used as references for oxidation state of Ti^{2+} and TiO_2 was used as reference for oxidation state of Ti^{4+}. For the classical doping, FeO was used as references for oxidation state of Fe^{2+} while Fe_2O_3 and Fe_3O_4 was used as references for oxidation state of $Fe^{3+, 2+}$ (mix between Fe^{2+} and Fe^{3+}) and Fe^{4+}, respectively. In case of Co oxidation state, CoO and Co_3O_4 was used as references for oxidation state of Co^{2+} and $Co^{3+, 2+}$, respectively. The XANES spectra at Ti *K*-egde of composite samples exhibit the Ti^{4+} valence and the absorption edge and edge shift are shown in Table 4.5. Figure 22(a) shows the XANES spectra on Fe *K*-edge of investigated samples. The feature of XANES spectra of Fe-doped TNTs samples at Fe *K*-edge look very similar to the XANES spectra of Fe_2O_3 as references for oxidation state of Fe^{3+}. However, the feature of XANES spectra of Fe-doped TNTs at x = 0.05 at Fe *K*-edge look like to the XANES spectra of FeO as references for oxidation state of Fe^{2+}. The absorption edge position and edge shift are summarized in Table 4.6. The features of XANES spectra of Co-doped TNTs samples at Co K-edge look very similar to the XANES spectra of CoO. The edge position of samples does not change with respect to the edge position of CoO as references for oxidation state of Co^{2+} and the absorption edge and edge shift are presented in Table 4.7. The effect of Fe and Co state to electrical properties of Fe/Co-doped TNTs will be discussed in section 4.8.

Table 4.5 Absorption edge and oxidation state at Ti *K*-edge of Fe-doped TNTs samples at room temperature.

Sample	Absorption edge at Ti (eV)	Edge shift at Ti (eV)	Valence state at Ti
TiO	4975.44	-	2+
TiO_2-anatase	4983.52	0	4+
TiO_2-rutile	4983.52	0	4+
x = 0.05	4983.32	0.2	4+
x = 0.1	4983.32	0.2	4+
x = 0.2	4983.32	0.2	4+
x = 0.3	4983.32	0.2	4+
x = 0.4	4983.32	0.2	4+

Table 4.6 Absorption edge and oxidation state at Fe *K*-edge of Fe-doped TNTs samples at room temperature.

Sample	Absorption edge at Fe (eV)	Edge shift at Fe (eV)	Valence state at Fe
FeO	7120.21	0	2+
Fe_2O_3	7126.31	6.10	3+
Fe_3O_4	7124.25	4.04	2+, 3+
x = 0.05	7121.60	1.39	2+
x = 0.1	7126.12	5.91	3+
x = 0.2	7125.47	5.26	3+
x = 0.3	7125.31	5.10	3+
x = 0.4	7126.33	6.12	3+

Table 4.7 Absorption edge and oxidation state at Co *K*-edge of Co-doped TNTs samples at room temperature.

Sample	Absorption edge at Co (eV)	Edge shift at Co (eV)	Valence state at Co
CoO	7718.64	0	2+
Co_3O_4	7720.71	2.07	2+, 3+
x = 0.05	7718.67	0.03	2+
x = 0.1	7718.67	0.03	2+
x = 0.2	7719.70	1.06	2+
x = 0.3	7719.70	1.06	2+
x = 0.4	7719.70	1.06	2+

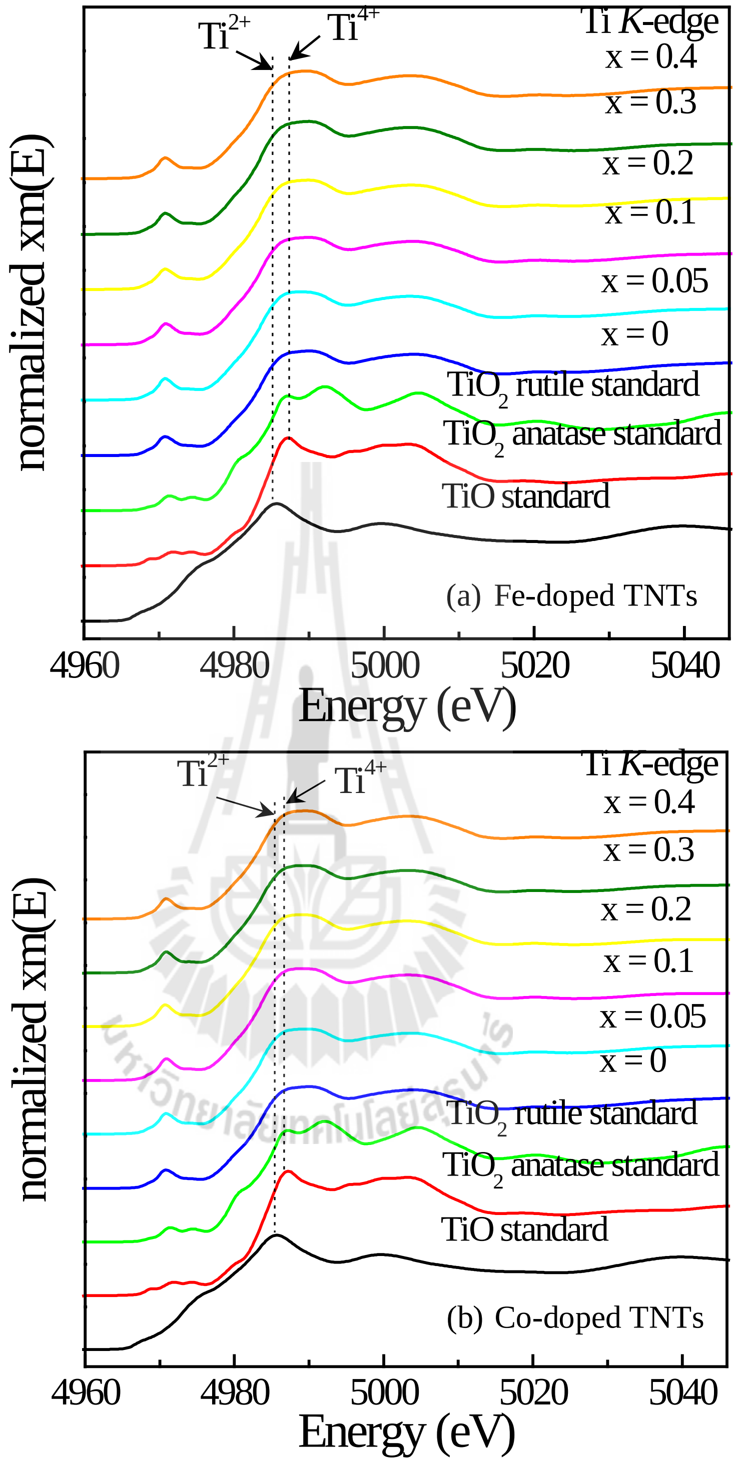

Figure 4.21 XANES spectra at the Ti *K*-edge for TiO, TiO_2 anatase, TiO_2 rutile standard, and XANES spectra of samples (a) Fe-doped TNTs and (b) Co-doped TNTs.

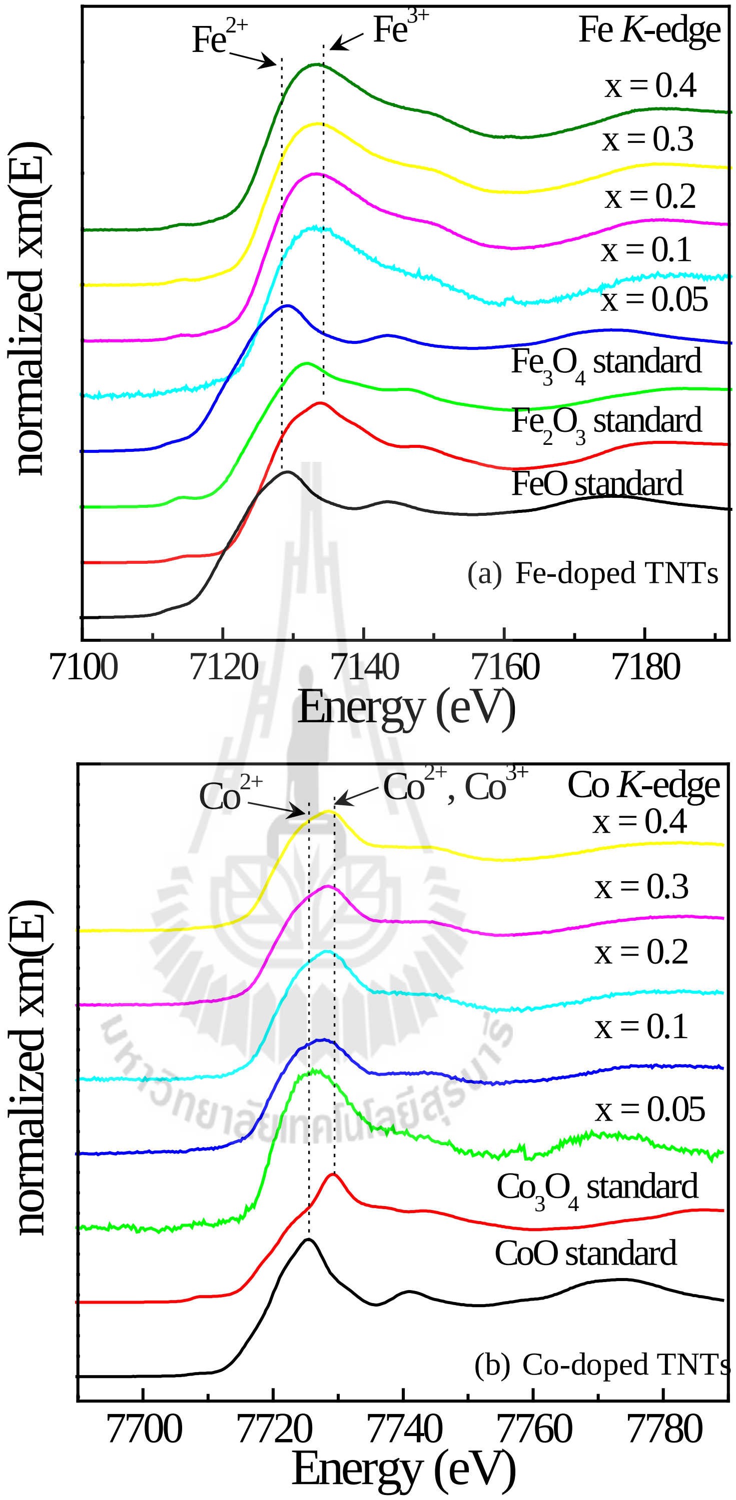

igure 4.22 XANES spectra at the Fe *K*-edge and Co *K*-edge for FeO, Fe_2O_3, Fe_3O_4 CoO and Co_3O_4 standard, and XANES spectra of samples (a) Fe-doped TNTs and (b) Co-doped TNTs.

4.6 The surface chemistry of TNTs and Fe/Co-doped TNTs

The surface chemistry of TNTs and Fe/Co-doped TNTs were examined by FTIR. Figure 4.23 shows large amounts of adsorbed water and hydroxyl groups exist for TNTs and Fe/Co-doped TNTs. The presence of crystallographic water molecular in the sample is confirmed by appearance of a characteristic peak at 1630 cm^{-1} that can be assigned to the H-O-H deformation mode ($\delta_{H\text{-}O\text{-}H}$). The broad intense band at 3418 cm^{-1} and 3169 cm^{-1} can be attributed to surface OH stretching mode oscillations. As a result of the strong interaction between Ti ions and OH groups within the tubular structure, locate at 3169 cm^{-1} from Ti-OH bonds is observed (Hu *et al.*, 2009). At lower wavenumbers, all the samples exhibit three vibrations: The band near 470 cm-1 is attributed to the Ti-O-Ti vibrations of the interconnected octahedral that are rigid units responsible for the formation of the tube wall; the band at 680 cm^{-1} is attributed to the vibrations of bridging oxygen atoms coordinated with Na ions polymerizing the Ti-O-Na clusters; and the band at 902 cm^{-1} is related with four coordinated Ti-O stretching modes that involve nonbridging oxygen atoms coordinated with Na+.

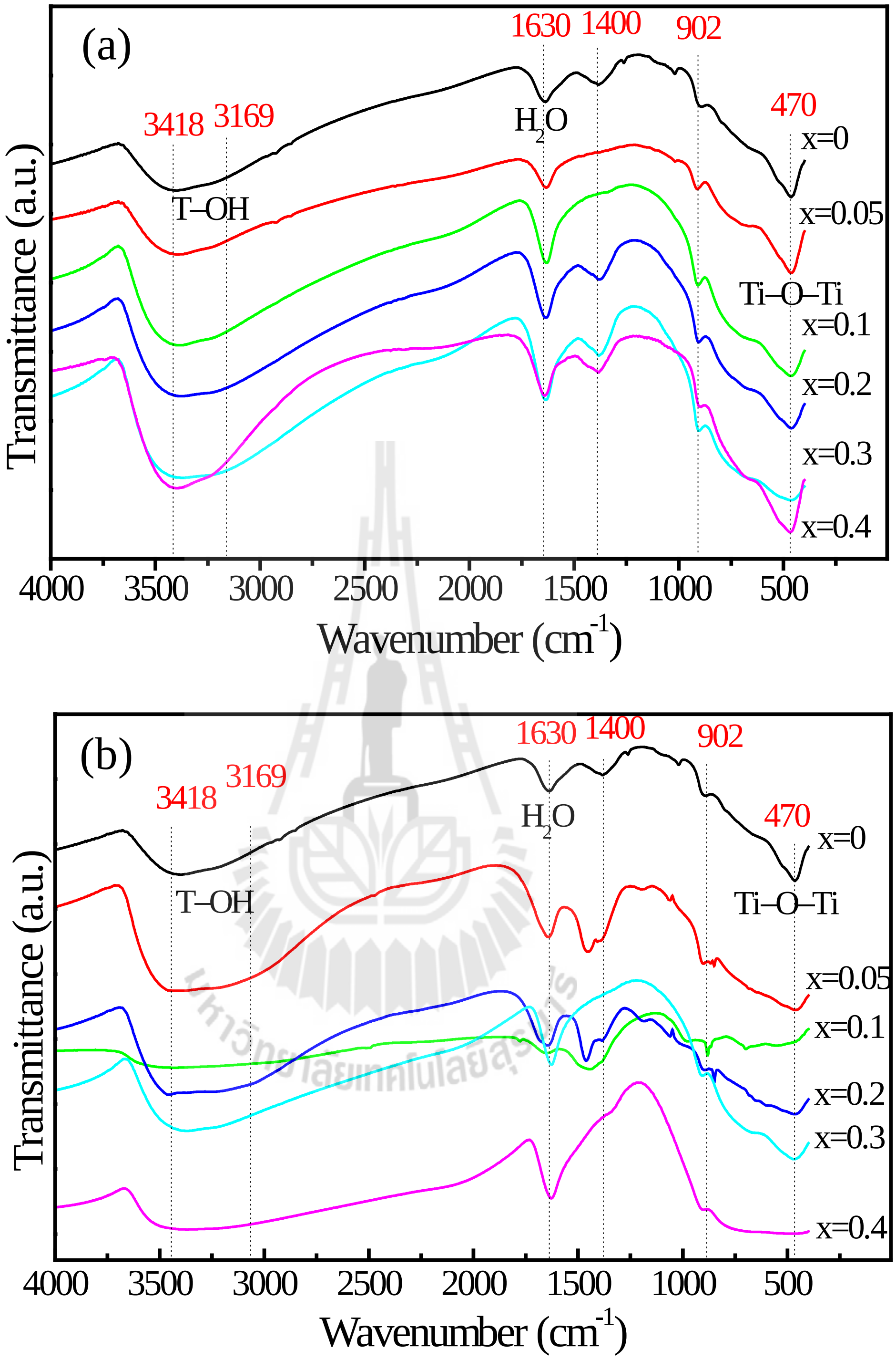

Figure 4.23 FT-IR spectra of Fe/Co-doped TNTs (a) Fe-doped TNTs and (b) Co-doped TNTs.

4.7 The optical properties of undoped TNTs and Fe/Co-doped TNTs

The UV-Vis absorption spectra of undoped TNTs and Fe/Co-doped TNTs are shown in Figure 4.22. All the samples were presented absorption at about 285 nm and the absorption edge in sample show red shift with increasing Fe/Co doping. For Fe/Co-doped TNT show extended absorption spectra into visible region in the rage of 400-800 nm (Inturi *et al.*, 2014). Moreover, red shift related with the presence of cobalt or iron ions can be attributed to a charge transfer transition between the cobalt or iron ions electrons and TNTs conduction or valence band (Yuan *et al.*, 2013; Inturi *et al.*, 2014; Zhu *et al.*, 2004; Liang and Li, 2009). The TiO_2 nanotubes reportedly have an indirect band gap (E_g). The following plot relation was used (Pang and Abdullah, 2012; Yuan *et al.*, 2013):

$$\alpha hv = A(hv - E_g)^n \tag{4.2}$$

Where α is the absorption coefficient, h is the Planck constant, v is the wavenumber, A is a constant and E_g is the energy band gap energy in with n = 1/2 for the direct band gap material and n = 2 for indirect band gap. The E_g can be calculated from the plot of $(\alpha hv)^{1/2}$ vs. hv allowing us to estimate the optical band gab by dropping a line from the maximum slope of the curve to x-axis (see Figure 4.23). The estimate indirect band gaps of all the samples are shown in Table 4.5. Interestingly, we have observed that there is a decrease in the band gap with increasing Fe/Co content calculated for Fe- and Co-doped TNTs samples. This decrease exhibits redshifts in the absorption spectra, compared to that of the undoped TNTs. The effect of doping on E_g is shown in Figure 4.24. The band edge absorption of nanometer-sized semiconductor materials is mainly related to two primary causes: quantum size effect (blueshift) and surface and interface effect or electronic structure (redshift) modifications. Generally, the quantum size effect led to the blueshift of E_g with decrease of particle size down to less than a few nanometers, while the surface and interface effect induces the redshift (Barreca *et al.*, 2003). In our work since the crystallite size is in the range of 13-26 nm, the difference the absorption band edge due to the quantum size effect is not observable. Obviously, the surface and interface effect should be responsible for the variation of the absorption band edge. The slight red shift in band gap possibly due to Fe, Co doping induces band edge binding. The change in the energy band gaps of the samples is possible might be the *sp*-*d* exchange interactions between the band electron and localized *d* electron of the Fe^{3+}, Co^{2+} ions substituting Ti ions. The *s*-*d* and *p*-*d* exchange interactions give rise to negative correction and positive correction to the conduction-band and the valance band edges, leading to in a band gap norrowing (Noipa *et al.*, 2014). These are similar to those of Fe-doped TiO_2 nanotubes reported in literatures (Yuan *et al.*, 2013; Pang and Abdullah, 2012). Sun and Li (Sun and Li, 2003) have reported band gap values 3.1 eV for TNTs prepared by hydrothermal method. Pang and Abdullah (2013) have reported indirect band gap values about 3.11 eV for udoped TNTs and ranging from to 2.60 eV to 2.83 eV for Fe-doped TNTs synthesized by hydrothermal method. Moreover, Yuan *et al.* (2013) have reported indirect band gap values ranging from 3.23eV to 3.26 eV for undoped TNTs and ranging from 2.91 eV to 3.04 eV for Fe-doped TNTs.

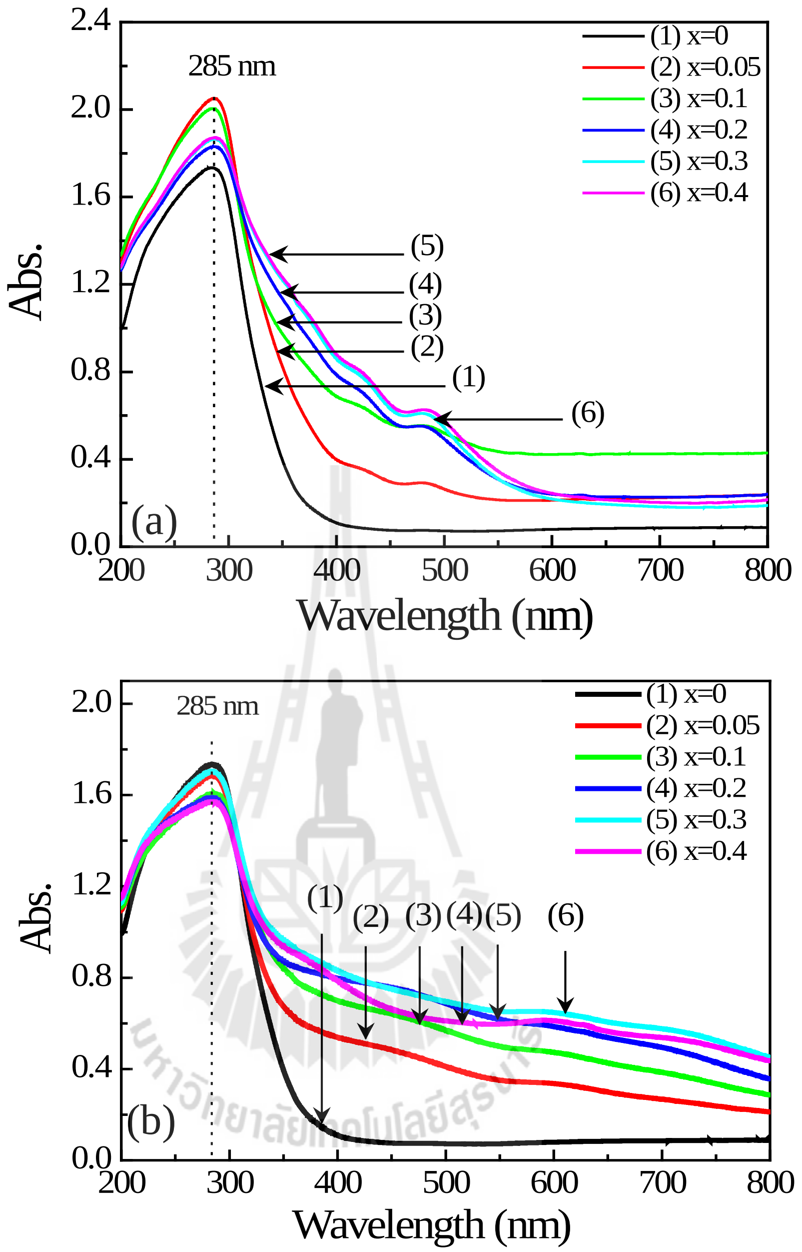

Figure 4.24 Room-temperature optical absorbance spectra of undoped TNTs and Fe/Co-doped TNTs prepared by hydrothermal method at 130 °C for 24 h (a) Co-doped TNTs and (b) Fe-doped TNTs.

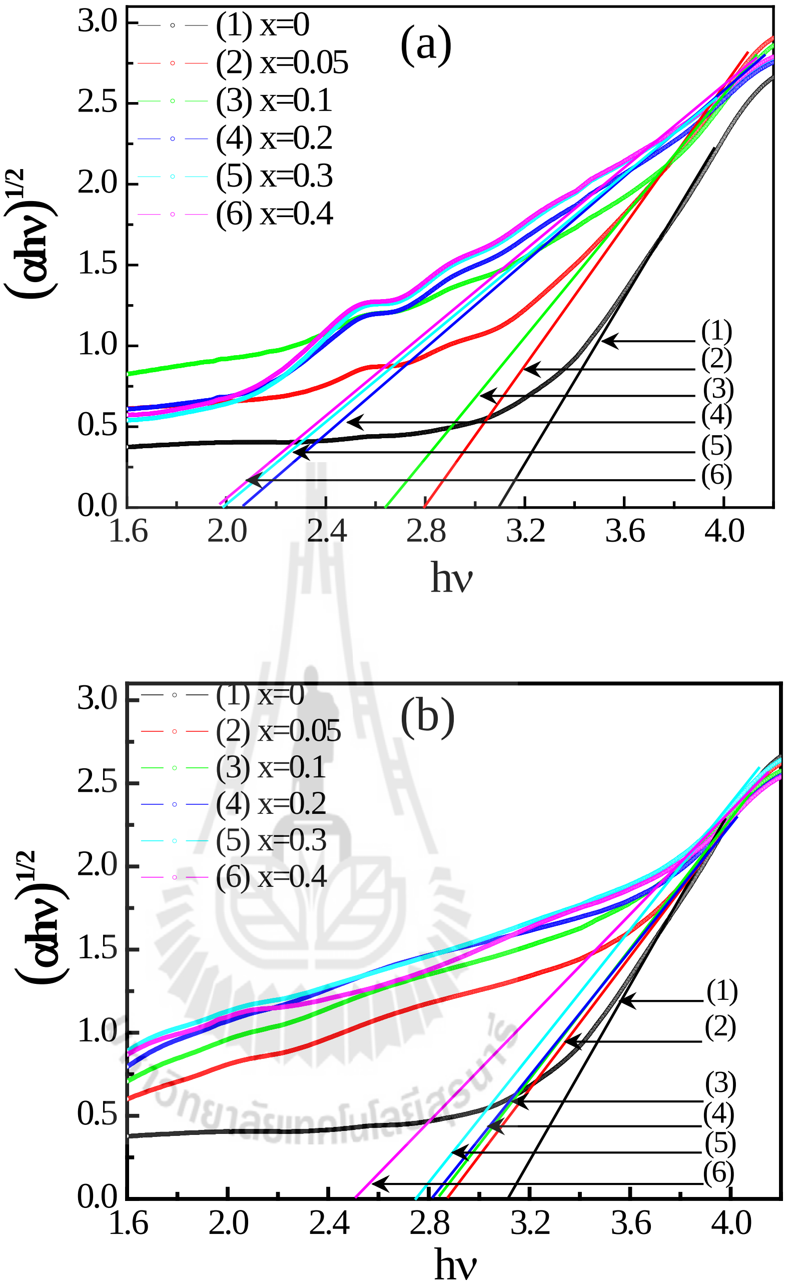

Figure 4.25 Plot of $(\alpha h\nu)^{1/2}$ as function of photon energy ($h\nu$) for undoped TNTs and Fe/Co -doped TNTs prepared by hydrothermal method at 130 °C for 24 h (a) Fe-doped TNTs (b) Co-doped TNTs.

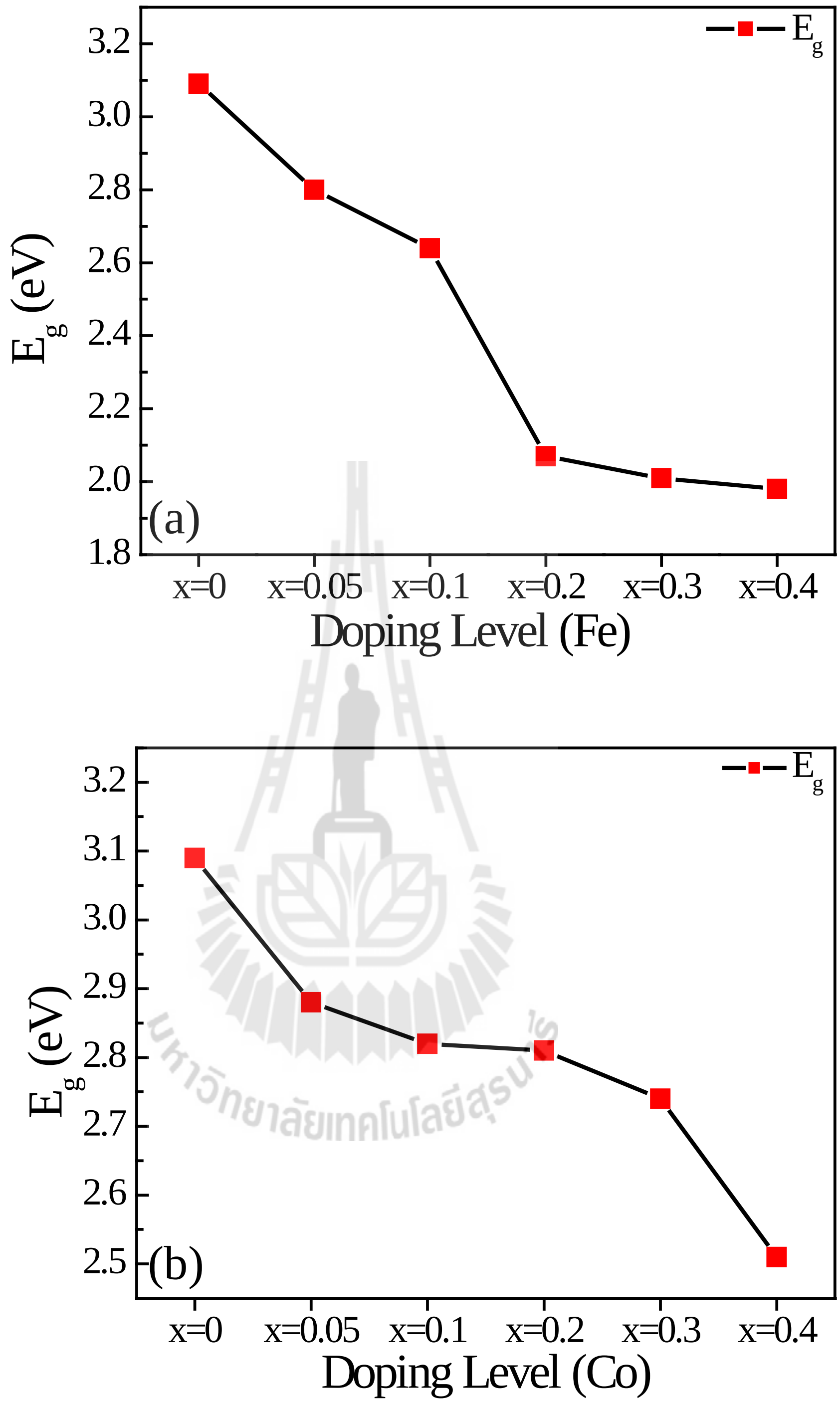

Figure 4.26 The effect of Fe/Co-doping on the band gap energy (E_g) of (a) Fe-doped TNTs and (b) Co-doped TNTs prepared by hydrothermal method at 130 °C for 24 h.

Table 4.8 Summary of indirect band gap energy (E_g) of undoped TNTs and TM-doped TNTs prepared by hydrothermal method at 130 °C for 24 h.

Doping level	E_g (eV) of TM-doped TNTs	
	Fe doping	Co doping
x=0	3.09	3.09
x=0.05	2.80	2.88
x=0.1	2.64	2.82
x=0.2	2.07	2.81
x=0.3	2.01	2.74
X=0.4	1.98	2.51

4.8 Magnetic properties of magnetic ions in Fe/Co-doped TNTs

Figure 4.27 shows the field dependence of the specific magnetization (*M-H* curve) of undoped TNTs samples, obtained from VSM measurements at room temperature (RT). The undoped TNTs sample exhibits a diamagnetic behavior.

The magnetization curves (*M-H*) of Fe/Co-doped TNTs obtained from VSM measurements at room temperature (RT) are shown in Figure 4.26. For Fe/Co-doped TNTs, the hysteresis loop is observed with S-shaped for x=0.05 (Fe-doped TNTs) and x=0.05-0.1 (Co-doped TNTs), which indicate the ferromagnetic (FM) behavior nature of the sample as shown in Figures 4.28(a) and (b), respectively. With higher concentration of Fe ions and Co ions, the magnetization of samples does not saturate even at the maximum field of 10 kOe corresponding to strong paramagnetic (PM) component of the samples. The observed paramagnetism in our samples may be related to the impurity phase of TM oxide such as iron oxide or cobalt oxides but not observed in the XRD results. These result are similar those reported in Fe-doped ZnO nanoparticles (Kumar *et al.*, 2014). As the result of Fe-doped TNTs at $x = 0.05$, the sample showed well RT-FM with magnetization (M) at 10 kOe of 0.0028 emu/g, and coercivity (H_C) of approximately 1657 Oe.

In this work, the XPS results show evidence of Fe^{2+}, Fe^{3+} and Co^{2+}substitution in Ti^{4+} sites, which can be attributed to oxygen vacancy (V_O) in Fe-, and Co-doped TNT samples. Therefore, the RT-FM in this sample is suggested to the exchange interactions between spin of Fe^{3+} or Fe^{2+}, Co^{2+} and V_O on the surface of sample. This direct ferromagnetic coupling is called F-center exchange (FCE), as proposed by Coey et al.(Coey *et al.*, 2010) It might be that V_O can create magnetic moments on neighboring Fe-ions and Co-ions of $Fe^{3+} - \nabla - Fe^{3+}$ or $Fe^{2+} - \nabla - Fe^{2+}$or $Co^{2+} - \nabla - Co^{2+}$ where ∇ denotes a V_O. The RT-FM result showed similar result of work reported by Xiaoyan et al.(Xiaoyan *et al.*, 2006).

Table 4.9 Summary of magnetization (*M*) of undoped TNTs and Fe/Co-doped TNTs prepared by hydrothermal method at 130 °C for 24 h.

Doping level	*M* at 10 kOe (emu/g) from VSM	
	Fe doping	Co doping
x=0	-	-
x=0.05	0.0028	0.0060
x=0.1	0.0150	0.0075
x=0.2	0.0497	0.0127
x=0.3	0.0771	0.0148
x=0.4	0.1000	0.0198

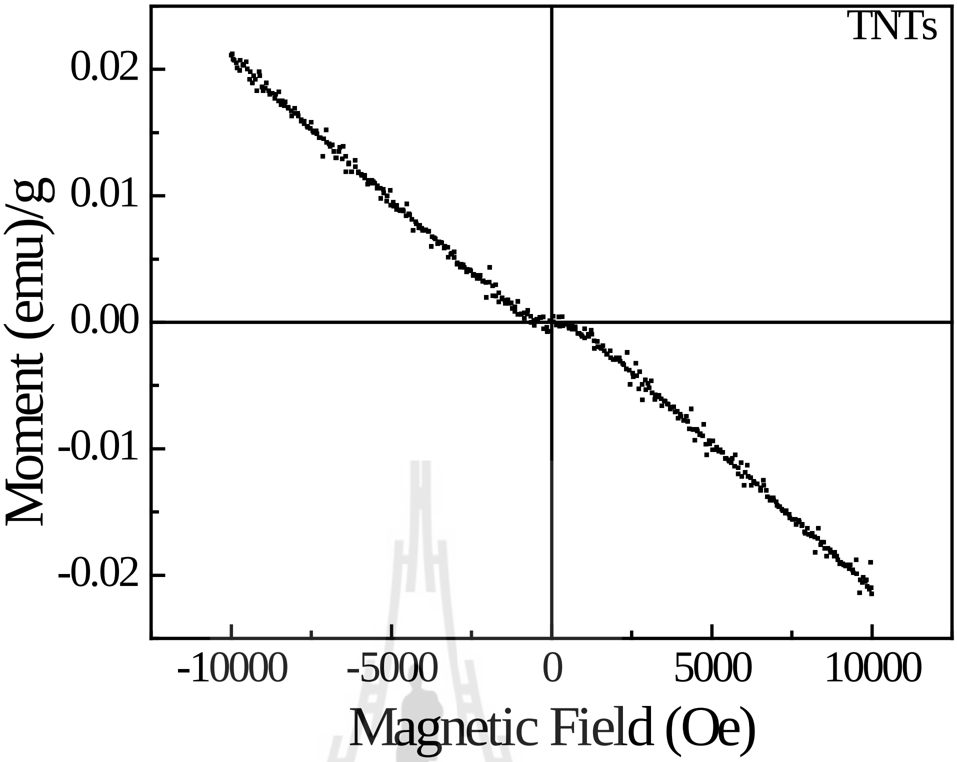

Figure 4.27 *M-H* cures at 300 K obtained from VSM measurements of undoped TNTs prepared by hydrothermal method at 130 °C for 24 h.

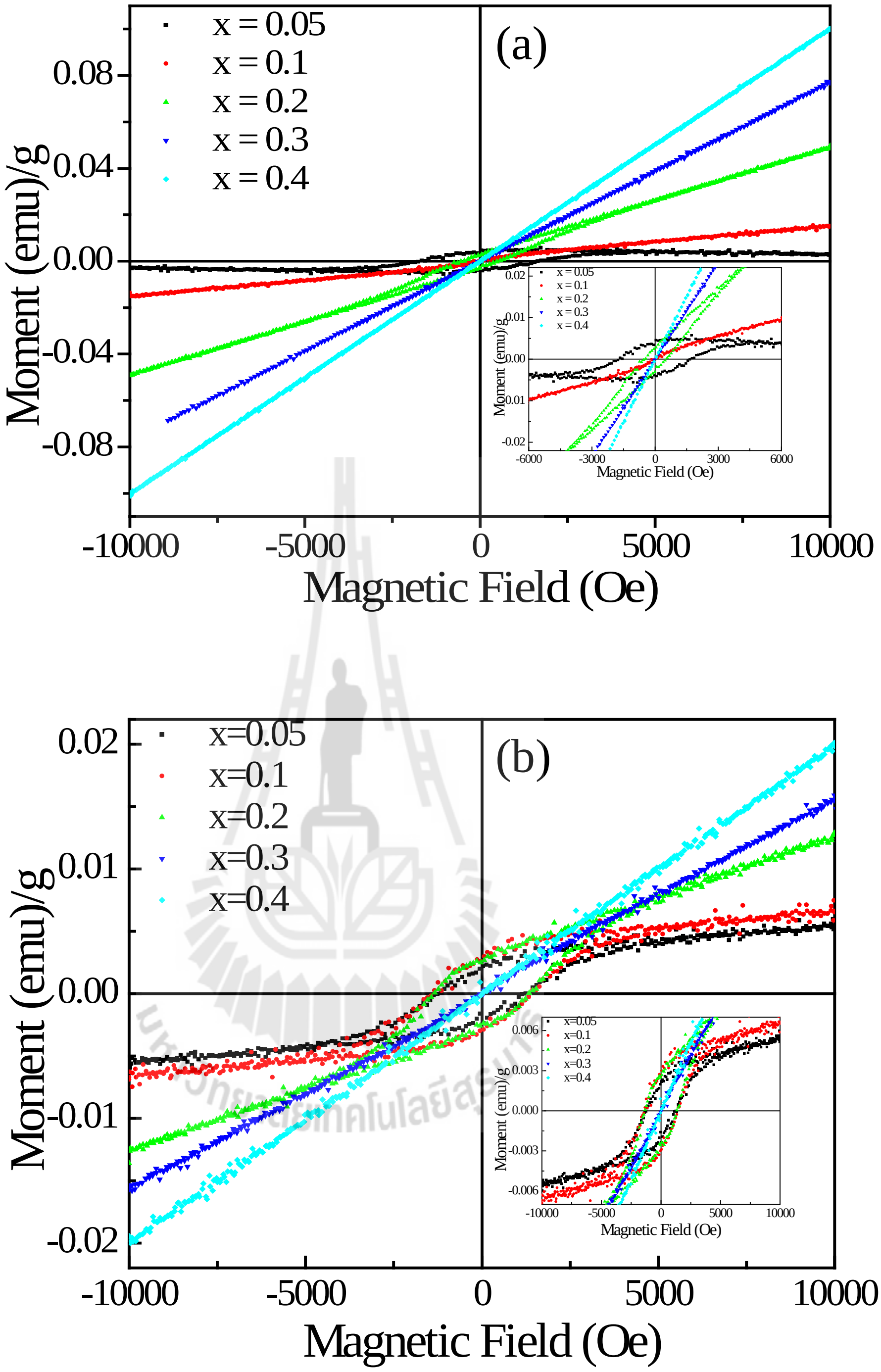

Figure 4.28 *M-H* cures at 300 K obtained from VSM measurements of undoped TNTs prepared by hydrothermal method at 130 °C for 24 h (a) Fe-doped TNTs and (b) Co-doped TNTs.

4.9 Dielectric properties of undoped TNTs and Fe/Co-doped TNTs

4.9.1 Temperature dependence of dielectric properties of the undoped TNTs and Fe/Co-doped TNTs

Figures 4.29-4.31(a)-(b) show the temperature dependence of the dielectric constant (ε') and loss tangent (tanδ) between -50 °C to 200 °C at the frequency range of 10^2 to 10^6 Hz for undoped TNTs and Fe/Co-doped TNTs bulks prepared at 130 °C for 24 h. For the undoped TNTs as shown in Figure 4.29, at the frequency of 10^2 Hz, the dielectric constant tends to increases with increasing temperature. This dielectric behavior is caused by the dc conductivity, which is usually dependence on temperature (Wu *et al.*, 2002). However, when the temperature higher than 40 °C, the ε' decreases with increasing temperatures. This is due to transformation from trititanate ($H_2Ti_3O_7$) to TiO_2-anatase phase. Figure 4.31(c)-(f) show the dielectric properties of Fe/Co-doped TNTs different concentrations of Fe and Co doping ions. All samples exhibit high dielectric constant values of about 10^4-10^5 at 30 °C and 10^3 Hz. The dielectric constant (ε') tends to increase with increasing measured temperature. However, at the low temperature the charge carriers cannot orient themselves with respect to the direction of the applied field. As the temperature increases, the charge carriers get enough excitation thermal energy to change the polarization in the external field more easily leading to an increase of the dielectric constant (Bayoumi, 2007). Figures 4.31(c-f) show temperature dependence of dielectric constant (ε') and loss tangent (tanδ) between -50 °C to 200 °C over the frequency range of 10^2-10^6 Hz for undoped TNTs and Fe/Co-doped TNTs with different concentrations, when the temperature increased higher than $T\varepsilon_m$ ($T\varepsilon_m$ correspond to the temperature at which the dielectric constant reaches the maximum as shown in Table 4.7) the dielectric constant (ε') of all samples decreased. This observation might be a result from an effect of phase transformation of the Fe/Co-doped TNTs-based compounds. The dielectric properties of all the samples decrease with increasing frequency because at the higher frequency the dipole does not follow the alternating field. With the frequency up to 10^5 Hz, the rapid decrease in the dielectric constant was observed at a low temperature range, corresponding to the existence of the loss tangent peak. Both rapid decreases in the dielectric constant and the relaxation peak of the loss tangent shifted to a higher temperature range with increasing frequency. This indicates the thermally activated mechanism of this dielectric relaxation process.

Figure 4.32(a) shows the SEM images of TNTs as–calcined and the calcined samples: Figures 4.32(b)–(e) are the samples calcined for 2 h at 80, 120, 160, and 200 °C, respectively. The SEM images show both nanotube-like structures and particles. The structure of nanotubes was destroyed and changed into particles with increasing temperature (see in Figures 4.32(b)–(f)). In the temperature range 25 to 200 °C, desorption of water form nanotube pores result in the removal of crystallographic water from titanate nanotube. This process is accompanied by decrease in intensity of trititanate ($H_2Ti_3O_7$) (see in Figure 4.32(f)), due to the weight loss and shrinkage of the nanotube volume. According to TGA data, approximately 11-12 wt% of mass is loss during the dehydration of crystallographic water. At the temperatures above 80 °C, the removal of the remaining water results in phase transformation of $H_2Ti_3O_7$ to anatase-type TiO_2.

Normally, water molecules belong to atypical polarized molecule. Hu *et al*. (2010), reported the present water intercalated TNTs can well keep the relatively high dielectric constant. Therefore, the change in dielectric properties of the bulk TNTs can be correlated to the changes in nanostructure dehydration and phase transformation. This can cause lower carrier mobility for the TNTs, leading to the decrease in dielectric constant (ε') and loss tangent (tan δ) of the TNTs.

Table 4.10 Summary of Tε_m correspond to the temperature at which the dielectric constant (ε') reaches the maximum at 10^3 Hz of undoped TNTs and Fe/Co-doped TNTs prepared by hydrothermal at 130 °C for 24 h.

Doping level	Tε_m (°C)		Dielectric constant (ε')	
	Fe doping	Co doping	Fe doping	Co doping
x=0	30	30	55400	55400
x=0.05	90	80	48300	29100
x=0.1	90	80	41700	27800
x=0.2	90	80	46100	33900
x=0.3	90	90	49900	31600
x=0.4	90	80	54400	33100

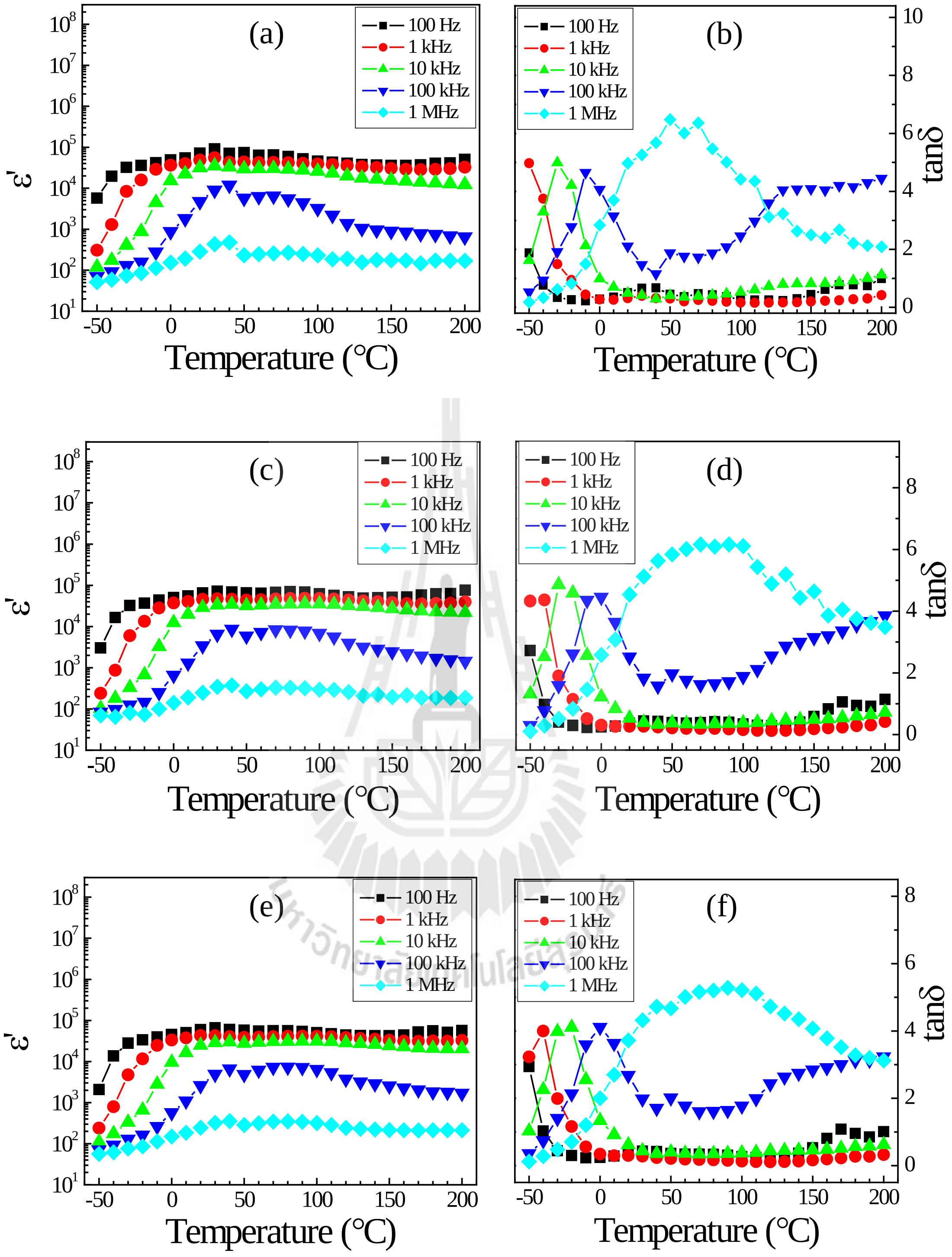

Figure 4.29 Temperature dependence of dielectric constant (ε') and loss tangent (tanδ) at the frequency range of 10^2-10^6 Hz of Fe-doped TNTs (a)-(b) x = 0, (c)-(d) x = 0.05 and (e)-(f) x = 0.1.

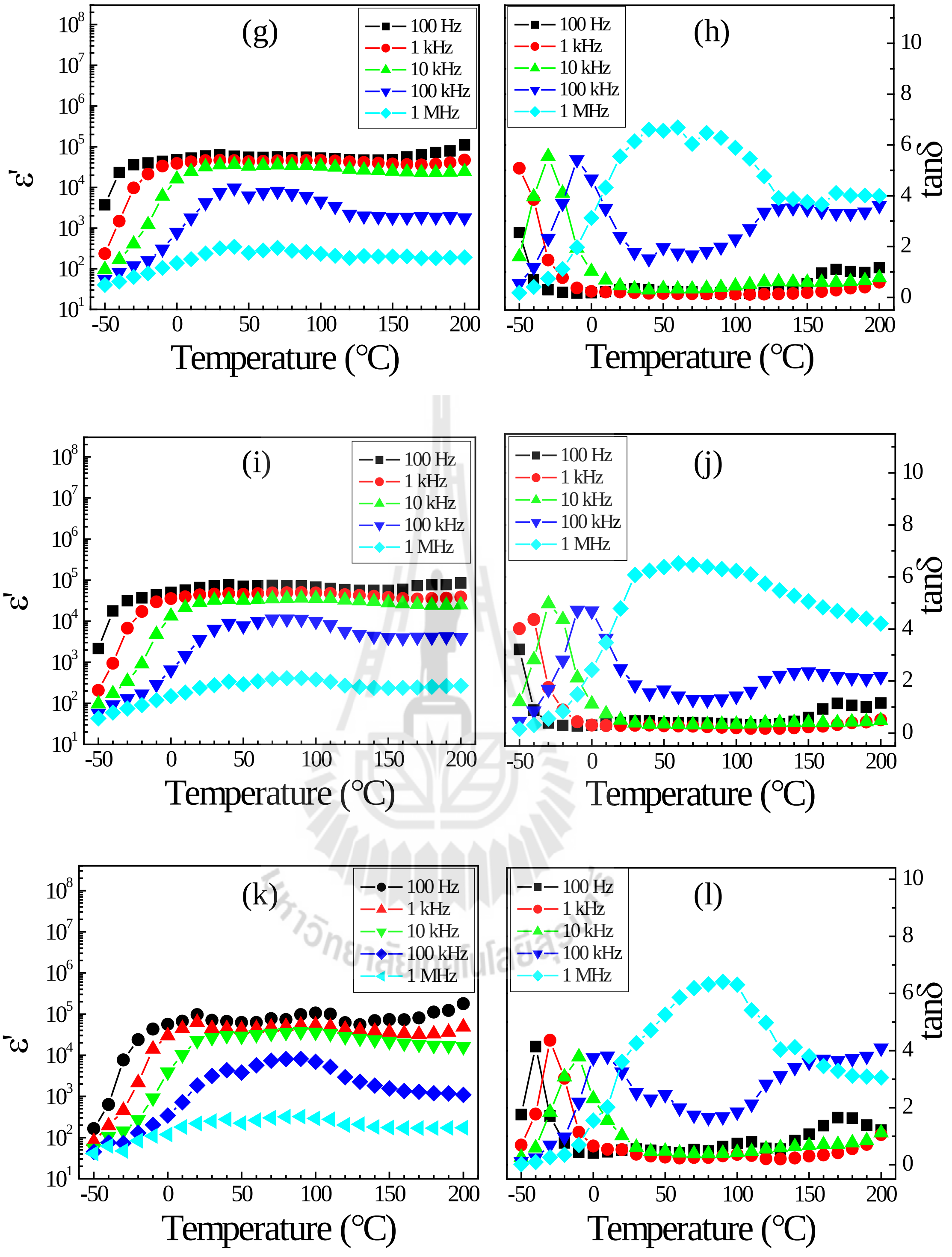

Figure 4.29 Temperature dependence of dielectric constant (ε') and loss tangent (tanδ) at the frequency range of 10^2-10^6 Hz of Fe-doped TNTs (g)-(h) x = 0.2, (i)-(j) x = 0.3 and (k)-(l) x = 0.4.

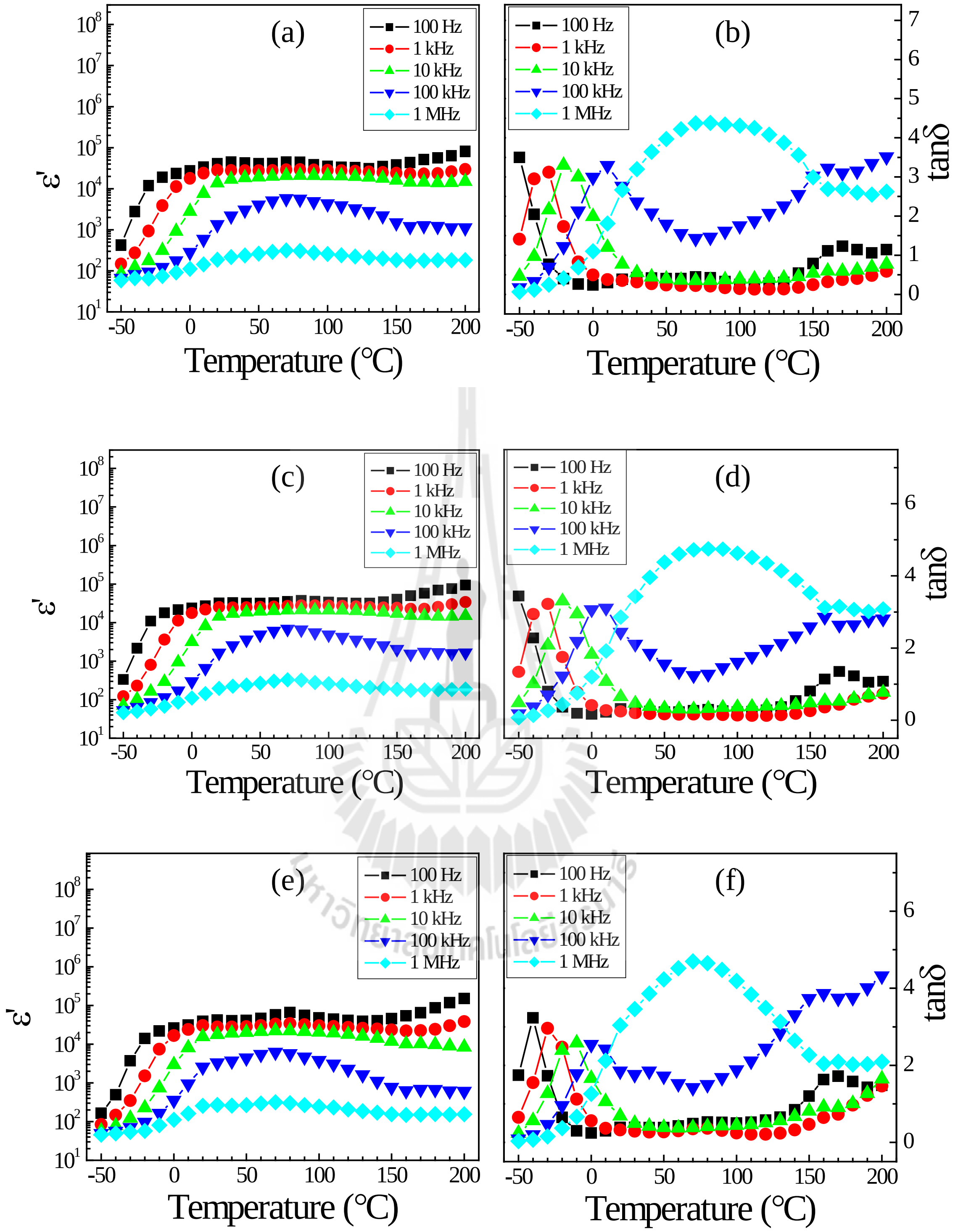

Figure 4.30 Temperature dependence of dielectric constant (ε') and loss tangent (tanδ) at the frequency range of 10^2-10^6 Hz of Co-doped TNTs (a)-(b) x = 0, (c)-(d) x = 0.05 and (e)-(f) x = 0.1.

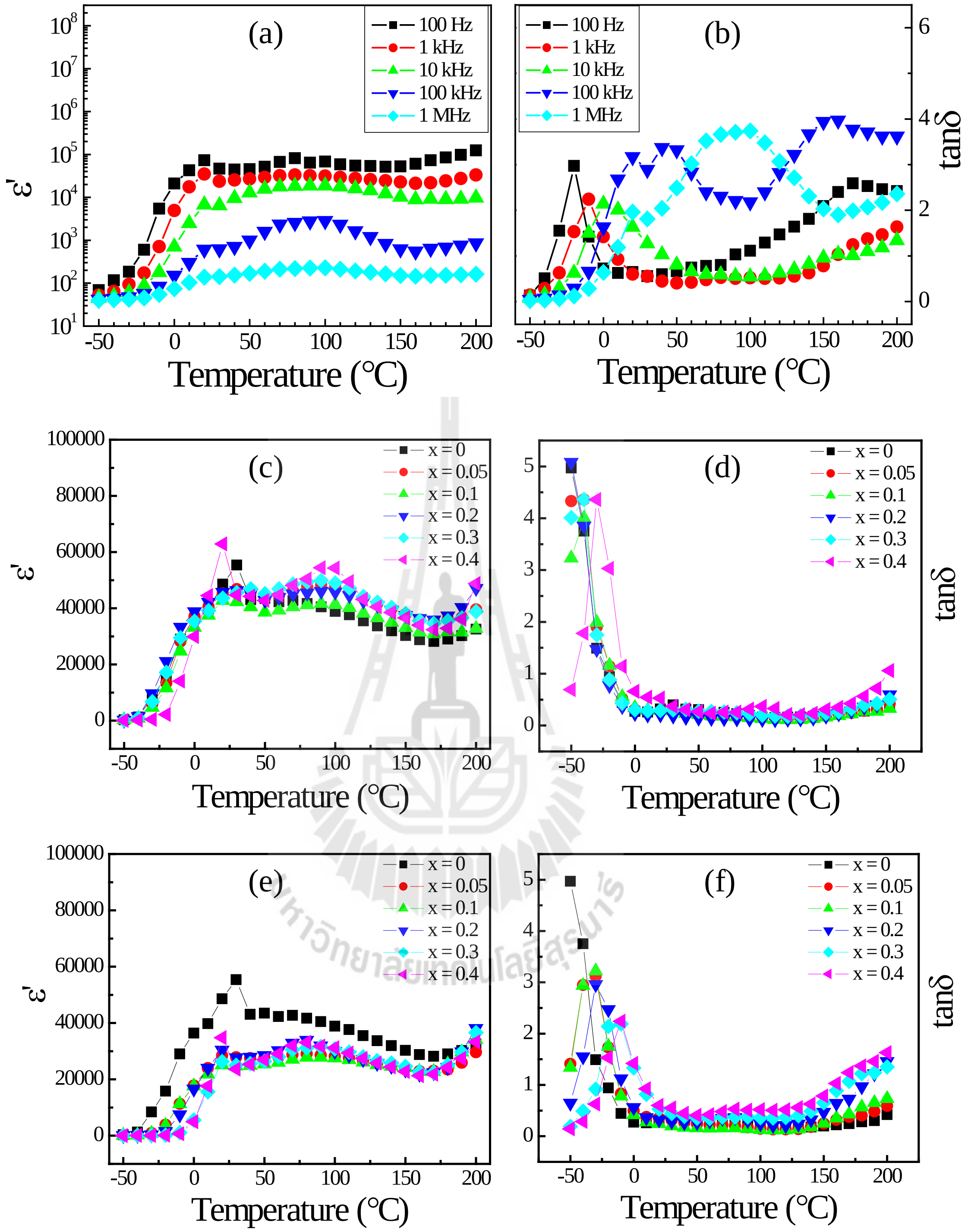

Figure 4.31 Temperature dependence of dielectric constant (ε') and loss tangent (tanδ) at the frequency range of 10^2-10^6 Hz of (a)-(b) Co-doped TNTs x = 0.4, (c)-(d) Fe-doped TNTs and (e)-(f) Co-doped TNTs with different concentration

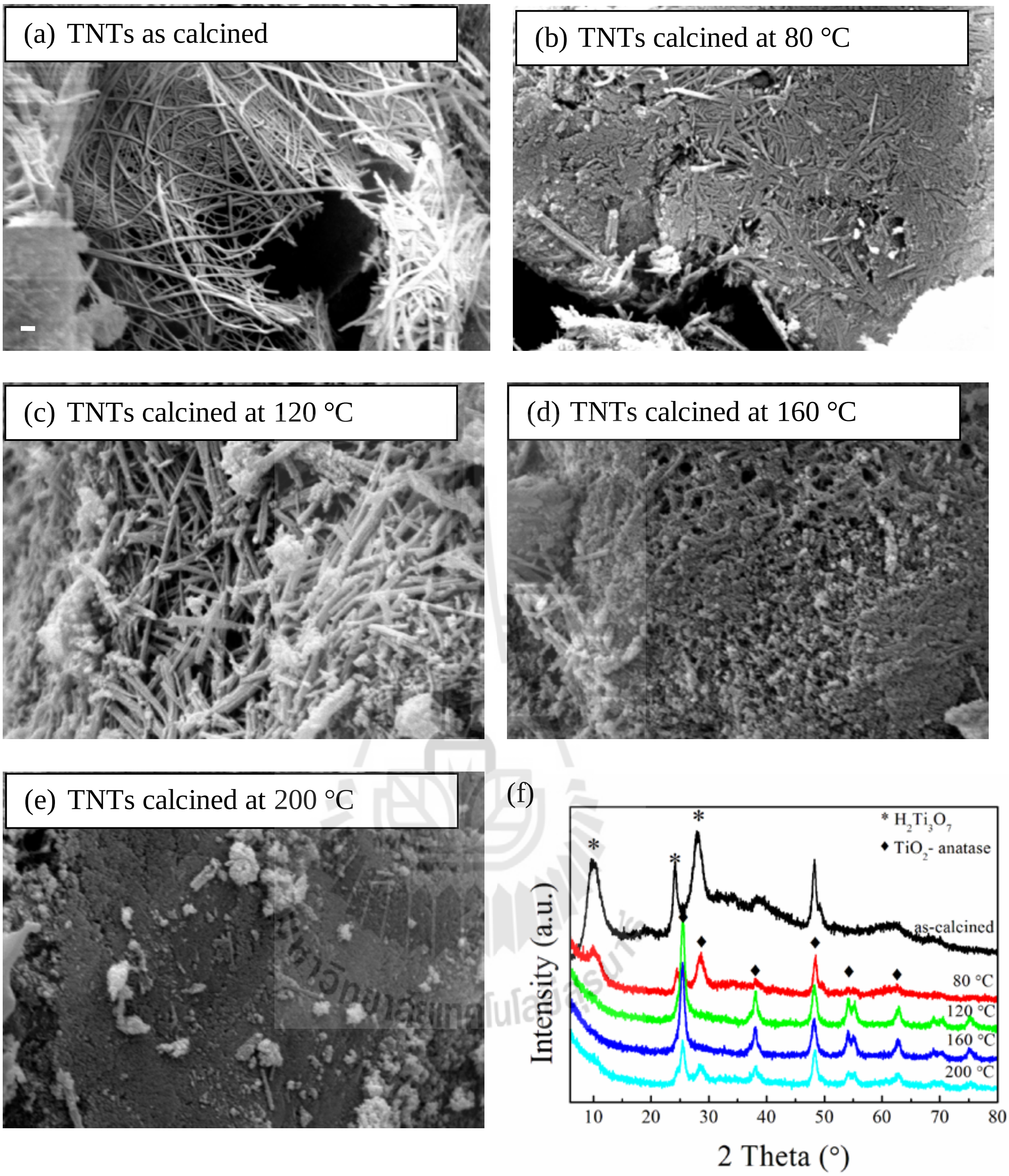

Figure 4.32 SEM images of (a) undoped TNTs prepared at 130 °C for 24 h, and TNTs calcined for 2 h at (b) 80, (c) 120, (d) 160, (e) 200 °C and (f) XRD patterns of TNTs as calcined and calcined for 2 h at 80, 120, 160, and 200 °C.

4.9.2 Frequency dependence of the dielectric properties of the undoped TNTs and Fe/Co-doped TNTs

The mechanism of the dielectric relaxation can be knowledge by consider the frequency dependence of the dielectric properties (Liu *et al.*, 2004). The frequency dependence of the dielectric constant (ε') and loss tangent (tanδ) at the selected temperature -30-30 °C over the frequency range 10^2 Hz to 10^6 Hz for the undoped TNTs and Fe/Co-doped TNTs prepared at 130 °C for 24 h as shown in Figures 4.33-4.34. All of the samples show the dielectric relaxation behavior. The loss tangent (tanδ) of all samples clearly shows a Debye-like relaxation peak shifting to higher frequencies with increasing temperature. All of the samples exhibit giant dielectric behavior with dielectric constant of 10^4-10^6 at 100 Hz and 30 °C. It is found that the dielectric constant (ε') rapidly decreases with increasing frequencies. The rapid decrease in ε' is accompanied with the observed tanδ peak for the sample. This indicates the dielectric relaxation behavior in dielectric materials (Wu *et al.*, 2002; Thongbai *et al.*, 2008). For undoped TNTs sample, the temperature increase higher than 40 °C, it is likely that the relaxation peak in sample slightly shifts to lower frequency. The decrease in dielectric constant (ε') may be due to the decrease in trititanate intensity phase and phase transformation of TNTs. This can cause lower carrier mobility for the TNTs, leading to the decrease in dielectric constant (ε') and loss tangent tan (tanδ) of the TNTs. The overall dielectric relaxation of Fe/Co-doped TNTs samples shifts to higher frequency at higher temperature similar to that observed in CCTO ceramics reported in the literature (Maensiri *et al.*, 2007; Sinclair *et al.*, 2002). This observation might be a result from an effect of heating process. This dielectric relaxation behavior is suggested to the thermally activated mechanism.

This high dielectric constant value is effect of influence of the dc conduction produced in the samples (Wu *et al.*, 2002).

The dielectric response behavior is closely related to the Maxwell-Wagner polarization or interfacial polarization. The dielectric behavior should be related to the short–range motion of electrons and other charge carriers (e.g., atoms, molecules, ions, holes, vacancies, and hydration water molecules stored in the sample) under the influence of an applied the electric field. Figures 4.33-4.34 show the variation of dielectric constant, loss tangent and dielectric loss of undoped TNTs and Fe/Co-doped TNTs samples over the frequency range from 10^2 Hz to 10^6 Hz as a function of the temperature ranging from -30 to 30 °C. The dielectric loss and loss tangent peaks were observed shifts to higher frequencies with increasing temperatures. The result confirms the thermally activated relaxation.

To understand the physical nature of observed dielectric relaxations in undoped TNTs and Fe/Co-doped TNTs samples, the data of the dielectric spectra were fitted by Cole-Cole equation (Thongbai *et al.*, 2012; Liu *et al.*, 2005) combined with the term of dc conductivity (σ_{dc}), as follows:

$$\varepsilon^* = \varepsilon' - j\varepsilon'' = \varepsilon_\infty + \frac{\varepsilon_s - \varepsilon_\infty}{1+\left(j\omega\tau\right)^\alpha} - j\frac{\sigma_{dc}}{\omega\varepsilon_0} \tag{4.3}$$

where ε_s and ε_∞ are the static and the high frequency limits of dielectric permittivity, respectively, τ s is the relaxation time, and α is a constant ($0 \le \alpha \le 1$). For an ideal Debye relaxation, $\alpha = 1$, the dipole moments in materials have a unique relaxation time. In case of α < 1, it implies that the electric dipoles in materials show a distribution of the relaxation time, leading to a broaden peak whose shape is wider than a Debye peak. From the fitting result, we can calculate the dielectric relaxation time (τ) at difference temperatures using the Arrhenius law (Putjuso *et al.*, 2011; Thongbai *et al.*, 2012):

$$\tau = \tau_0 \exp\left(\frac{E_a}{k_B T}\right) \tag{4.4}$$

where E_a is the activation energy for relaxation process, τ_0 is the pre-exponential factor, k_B is the Boltzmann constant, and T is the absolute temperature. Figure 4.35 shows the Arrhenius plots and values for the activation energy energies of grain (E_{ag}). In this condition, the relaxation activation energy (E_a) of undoped TNTs and Fe/Co-doped TNTs can be calculated as summarized in Table 4.8. The relaxation time of all samples decreases with increasing temperature, indicating the faster rate of polarization at high temperature. From the conductivity process, the activation energy for the thermally activated hopping process in grain was calculated by the Arrhenius law (Lin *et al.*, 2008):

$$\sigma_{dc} = \sigma_0 \exp\left(-\frac{E_a}{k_B T}\right) \tag{4.5}$$

where E_a is the activation energy for the conduction, σ_0 is the pre-exponential factor, k_B is the Boltzmann constant and T is the absolute temperature. Figure 4.36 shows the Arrhenius plots of the grain conductivities for undoped TNTs and Fe/Co-doped TNTs samples, plotted in the temperature range from 243 to 303 K (-30 to 30 °C) and the activation energies obtained from fitting by Eq. (4.5). The conductivity increases with increasing temperature as expected from the semiconducting behavior (Sivakumar *et al.*, 2007). The activation energies ($E_{a\sigma dc}$) of undoped TNTs and Fe/Co-doped TNTs can be calculated as summarized in Table 4.8. It can be seen that the activation energy of the undoped TNTs bulks is about 0.451 eV. This value is slightly less than the activation energies ($E_{a\sigma dc}$) obtained for electrical transport in nanotubes, which was reported to be cal. 0.57 eV (Thorne *et al.*, 2005). Therefore, the difference in activation energy between this report and the previous work might be attributed to the difference in surface state between the nanotubes from different condition or the difference in oxygen vacancy concentration. For Fe-doped TNTs, with increasing the concentration of Fe, the activation energies of Fe-doped TNTs samples were found to decrease. From the result of XPS, this acceptor doping Fe makes charge compensation mechanism active to create oxygen vacancy in the lattice, creating electric dipoles. The increase in the dielectric constant might be associated with the decreases in the activation energy. Obviously, the addition of doping Co (x = 0.1 to 0.3) makes the corresponding activation energy increase (~0.61 eV), and $E_{a\sigma dc}$ is almost independent of the variation in the added concentration of Co doping. This could be ascribed to the variation in the grain boundary characters for undoped TNTs and Co-doped TNTs bulks, and the added content of Co changes might be only the thickness of the grain boundary layers but not the intrinsic properties (Lin *et al.*, 2008). For the traditional sodium titanate nanotubes, abundant reports have confirmed that ions and/or electrons are the conductive species at low temperatures. Maurya *et* *al*. (2006) proposed the existence of electronic hopping and/or interlayer ionic conduction or polaron conduction in layered $Na_{2-x}K_xTi_3O_7$ (x =0.2, 0.3, 0.4) and copper doped $Na_{1.7}K_{0.3}Ti_3O_7$ ceramics (Maurya *et al.*, 2006). In addition, Shripal et al. (2007) concluded that electronic hopping with exchangeable interlayer ionic conduction exists in Fe^{3+} doped layered $Na_2Ti_3O_7$ ceramics and manganese doped polycrystalline $Na_2Ti_3O_7$. The increase in the dielectric constant might be associated with the decreases in the activation energy.

Table 4.11 Activation energy (E_a) calculated from relaxation time and conductivity of undoped TNTs and Fe/Co-doped TNTs bulks.

Doping level	Activation energy for relaxation E_a (eV)		Activation energy of conductivity $E_{a\sigma dc}$ (eV)	
	Fe doping	Co doping	Fe doping	Co doping
x=0	0.523	0.523	0.451	0.451
x=0.05	0.530	0.553	0.431	0.344
x=0.1	0.496	0.574	0.412	0.503
x=0.2	0.483	0.733	0.142	0.575
x=0.3	0.479	0.844	0.373	0.609
x=0.4	0.658	0.439	0.420	0.473

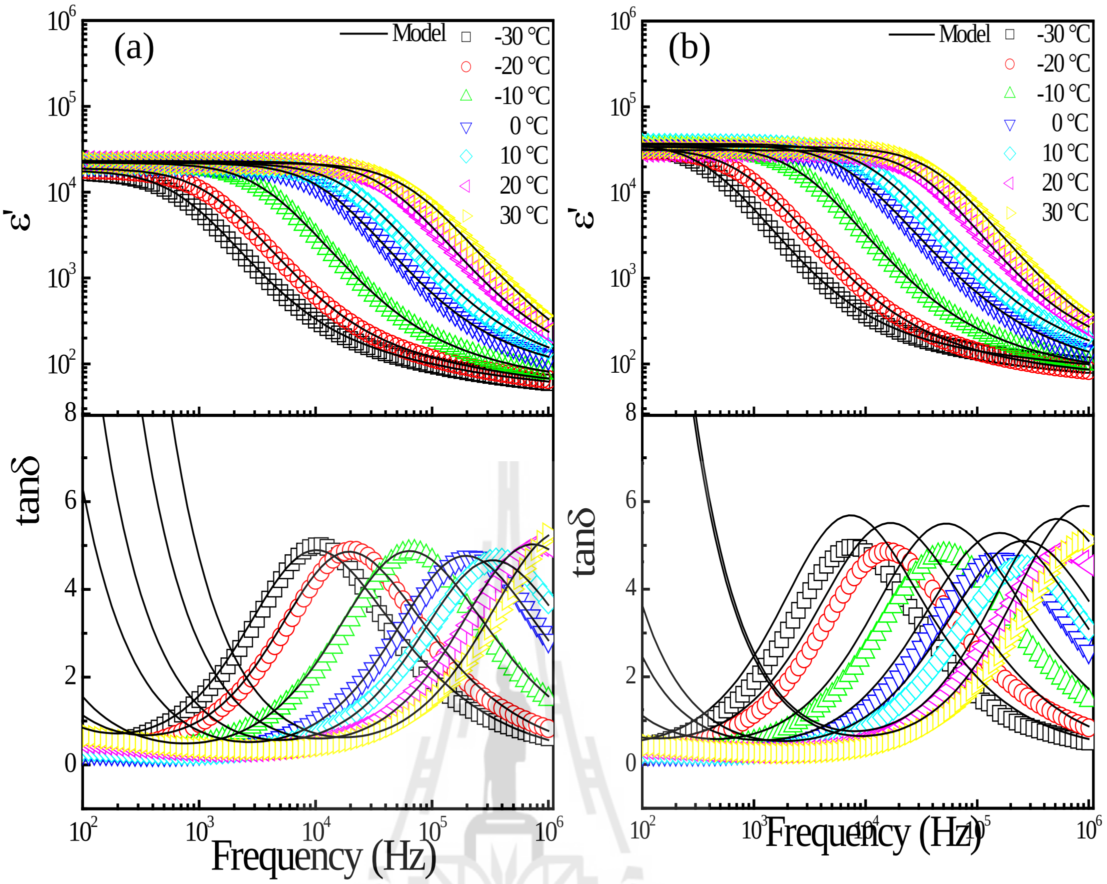

Figure 4.33 Frequency dependence of dielectric constant (ε'), loss tangent (tanδ) and dielectric loss (ε'') of Fe-doped TNTs (a) x = 0 and (b) x = 0.05 over the frequency range from 10^2 - 10^6 Hz as a function of the temperature ranging from -30 to 30 °C.

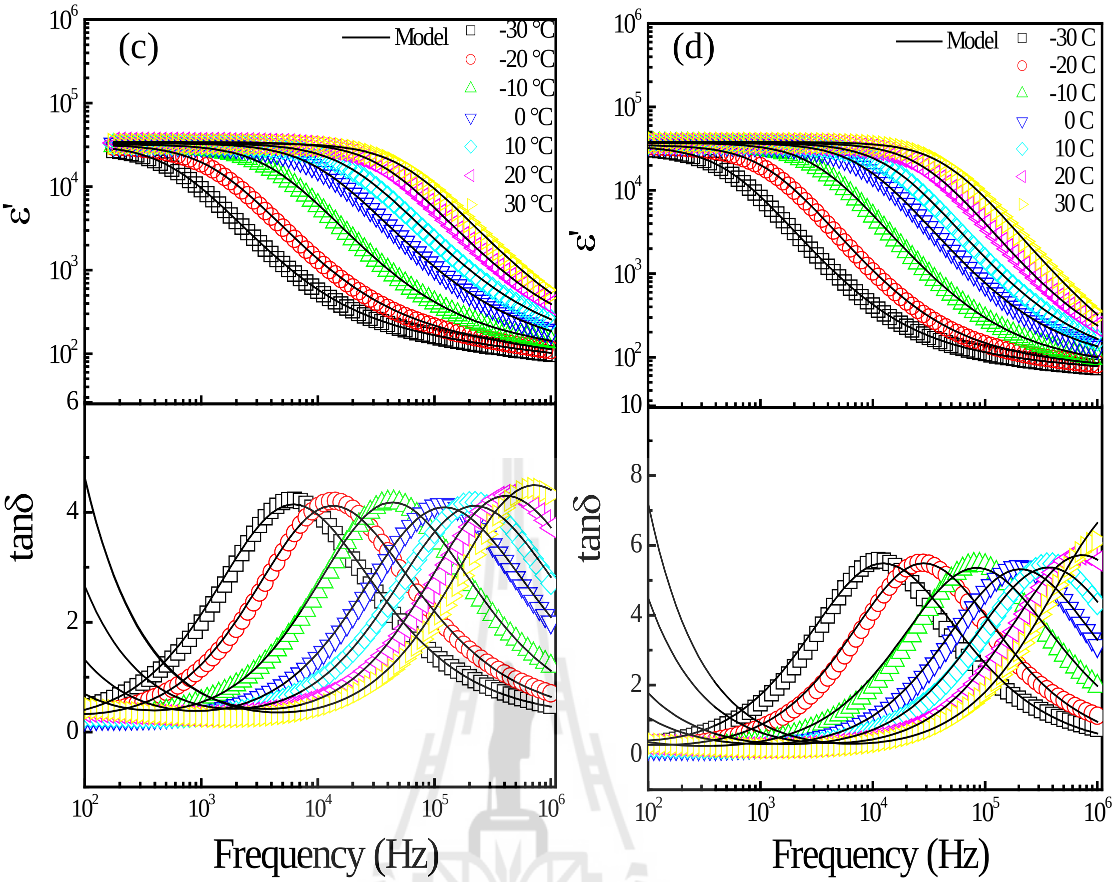

Figure 4.33 Frequency dependence of dielectric constant (ε'), loss tangent (tanδ) and dielectric loss (ε'') of Fe-doped TNTs (c) x = 0.1 and (d) x = 0.2 over the frequency range from 10^2 - 10^6 Hz as a function of the temperature ranging from -30 to 30 °C. (Cont.)

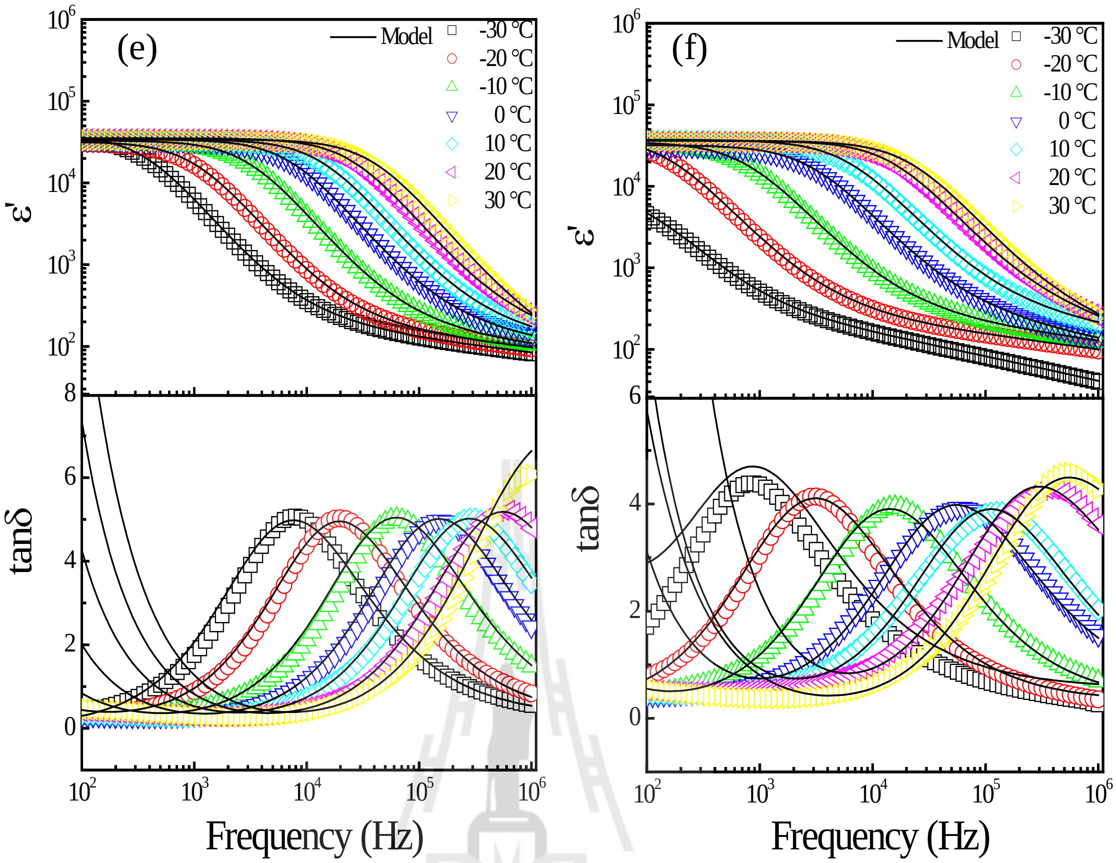

Figure 4.33 Frequency dependence of dielectric constant (ε'), loss tangent (tanδ) and dielectric loss (ε'') of Fe-doped TNTs (e) x = 0.3 and (f) x = 0.4 over the frequency range from 10^2 - 10^6 Hz as a function of the temperature ranging from -30 to 30 °C. (Cont.)

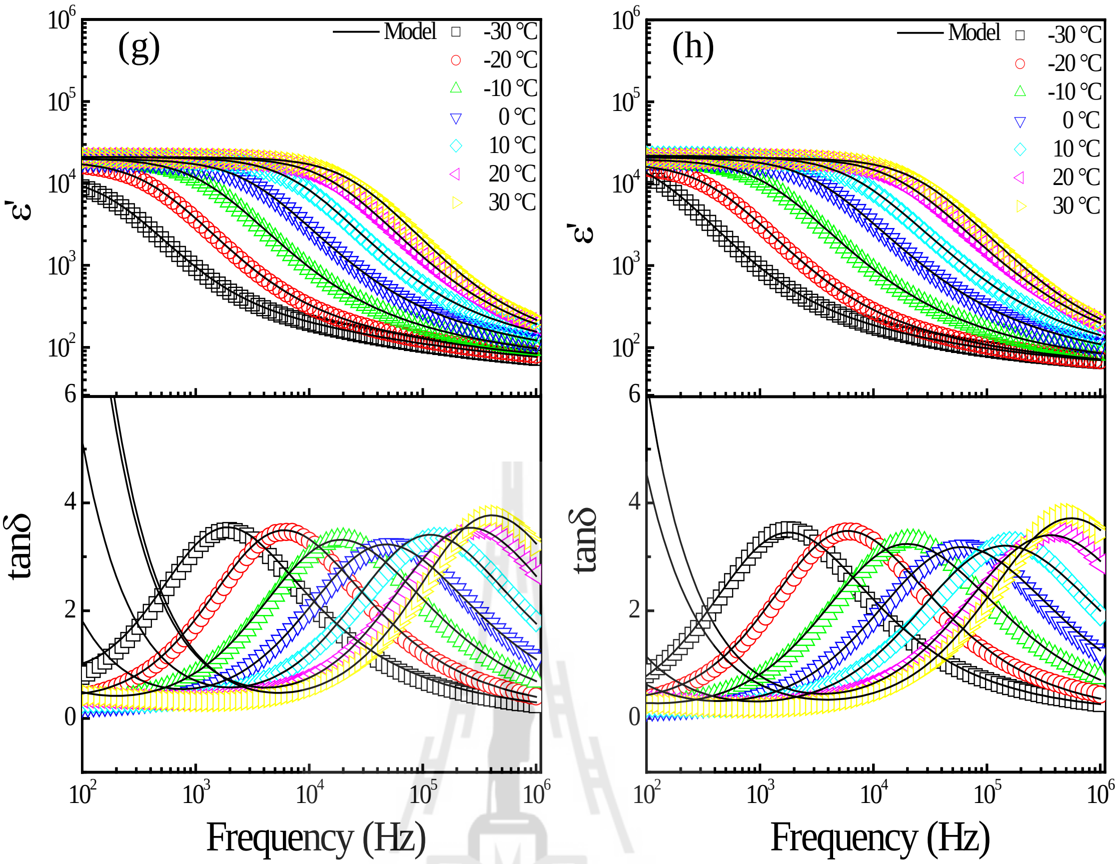

Figure 4.34 Frequency dependence of dielectric constant (ε'), loss tangent (tanδ) and dielectric loss (ε'') of Co-doped TNTs (a) x = 0.05 and (b) x = 0.1 over the frequency range from 10^2 - 10^6 Hz as a function of the temperature ranging from -30 to 30 °C.

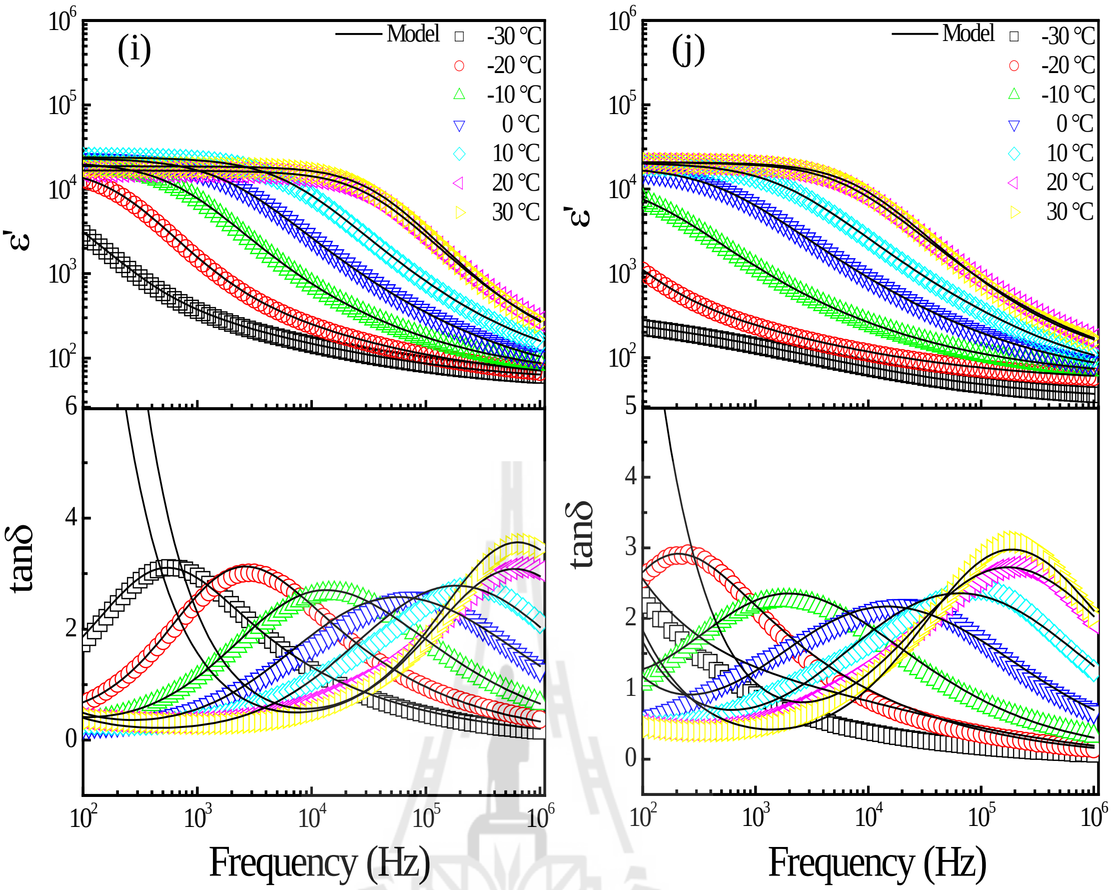

Figure 4.34 Frequency dependence of dielectric constant (ε'), loss tangent (tanδ) and dielectric loss (ε'') of Fe-doped TNTs (c) x = 0.2 and (d) x = 0.3 over the frequency range from 10^2 - 10^6 Hz as a function of the temperature ranging from -30 to 30 °C. (Cont.)

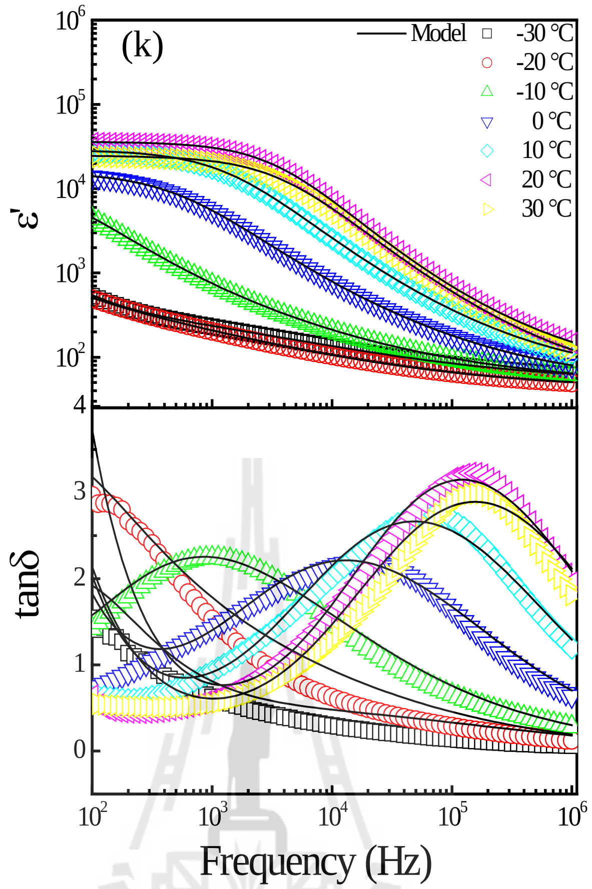

Figure 4.34 Frequency dependence of dielectric constant (ε'), loss tangent (tanδ) and dielectric loss (ε'') of (k) Fe-doped TNTs at x = 0.4 over the frequency range from 10^2 - 10^6 Hz as a function of the temperature ranging from -30 to 30 °C. (Cont.)

.

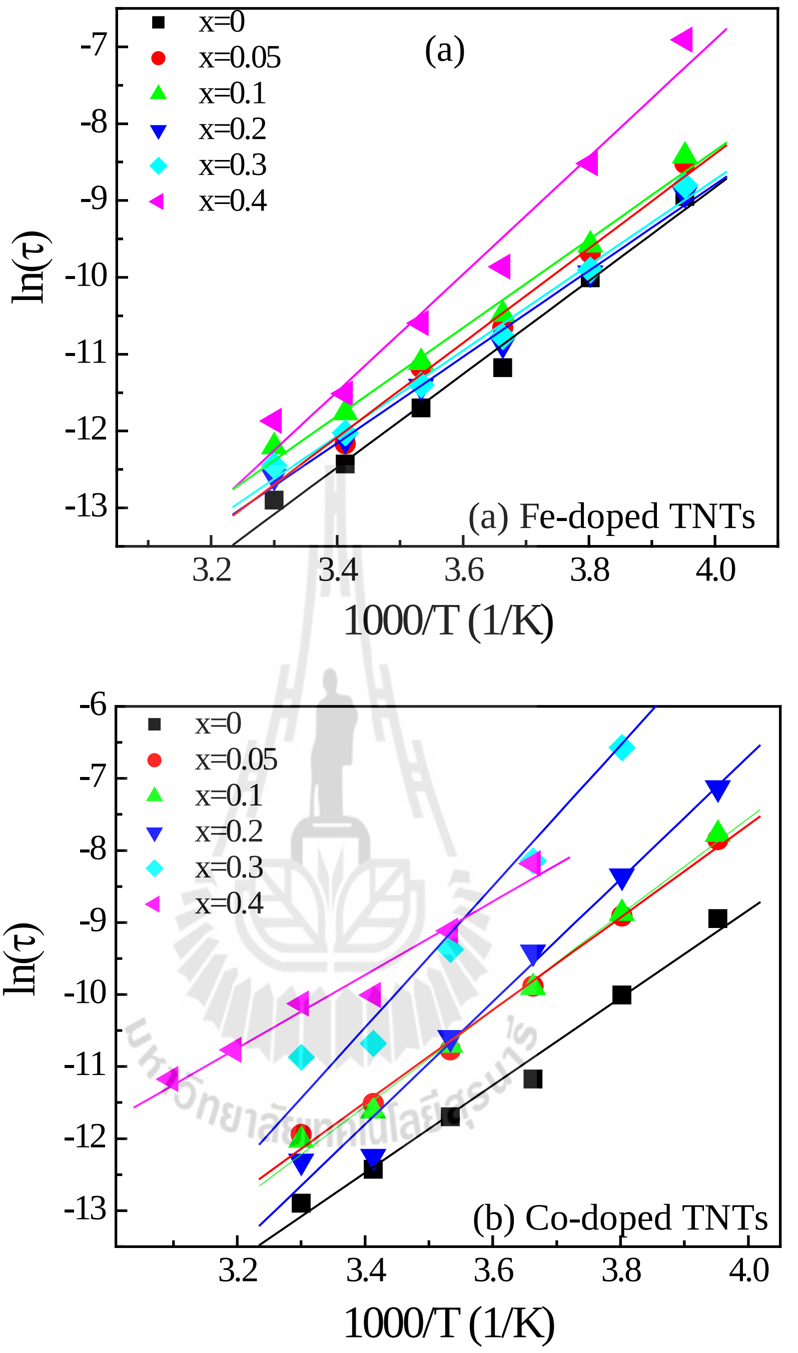

Figure 4.35 The temperature dependence of relaxation time of (a) Fe-doped TNTs and (b) Co-doped TNTs prepared at 130 °C for 24 h; the solid lines are the data fitted by an Arrhenius law.

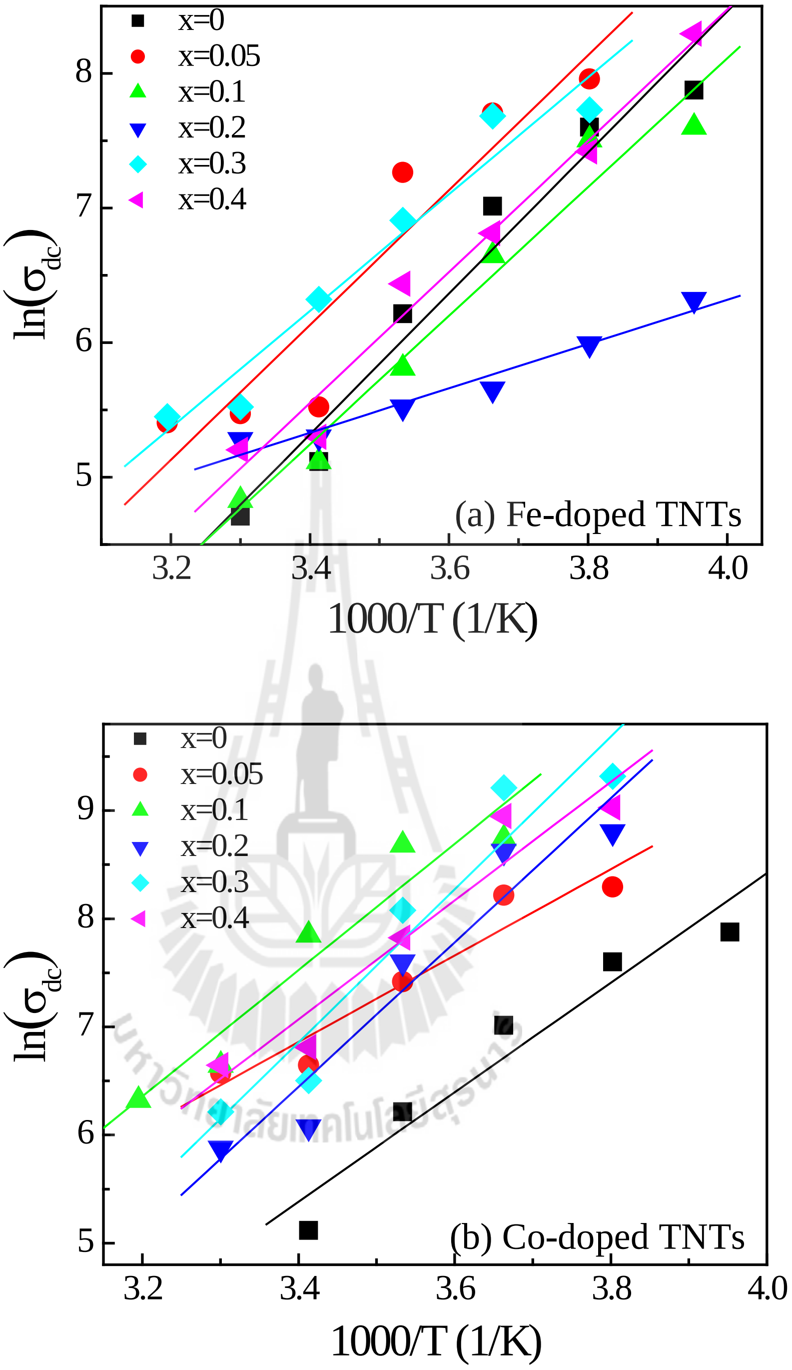

Figure 4.36 The temperature dependence of conductivity of (a) Fe-doped TNTs and (b) Co-doped TNTs prepared at 130 °C for 24 h; the solid lines are the data fitted by an Arrhenius law.

4.9.3 Impedance spectroscopy of undoped TNTs and Fe/ Co-doped TNTs samples

The impedance of electroceramics has been modeled using an equivalent circuit consisting of two parallel *RC* elements related in series: one for the semiconductive grain contribution, and the other for grain boundary (GB) response (Xue *et al.*, 2015; Laokul *et al.*, 2012). For such a circuit, each *RC* element gives rise to (ideally) a semicircular arc in impedance complex plane plots, Z^* and a plateau in spectroscopic plots of the real component of the permittivity (or *C*) (Sinclair *et al.*, 2002). Normally, the complex impedance, Z^* is calculated as

$$Z^* = Z' - jZ'' = \frac{1}{j\omega C_0 \varepsilon^*} \tag{4.6}$$

where Z' and Z'' are the real part and imaginary part of complex impedance (Z^*). Z' and Z'' are associated with the resistance and capacitance of a materials, respectively.

Figures 4.37-4.38 show the complex impedance plane plot at two temperature ranges low and relative high. Figures 4.37(a)-(b) show the complex impedance Z^* plot (Z' *vs* Z'') of the undoped TNTs sample at room temperature. The observed two semicircular arcs indicate that there are at least two electrical responses in bulk TNTs. The large semicircle at low frequency can be assigned to the resistance of grain boundary (R_{gb}, GB) while the small one at high frequency represents the resistance of grain (R_g) (Putjuso *et al.*, 2011; Sinclair *et al.*, 2002; Xue *et al.*, 2015). These impedance semicircles became smaller with increasing temperature, confirming the semiconductor-like behavior of these materials (Laokul *et al.*, 2012). In addition, it is found that the diameter of the small semicircle decreases with increasing temperature like the large semicircle does. First of all, the impedance spectra of Fe-doped TNTs at x = 0.05 (see in Figure 4.37(c)-(d)) are used as the example to describe the general feature of the impedance spectra instead of Fe/Co-doped samples. These impedance semicircles decrease with increasing temperature. However, for Fe-doped TNTs at x = 0.4 in the temperature of -50 and -40 °C and Co-doped TNTs in some low temperature, only the semicircular arc at a low frequency range can be observed in the measured frequency range. These results are similar to those reported for CCTO and CCTO/ST ceramics (Thongbai *et al.*, 2012; Xue *et al.*, 2015). As a result, it indicates that synthetic Fe/Co-doped TNTs bulks are electrically heterogeneous, consisting of semiconducting grain and insulating GBs.

According to the complex impedance can be expressed as

$$Z^* = Z' - jZ'' = \frac{1}{R_g^{-1} + j\omega C_g} + \frac{1}{R_{gb}^{-1} + j\omega C_{gb}}, \qquad (4.7)$$

$$Z' = \frac{R_g}{1+(\omega R_g C_g)^2} + \frac{R_{gb}}{1+(\omega R_{gb} C_{gb})^2}, \qquad (4.8)$$

$$Z'' = R_g\left[\frac{\omega R_g C_g}{1+(\omega R_g C_g)^2}\right] + R_{gb}\left[\frac{\omega R_{gb} C_{gb}}{1+(\omega R_{gb} C_{gb})^2}\right], \qquad (4.9)$$

The complex impedance plan plot $-Z''$ vs. Z', obtained from equations (4.7) to can be almost used to fit the experimental data. Usually, $-Z''$ vs. Z' is greater ascribed by using the Cole-Cole equation, is given by

$$Z^* = Z' - jZ'' = \frac{1}{R_g^{-1} + (j\omega C_g)^{\alpha}} + \frac{1}{R_{gb}^{-1} + (j\omega C_{gb})^{\beta}} \tag{4.10}$$

where α and β are constant values and $0 \leq \alpha$, $\beta \leq 1$.

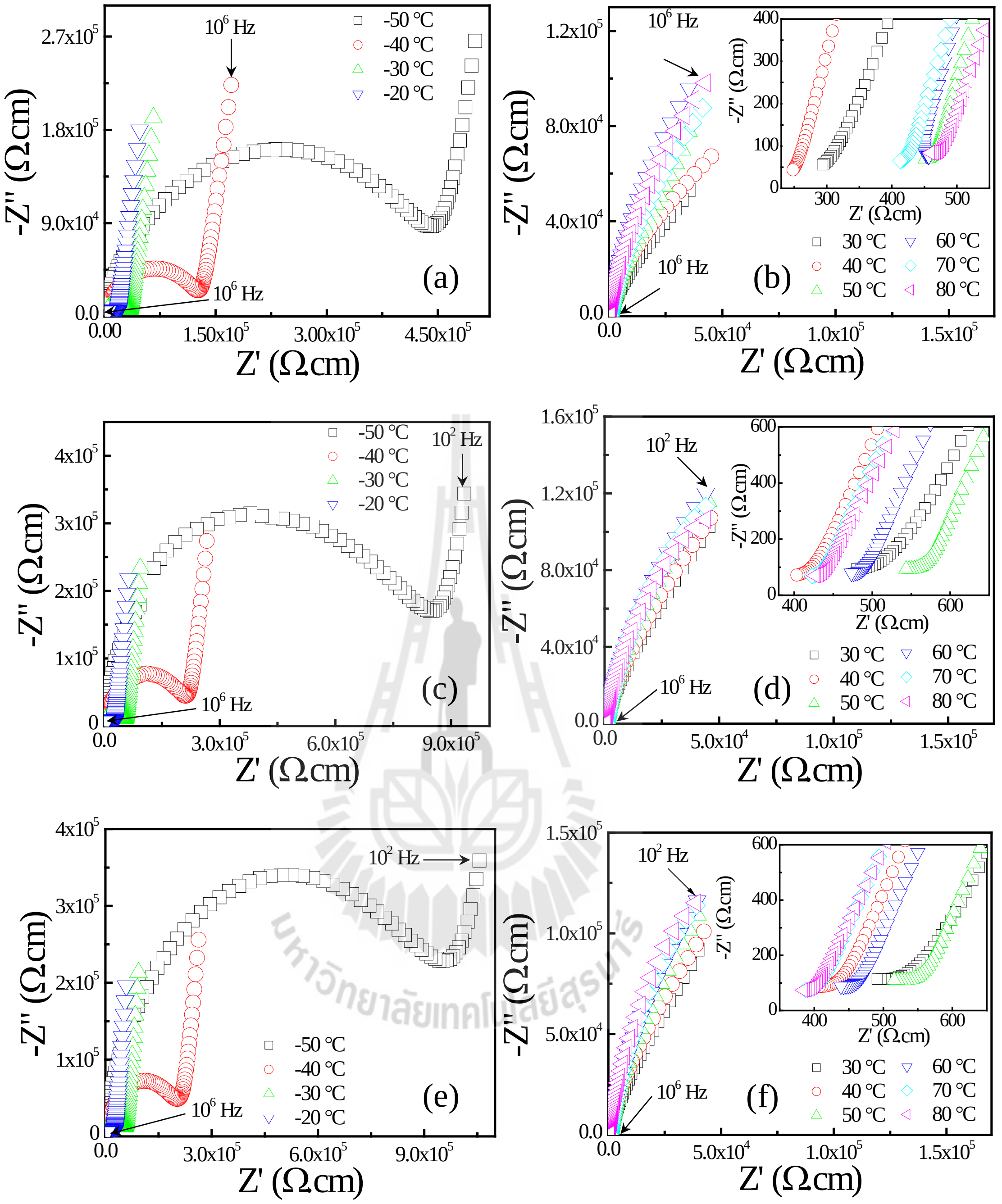

Figure 4.37 Impedance spectra of Fe-doped TNTs (a)-(b) x = 0, (c)-(d) x = 0.05 and (e)-(f) x = 0.1 prepared by hydrothermal method at 130 °C for 24 h at various temperatures; inset is an expanded view of high frequency data close to the origin.

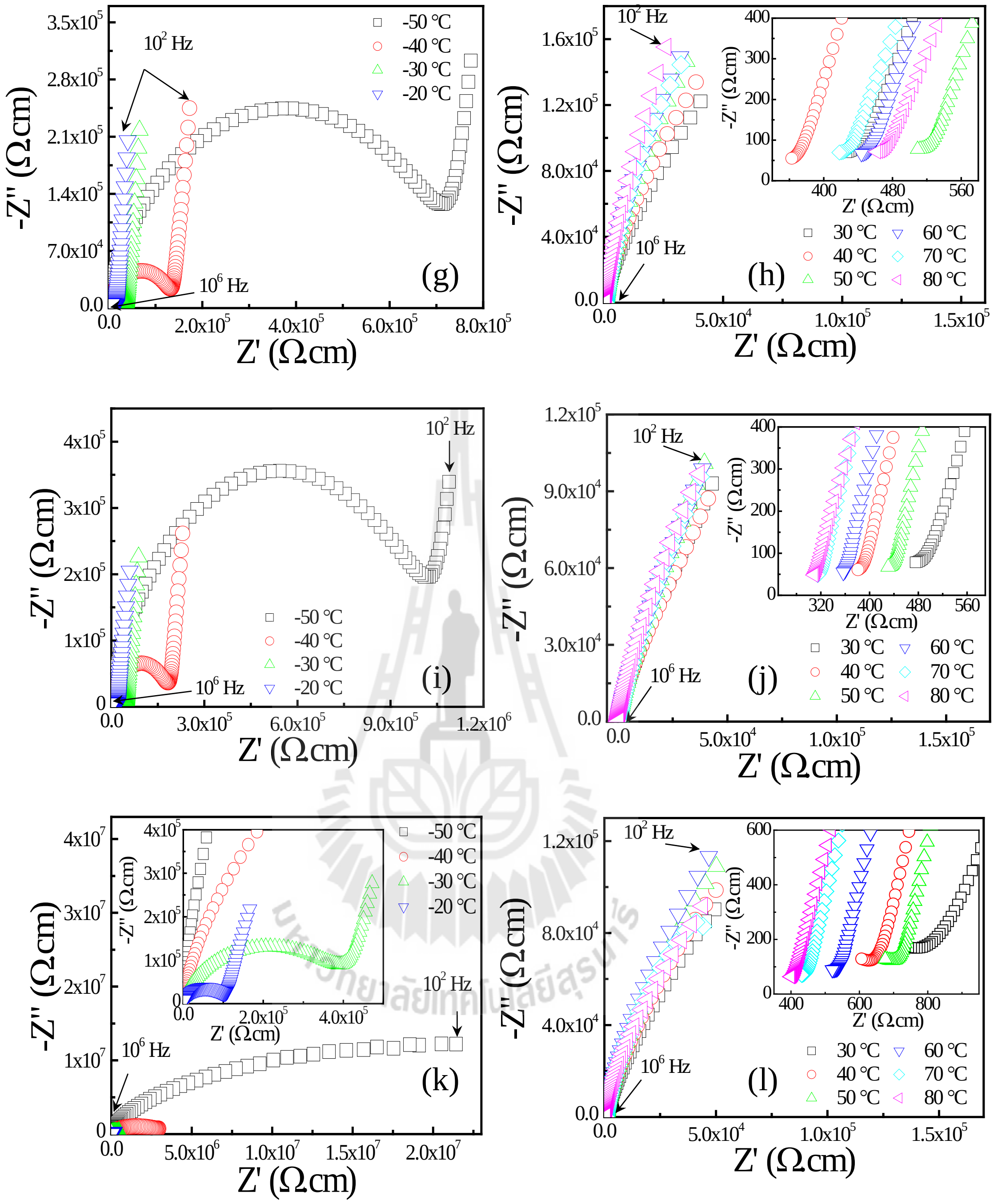

Figure 4.37 Impedance spectra of Fe-doped TNTs (g)-(h) x = 0.2, (i)-(j) x = 0.3 and (k)-(l) x = 0.4 prepared by hydrothermal method at 130 °C for 24 h at various temperatures; inset is an expanded view of high frequency data close to the origin. (Cont.)

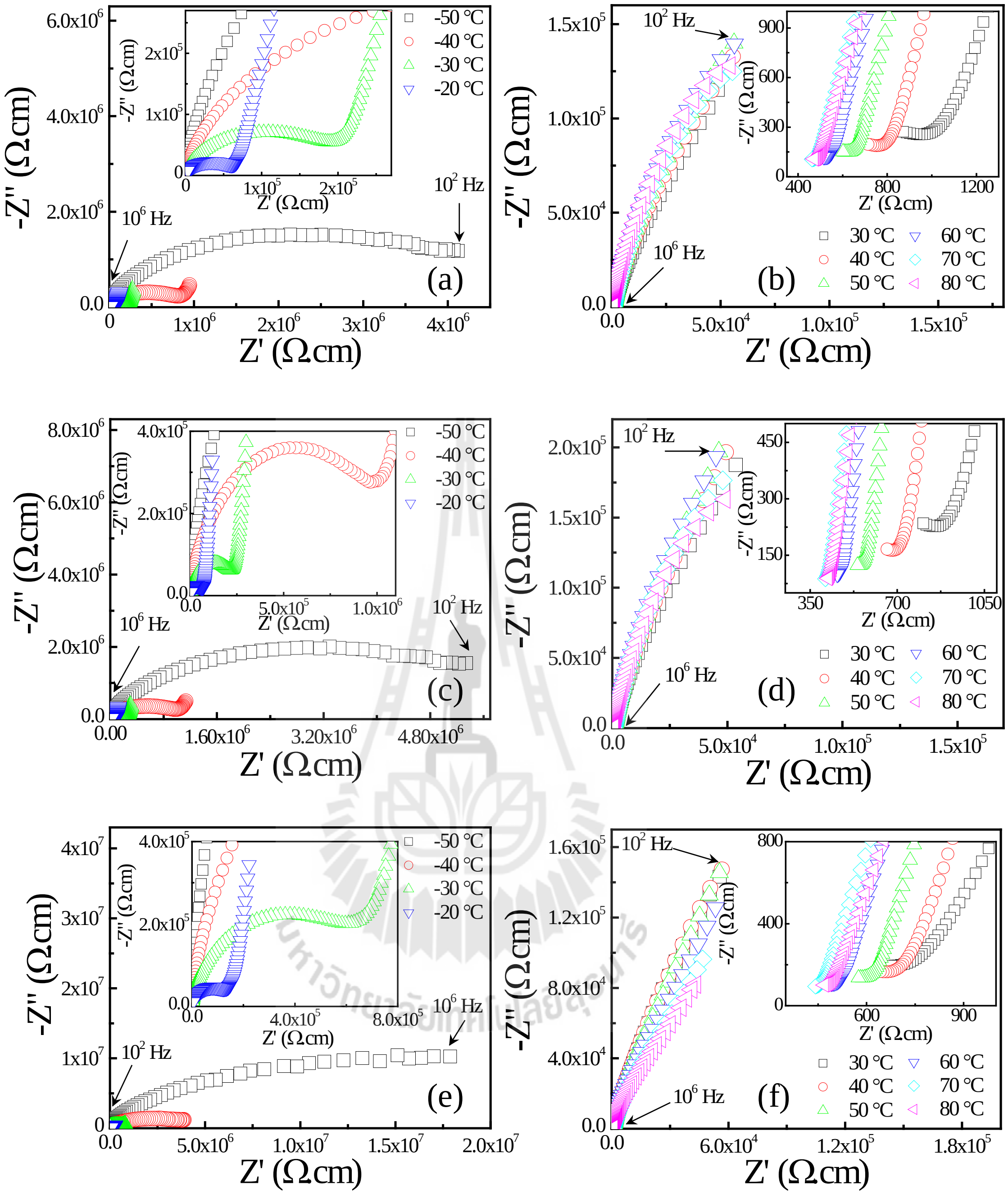

Figure 4.38 Impedance spectra of Co-doped TNTs (a)-(b) x = 0.05, (c)-(d) x = 0.1 and (e)-(f) x = 0.2 prepared by hydrothermal method at 130 °C for 24 h at various temperatures; inset is an expanded view of high frequency data close to the origin.

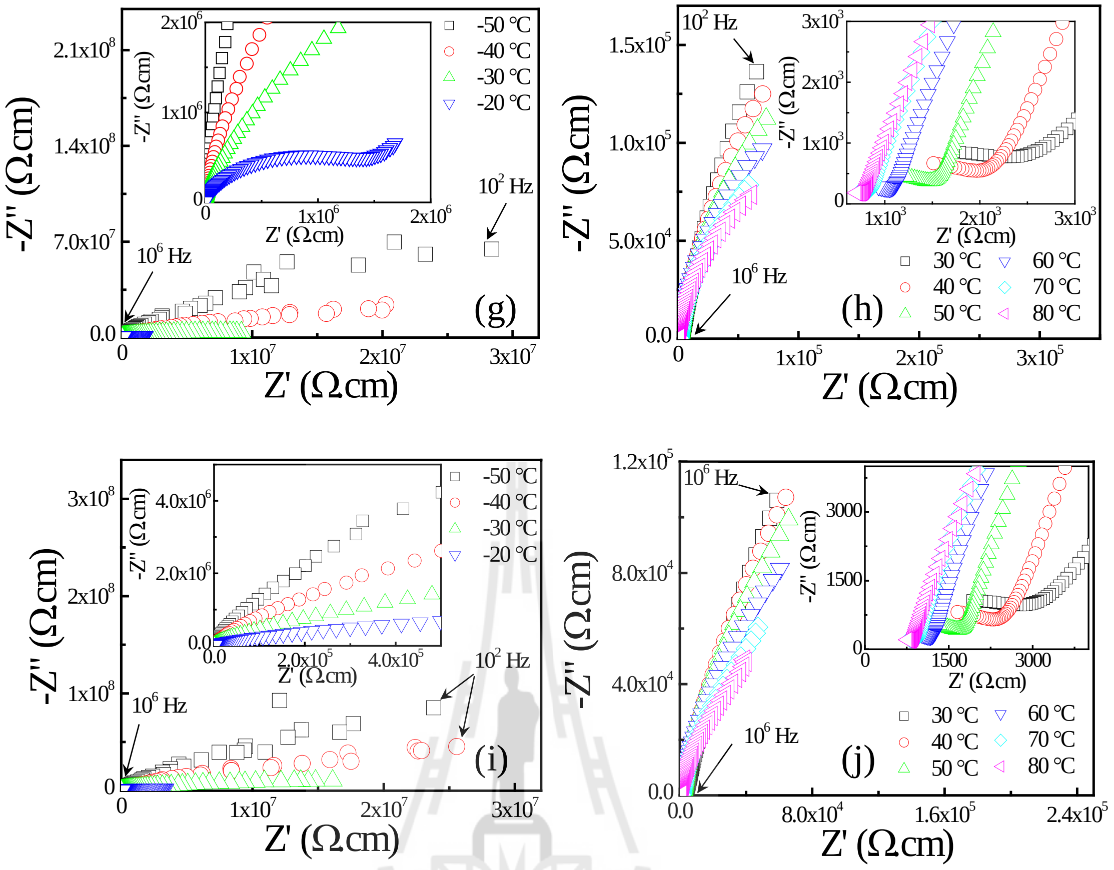

Figure 4.38 Impedance spectra of Co-doped TNTs (g)-(h) x = 0.3 and (i)-(j) x = 0.4 prepared by hydrothermal method at 130 °C for 24 h at various temperatures; inset is an expanded view of high frequency data close to the origin. (Cont.)

4.9.4 The effect of Fe/Co-doping concentration on dielectric properties

Figure 4.39 illustrates the Fe/Co doping concentration dependence of the dielectric constant (ε′) and loss tangent (tanδ) at 10^3 Hz and 30 °C. Obviously, the dielectric constant of the TNTs-based samples increases as the Fe doping and decreases as Co doping, in particular, the loss tangent decreases. Figures 4.40 and 4.41 show the frequency dependence of dielectric properties dielectric constant (ε′) and loss tangent (tanδ) at the 30 °C of Fe-doped TNTs and Co-doped TNTs, respectively with difference concentrations; inset is an expanded view of low frequency data close to the origin. All the samples exhibit high dielectric behavior with a dielectric constant (ε′) of about 10^4–10^5 at 100 Hz and room temperature. Fe-doped TNTs for $x \leq 0.05$, at the frequency of 10^3 Hz, the ε′ increases with increasing concentrate of Fe doping ions. This may be due to effect of phase transition of the TNTs-based compounds. However, when $x \geq 0.3$, the ε′ decreases with increasing concentrate of Fe doping ions compared to the samples with x = 0-0.2. This may be due to the amount of Fe doping in TNTs-based compounds, which can cause a lower carriers mobility for the Fe-doped TNTs samples that contain low concentration of Fe doping ions. The values of ε′ and tanδ at 10^3 Hz and 30 °C of all the samples are summarized in Table 4.9. Moreover, tanδ values of the Fe/Co-doped TNTs samples are lower than those of the undoped TNTs sample. It is possible that Fe^{2+} or Fe^{3+} can replace Ti^{4+}. This substitution pins the oxygen vacancies causing the flow of mobile charge easier, leading to the increases in ε′ and decreases in tanδ for the Fe-doped TNTs. Figure 4.80 shows the dielectric properties of the undoped and Co-doped TNTs. As shown in Figure 4.81, in the frequency range of 10^4 to 10^6 Hz, it is found that ε′ rapidly decreases with increasing frequency. The rapid decrease in ε′ is accompanied by the observed tanδ peak in all the samples. This indicates the dielectric relaxation behavior in dielectric materials. For $x \leq 0.2$, it is likely that the relaxation peak in the samples slightly shifts to lower frequencies. However, when $x \geq 0.3$, the relaxation peak significantly moves to lower frequencies than in the samples with $x = 0$ to 0.2. This may be due to the decrease in trititanate phase, which can induce lower carrier mobility in the Co-doped TNTs with high Co doping concentration. The dielectric response behavior is closely related to the Maxwell-Wagner polarization. These different dielectric properties between the undoped TNTs and Fe/Co-doped TNTs samples should be related to the short-range motion of electrons and other charge carriers (e.g., atoms, molecules, ions, holes, vacancies, and hydration water molecules stored in the sample) under the influence of the applied electric field.

In addition, the electrical properties of the internal interface were characterized by impedance spectroscopy, which is a powerful tool for separating the grain and GB effects. Impedance complex plane plots (Z^* plots) at a temperature of 30 °C and their expanded view of high frequency data close to the origin for all the samples are shown in Figure 4.42 and inset (a), respectively. As shown in inset (a), the non-zero intercepts of all the samples are also observed. Thus, these results indicate the existence of two electrical responses in the samples, i.e., grain and grain boundary. It can be seen that Fe or Co doping has influenced the impedance characteristic of the high and low electrical-resistivity parts, especially the low electrical-resistivity part. The expected diameter of each semicircular arc indicating the grain boundary tends to decrease with the increasing concentration of Fe or Co doping. These results are similar to those reported for Sr-doped CCTO ceramics prepared by a conventional solid state reaction method (Xue *et al.*, 2009). This phenomenon suggests that the Fe or Co doping influences the TNTs by at least two possible ways, substitution and second phase, with cooperate to result in that at a certain doping concentration of the electrical properties occur. Therefore, the dielectric response behavior in Fe/Co-doped TNTs might be significantly influenced by the electrical characteristics of GBs as well.

Table 4.12 Summary of dielectric constant (ε') and loss tangent (tanδ) at 30 °C and 10^3 Hz of undoped TNTs and Fe/Co-doped TNTs.

Doping Level	Dielectric constant (ε')		tanδ	
	Fe doping	Co doping	Fe doping	Co doping
x = 0	4.07×10^4	4.07×10^4	0.397	0.397
x = 0.05	4.68×10^4	2.78×10^4	0.273	0.316
x = 0.1	4.23×10^4	2.47×10^4	0.278	0.197
x = 0.2	4.63×10^4	2.77×10^4	0.189	0.288
x = 0.3	4.56×10^4	2.5×10^4	0.302	0.443
x = 0.4	4.47×10^4	1.3×10^4	0.371	0.551

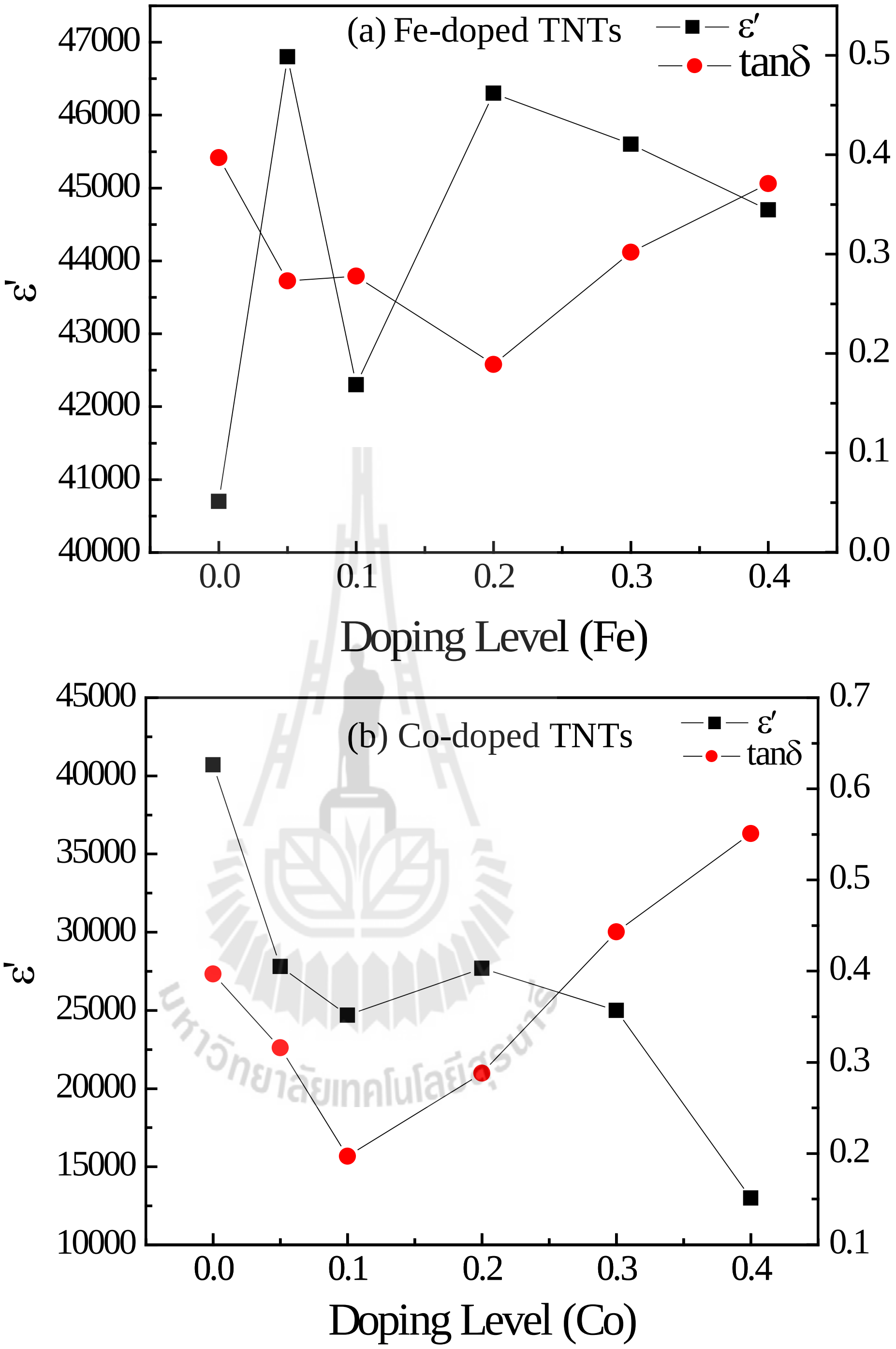

Figure 4.39 Impedance spectra of (a) Fe-doped TNTs and (b) Co-doped TNTs prepared by hydrothermal method at 130 °C for 24 h at 30 °C; inset is an expanded view of high frequency data close to the origin.

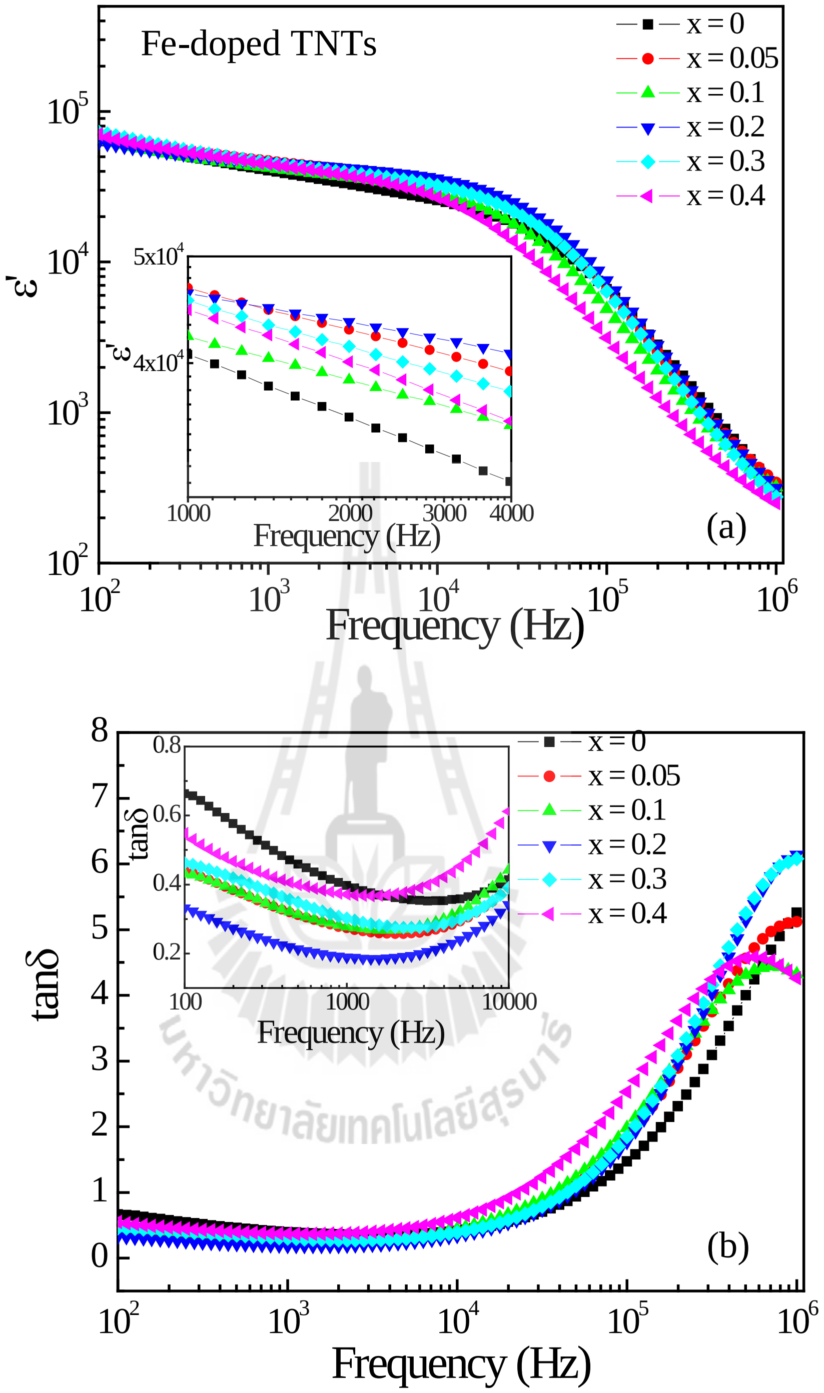

Figure 4.40 Frequency dependence of dielectric properties dielectric constant (ε') (a) and (b) loss tangent (tanδ) at the 30 °C of undoped TNTs and Fe-doped TNTs with difference concentration; inset is an expanded view of low frequency data close to the origin.

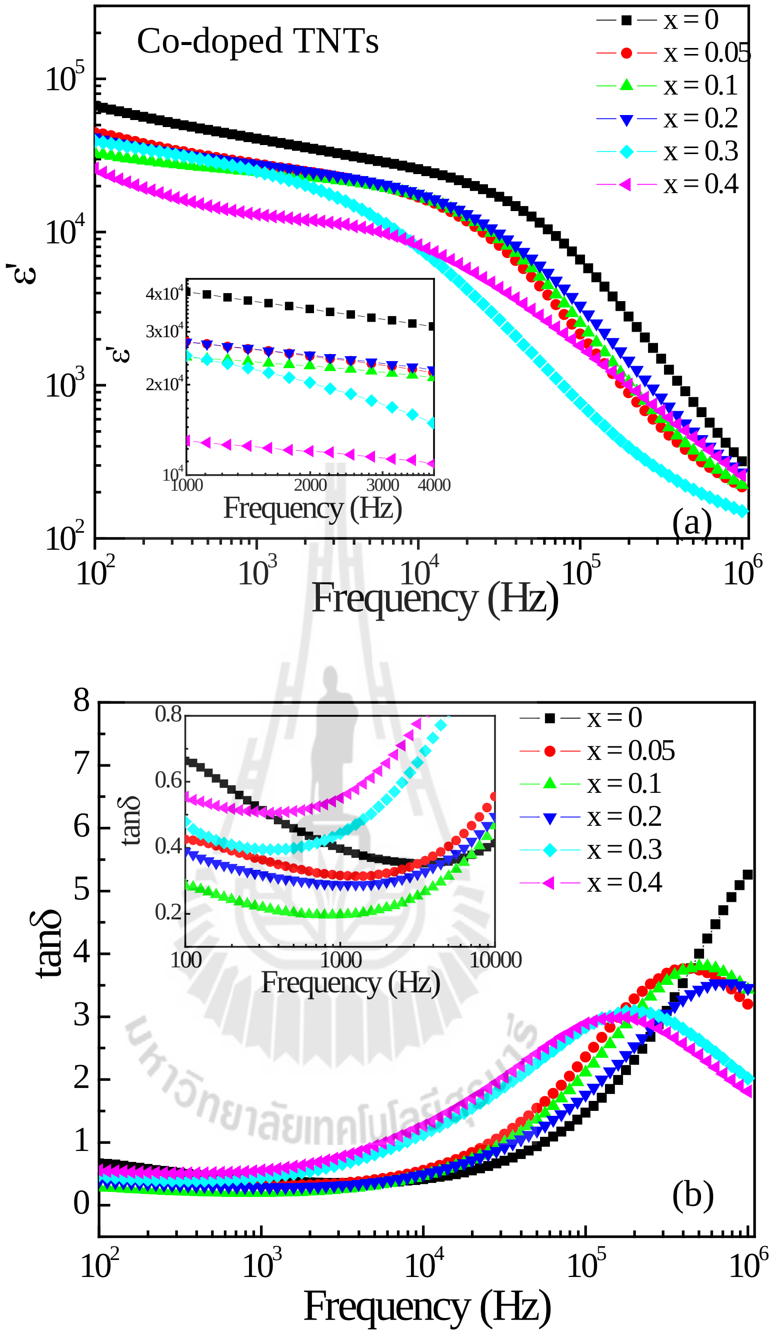

Figure 4.41 Frequency dependence of dielectric properties dielectric constant (ε') (a) and (b) loss tangent (tanδ) at the 30 °C of undoped TNTs and Co-doped TNTs with difference concentration inset is an expanded view of low frequency data close to the origin.

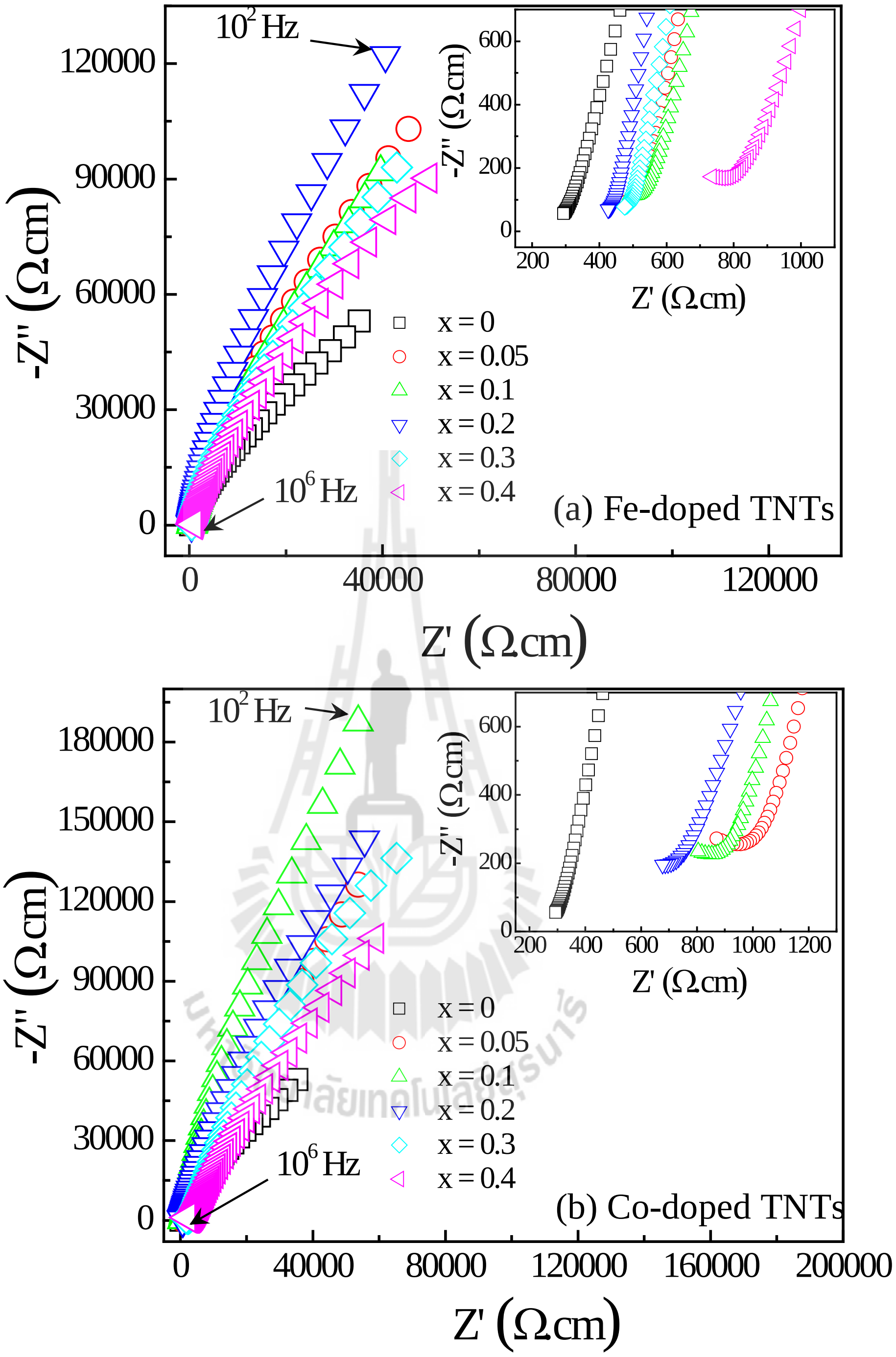

Figure 4.42 Impedance spectra of (a) Fe-doped TNTs and (b) Co-doped TNTs prepared by hydrothermal method at 130 °C for 24 h at 30 °C; inset is an expanded view of high frequency data close to the origin.

4.9.5 The effect of the dc bias on the dielectric properties for undoped TNTs and Fe/Co-doped TNTs

In general, the electronic and ionic polarizations are main contributors at high frequencies, whereas at low frequencies, the dipolar and interfacial polarizations are the only contributors. In case of dc bias voltage, slight variation was observed in the low frequency region where the grain boundary contribution of dielectric constant is resolved (Prakash *et al.*, 2013). Figures 4.43-4.44 show the effect of applied dc bias on the frequency dependence of ε' and tanδ for undoped TNTs and Fe/Co-doped TNTs samples at room temperature. These results strongly support the electrode effect on the dielectric properties of the bulk TNTs. For undoped TNTs, the ε' at the frequency range of 10^2–10^4 Hz for the TNTs decreases with the increasing applied voltage from 0 to 10 V, whereas ε' values at frequencies higher than 2.5 kHz do not change (Figure 4.43(a)). These results suggest that, with the increasing applied voltage, the accumulated charge carriers are becoming more and more able to overcome the potential at the grain boundary. This implies that the accumulated charge carriers become mobile charges. Consequently, the intensity of the space charge polarization at this region is decreased by the increase in the applied voltage, while the conductivity increased due to the increase in the mobile charge. This is confirmed by the observed exponential increase in a low-frequency tanδ under the higher applied voltage, as shown in Figure 4.43(a). The tanδ of the bulk TNTs under 0–10 V gradually increases with increasing frequencies in the lower frequency range (< ~10^4 Hz) and then increases at the higher frequency ranges (10^4–10^5 Hz), and finally decreases at the higher frequency ranges (< ~10^5 Hz). The rapid decrease in the dielectric constant and the corresponding relaxation peak of the loss tangent appeared, indicating the relaxation behavior. The dielectric constant (ε') of the Fe-doped TNTs for x = 0.05 as a function of frequency under the dc-bias voltage is illustrated in Figure 4.43(b). From this figure, it is found that, the dielectric constant (ε') of the sample increases gradually under the dc-bias 0-10 V in the low frequency (10^2 Hz). The application of dc-bias enables the release of conduction electrons and makes the electron hopping easier through the nanotubes, resulting in remarkable contributions to space charge polarization within the nanotubes. The overall dielectric relaxation behavior of undoped TNTs and Fe/Co-doped TNTs samples, it is also seen that the dielectric constant of the samples decreases logarithmically with frequency. This logarithmic variation can be explained in terms of the response of the dipoles to the applied electrical field. At the low frequencies, the dipoles within the sample get enough time to orient themselves and therefore the dielectric constant is high. However, at the high frequencies, the dipoles cannot follow the change in the electric field and therefore the relaxation phenomena takes place and ε' becomes low and nearly independent on frequency. However, for Fe doping x = 0.05 and Co doping x = 0.05 and 0.1, the dielectric constant of the sample increases with application of dc-bias and after a certain relaxation frequency dielectric constant of the sample become low and nearly independent on the frequency.

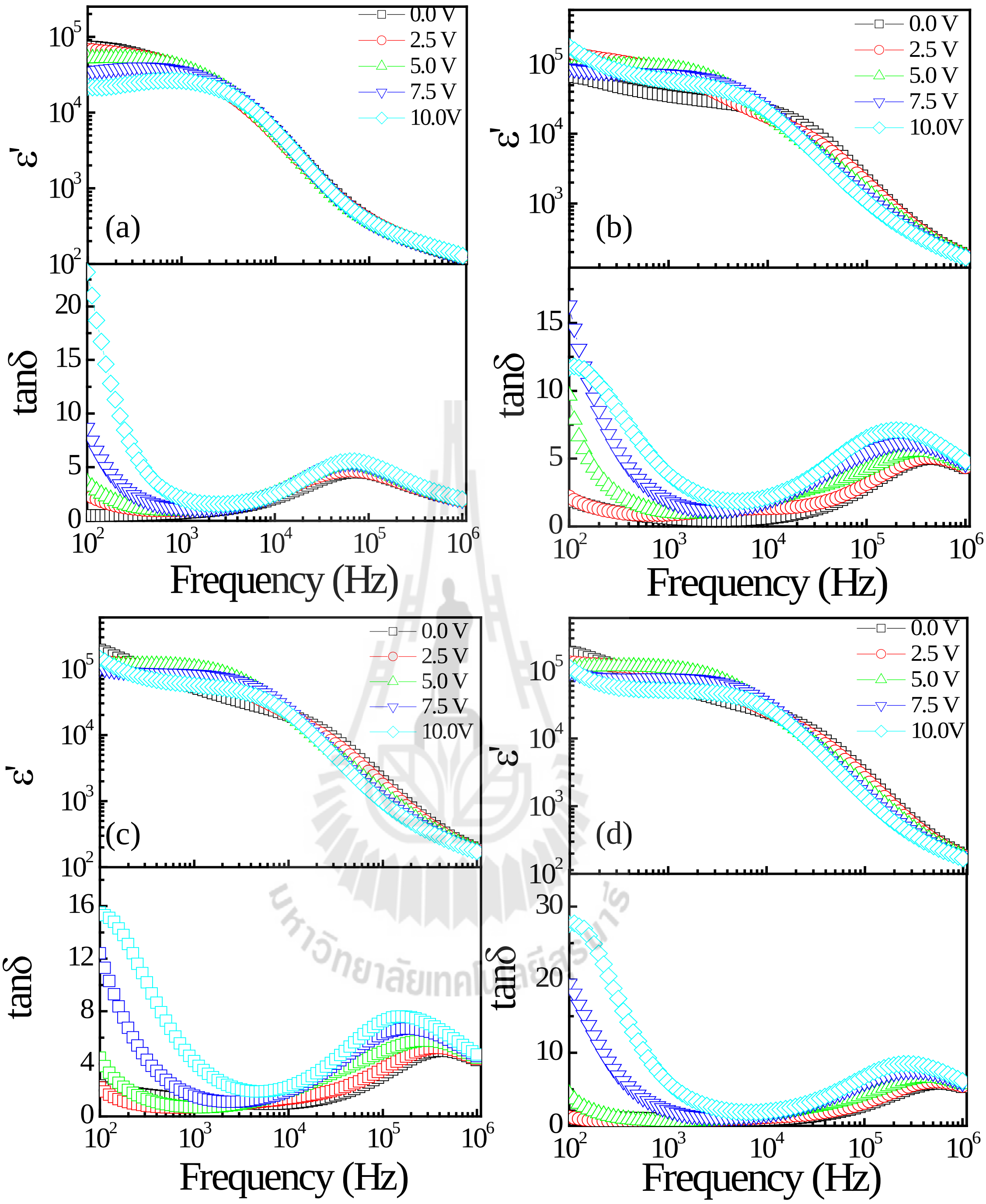

Figure 4.43 Frequency dependence of ε' and tanδ as a function dc bias voltage under 0–10 V at room temperature of Fe-doped TNTs (a) x = 0, (b) x = 0.05, (c) x = 0.1 and (d) x = 0.2 prepared by hydrothermal method at 130 °C for 24 h.

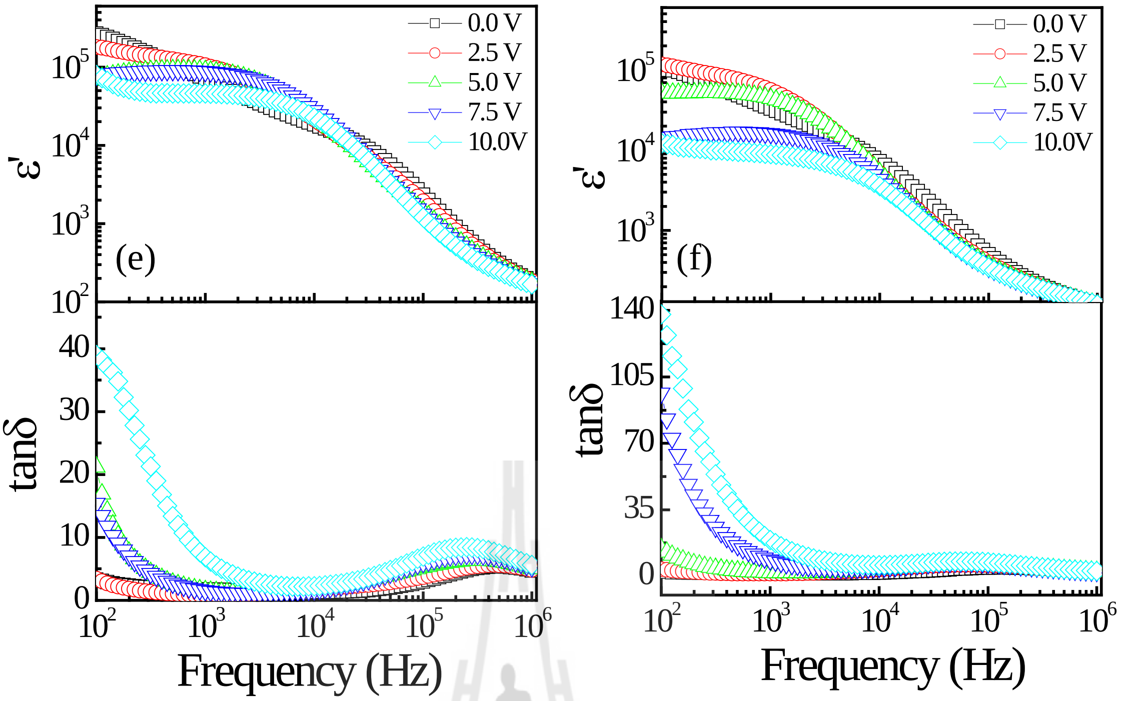

Figure 4.43 Frequency dependence of ε' and tanδ as a function dc bias voltage under 0–10 V at room temperature of Fe-doped TNTs (e) x = 0.3 and (f) x = 0.4 prepared by hydrothermal method at 130 °C for 24 h. (Cont.)

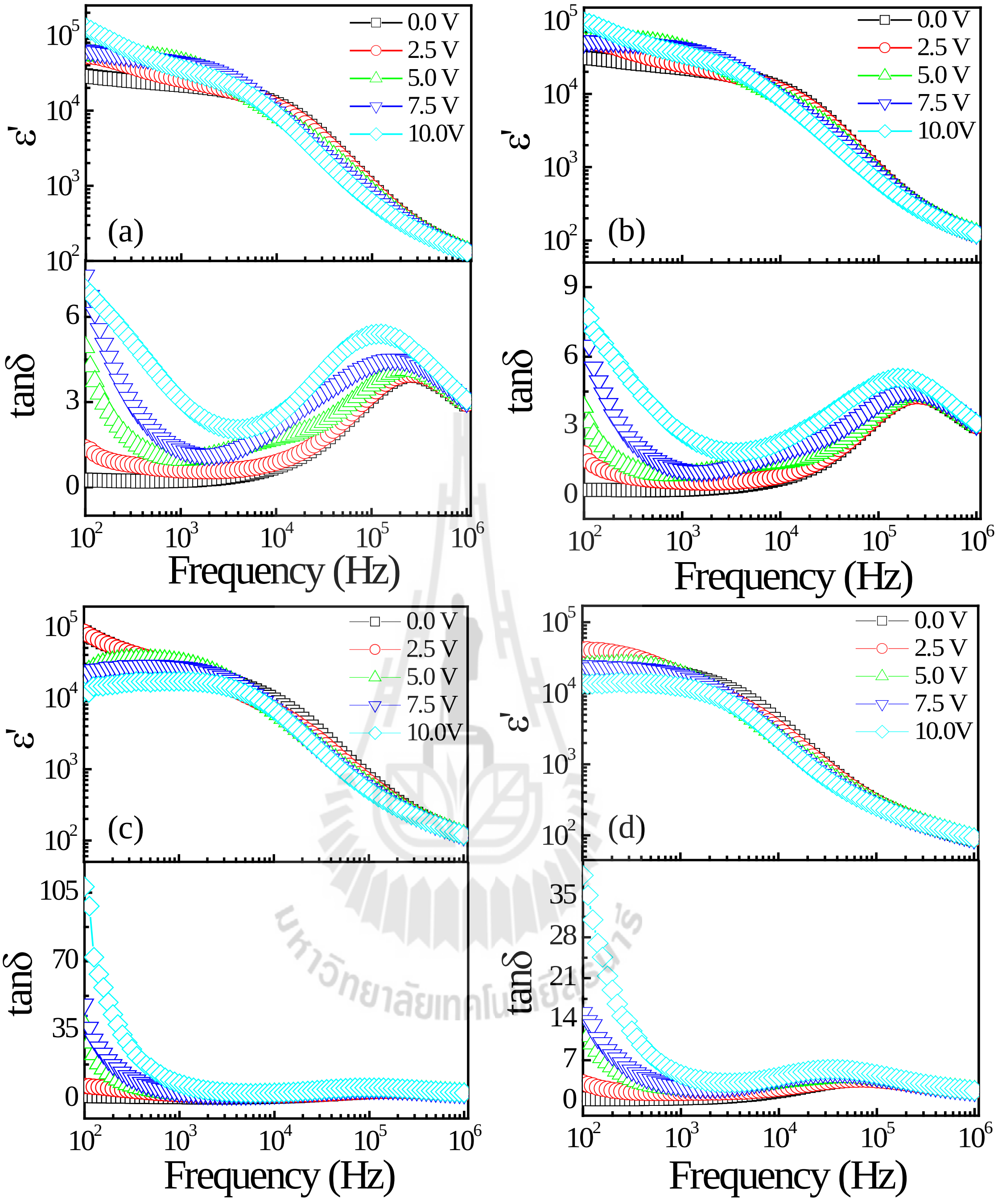

Figure 4.44 Frequency dependence of ε' and tanδ as a function dc bias voltage under 0–10 V at room temperature of Co-doped TNTs (a) x = 0, (b) x = 0.05, (c) x = 0.1 and (d) x = 0.2 prepared by hydrothermal method at 130 °C for 24 h.

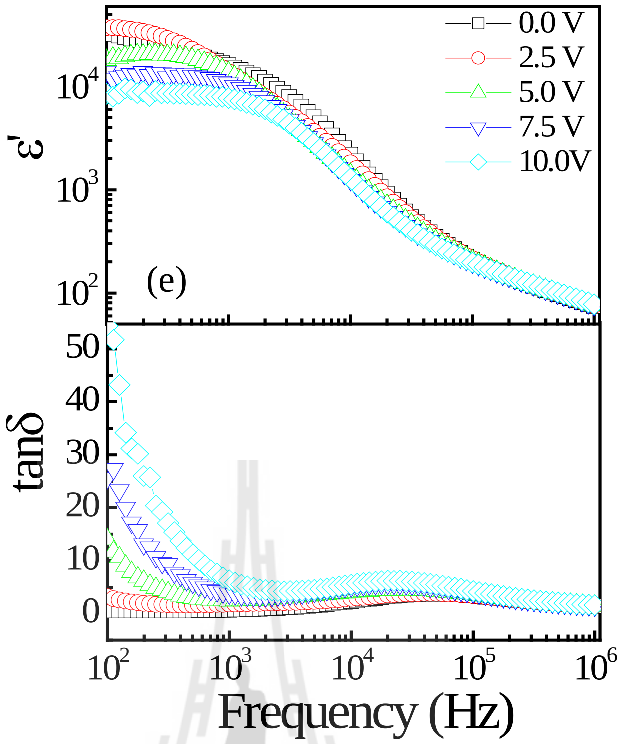

Figure 4.44 Frequency dependence of ε' and tanδ as a function dc bias voltage under 0–10 V at room temperature of Co-doped TNTs (e) x = 0.4 prepared by hydrothermal method at 130 °C for 24 h. (Cont.)

4.9.6 Impedance spectroscopy as a function of dc bias at room temperature for undoped TNTs and Fe/Co-doped TNTs samples

Figures 4.45-4.46 show the complex impedance plot of undoped TNTs and Fe/Co-doped TNTs at room temperature for various dc bias under 0-10 V. Two impedance semicircles corresponding to the grain and grain boundary are clearly observed in all of the samples. The observation suggests that the electrically heterogeneous structure exists in undoped TNTs and Fe/Co-doped TNTs samples and the core/shell model is appropriate for further analysis. As demonstrated in Figure 4.45(a), with the increasing dc bias voltage from 0 to 10 V, the diameter of the large semicircular arc significantly decreases. These results indicate that the enhanced arcs in the low frequency range contain two overlapped arcs, and thus the surface-layer and grain boundary effects are roughly separated. When increasing dc bias, the grain resistance is larger and the bulk (small semicircle) relaxation peak shifts to lower frequency. The interfacial polarizations of the surface layer and grain boundaries are suppressed by applying dc bias and the bulk polarization dependent on biases. These results are similar to those observed in the CuO ceramics reported in literatures (Putjuso *et al.*, 2011; Prakash *et al.*, 2013). Putjuso *et al*. (Thorne *et al.*, 2005; Putjuso *et al.*, 2011), observed the dielectric properties of CuO ceramics as a function of dc bias. They also found that ε' slightly decreased with the increasing dc bias voltage from 0 to 10 V. This behavior indicates that the capacitance from the external effect gradually decreased when the dc bias was applied to the CuO sample. Furthermore, Prakash *et al*. (2013) explained that this dielectric behavior as a function of dc bias is the effect of grain boundary Schottky barrier model potential.

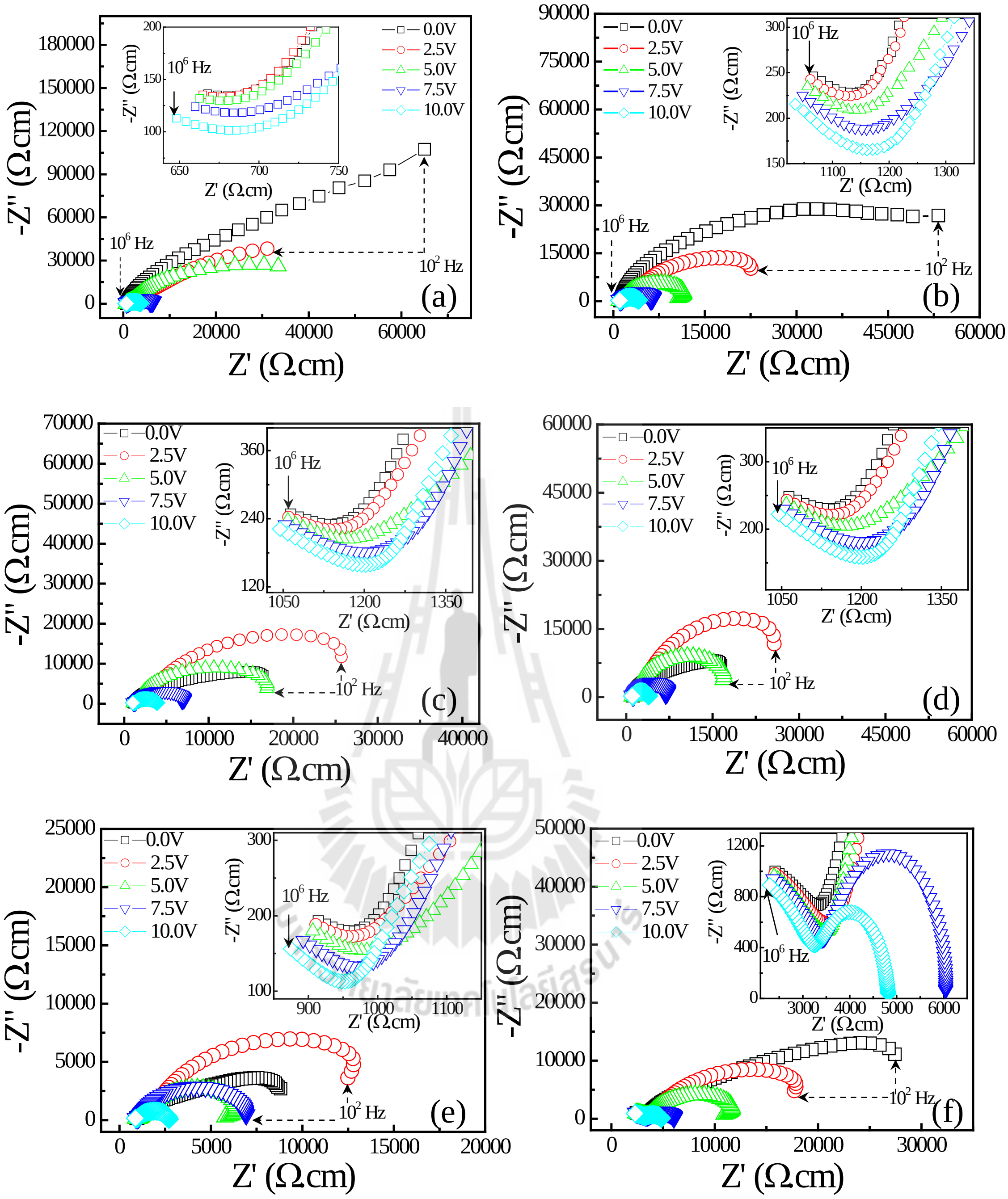

Figure 4.45 Impedance spectra of Fe-doped TNTs (a) x = 0, (b) x = 0.05 and (c) x = 0.1,(d) x = 0.2, (e) x = 0.3 and (f) x = 0.4 prepared by hydrothermal method at 130 °C for 24 h at various dc bias voltage; inset is an expanded view of high frequency data close to the origin.

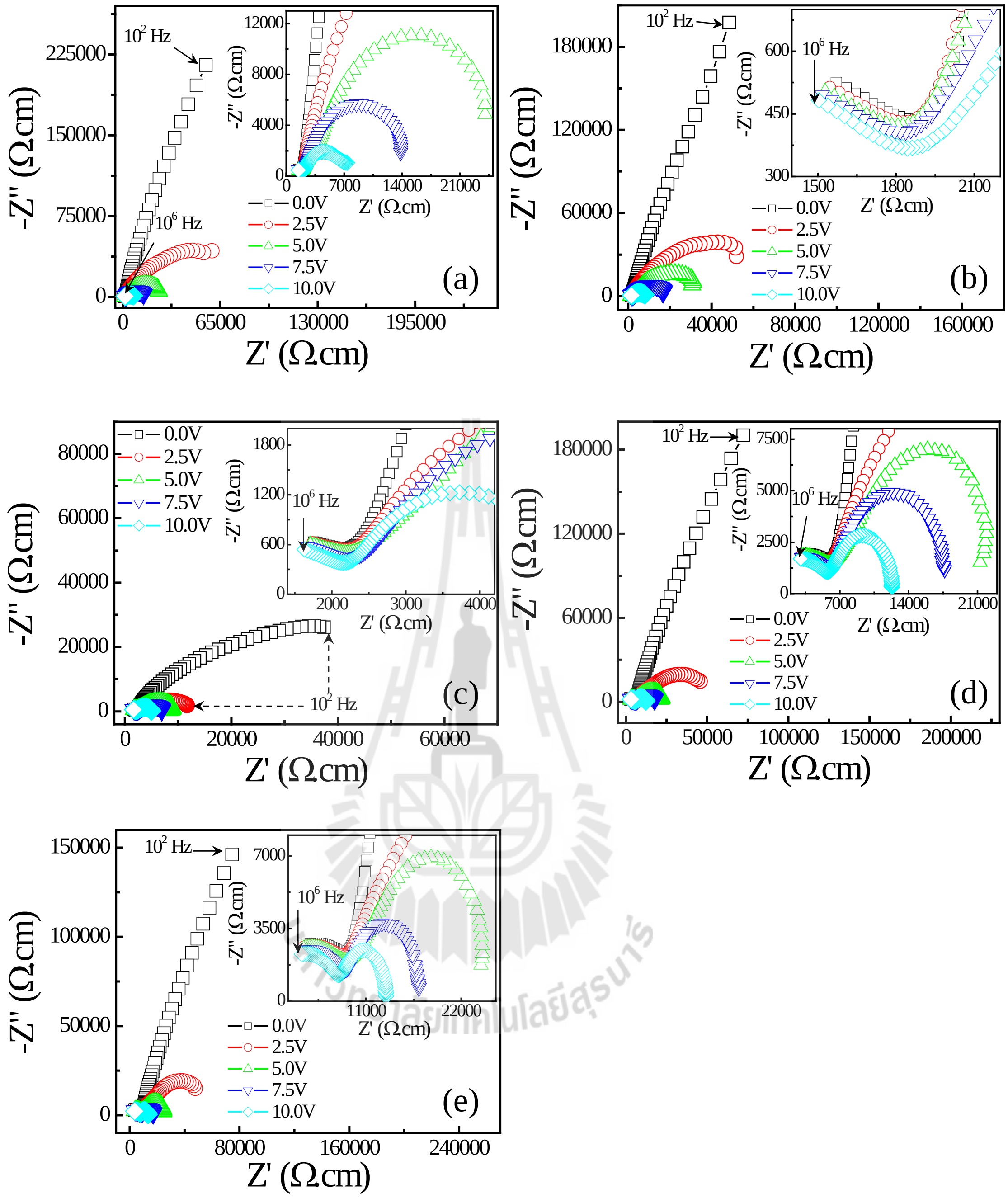

Figure 4.46 Impedance spectra of Co-doped TNTs (a) x = 0.05, (b) x = 0.1 and (c) x = 0.2,(d) x = 0.3 and (e) x = 0.4 prepared by hydrothermal method at 130 °C for 24 h at various dc bias voltage; inset is an expanded view of high frequency data close to the origin.

4.10 Non-Ohmic properties

Generally, the impedance spectroscopy measurements allow us to separate the transport contributions of the grain and grain boundary. The varistor-capacitor characteristics in undoped TNTs and Fe/Co-doped TNTs bulks might also be associated with the grain boundary regions and correlated barrier height. Normally, the Schottky barriers are created in many functional electrostatic between the grain and grain boundary regions so that the grain boundaries act as an extrinsic source of impedance. In many cases, Schottky potential barriers are created at interfaces between grains due to charge trapping at acceptor states, resulting in the bending of the conduction band across the grain boundary. This band bending produces an effective potential barrier and depletion layer for conduction electrons between the grain and grain boundary regions (Lin *et al.*, 2008). Due to the obvious grain and grain boundary characters, it would be possible to use a Schottky barrier to describe the effect of the grain boundary for undoped TNTs and Fe/Co-doped TNTs bulks.

In this work, we study the non-linear current density- electric field (J-E) properties of undoped TNTs and Fe/Co-doped TNTs.

Non-linear J-E was investigated in order to study the physical nature of electrical transport at the GBs of undoped and Fe/Co-doped TNTs. The current density-electric field (J-E) characteristic was measured at various temperatures by using a high voltage measurement unit (Keithley Model 247). The two most important parameters related to the non-Ohmic properties, i.e., nonlinear coefficient (α) and breakdown field (E_b), of the bulk TNTs-based sample can be calculated from these curves of J-E. The breakdown electric field (E_b) was obtained at J = 1 mA cm^{-2}. The non linear coefficient (α) values were calculated over the range of J = 1-10 mA cm^{-2}.

The nonlinear coefficient (α) and breakdown field (E_b) of the sample can be calculated from the curve of *J-E* following formula (Xue *et al.*, 2015; Thongbai *et al.*, 2012):

$$\alpha = \frac{\log(J_2 / J_1)}{\log(E_2 / E_1)} \tag{4.6}$$

where E_1 and E_2 are the voltage at current values of J_1 = 1 mA and J_2 = 1 mA, respectively.

Figures 4.47-4.48(a) show the non-linear *J-E* properties of all samples at different temperature. The nonlinear coefficient (α) and breakdown electric field (E_b) values of all samples at various temperatures are summarized in Table 4.7. The non-ohmic behavior tended to be linear ohmic as the temperature increased (as seen in Figures 4.106(a)-4.110(a) for Co-doped TNTs, indicating a temperature like effect on the Schottky barrier. The conduction in the breakdown region should be related to the thermion of the Schottky type (Thongbai *et al.*, 2012; Chung *et al.*, 2004). It was found that the breakdown electric field (E_b) of TNTs bulk samples was significantly decreased by Fe^{3+} or Co^{2+} doping (as shown in Figure 4.49). However, the Fe or Co doping concentration did not affect the E_b value. The non linear properties of undoped TNTs were degraded as Fe^{3+} ions or Co^{2+} ions were substituted for Ti^{4+} sites. Substitution of Fe into TNTs with nominal chemical composition of $Na_{0.036}$ $H_{1.964}$ $(Ti_{3-x}Fe_x)O_7$ or $Na_{0.036}$ $H_{1.964}$ $(Ti_{3-x}Co_x)O_7$ (x = 0-0.4) caused a decrease in dc conduction activation energy. According to a previous work (Thongbai *et al.*, 2014), the high potential barriers at internal interfaces of the CCTO/CTO composite were greatly degraded by La^{3+} doping. The creation of conduction electron due to charge compensation for La^{3+} ions substituted into Ca^{2+} sites is proposed as primary cause. In this work, electronic charge compensation by conduction electrons may have existed due to Fe^{3+} ions or Co^{2+} ions being substituted into Ti^{4+} sites. This may have been the primary cause of the degradation of nonlinear properties. To study the effect of Fe^{3+} and Co^{2+} doping ions on the formation of electrostatic potential barriers at internal interface of TNTs (nonlinear J-E properties). As shown in Figures 4.47-4.48, in case of Fe doping the E_b linearly increased with increasing temperature, whereas for Co doping the E_b decreased with increasing temperature. This indicated the influence of temperature upon the electrostatic potential barriers at internal interfaces.

The electric conduction in the pre-breakdown region is dominated by thermionic emission of Schottky type. The emission is related to electric field and temperature. Therefore, the electric current density (J) and electric field (E) will follow the relationship (Xue *et al.*, 2015; Lin *et al.*, 2008).

$$\ln J = \frac{\beta E^{1/2}}{k_B} + \left[\ln AT^2 - \frac{\Phi_B}{k_B T} \right] \tag{4.7}$$

In Eq. (4.7) is expressed as:

$$\ln J_0 = \ln AT^2 - \frac{\Phi_B}{k_B T} \tag{4.8}$$

where Φ_B is the Schottky potential-energy barrier, A is the Richardson’s constant, k_B is the Boltzmann constant, T is the temperature (K), and β is a constant related to the potential barrier width. Figures 4.47-4.48 shows the fitted results, indicating a good linear relationship between ln$J$ vs. $E^{1/2}$. Value of lnJ_0 at various temperature were calculated from the plots of ln$J$ versus $E^{1/2}$ by linearly fitting data at E=0. J_0 is the extrapolated value to E=0. Then, we plot the curves of J_0 versus 1/T. As shown in Figures 4.51-4.52, a good linear relationship between J_0 and temperature was observed. Therefore, the electric potential barrier Φ_B can be derived from the slopes of the plots. Values of Φ_B of all samples are summarized in Table 4.8. The results demonstrate that the addition of Fe^{3+} and Co^{2+} makes the potential barrier increase as compared to the TNTs sample and Φ_B of the Fe/Co-doped TNTs samples is almost independent of the doping concentration of Fe or Co.

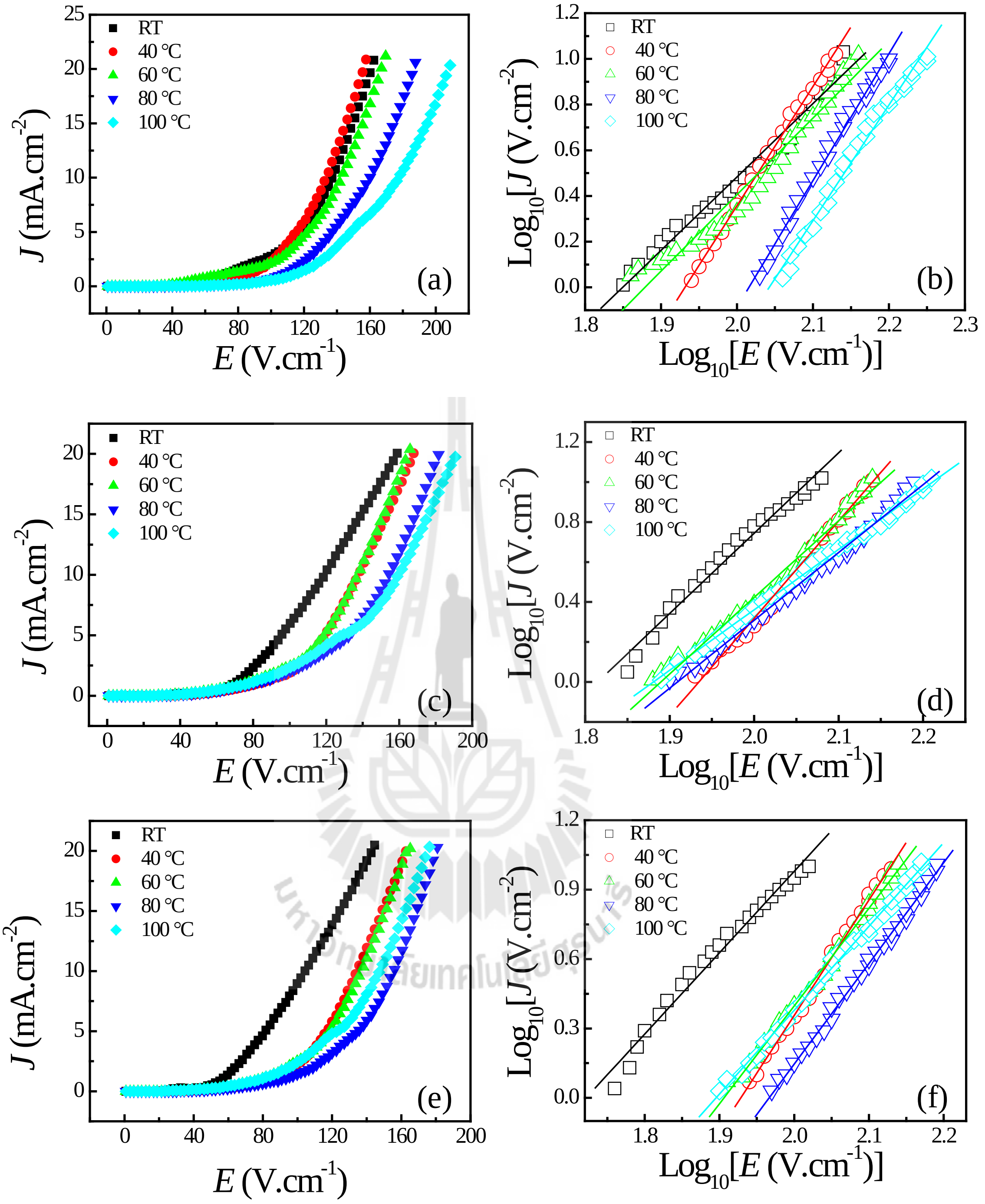

Figure 4.47 Current density-electric field *(J-E)* curves and plots of log*(J)* versus log*(E)* of Fe-doped TNTs (a-b) x = 0, (c-d) x = 0.05 and (e-f) x = 0.1, the solid lines are the best fit to the $I = V^{\alpha}$ equation.

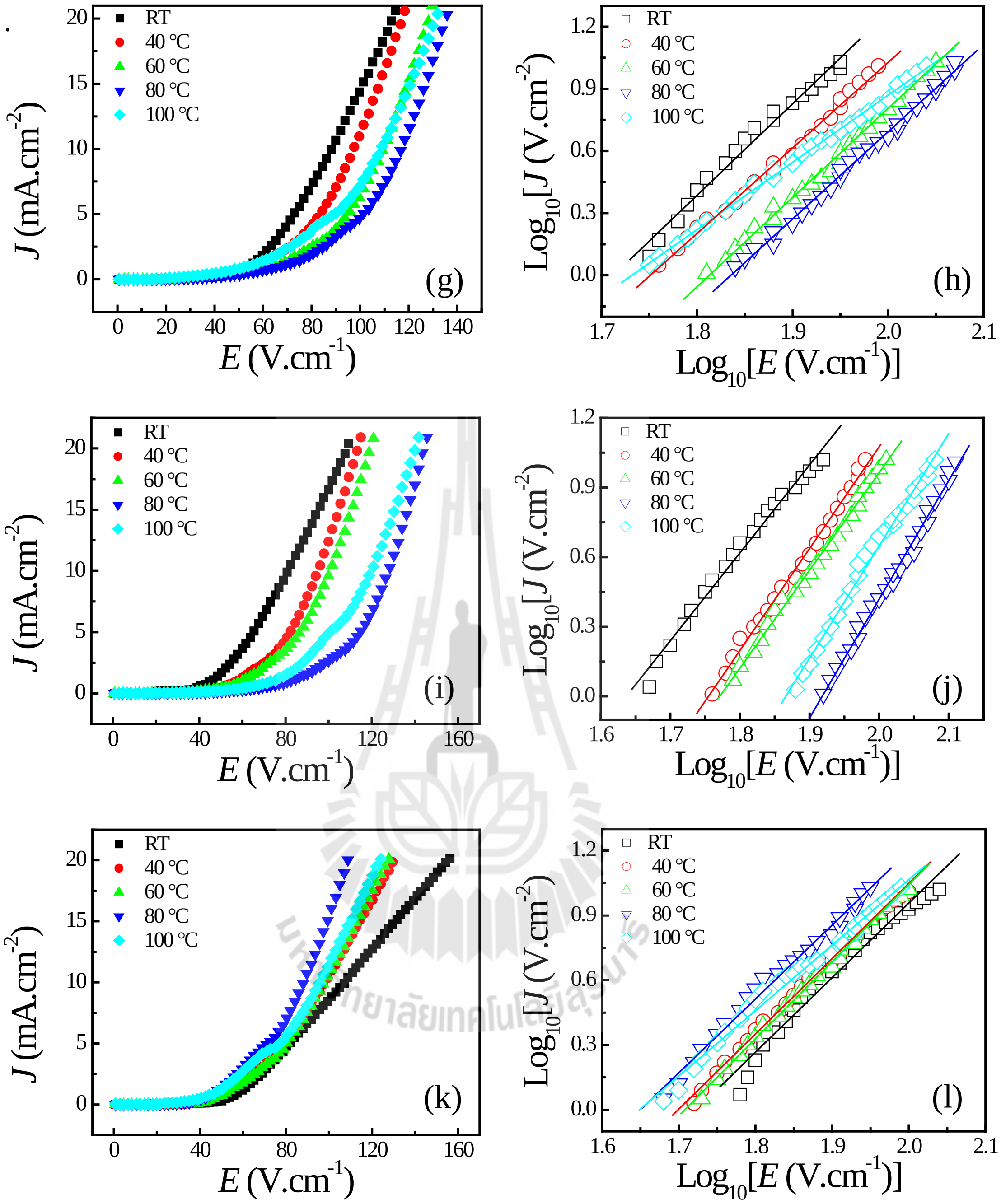

Figure 4.47 Current density-electric field *(J-E)* curves and plots of log*(J)* versus log*(E)* of Fe-doped TNTs (g-h) x = 0.2, (i-j) x = 0.3 and (k-l) x = 0.4, the solid lines are the best fit to the $I = V^{\alpha}$ equation. (Cont.)

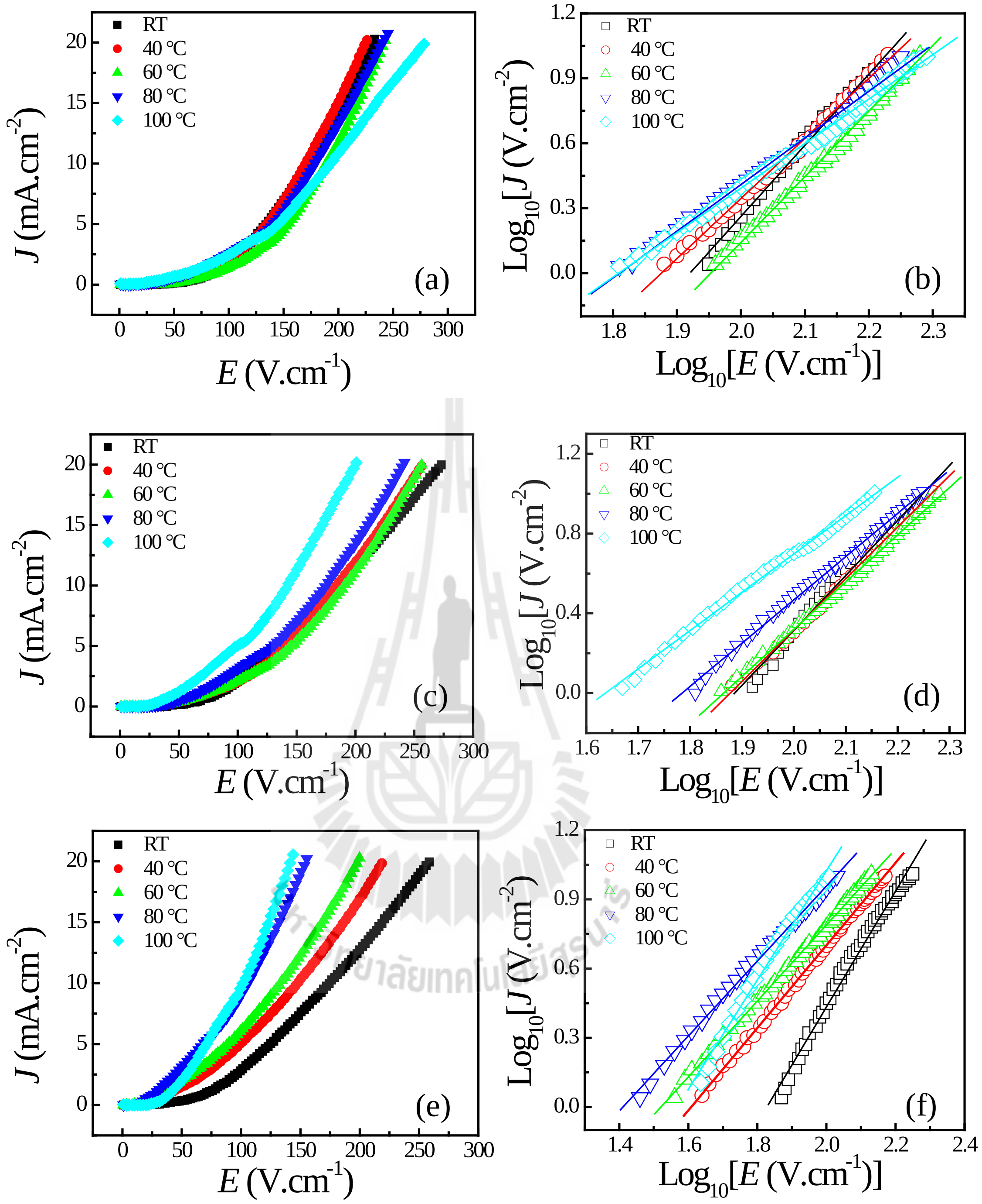

Figure 4.48 Current density-electric field *(J-E)* curves and plots of log*(J)* versus log*(E)* of Co-doped TNTs (a-b) x = 0.05, (c-d) x = 0.1 and (e-f) x = 0.2, the solid lines are the best fit to the $I = V^{\alpha}$ equation.

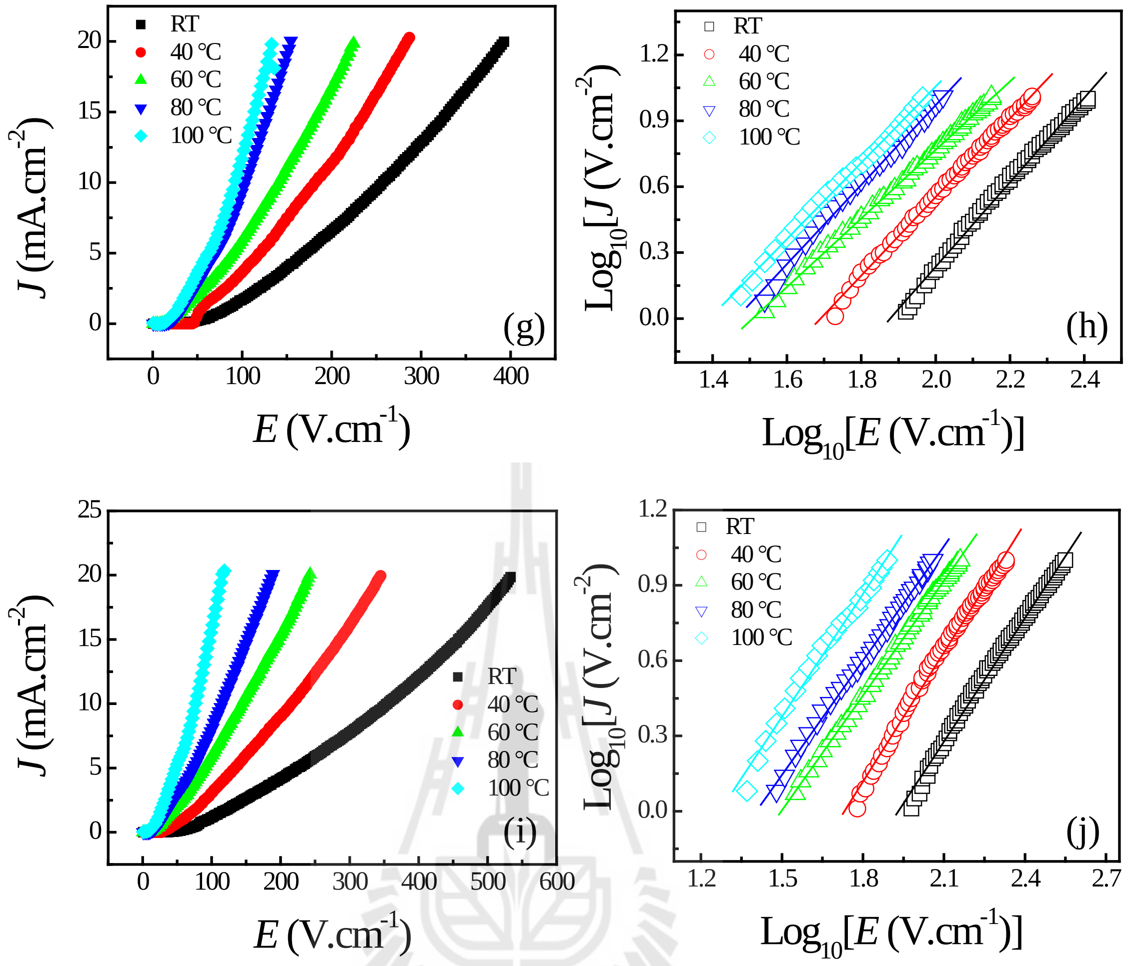

Figure 4.48 Current density-electric field *(J-E)* curves and plots of log*(J)* versus log*(E)* of Co-doped TNTs (d) x = 0.3and (e) x = 0.2, the solid lines are the best fit to the $I = V^{\alpha}$ equation. (Cont.)

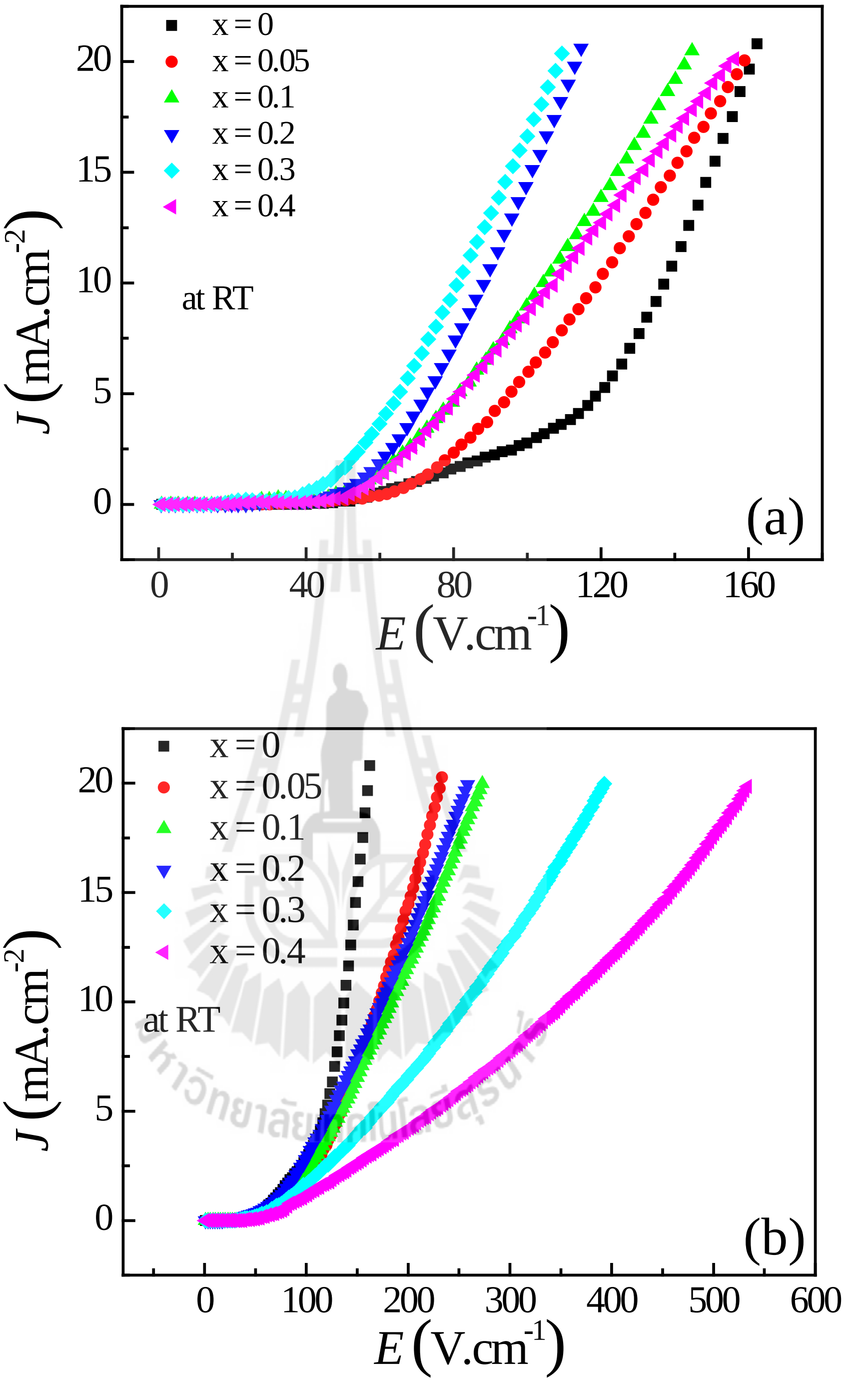

Figure 4.49 Current density-electric field (*J-E*) curves of undoped TNTs (a) Fe-doped TNTs (b) Co-doped TNTs with difference concentration.

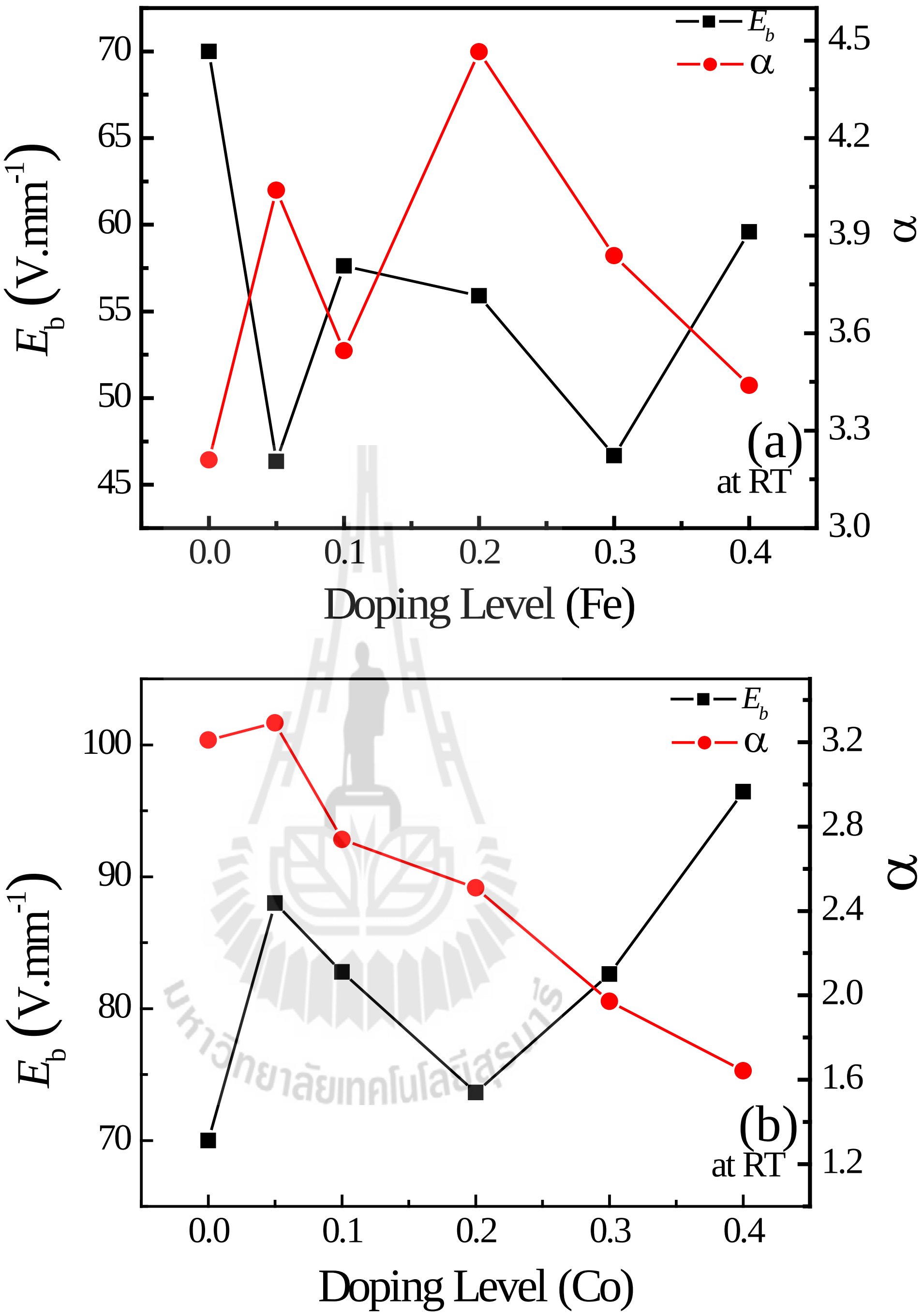

Figure 4.50 Plots of log(J) versus log(E), the solid lines are the best fit to the $I = V^{\alpha}$ equation.

Table 4.13 Summary of Non-linear coefficient (α), breakdown voltage (E_b) at various temperatures, of undoped TNTs and Fe/Co-doped TNTs bulks.

Doping Level	Fe-doped TNTs									
	α					E_b (V/cm)				
	RT	40 °C	60 °C	80 °C	100 °C	RT	40 °C	60 °C	80 °C	100 °C
x = 0	3.21	5.20	3.36	5.46	5.02	70	87	73	107	113
x = 0.05	4.04	4.84	3.83	3.41	3.04	46	55	49	52	51
x = 0.1	3.55	4.95	4.21	4.32	3.60	57	86	82	93	80
x = 0.2	4.47	4.13	4.33	4.21	3.22	56	58	65	69	56
x = 0.3	3.84	4.44	4.28	5.03	4.70	47	58	62	83	75
x = 0.4	3.44	3.46	3.53	3.38	3.00	60	52	54	48	48
Doping Level	Co-doped TNTs									
	α					E_b (V/cm)				
	RT	40 °C	60 °C	80 °C	100 °C	RT	40 °C	60 °C	80 °C	100 °C
x = 0	3.21	5.20	3.36	5.46	5.02	70	87	73	107	113
x = 0.05	3.29	2.80	3.04	2.16	2.05	89	77	91	65	65
x = 0.1	2.74	2.56	2.36	2.17	1.92	83	76	73	64	47
x = 0.2	2.51	1.78	1.64	1.63	2.37	74	43	36	29	43
x = 0.3	1.97	1.79	1.56	1.81	1.73	83	54	35	35	30
x = 0.4	1.64	1.71	1.52	1.52	1.64	96	60	35	20	23

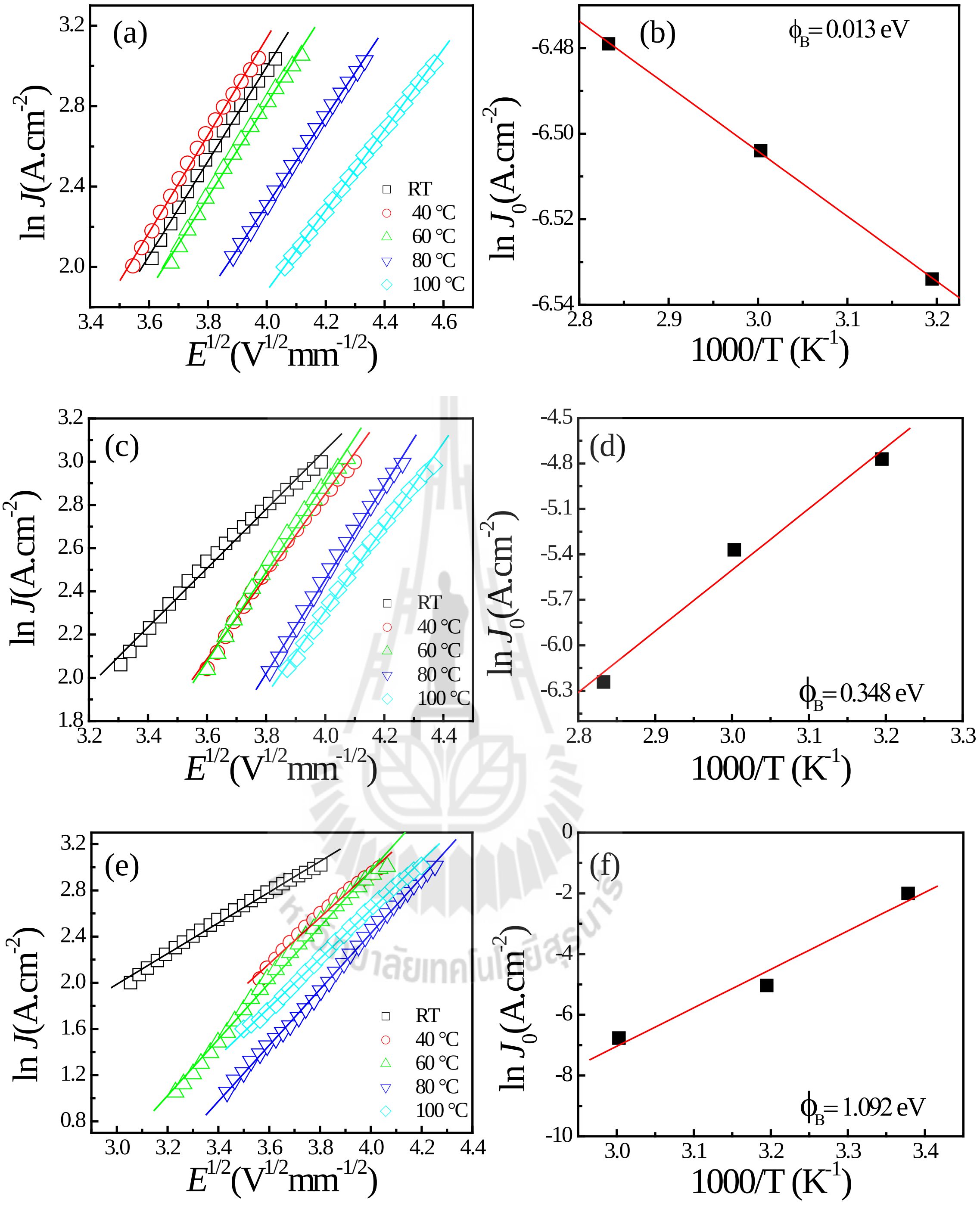

Figure 4.51 Plot of (a) ln$J$ versus $E^{1/2}$ and (b) lnJ_0 versus 1000/T of Fe-doped TNTs (a)-(b) x = 0.0, (c)-(d) x = 0.05 and (e)-(f) x = 0.1.

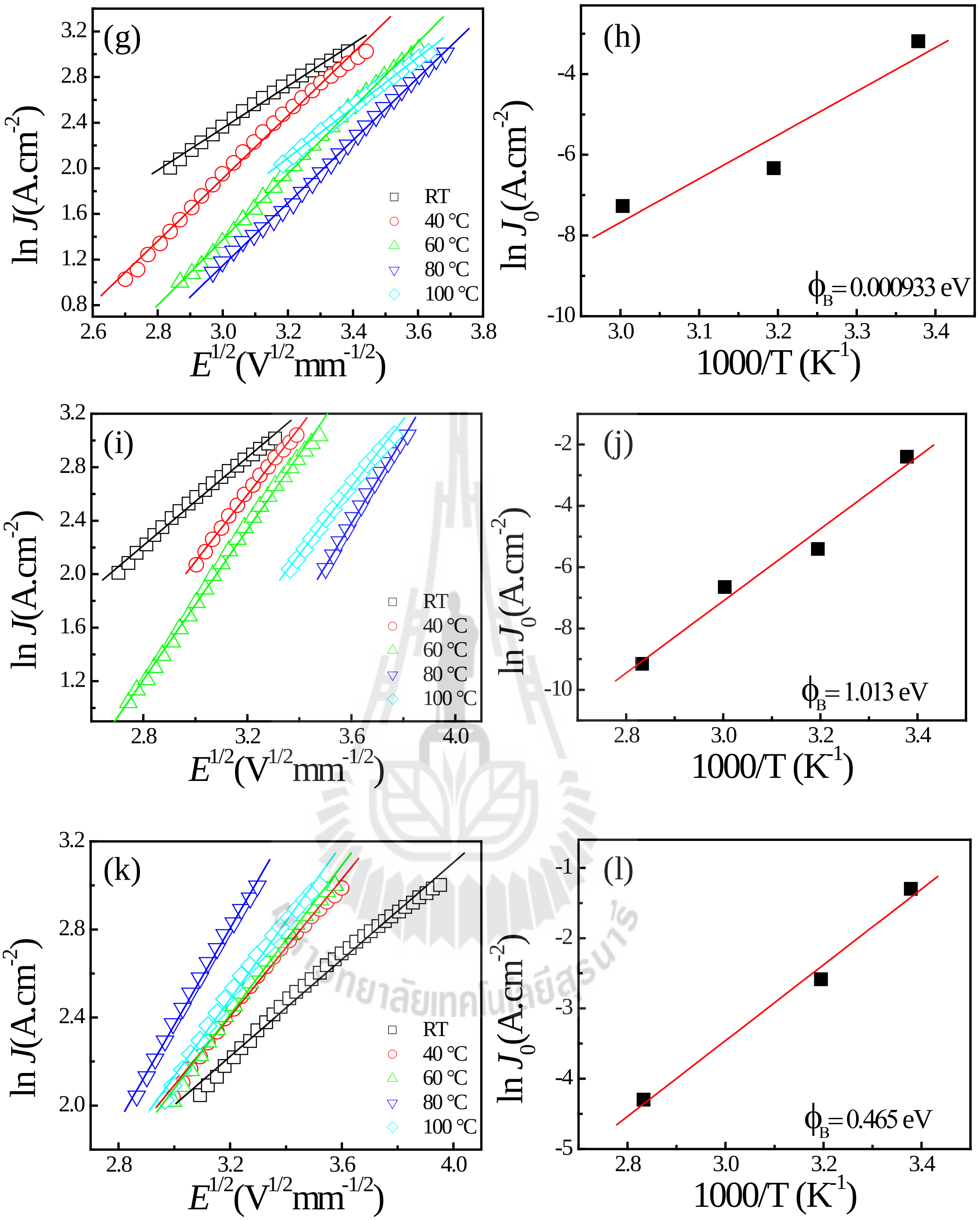

Figure 4.51 Plot of (a) ln$J$ versus $E^{1/2}$ and (b) lnJ_0 versus 1000/T of Fe-doped TNTs (g)-(h) x = 0.2, (i)-(j) x = 0.3 and (k)-(l) x = 0.4. (Cont.)

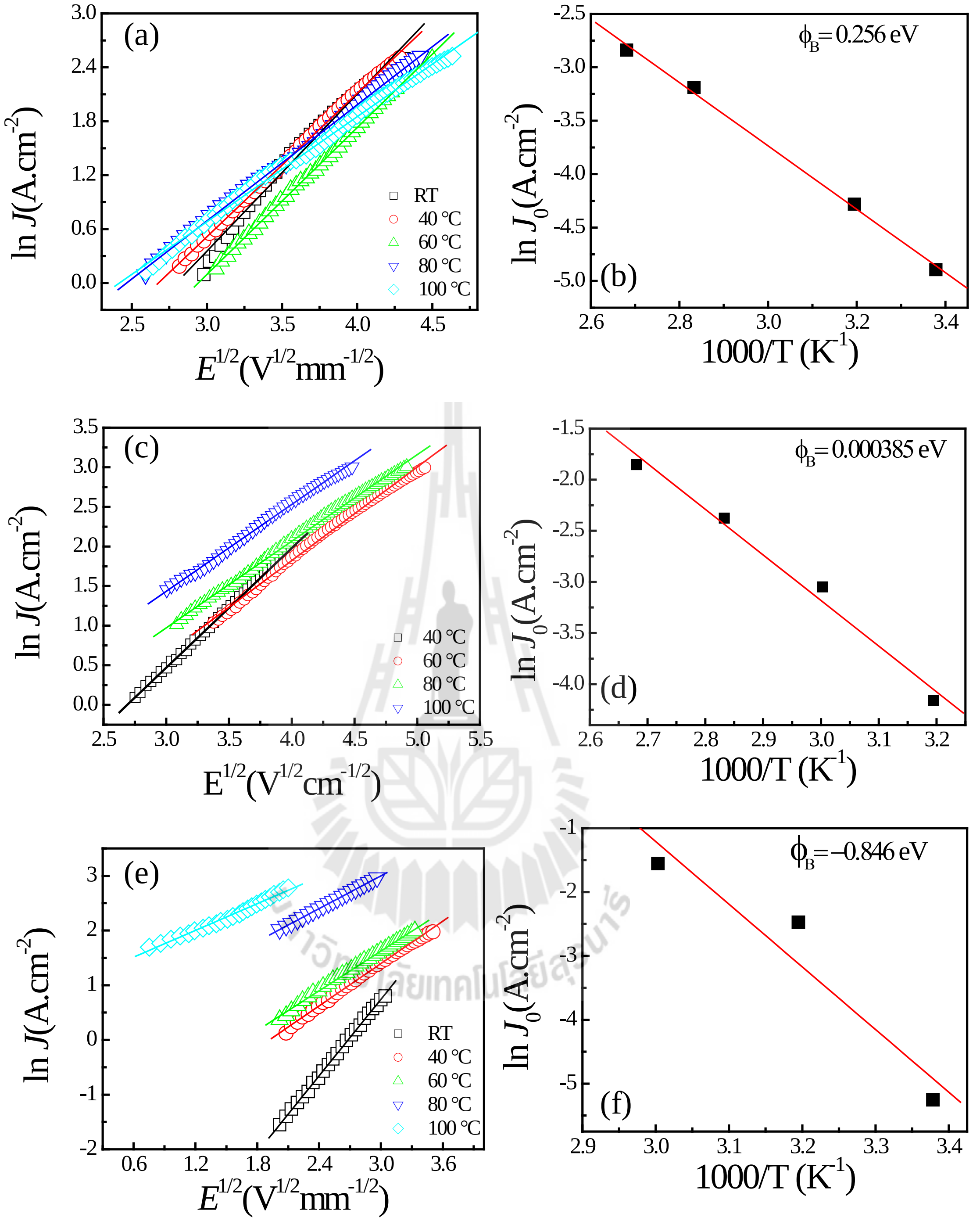

Figure 4.52 Plot of (a) ln$J$ versus $E^{1/2}$ and (b) lnJ_0 versus 1000/T of Co-doped TNTs (a)-(b) x = 0.05, (c)-(d) x = 0.1 and (e)-(f) x = 0.2.

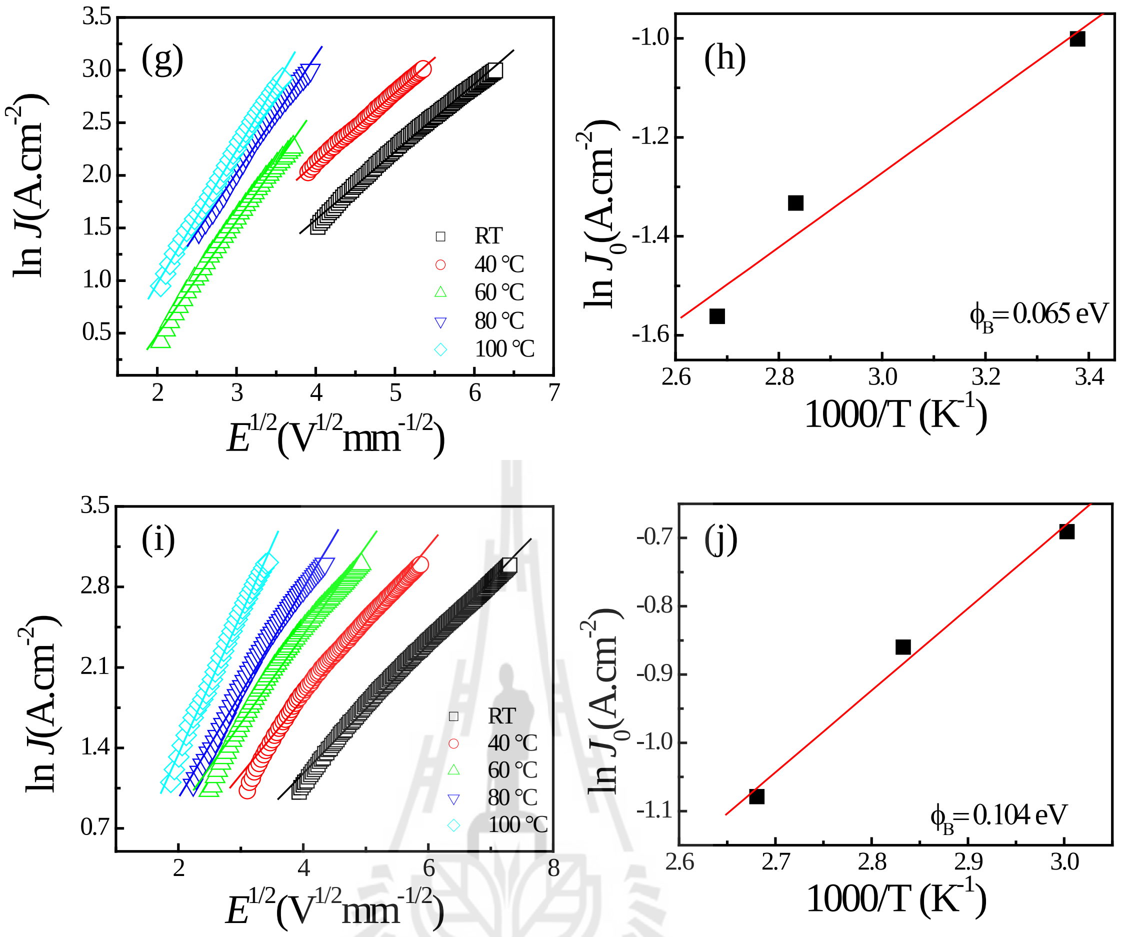

Figure 4.52 Plot of (a) ln$J$ versus $E^{1/2}$ and (b) lnJ_0 versus 1000/T of Fe-doped TNTs (d) x = 0.3 and (e) x = 0.4. (Cont.)

Table 4.14 Summary of the Shcottky potential energy barrier height (Φ_b) of undoped TNTs and Fe/Co-doped TNTs bulks

Doping	Φ_b (eV)	
Level	Fe doping	Co doping
x = 0	0.013	0.013
x = 0.05	0.348	0.256
x = 0.1	1.092	0.385
x = 0.2	0.933	0.846
x = 0.3	1.013	0. 065
x = 0.4	0.465	0.104

CHAPTER V

CONCLUSIONS AND SUGGESTIONS

5.1 Conclusion

TNTs and Fe/Co-doped TNTs were successfully prepared by a hydrothermal method at 130 °C for 24 h. The XRD, FTIR and SEAD results indicated that all the samples had a trititanate ($A_2Ti_3O_7$, A = Na or H) structure without any impurity phases, indicating that Fe and Co ions were substituted in Ti^{4+} sites. The average crystallite sizes were obtained to be about 13−25 nm. The morphology of all the samples consisted of uniform nanotubes long cylinders having a hollow cavity positioned at their centre and lying along their length. The diameters of the nanotubes were of about 7-15 nm with lengths of several hundreds of nanometer or micrometer in scales. The wall involved multilayer about 3-4 layers. HRTEM micrographs revealed the distances between layers of about 0.782-0.788 nm. The TGA and FTIR results indicated that the large amount of water molecules for TNTs was within the nanotubes. The oxygen vacancy was confirmed by XANES and XPS measurements, which presented that most of the TM ions were in the Fe^{2+}, Fe^{3+} and Co^{2+} state, while valence state of Ti was Ti^{4+}. The RT-FM observed in this sample was possibly due to the exchange interactions between spin of Fe^{3+} or Fe^{2+}, Co^{2+} and oxygen vacancy on the surface of sample. The observed paramagnetic signal was resulted from the free ions of TM without magnetic impurities. UV-vis spectra showed a redshift of band gap energy that the change in the energy band gaps of the samples is possible and is due to be the *sp-d* exchange interactions between the band electron and localized *d* electron of the Co^{2+}, Fe^{3+} ions substituting Ti ions.

All of the samples exhibited a high dielectric constant (ε') of about 10^4–10^5 at 100 Hz at room temperature. For Fe/Co-doped TNTs, the ε' increased with increasing concentration of Fe doping ions, whereas, the ε' decreased with increasing concentration of Co doping ions. This phenomenon indicated that the Fe or Co doping had influences on the TNTs by at least two possible ways, i.e., substitution and second phase, with cooperation to result in that at a certain doping concentration of the electrical properties occurred. Interestingly, the loss tangent (tanδ) of Fe/Co-doped TNTs significantly decreased, while ε' remained high. When the temperature increased higher than $T\varepsilon_m$, $\varepsilon'$of all samples decreased. Changes in dielectric properties of the bulk TNTs can be correlated to the changes in nanostructure, dehydration and phase transformation. This can cause lower carrier mobility in the TNTs, leading to the decrease in ε' and tanδ. The dielectric response behavior could be attributed to the Maxwell-Wagner polarization mechanism. The dielectric behavior was likely related to the short–range motion of electrons and other charge carriers (e.g., atoms, molecules, ions, holes, vacancies, and hydration water molecules stored in the sample) under an applied electric field. The dielectric relaxation was observed in all the samples and could be ascribed by Cole-Cole model.The dielectric constant of the samples were well fitted by the Cole-Cole equation. The complex impedance spectroscopy indicated that the bulk Fe/Co-doped TNTs were heterogeneous electrical properties, containing of semiconducting part and insulating part of internal interfaces. These results indicated that the dielectric relaxation was closely related to the conductivity of the grain interiors.

The ε′ values at the low frequencies for the TNTs decreased with increasing applied DC voltage bias. These results suggested that, with increasing the applied DC voltage, the accumulated charge carriers become mobile charges. These charges can move across the potential barrier at internal interfaces such as the grain boundaries. Consequently, the intensity of the space charge polarization at this region was decreased by increasing the applied DC voltage, while the conductivity was enhanced due to the increase in the mobile charges. This resulted in a decrease in ε′. However, ε′ of the Fe-doped TNTs (x = 0.05) and Co-doped TNTs (x = 0.05 and 0.1) increased gradually under the DC bias from 0 to 10 V compared with that of the undoped TNTs in the low frequency range (10^2 Hz). The application of DC bias activated the conduction electrons to make the electron hopping easier through the nanotubes. This resulted in remarkable contributions to space charge polarization within the nanotubes, leading to the increase in ε′The electrical properties were characterized by an impedance spectroscopy. With the increasing DC bias voltage from 0 to 10 V, the diameter of the large semicircular arc significantly decreased. This result-indicated that the dielectric behavior as a function of DC bias was correlated to the electrical response of internal interfaces due to the formation of potential barrier. According to the investigation of nonlinear current-voltage behavior, the electric conduction in the pre-breakdown region was dominated by thermionic emission of Schottky type.

The nonlinear properties of TNTs were degraded as Fe^{3+} ions or Co^{2+} ions were substituted for Ti^{4+} sites. The nonlinear behavior tended to be linear Ohmic as the temperature increased, indicating a temperature-like effect on the Schottky barrier.

It would be possible to use a Schottky barrier to describe the effect of the internal interfaces (e.g., grain boundary) for bulk TNTs and Fe/Co-doped TNTs.

The dielectric relaxation of all bulk TiO_2-based nanotubes was primarily caused by the interfacial polarization mechanism. This type of relaxation was likely to be caused by the Maxwell-Wagner polarization relxation induced by the heavy charge accumulation at interface between $Ti_3O_7^{2-}$ skeleton layers and H_2O molecule layer. This had a remarkable influence on the dielectric response, electrical characteristics of grain boundary, and related non-linear current voltage properties.

5.2 Suggestions

From the results obtained in this study, there are some important points that are not well understood and further study is needed. These include the following issues:

(1) The explanation of the dielectric behavior of bulk TiO_2-based nanotubes system is still unclear and uncompleted. Therefore, clear exploration of its origin of giant dielectric in this system should be explored.

(2) Investigation of composition of each element presented in the samples using inductively coupled plasma-mass spectrometry (ICP-MS) should be carried out.

(3) Investigation of local structures using EXAFS is needed to confirm the substitution of dopants in ferromagnetic Fe/Co-doped TNTs system.

(4) Investigation of the Curie temperature (T_c) using SQUID is required to confirm the T_c in ferromagnetic Fe/Co-TNTs system.

(5) Investigation of the electrochemical properties of TiO_2-based nanotubes system is needed to confirm the electrical conductivity values.

All these issues would allow more understanding on the structure and properties of bulk TiO_2-based nanotubes system.

REFERENCES

REFERENCES

Barreca, D., Bruno, G., Gasparotto, A., Losurdo, M. and Tondello, E. (2003). Nanostructure and optical properties of CeO2 thin films obtained by plasma-enhanced chemical vapor deposition. **Materials Science and Engineering: C** 23: 1013.

Barsoukov, E. and Macdonald, J. R. (2005). **Impedance spectroscopy**. 111 River Street, Hoboken, NJ 07030: John Wiley & Sons, Inc., Hoboken, New Jersey.

Bavykin, D. V., Friedrich, J. M., Lapkin, A. A. and Walsh, F. C. (2006). Stability of aqueous suspensions of titanate nanotubes. **Chemistry of Materials** 18: 1124.

Bayoumi, W. (2007). Structural and electrical properties of zinc-substituted cobalt ferrite. **Journal of Materials Science** 42: 8254.

Chen, Q., Zhou, W., Du, G. H. and Peng, L. M. (2002). Trititanate nanotubes made via a single alkali treatment. **Advanced Materials** 14: 1208.

Chung, S.-Y., Kim, I.-D. and Kang, S.-J. L. (2004). Strong nonlinear current-voltage behaviour in perovskite-derivative calcium copper titanate. **Nature Materials** 3: 774.

Coey, J. M. D., Stamenov, P., Gunning, R. D., Venkatesan, M. and Paul, K. (2010). Ferromagnetism in defect-ridden oxides and related materials. **New Journal of Physics** 12: 053025.

Djenadic, R. R., Nikolic, L. M., Giannakopoulos, K. P., Stojanovic, B. and Srdic, V. V. (2007). One-dimensional titanate nanostructures: Synthesis and characterization. **Journal of the European Ceramic Society** 27: 4339.

Dmistry, V., Bavykin and Walsh, F. C. (2010). **Titanate nantube and titania nanotubes synthesis, properties and application**. Science park, Milton road, Cambridge CB4 OWF, UK (2010): The royal society chemistry.

Du, G. H., Chen, Q., Che, R. C., Yuan, Z. Y. and Peng, L.-M. (2001). Preparation and structure analysis of titanium oxide nanotubes. **Applied Physics Letters** 79: 3702.

Dubey, A. K., Singh, P., Singh, S., Kumar, D. and Parkash, O. (2011). Charge compensation, electrical and dielectric behavior of lanthanum doped $CaCu_3Ti_4O_{12}$. **Journal of Alloys and Compounds** 509: 3899.

Hench, L. L. and West, J. K. (1990). **Principle of electronic material and devives** Boston Burr Ridge,: McGraw-Hill.

Hodos, M., Horváth, E., Haspel, H., Kukovecz, Á., Kónya, Z. and Kiricsi, I. (2004). Photosensitization of ion-exchangeable titanate nanotubes by CdS nanoparticles. **Chemical Physics Letters** 399: 512.

Hoyer, P. (1996). Formation of a titanium tioxide nanotube array. **Langmuir** 12: 1411.

Hu, F., Ding, F., Song, S. and Shen, P. K. (2006). Pd electrocatalyst supported on carbonized TiO_2 nanotube for ethanol oxidation. **Journal of Power Sources** 163: 415.

Hu, W., Li, L., Li, G., Meng, J. and Tong, W. (2009). Synthesis of titanate-based nanotubes for one-dimensionally confined electrical properties. **The Journal of Physical Chemistry C** 113: 16996.

Hu, W., Li, L., Tong, W. and Li, G. (2010). Water-titanate intercalated nanotubes: fabrication, polarization, and giant dielectric property. **Physical Chemistry Chemical Physics** 12: 12638.

Hu, W., Li, L., Tong, W. and Li, G. (2010). Water-titanate intercalated nanotubes: fabrication, polarization, and giant dielectric property. **Physical Chemistry Chemical Physics** 12: 12638.

Hung, W.-C., Chen, Y.-C., Chu, H. and Tseng, T.-K. (2008). Synthesis and characterization of TiO2 and Fe/TiO2 nanoparticles and their performance for photocatalytic degradation of 1,2-dichloroethane. **Applied Surface Science** 255: 2205.

Iijima, S. (1991). Helical microtubules of graphitic carbon. **Nature** 354: 56.

Inturi, S. N. R., Boningari, T., Suidan, M. and Smirniotis, P. G. (2014). Visible-light-induced photodegradation of gas phase acetonitrile using aerosol-made transition metal (V, Cr, Fe, Co, Mn, Mo, Ni, Cu, Y, Ce, and Zr) doped TiO_2. **Applied Catalysis B: Environmental** 144: 333.

Jumpatam, J., Thongbai, P., Kongsook, B., Yamwong, T. and Maensiri, S. (2012). High permittivity, low dielectric loss, and high electrostatic potential barrier in $Ca_2Cu_2Ti_4O_{12}$ ceramics. **Materials Letters** 76: 40.

Jung, J. H., Kobayashi, H., van Bommel, K. J. C., Shinkai, S. and Shimizu, T. (2002). Creation of Novel Helical Ribbon and Double-Layered Nanotube TiO_2 Structures Using an Organogel Template. **Chemistry of Materials** 14: 1445.

Kasuga, T., Hiramatsu, M., Hoson, A., Sekino, T. and Niihara, K. (1998). Formation of titanium oxide nanotube. **Langmuir** 14: 3160.

Kumar, K., Chitkara, M., Sandhu, I. S., Mehta, D. and Kumar, S. (2014). Photocatalytic, optical and magnetic properties of Fe-doped ZnO nanoparticles prepared by chemical route. **Journal of Alloys and Compounds** 588: 681.

Laokul, P., Thongbai, P., Yamwong, T. and Maensiri, S. (2012). High Dielectric Permittivity and Maxwell-Wagner Polarization in Magnetic $Ni_{0.5}Cu_{0.3}Zn_{0.2}Fe_2O_4$ Ceramics. **J Supercond Nov Magn** 25: 1195.

Lee, J.-H., Leu, I.-C., Hsu, M.-C., Chung, Y.-W. and Hon, M.-H. (2005). Fabrication of Aligned TiO2 One-Dimensional Nanostructured Arrays Using a One-Step Templating Solution Approach. **The Journal of Physical Chemistry B** 109: 13056.

Liang, H.-c. and Li, X.-z. (2009). Effects of structure of anodic TiO_2 nanotube arrays on photocatalytic activity for the degradation of 2,3-dichlorophenol in aqueous solution. **Journal of Hazardous Materials** 162: 1415.

Li, M., Feteira, A. and Sinclair, D. C. (2005). Origin of the high permittivity in $(La_{0.4}Ba_{0.4}Ca_{0.2})(Mn_{0.4}Ti_{0.6})$ ceramics. **Journal of Applied Physics** 98: 084101.

Lin, Y. H., Cai, J., Li, M., Nan, C. W. and He, J. (2008). Grain boundary behavior in varistor-capacitor TiO_2- rich $CaCu_3Ti_4O_{12}$ ceramics. **Journal of Applied Physics** 103: 074111.

Liu, J., Duan, C.-g., Mei, W. N., Smith, R. W. and Hardy, J. R. (2005). Dielectric properties and Maxwell-Wagner relaxation of compounds $A Cu_3Ti_4O_{12}$ (A=Ca, $Bi_{2/3}$, $Y_{2/3}$, $La_{2/3}$). **Journal of Applied Physics** 98: 093703.

Liu, J., Duan, C.-G., Yi, W.-G., Mei, W. N., Smith, R. W. and Hardy, J. R. (2004). Large dielectric constant and Maxwell wagner-relaxation ins $B_{2/3}Cu_3Ti_4O_{12}$. **Physical Review B** 70: 144106

Liu, M., Piao, L., Ju, S., Lu, W., Zhao, L., Zhou, C. and Wang, W. (2010). Fabrication of micrometer-scale spherical titanate nanotube assemblies with high specific surface area. **Materials Letters** 64: 1204.

Ma, R., Bando, Y. and Sasaki, T. (2003). Nanotubes of lepidocrocite titanates. **Chemical Physics Letters** 380: 577.

Ma, R., Fukuda, K., Sasaki, T., Osada, M. and Bando, Y. (2005). Structural features of titanate nanotubes/nanobelts revealed by raman, x-ray absorption fine structure and electron diffraction characterizations. **The Journal of Physical Chemistry B** 109: 6210.

Maensiri, S., Thongbai, P. and Yamwong, T. (2007). Giant dielectric permittivity observed in CaCu3Ti4O12/(Li,Ti)-doped NiO composites. **Applied Physics Letters** 90: 202908.

Maurya, D., Kumar, J. and Shripal (2006). Dielectric-spectroscopic and ac conductivity investigations on copper doped layered $Na_{1.7}K_{0.3}Ti_3O_7$ ceramics. **Journal of Applied Physics** 100: 034103.

Morgado Jr, E., de Abreu, M. A. S., Moure, G. T., Marinkovic, B. A., Jardim, P. M. and Araujo, A. S. (2007). Effects of thermal treatment of nanostructured trititanates on their crystallographic and textural properties. **Materials Research Bulletin** 42: 1748.

Morgado Jr, E., de Abreu, M. A. S., Pravia, O. R. C., Marinkovic, B. A., Jardim, P. M., Rizzo, F. C. and Araújo, A. S. (2006). A study on the structure and thermal stability of titanate nanotubes as a function of sodium content. **Solid State Science** 8: 888.

Mozia, S., Borowiak-Paleń, E., Przepiórski, J., Grzmil, B., Tsumura, T., Toyoda, M., Grzechulska-Damszel, J. and Morawski, A. W. (2010). Physico-chemical properties and possible photocatalytic applications of titanate nanotubes synthesized via hydrothermal method. **Journal of Physics and Chemistry of Solids** 71: 263.

Nakahira, A., Kato, W., Tamai, M., Isshiki, T., Nishio, K. and Aritani, H. (2004). Synthesis of nanotube from a layered $H_2Ti_4O_9 \cdot H_2O$ in a hydrothermal treatment using various titania sources. **Journal of Materials Science** 39: 4239.

Niu, L., Shao, M., Wang, S., Lu, L., Gao, H. and Wang, J. (2008). Titanate nanotubes: preparation, characterization, and application in the detection of dopamine. **Journal of Materials Science** 43: 1510.

Noipa, K., Rujirawat, S., Yimnirun, R., Promarak, V. and Maensiri, S. (2014). Synthesis, structural, optical and magnetic properties of Cu-doped ZnO nanorods prepared by a simple direct thermal decomposition route. **Applied Physics A** 117: 927.

Ou, H.-H. and Lo, S.-L. (2007). Review of titania nanotubes synthesized via the hydrothermal treatment: fabrication, modification, and application. **Separation and Purification Technology** 58: 179.

Pang, Y. L. and Abdullah, A. Z. (2012). Effect of low Fe^{3+} doping on characteristics, sonocatalytic activity and reusability of TiO_2 nanotubes catalysts for removal of Rhodamine B from water. **Journal of Hazardous Materials** 235–236: 326.

Prakash, T., Murty, B. S., Kaskhedikar, A. R. and Peshwe, P. D. (2013). Crystallite size effect on voltage tunable giant dielectric permittivity of nanocrystalline CuO. **Electronic Materials Letters** 9: 59.

Prakash, T., Ramasamy, S. and Murty, B. S. (2013). Effect of DC bias on dielectric properties of nanocrystalline $CuAlO_2$. **Electronic Materials Letters** 9: 207.

Putjuso, T., Manyum, P., Yimnirun, R., Yamwong, T., Thongbai, P. and Maensiri, S. (2011). Giant dielectric behavior of solution-growth CuO ceramics subjected to dc bias voltage and uniaxial compressive stress. **Solid State Sciences** 13: 158.

Ram, P., Choudhary, R. J., Chandra, L. S. S., Lakshmi, N. and Phase, D. M. (2007). Electrical and magnetic transport properties of Fe_3O_4 thin films on a GaAs(100) substrate. **Journal of Physics: Condensed Matter** 19: 486212.

Schileo, G., Luisman, L., Feteira, A., Deluca, M. and Reichmann, K. (2013). Structure–property relationships in $BaTiO_3$–$BiFeO_3$–$BiYbO_3$ ceramics. **Journal of the European Ceramic Society** 33: 1457.

Seo, H.-K., Kim, G.-S., Ansari, S. G., Kim, Y.-S., Shin, H.-S., Shim, K.-H. and Suh, E.-K. (2008). A study on the structure/phase transformation of titanate nanotubes synthesized at various hydrothermal temperatures. **Solar Energy Materials and Solar Cells** 92: 1533.

Shah, L. R., Ali, B., Zhu, H., Wang, W. G., Song, Y. Q., Zhang, H. W., Shah, S. I. and Xiao, J. Q. (2009). Detailed study on the role of oxygen vacancies in structural, magnetic and transport behavior of magnetic insulator: Co-CeO(2). **Journal of physics. Condensed matter : an Institute of Physics journal** 21: 486004.

Sinclair, D. C., Adams, T. B., Morrison, F. D. and West, A. R. (2002). $CaCu_3Ti_4O_{12}$: One-step internal barrier layer capacitor. **Applied Physics Letters** 80: 2153.

Sivakumar, N., Narayanasamy, A., Shinoda, K., Chinnasamy, C. N., Jeyadevan, B. and Greneche, J.-M. (2007). Electrical and magnetic properties of chemically derived nanocrystalline cobalt ferrite. **Journal of Applied Physics** 102: 013916.

Smith, A. E., Calvarese, T. G., Sleight, A. W. and Subramanian, M. A. (2009). An anion substitution route to low loss colossal dielectric $CaCu_3Ti_4O_{12}$. **Journal of Solid State Chemistry** 182: 409.

Sreekantan, S. and Wei, L. C. (2010). Study on the formation and photocatalytic activity of titanate nanotubes synthesized via hydrothermal method. **Journal of Alloys and Compounds** 490: 436.

Su, Y. H., Yin, Z. F., Xin, H. L., Zhang, H. Q., Sheng, J. Y., Yang, Y. L., Du, J. and Ling, C. Q. (2011). Optimized antimicrobial and antiproliferative activities of titanate nanofibers containing silver. **International journal of nanomedicine** 6: 1579.

Subramanian, M. A., Li, D., Duan, N., Reisner, B. A. and Sleight, A. W. (2000). High Dielectric Constant in $ACu_3Ti_4O_{12}$ and $ACu_3Ti_3FeO_{12}$ Phases. **Journal of Solid State Chemistry** 151: 323.

Sun, X. and Li, Y. (2003). Synthesis and characterization of ion-exchangeable titanate nanotubes. **Chemistry – A European Journal** 9: 2229.

Thongbai, P., Jumpatam, J., Putasaeng, B., Yamwong, T., Amornkitbamrung, V. and Maensiri, S. (2014). Effects of La3+ doping ions on dielectric properties and formation of Schottky barriers at internal interfaces in a $Ca_2Cu_2Ti_4O_{12}$ composite system. **J Mater Sci: Mater Electron** 25: 4657.

Thongbai, P., Putasaeng, B., Yamwong, T. and Maensiri, S. (2012). Current-voltage nonlinear and dielectric properties of $CaCu_3Ti_4O_{12}$ ceramics prepared by a simple thermal decomposition method. **Journal of Materials Science** 23: 795.

Thongbai, P., Vangchangyia, S., Swatsitang, E., Amornkitbamrung, V., Yamwong, T. and Maensiri, S. (2012). Non-Ohmic and dielectric properties of Ba-doped $CaCu_3Ti_4O_{12}$ ceramics. **J Mater Sci: Mater Electron** 24: 875.

Thongbai, P., Yamwong, T. and Maensiri, S. (2008). Correlation between giant dielectric response and electrical conductivity of CuO ceramic. **Solid State Commun.** 147: 385.

Thorne, A., Kruth, A., Tunstall, D., Irvine, J. T. S. and Zhou, W. (2005). Formation, structure, and stability of titanate nanotubes and their proton conductivity. **The Journal of Physical Chemistry B** 109: 5439.

Tsai, C.-C. and Teng, H. (2006). Structural features of nanotubes synthesized from NaOH treatment on TiO_2 with different post-treatments. **Chemistry of Materials** 18: 367.

Tsai, C.-C. and Teng, H. (2008). Nanotube formation from a sodium titanate powder via low-temperature acid treatment. **Langmuir** 24: 3434.

Umek, P., Cevc, P., Jesih, A., Gloter, A., Ewels, C. P. and Arčon, D. (2005). Impact of structure and morphology on gas adsorption of titanate-based nanotubes and nanoribbons. **Chemistry of Materials** 17: 5945.

Umek, P., Pregelj, M., Gloter, A., Cevc, P., Jagličić, Z., Čeh, M., Pirnat, U. and Arčon, D. (2008). Coordination of intercalated Cu^{2+} sites in copper doped sodium titanate nanotubes and nanoribbons. **The Journal of Physical Chemistry C** 112: 15311.

von A R H. (1954). Dielectric Materials and Applications. **Massachusetts: Massachusetts Institute of Technology (MIT) press.**

Wang, W., Savadogo, O. and Ma, Z.-F. (2012). Preparation of new titanium oxy nitride based electro catalysts using an anhydrous sol-gel method for water electrolysis in acid medium. **International Journal of Hydrogen Energy** 37: 7405.

Wu, D., Liu, J., Zhao, X., Li, A., Chen, Y. and Ming, N. (2006). Sequence of Events for the Formation of Titanate Nanotubes, Nanofibers, Nanowires, and Nanobelts. **Chemistry of Materials** 18: 547.

Wu, J., Nan, C. W., Lin, Y. and Deng, Y. (2002). Giant dielectric permittivity observed in Li and Ti doped NiO. **Physical Review Letters** 89: 30.

Xiaoyan, P., Dongmei, J., Yan, L. and Xueming, M. (2006). Structural characterization and ferromagnetic behavior of Fe-doped TiO_2 powder by high-energy ball milling. **Journal of Magnetism and Magnetic Materials** 305: 388.

Xue, H., Guan, X., Yu, R. and Xiong, Z. (2009). Dielectric properties and current–voltage nonlinear behavior of $Ca_{1-x}Sr_xCu_3Ti_4O_{12}$ ceramics. **Journal of Alloys and Compounds** 482: L14.

Xue, R., Liu, D., Chen, Z., Dai, H., Chen, J. and Zhao, G. (2015). Dielectric and Nonohmic Properties of $CaCu_3Ti_4O_{12}/SrTiO_3$ Ceramics. **Journal of Elec Materi** 44: 1088.

Yimnirun, R., Ananta, S. and Laoratanakul, P. (2005). Dielectric and ferroelectric properties of lead magnesium niobate–lead zirconate titanate ceramics prepared by mixed-oxide method. **Journal of the European Ceramic Society** 25: 3235.

Yoshida, R., Suzuki, Y. and Yoshikawa, S. (2005). Effects of synthetic conditions and heat-treatment on the structure of partially ion-exchanged titanate nanotubes. **Materials Chemistry and Physics**: 409.

Yuan, R., Zhou, B., Hua, D. and Shi, C. (2013). Enhanced photocatalytic degradation of humic acids using Al and Fe co-doped TiO_2 nanotubes under UV/ozonation for drinking water purification. **Journal of Hazardous Materials** 262: 527.

Zhang, L., Lin, H., Wang, N., Lin, C. and Li, J. (2007). The evolution of morphology and crystal form of titanate nanotubes under calcination and its mechanism. **Journal of Alloys and Compounds** 431: 230.

Zhang, M., Jin, Z., Zhang, J., Guo, X., Yang, J., Li, W., Wang, X. and Zhang, Z. (2004). Effect of annealing temperature on morphology, structure and photocatalytic behavior of nanotubed $H_2Ti_2O_4(OH)_2$. **Journal of Molecular Catalysis A: Chemical** 217: 203.

Zhang, S., Peng, L. M., Chen, Q., Du, G. H., Dawson, G. and Zhou, W. Z. (2003). Formation Mechanism of $H_2Ti_3O_7$ Nanotubes. **Physical Review Letters** 91: 256103.

Zhao, J., Wang, X., Sun, T. and Li, L. (2007). Crystal phase transition and properties of titanium oxide nanotube arrays prepared by anodization. **Journal of Alloys and Compounds** 434–435: 792.

Zhu, J., Deng, Z., Chen, F., Zhang, J., Chen, H., Anpo, M., Huang, J. and Zhang, L. (2006). Hydrothermal doping method for preparation of Cr^{3+}-TiO_2 photocatalysts with concentration gradient distribution of Cr^{3+}. **Applied Catalysis B: Environmental** 62: 329.

Zhu, J., Zheng, W., He, B., Zhang, J. and Anpo, M. (2004). Characterization of Fe–TiO_2 photocatalysts synthesized by hydrothermal method and their photocatalytic reactivity for photodegradation of XRG dye diluted in water. **Journal of Molecular Catalysis A: Chemical** 216: 35.

APPENDICES

APPENDIX A

PAPER PUBLICATIONS

1. **Kasian P**, Yamwong T, Thongbai P, Rujirawat S, Yimnirun R, and Maensiri S. The Dc bias Voltage Effect and Non-Linear Dielectric properties of Titanate Nanotubes, Journal Nanoscience Nanotechnology 15, (2015)

2. **Kasian P**, Yamwong T, Thongbai P, Rujirawat S, Yimnirun R, and Maensiri S. Co-doped titanate nanotubes. Synthesis, characterization, and properties, Jpn. Journal Apply Physics. 53, 06JG12, (2014).

3. **Kasian P**, Yamwong T, Thongbai P, Rujirawat S, Yimnirun R, and Maensiri S. Structure, magnetic, and dielectric properties of Fe-doped titanate nanotubes (TNTs) prepared by hydrothermal route. (Manuscript)

APPENDIX B

PRESENTATIONS

1. **Kasian P**, Yamwong T, Thongbai P, Rujirawat S, Yimnirun R, and Maensiri S. Structure and Electrical properties of Titanate-based Nanotubes. **The 4th Thailand International Nanotechnology Conference 2014**; November 25-28, 2014, Thailand Science Park Convention Center, Pathumthani, Thailand. (Oral presentation)

2. **Kasian P**, Yamwong T, Thongbai P, Rujirawat S, Yimnirun R, and Maensiri S. Structure, magnetic, and dielectric properties of Fe-doped titanate nanotubes (TNTs) prepared by hydrothermal route. **The 9th Meeting on Ferroelectrics jointly with 9th Asian Meeting on Electroceramics (AMF-AMEC 2014)**; October 26-30, 2014 International Convention Center, Shanghai, China. (Oral presentation)

3. **Kasian P**, Yamwong T, Thongbai P, Rujirawat S, Yimnirun R, and Maensiri S. The dc bias voltage effect and non-linear dielectric properties of giant dielectric titanate nanotubes. **NANO KOREA 2014 Symposium**; July 2-4, 2014, Coex, Seoul, Korea. (Poster presentation)

4. **Kasian P**, Yamwong T, Thongbai P, Rujirawat S, Yimnirun R, and Maensiri S. Dielectric properties of Titanate Nanotubes prepared by hydrothermal route. **The 3rd Academic Conference on Natural Science for Master and PhD**. **Students from**

ASEAN countries (CASEAN-2013); November 11-15, 2013, Phnom Penh, Cambodia. (Poster presentation)

5. **Kasian P**, Yamwong T, Thongbai P, Rujirawat S, Yimnirun R, and Maensiri S. Co-doped titanate nanotubes: Synthesis, characterization, and properties. **26th International Microprocessor and Nanotechnology Conference**; November 3-12, 2014, Royton Sapporo, Hokkaido, Japan. (Poster presentation)

CURRICULUM VITAE

Name: Miss Pristanuch Kasian

Date of Birth: 31st January 1984

Place of Birth: Ubon Ratchathani, Thailand.

Education:

2010-2015 **PhD candidate in Physics**

School of Physics, Institute of Science Suranaree University of Technology, NakhonRatchasima, Thailand

Dielectric properties of titanate nanotubes prepared by hydrothermal route

2008-2010 **M.Sc. (Physics)**

Department of Physics, Faculty of Science,

Ubon Ratchathani University, Ubon Ratchathani, Thailand

Synthesis of CuO Nanostructures by Thermal Method

2003-2007 **B. Sc. (Physics)**

Department of Physics, Faculty of Science, Ubon Ratchathani University, Ubon Ratchathani, Thailand.